



**University of  
Nottingham**  
UK | CHINA | MALAYSIA

# **Dissecting the ultrastructure of meiotic chromosomes and the role of the chromosome periphery using advanced imaging**

Thesis submitted to the University of Nottingham for the degree of  
Doctor of Philosophy (PhD)

March 2025

Eva Louise Simpson BSc MSc

20312273

Under the supervision of Dr Daniel Booth, Prof Andrew McAinsh, Prof  
Ramiro Alberio, Prof David Bates

School of Medicine

University of Nottingham

## Declaration

I confirm that the work presented in this thesis is my own work, except where stated in the text. The material and figures included in Chapter 3 draw heavily on my previously published research paper (Cisneros-Soberanis & Simpson et al., 2024), and the materials and figures included in Chapter 4 draw heavily on my research paper (Simpson & Wetherall et al., 2024) currently in preprint. Both are presented in line with JCB journals' article reuse permissions policies. I understand the nature of plagiarism and that it is a serious academic offence. I confirm that no material in this project has been plagiarised.

**Name:** Eva Louise Simpson

A handwritten signature in black ink, appearing to read 'E. Simpson', written in a cursive style.

**Signed:**

**Date:** 30.03.25

## Abstract

Understanding the three-dimensional structure of chromosomes is essential for elucidating the mechanisms that govern their behaviour during cell division. However, detailed ultrastructural analysis of chromosomes in oocytes has been limited by technical challenges associated with imaging large, spherical cells. This thesis describes the development and application of a three-dimensional correlative light and electron microscopy (3D-CLEM) pipeline to overcome these challenges and enable high-resolution visualisation of chromosomal architecture during meiosis.

The 3D-CLEM workflow was first established and optimised using mitotic cells, allowing for precise correlation between fluorescence and electron microscopy images. This approach led to the generation of a high-resolution 'mitotic atlas', enabling the structural classification and quantitative comparison of mitotic chromosomes. Notably, this work contributed to the identification and characterisation of a novel chromatin state—plateaued compaction—recently reported in Cisneros-Soberanis & Simpson et al., (2024).

Following successful implementation in mitotic systems, the pipeline was applied to mouse oocytes to investigate the organisation and function of the chromosome periphery during meiosis. Immunolabelling and correlative imaging confirmed the presence of the proliferation marker Ki-67 at the periphery of meiotic chromosomes, establishing its role as a key organiser of this structural domain. Targeted disruption of the periphery revealed its critical importance for maintaining chromosome integrity, with its removal resulting in altered chromatin

morphology and disorganisation within the meiotic spindle. This exciting discovery led to a second publication currently in pre-print and under review with Nature Comms (Simpson et al., 2024)

Finally, the pipeline was extended to the study of human oocytes, where it enabled the first three-dimensional reconstructions of meiotic chromosomes. These early datasets demonstrate the challenges associated with analysis of these cell types and defines key characteristics to make this work possible. Following development of the technique for handling human oocytes the feasibility of 3D-CLEM for human oocyte research was proven and the data provides a foundation for future investigations into chromosomal architecture in human meiosis.

In summary, this work establishes and validates a novel 3D-CLEM approach for high-resolution structural analysis of chromosomes in large mammalian oocytes. The pipeline has been successfully applied to both mouse and human cells, yielding new insights into the role of the chromosome periphery and enabling enhanced visualisation of chromosome structure during meiosis. This methodological advancement opens new avenues for investigating the ultrastructure of chromosomes and associated sub-nuclear compartments in rare or challenging cell types.

## Acknowledgements

Firstly, I would like to thank my supervisors for their support during this PhD. Particularly, Dan who provided support, advice and guidance in all aspects of this project and without whom there would not be a project on this paper today. The rest of Booth Lab, both past and present, I am so grateful to have worked within such a skilled and supportive research group.

I would also like to extend my gratitude to all the collaborators involved in this project, including Andrew McAinsh and his group at the University of Warwick, especially Cerys and Aleksandra; Suzanne Madgwick and Ben Wetherall at the University of Newcastle; and Alison Beckett at the University of Liverpool, whose support was especially appreciated.

To my friends, George, Zarah, Grace, Michaela, Kathryn and Pippa, thank you for every wine and painting evening, Portland coffee trip and the endless karaoke. Unfortunately, you are all now stuck with me forever.

To my family. You have supported me unconditionally and I would not have been able to get through this PhD without you. Mum and Dad, you were always there for me whenever I needed you and without you, I would not have been able to do this PhD. I have definitely not thanked you enough. Rachel and Simon, you have always been reassuring and encouraging and willing to listen to me complain or talk about complete nonsense for hours and I appreciate every second. Finley and Mila, you are the best things in the world and your little cuddles always made me feel better when I was having a hard time. I cannot put into words how grateful I am for you all. I hope I've made you proud.

## Contents

|  |           |
|--|-----------|
| <b>Declaration .....</b>   | <b>1</b>  |
| <b>Abstract .....</b>  | <b>2</b>  |
| <b>Acknowledgements .....</b>                                    | <b>4</b>  |
| <b>Contents .....</b>  | <b>5</b>  |
| <b>List of Figures .....</b>                                     | <b>12</b> |
| <b>List of Tables .....</b>                                      | <b>16</b> |
| <b>List of Abbreviations .....</b>                               | <b>17</b> |
| <b>1. Introduction .....</b>                                     | <b>21</b> |
| 1.1. Importance of cell division.....                            | 21        |
| 1.1.1. The Cell Cycle .....                                      | 22        |
| 1.1.2. Mitosis .....   | 25        |
| 1.1.3. Meiosis .....   | 30        |
| 1.1.4. Oocytes.....  | 33        |
| 1.1.5. Aneuploidy .....  | 35        |
| 1.2. Chromosomal ultrastructure .....                            | 40        |
| 1.2.1. Definition and historical background .....                | 40        |
| 1.2.2. Basic structure and organisation of chromosomes .....     | 44        |
| 1.2.3. Chromosome territories and positioning within the nucleus |           |

|  |           |
|--|-----------|
| 1.2.4. Chromosome components .....                                   | 47        |
| 1.3. Ki67 .....  | 59        |
| 1.3.1. Ki67 background .....   | 59        |
| 1.3.2. Use as a proliferation marker.....                            | 60        |
| 1.3.3. Ki67 and the Chromosome Periphery.....                        | 61        |
| 1.4. Advanced Imaging Techniques .....                               | 66        |
| 1.4.1. Overview of imaging techniques used in chromosome<br>research | 66        |
| 1.4.2. Fluorescence microscopy and super-resolution microscopy       | 67        |
| 1.4.3. Electron microscopy .....                                     | 71        |
| 1.4.4. Correlative Light-Electron Microscopy (3D-CLEM) .....         | 75        |
| 1.5. Research Objectives and Hypotheses .....                        | 77        |
| Hypotheses .....   | 77        |
| Aims .....   | 77        |
| Significance of the Research:.....                                   | 78        |
| <b>2. Methods .....</b>  | <b>79</b> |
| 2.1. Cell Biology .....  | 79        |
| 2.1.1. Cell types used.....  | 79        |
| 2.1.2. Cell Culture.....   | 80        |
| 2.1.3. Cell Storage .....  | 81        |

|   |     |
|---|-----|
| 2.1.4. Mycoplasma testing.....              | 81  |
| 2.1.5. Cell counting and seeding.....       | 82  |
| 2.2. Mouse Oocytes.....                     | 83  |
| 2.2.1. Collection and Culture.....          | 83  |
| 2.2.2. Ki67 Knockdown.....                  | 84  |
| 2.3. Human Oocyte collection.....           | 85  |
| 2.3.1. Donation to Research.....            | 85  |
| 2.3.1. Oocyte collection and transport..... | 85  |
| 2.3.2. Oocyte Fixation.....                 | 86  |
| 2.4. Light Microscopy.....                  | 86  |
| 2.4.1. Immunofluorescence.....              | 86  |
| 2.4.2. Confocal Microscopy.....             | 88  |
| 2.4.3. Live Imaging.....                    | 90  |
| 2.5. Electron Microscopy.....               | 91  |
| 2.5.1. 3D-CLEM protocol.....                | 91  |
| 2.5.2. SBF-SEM microscope set up.....       | 96  |
| 2.5.3. FIB-SEM microscope set-up.....       | 98  |
| 2.5.4. EM Imaging of mouse oocytes.....     | 100 |
| 2.5.5. Greyscale analysis.....              | 100 |
| 2.6. AMIRA Modelling.....                   | 101 |

|           |  |            |
|-----------|--|------------|
| 2.6.1.    | Analysis of Light Microscopy Data using AMIRA .....  | 101        |
| 2.6.2.    | Analysis of Electron Microscopy Data Using AMIRA .....   | 101        |
| 2.6.3.    | Generating Surfaces.....   | 102        |
| 2.7.      | Statistical Analysis.....  | 104        |
| <b>3.</b> | <b>Establishing 3D-CLEM for chromosomal investigation of somatic cells and generating the first “mitotic chromosome atlas”</b> | <b>105</b> |
| 3.1.      | Introduction .....   | 105        |
| 3.2.      | Hypothesis and Aims .....  | 107        |
|           | Hypothesis.....  | 107        |
|           | Aims .....   | 108        |
| 3.3.      | Results.....   | 109        |
| 3.3.1.    | Optimisation of the pipeline.....  | 109        |
| 3.3.2.    | Mitotic Chromosome Atlas .....   | 146        |
| 3.4.      | Discussion .....   | 156        |
| <b>4.</b> | <b>Role of Ki67 in meiotic cells.....</b>  | <b>168</b> |
| 4.1.      | Introduction .....   | 168        |
| 4.2.      | Hypothesis and Aims .....  | 169        |
|           | Hypothesis.....  | 169        |
|           | Aims .....   | 169        |

|           |   |            |
|-----------|---|------------|
| 4.3.      | Results.....  | 170        |
| 4.3.1.    | Ki67 is present on the periphery of meiotic chromosomes<br>170  |            |
| 4.3.2.    | Ki67 Live Imaging Phenotypes .....  | 171        |
| 4.3.3.    | Super-resolution light microscopy to investigate<br>chromosome changes following Ki67 depletion ..... | 182        |
| 4.3.4.    | Electron microscopy to study ultrastructural chromosome<br>changes following Ki67 depletion .....     | 189        |
| 4.4.      | Discussion .....  | 209        |
| <b>5.</b> | <b>Advanced Imaging of Human Oocytes and the First<br/>Whole Oocyte 3D Model .....</b>                | <b>219</b> |
| 5.1.      | Introduction .....  | 219        |
| 5.2.      | Hypothesis and Aims .....   | 221        |
|           | Hypothesis.....   | 221        |
|           | Aims .....  | 221        |
| 5.3.      | Methods.....  | 222        |
| 5.3.1.    | Fixation .....  | 222        |
| 5.3.2.    | Immunofluorescence.....   | 222        |
| 5.3.3.    | Fixed Oocyte Imaging .....  | 223        |
| 5.4.      | Results and discussion.....   | 224        |
| 5.4.1.    | Ki67 and the Periphery in Meiosis .....   | 224        |

|           |   |            |
|-----------|---|------------|
| 5.4.2.    | Human oocyte samples for 3D-CLEM .....      | 225        |
| 5.4.3.    | 3D-CLEM abnormalities in Human oocytes..... | 225        |
| 5.4.4.    | Visible chromosomes and kinetochores .....  | 237        |
| 5.4.5.    | Whole oocyte chromosome modelling.....      | 241        |
| 5.4.6.    | Optimisation for Human Oocytes .....        | 243        |
| 5.5.      | Discussion .....                            | 247        |
|           | Patient-derived oocyte variations .....     | 248        |
| <b>6.</b> | <b>Discussion .....</b>                     | <b>251</b> |
| 6.1.      | Summary of Research Aims .....              | 251        |
| 6.2.      | Mitotic Atlas: .....                        | 254        |
| 6.3.      | Ki67 in Meiosis.....                        | 255        |
| 6.4.      | Volume Imaging of Human Oocytes.....        | 256        |
| 6.5.      | Limitations .....                           | 258        |
|           | Throughput and Sample Size:.....            | 258        |
|           | Stage Variability in Meiosis: .....         | 259        |
|           | Technical Difficulties.....                 | 259        |
|           | Biological Sample Constraints .....         | 261        |
| 6.6.      | Significance and Future Directions.....     | 262        |
| <b>7.</b> | <b>Appendix .....</b>                       | <b>264</b> |
| 7.1.      | Professional Industry Placement.....        | 264        |

|  |            |
|--|------------|
| 7.2. Mitotic Atlas Images .....            | 266        |
| 7.3. Mitotic Atlas Quantitative Data ..... | 268        |
| <b>8. References .....</b>                 | <b>270</b> |

## List of Figures

- Figure 1.1. Cell cycle advancement and management
- Figure 1.2. Schematic of cells and chromosomes during Mitosis
- Figure 1.3. Stages of oocyte maturation and fertilisation
- Figure 1.4. Chromosomal abnormalities associated with aneuploidy
- Figure 1.5. First recorded image of chromosome structures
- Figure 1.6. Schematic of DNA condensation into chromosomes
- Figure 1.7. Core components of chromosomes
- Figure 1.8. Historical developments in the investigation of the CP
- Figure 1.9. Ki67 localisation to the chromosome periphery throughout mitosis.
- Figure 1.10. Ki67 identified as the organiser of the chromosome periphery.
- Figure 1.11. Altered chromosome structure as a result of Ki67 depletion.
- Figure 1.12. Confocal microscope schematic
- Figure 1.13. Electron microscopy schematic
- Figure 3.1. Optimisation of seeding density and substrate coating for Correlative Light and Electron Microscopy (3D-CLEM)
- Figure 3.2. Comparison of confocal and super-resolution microscopy for mitotic imaging
- Figure 3.3. Optimisation of tannic acid concentration for electron microscopy staining

- Figure 3.4. FIB-SEM imaging setup pipeline using the Zeiss Crossbeam 550
- Figure 3.5. Optimisation of FIB-SEM imaging parameters
- Figure 3.6. Comparison of FIB-SEM and SBF-SEM for whole cell imaging
- Figure 3.7. Correlative LM and EM chromosome reconstruction using SBF-SEM and FIB-SEM
- Figure 3.8. Comparison of segmentation tools in AMIRA
- Figure 3.9. Effect of smoothing on chromosome model geometry
- Figure 3.10. Deep learning training for chromosome modelling
- Figure 3.11. Optimised 3D-CLEM pipeline
- Figure 3.12. Identification of mitotic stages using fluorescence microscopy
- Figure 3.13. 3D-CLEM processing of cells
- Figure 3.14. Representative 3D-CLEM models of mitotic stages
- Figure 3.15. Quantification of mitotic chromosome ultrastructure using 3D-CLEM
- Figure 3.16. Nucleosome density plateaus from prometaphase to anaphase.
- Figure 4.1. Ki67 distribution during Meiosis I confirms chromosome periphery and reveals novel distribution.
- Figure 4.2. Imaging of chromosome segregation phenotypes following Ki67 knockdown

- Figure 4.3. Quantitative analysis of meiotic progression phenotypes following Ki67 knockdown.
- Figure 4.4. Quantification of chromosome count in control and Ki67 knockdown oocytes.
- Figure 4.5. Chromosome displacement analysis in control and Ki67 knockdown oocytes.
- Figure 4.6. Polar Body extrusion directionality in control and Ki67 knockdown oocytes.
- Figure 4.7. Maximum projection images of chromosomes in mouse oocytes under control and Ki67 knockdown conditions
- Figure 4.8. Super-resolution microscopy of fixed oocytes.
- Figure 4.9. Comparative line scan analysis of chromosomal periphery in control and Ki67 knockdown oocytes.
- Figure 4.10. Impact of Ki67 knockdown on chromosome morphology and organisation.
- Figure 4.11. Chromosome volume, DNA content, and 3D karyotype reconstruction in control and Ki67 knockdown cells.
- Figure 4.12. Assessment of chromosome distribution relative to chromosome volume in control and Ki67 knockdown cells.
- Figure 4.13. Chromosomal positioning at the edge of the exclusion zone in control and Ki67 knockdown oocytes.
- Figure 4.14. Quantitative comparison of chromosomal dimensions in control and Ki67 knockdown oocytes.
- Figure 5.1. Ki67 in human oocytes immunofluorescence.

- Figure 5.2. FIB-SEM imaging of a human oocyte.
- Figure 5.3. SBF-SEM imaging of a human oocyte.
- Figure 5.4. SBF-SEM imaging of human oocytes showing a lack of chromosomes.
- Figure 5.5. Structural abnormalities in the ZP and their impact on chromosome visualisation.
- Figure 5.6. Cytoplasmic abnormalities in human oocytes.
- Figure 5.7. Successful 3D-CLEM processing of an MII oocyte
- Figure 5.8. SBF-SEM whole oocyte chromosome modelling
- Figure 5.9. A summary of oocyte imaging highlights the selection criteria for successful imaging.

## List of Tables

- Table 1.1. Summary of aneuploidy prevalence
- Table 1.2. Cells and handling conditions used
- Table 2.1. Cells and handling conditions used.
- Table 3.1. Comparison of AMIRA segmentation tools
- Table 3.2. Deep learning parameters for chromosome modelling training
- Table 5.1. Immunofluorescence antibodies used for oocyte staining.
- Table 5.2. Human oocyte samples for 3D-CLEM.
- Table 5.3. Sample 3566 imaging parameters
- Table 5.4. Sample 3498 A imaging parameters
- Table 5.5. Sample 3498 B imaging parameters
- Table 5.6. Sample 3568 A&B imaging parameters
- Table 5.7. Sample 3572 imaging parameters
- Table 5.8. Sample 3574 imaging parameters
- Table 5.9. Sample 3573 imaging parameters
- Table 5.10. Key characteristics observed in LM imaging and their corresponding impact on EM outcomes.

## List of Abbreviations

| <b>Abbreviation</b> | <b>Definition</b>                                       |
|---------------------|---|
| CDK                 | Cyclin-Dependent Kinases                                |
| 2D                  | Two Dimensional   |
| 3C                  | Chromosome Conformation Capture                         |
| 3D-CLEM             | Three-dimensional Correlative Light Electron Microscopy |
| 3D-SIM              | Three-Dimensional Structured Illumination Microscopy    |
| A.U.                | Airy Unit   |
| A-ESEM              | Advanced Environmental Scanning Electron Microscopy     |
| AOQI                | Average Oocyte Quality Index                            |
| APC/C               | Anaphase-Promoting Complex/Cyclosome                    |
| ART                 | Assisted Reproduction Technology                        |
| BSA                 | Bovine Serum Albumin                                    |
| CENP-A              | Centromere Protein A                                    |
| CP                  | Chromosome Periphery                                    |
| CTRL                | Control   |
| ddH <sub>2</sub> O  | Double-Distilled H <sub>2</sub> O                       |
| DL                  | Deep Learning   |
| DNA                 | Deoxyribonucleic Acid                                   |
| EHT                 | Electron High Tension                                   |
| EM                  | Electron Microscopy                                     |
| ER                  | Endoplasmic Reticulum                                   |
| ESCRT               | Endosomal Sorting Complex Required for Transport        |

|         |   |
|---------|---|
| EZ      | Exclusion Zone                                |
| FBS     | Foetal Bovine Serum                           |
| FHA     | Forkhead-Associated Domain                    |
| FIB-SEM | Focused Ion Beam Scanning Electron Microscopy |
| FISH    | Fluorescence In-Situ Hybridisation            |
| GIS     | Gas Injection system                          |
| GLUT    | Glutaraldehyde                                |
| GV      | Germinal Vesicle                              |
| GVBD    | Germinal Vesicle Breakdown                    |
| HeLa    | Henrietta Lacks                               |
| HFEA    | Human Fertilisation and Embryology            |
| IBMX    | 2-isobutyl-1-methylxanthine                   |
| ICSI    | Intracytoplasmic Sperm Injection              |
| ipMTs   | Interpolar Microtubules                       |
| IVF     | In-Vitro Fertilisation                        |
| KD      | Knockdown                                     |
| KIF4    | Kinesin Superfamily Member 4                  |
| kMTs    | Kinetochores Microtubules                     |
| KOH     | Potassium Hydroxide                           |
| LM      | Light Microscopy                              |
| Mbp     | Million Base Pairs                            |
| MOMS    | Metaphase II Morphological Scoring System     |
| MPF     | Maturation-Promoting Factor                   |

|      |  |
|------|--|
| mSEM | Multibeam Scanning Electron Microscope |
| MTA  | Material Transfer Agreement            |
| NA   | Numerical Aperture                     |
| NaOH | Sodium Hydroxide                       |
| NEBD | Nuclear Envelope Breakdown             |
| PALM | Photoactivated Localization Microscopy |
| PB   | Polar Body                             |
| PBS  | Phosphate Buffered Saline              |
| PCOS | Polycystic Ovarian Syndrome            |
| PFA  | Paraformaldehyde                       |
| PLL  | Poly-L-Lysine                          |
| Rb   | Retinoblastoma Protein                 |
| RER  | Rough Endoplasmic Reticulum            |
| RNA  | Ribonucleic Acid                       |
| ROI  | Region of Interest                     |
| RPE  | Retinal Pigmented Epithelial           |
| RT   | Room Temperature                       |
| SAC  | Spindle Assembly Checkpoint            |
| SBF  | Serial Block Face                      |
| SEM  | Scanning Electron Microscopy           |
| SER  | Smooth Endoplasmic Reticulum           |
| SMC  | Structural Maintenance of Chromosomes  |
| SNR  | Signal to Noise Ratio                  |

|          |                                  |
|----------|----------------------------------|
| SSI      | Serial Sectioning Imaging        |
| STED     | Stimulated Emission Depletion    |
| TADs     | Topologically Associated Domains |
| TEM      | Transmission Electron Microscopy |
| Topo IIa | Topoisomerase IIa                |
| vEM      | Volume Electron Microscopy       |
| WLA      | Waltons Lead Aspartate           |

# 1. Introduction

## 1.1. Importance of cell division

Cell division is a fundamental biological process essential for the survival of an organism. It is required for tissue maintenance, growth, and reproduction. In humans, cell division is essential for developing new cells, repairing damaged tissues, and the production of offspring. Cell division is a complex process, and must be tightly regulated, as errors can lead to undesirable outcomes, such as aneuploidy, resulting in developmental disorders and diseases (Tandle & Camphausen, 2016). The mechanisms involved in cell division involve numerous structures and pathways. However, the key feature of cell division is the accurate replication and segregation of chromosomes (Tandle & Camphausen, 2016). Chromosomes, which carry the organism's genetic makeup, ensure that daughter cells receive the correct complement of genetic material, whether the intended outcome is identical or genetically varied cells (Nurse, 2000).

Mitosis and meiosis are the two possible forms of cell division. Both processes involve the division of cells; they are regulated differently to produce varied types of offspring. Mitosis occurs in somatic (non-reproductive) cells and produces two genetically identical daughter cells, which is important for tissue repair, growth, and body maintenance. The replication of genetic material during mitosis ensures the fidelity of somatic cells throughout their lifespan.

In comparison, meiosis is an alternative form of cell division that occurs in germ cells (sperm and oocytes), enabling sexual reproduction. Meiosis

introduces genetic variation through two key mechanisms: crossing over, where homologous chromosomes exchange genetic material, and independent assortment, where chromosomes are randomly distributed to daughter cells. These processes contribute to the genetic diversity seen in offspring. The outcome of meiosis is the production of haploid cells—sperm and oocytes—which each contain half the number of chromosomes found in somatic cells. Upon fertilisation, these haploid cells combine to restore the diploid chromosome number in the zygote, ensuring the continuation of species (Figure 1.2. and Figure 1.3.).

A comprehensive understanding of both mitosis and meiosis, in particular the various core elements of the cell division machinery, requires the ability to visualise and ‘map’ cell ultra-structure. This includes the ultrastructure of chromosomes during each stage, key for identifying the mechanisms underlying normal and abnormal cell division. Any errors that arise during these processes can lead to chromosomal abnormalities, such as aneuploidy, which can have severe consequences. To date, no complete, 3D ultra-structure atlas of all chromosomes, in all stages of cell division, exists.

### 1.1.1. The Cell Cycle

Cell division follows the cell cycle, which can be split into distinct stages for cell replication and has multiple checkpoints in which the process is monitored for success. The cell cycle stages include Interphase, Mitosis and Cytokinesis (Matthews et al., 2022). Interphase consists of three sub-phases, including G1 (Gap-1), S (synthesis) phase, and G2 (Gap-2), each of which

contributes to the growth and synthesis of deoxyribonucleic acid (DNA) and must all occur in sequence before progressing to the next stage (Sclafani & Holzen, 2007). M phase (Mitosis) follows G<sub>2</sub>, where duplicated DNA is compressed into chromosomes and equally divided into two identical daughter cells (Matthews et al., 2022). Cytokinesis is the 'final' stage of the cell cycle, and during this process, the cells are cleaved into two identical daughter cells. Following cytokinesis, the two daughter cells enter the cell cycle at G<sub>1</sub>, and the process from interphase to cytokinesis is repeated. This process repeats continually until the cell enters either quiescence (a reversible non-dividing state), senescence (a permanent non-dividing state) or some form of cell death (Kumari & Jat, 2021).

#### CDKs and Cyclins

Progression through the cell cycle is tightly regulated by Cyclin-Dependent Kinases (CDKs), which are enzymes that help control the cell cycle. These kinases work with cyclins, proteins that activate CDKs at specific points (Figure 1.1). CDKs and cyclins provide checkpoints that control the progression of the cell cycle, ensuring that the cell does not advance to the next stage with errors. Pacing the cell cycle allows time for repair pathways or realignments to occur, safeguarding genomic integrity and ensuring cell fidelity. This aids in preventing aneuploidies that could have detrimental effects.

During the first stage of the cell cycle, the CDK4/6-cyclin D complex is required for the transition from the G<sub>1</sub> to the S phase. Cyclin D binds to CDK4 and CDK6, which triggers them both to activate the retinoblastoma protein (Rb) (Pennycook & Barr, 2020; Rubin et al., 2020). Rb phosphorylation leads to the

release of E2F transcription factors, which promote gene expression required for DNA replication. E2F-dependent transcription results in the expression of E-type cyclins, further increasing CDK activity and, in turn, leading to more Rb phosphorylation (Pennycook & Barr, 2020; Rubin et al., 2020). This triggers more E2F-dependent transcription and creates a trigger point for progression into the S phase through the accumulation of cyclin E and cyclin A CDK activity (Matthews et al., 2022).

The positive feedback loop of E2F activation allows the accumulation of cyclin A–CDK2 activity. This is dependent on the inactivation of Anaphase-promoting complex/cyclosome (APC/C) activity. When E2F-dependent transcription is active and APC/C is inactive, the cell can progress and initiate the G2 phase (Matthews et al., 2022). This also acts as an S/G2 phase checkpoint, ensuring that DNA is not damaged, preventing the progression of the cell cycle and allowing for repair before the cell cycle continues, as well as ensuring DNA is only replicated once.

During G2, the CDK1-cyclin B complex is active, forming the maturation-promoting factor (MPF), which triggers the events leading to mitosis (Xu & Chang, 2007). The G2/M checkpoint prevents progression to the M phase if there is DNA damage, pausing progression for repair.

The ‘final’ stage of the cell cycle is mitosis. CDK1-cyclin B drives the progression through the M phase, ensuring chromosomes form correctly and align along the metaphase plate (Holder et al., 2019). The spindle assembly checkpoint (SAC) also regulates the process, ensuring the chromosomes are

securely attached to the microtubules before dividing into the two daughter cells, and the cycle begins again (Holder et al., 2019).

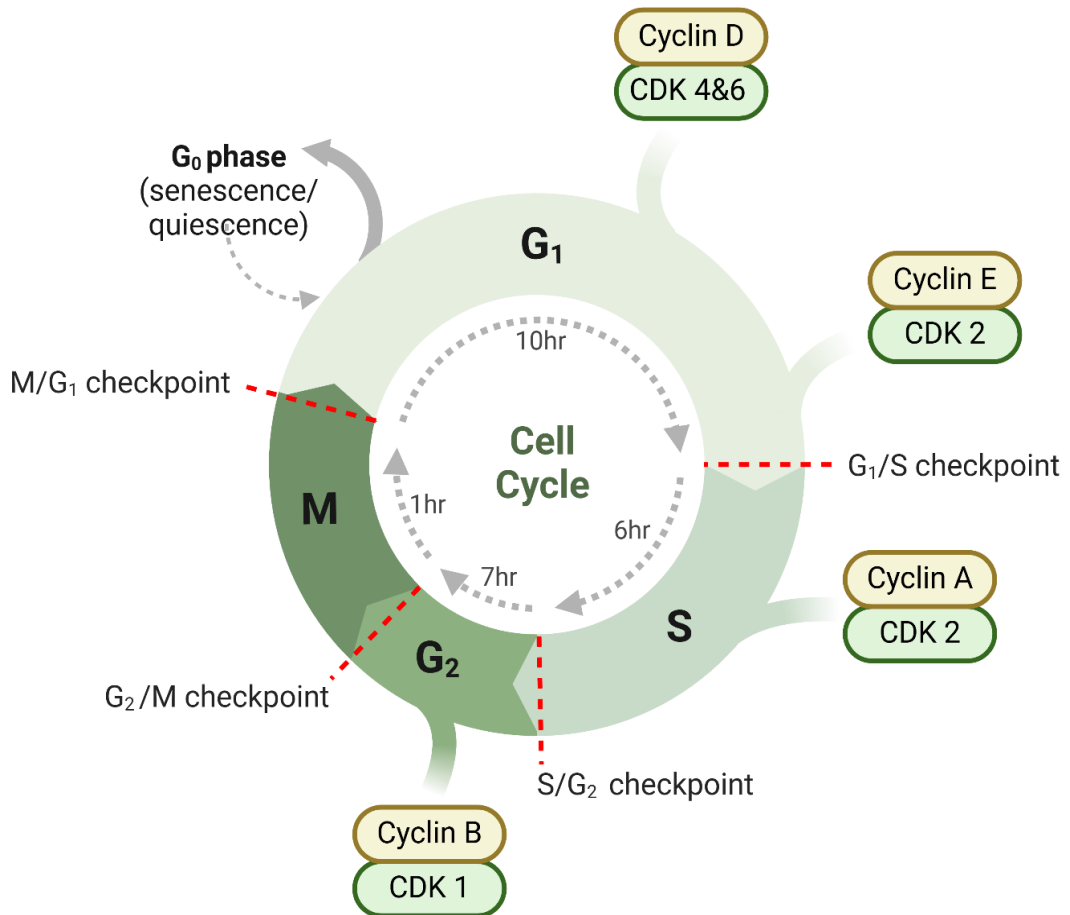


**Figure 1.1 Cell cycle advancement and management.** A schematic of the cell cycle and the associated CDK regulators. Cyclins and the associated CDKs that regulate the cell cycle are shown at the stages of the cell cycle they regulate. The CDK-cyclin complexes regulate cell cycle advancement through phosphorylation/dephosphorylation. The duration of each stage is shown on the inside, and the red lines indicate the checkpoints at which the cell cycle can either be paused or aborted and transition from the cell cycle to the G<sub>0</sub> phase. (Made using BioRender).

### 1.1.2. Mitosis

Mitosis is a process of cell division that occurs in somatic cells within the human body. The replication process involves splitting a single cell to produce

two identical daughter cells. Mitosis includes multiple stages, during which the chromosomes condense, align, separate, and decondense. These stages include interphase, prophase, prometaphase, metaphase, anaphase, and telophase (including cytokinesis) (Figure 1.2.).

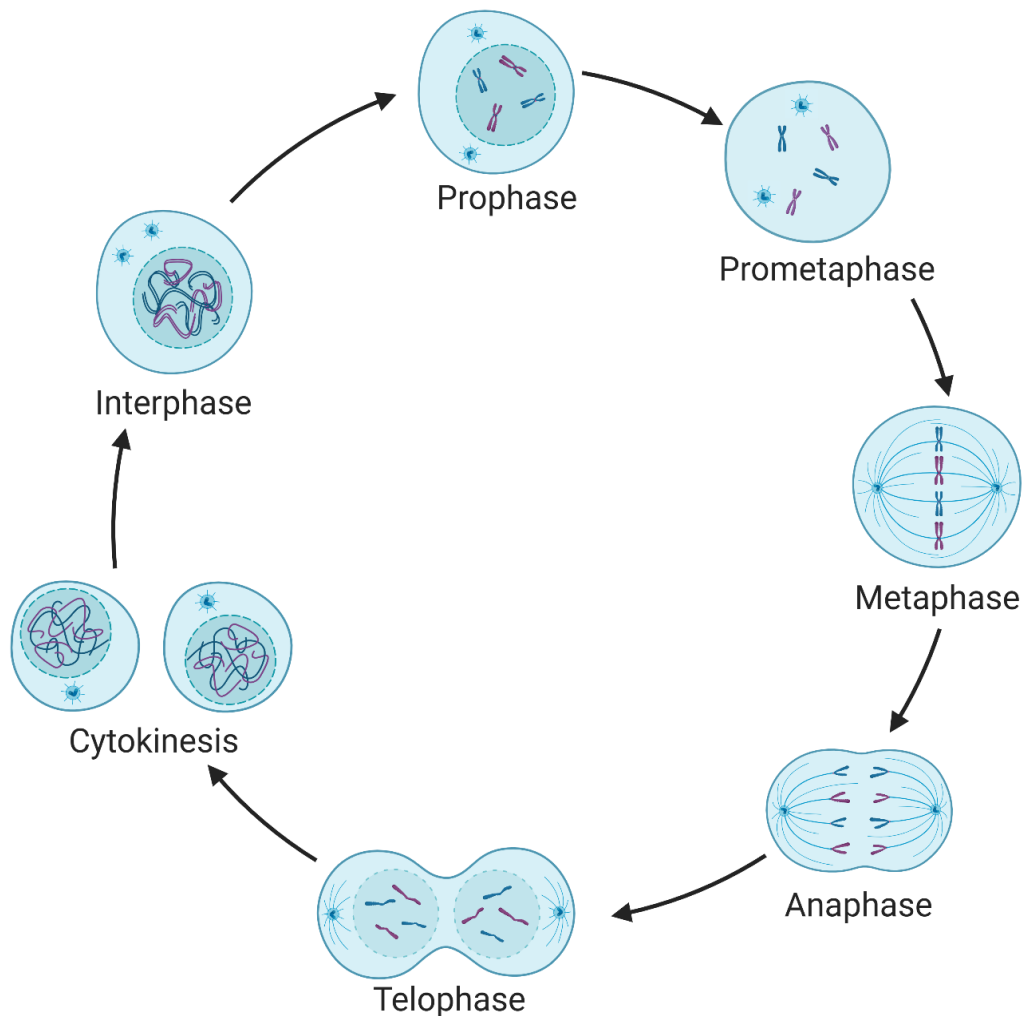


**Figure 1.2. Schematic of cells and chromosomes during Mitosis.** The structure of cells throughout mitosis. Interphase: The DNA remains in a strand-like structure but has been synthesised. Prophase: the nuclear envelope breaks down and the DNA starts to condense into chromosomes. Prometaphase: The nuclear envelope has completely broken down and the chromosomes have defined structures in the cytoplasm. Metaphase: The chromosomes are aligned along the metaphase plate, and the microtubules have attached to the centromeres. Anaphase: the chromosomes have divided and started to migrate towards the poles. Telophase: the chromosomes are at the poles of the cell and the nuclear envelope has started to reform. Cytokinesis: the cell has divided into

two daughter cells. This is the division pathway that all somatic cells follow within the cell cycle. (Made using BioRender).

### Prophase

Prophase is the first and longest stage of mitosis. DNA condenses into chromosomal structures, mediated by condensin II (Antonin & Neumann, 2016; Hirano, 2012). This produces chromosome pairs of two sister chromatids, held together by centromeres at the centre (discussed further in Section 1.2.3.). The centrosome consists of two centrioles duplicated during interphase, each migrating to the cell's opposite hemispheres (Nabais et al., 2020). These centrosomes are microtubule organising centres, and dynamic microtubules (aster microtubules) begin to extend from the centrioles (Nabais et al., 2020). A progression checkpoint occurs at the end of prophase, during which CDK1 is activated, and progression through mitosis from this point cannot be reversed (Matthews et al., 2022). Throughout Prophase, the nuclear envelope breaks down—this is essential for the microtubules to attach to the chromosomes during the later stages.

### Prometaphase

During Prometaphase, the chromosomes continue condensing until fully compact due to condensin I and condensin II interaction (Antonin & Neumann, 2016; Hirano, 2012). Microtubules polymerise and depolymerise as they extend from the centrioles, extending out in the cell, covering as much area as possible to locate and bind to a kinetochore of a chromosome (Meunier & Vernos, 2012). The most abundant microtubules in the cell are called interpolar microtubules (ipMTs); these do not bind to kinetochores and can interact with ipMTs from the

other hemisphere of the cell, aiding chromosome congression (Meunier & Vernos, 2012; Vanneste et al., 2011). Kinetochore microtubules (kMTs) are microtubules that attach to kinetochores and play a crucial role in chromosome alignment during metaphase by aiding in aligning chromosomes along the metaphase plate (equatorial plane of the cell).

### Metaphase

The chromosomes align along the metaphase plate, ready to divide into two groups. Proper alignment during this stage is essential for equal division of chromosomes during the following stages of mitosis. kMTs form bundles, called Kinetochore Fibres, which consist of a highly variable amount of kMTs, and are required to produce the force to separate the chromatids during anaphase (McAinsh & Kops, 2023; Meunier & Vernos, 2012). During metaphase, the SAC is a regulatory mechanism that ensures chromosomes are correctly aligned along the metaphase plate and securely attached to the spindle microtubules (McAinsh & Kops, 2023). This checkpoint prevents the cell from progressing to the next phase until these conditions are met, ensuring accurate chromosome segregation (McAinsh & Kops, 2023). When the SAC conditions are met, the cell can progress to Anaphase.

### Anaphase

Anaphase is the shortest stage of mitosis. K fibres bound to the kinetochores of the chromosomes pull the chromosomes apart towards the cell poles, as do ipMTs at the midzone (Myers & Collins, 2016). The centromeres divide due to the proteolysis of cohesin, and the sister chromatids are separated.

One chromatid of each chromosomal pair is pulled to each pole, resulting in two identical groups of chromosomes.

### Telophase

The nuclear envelope that dissolved during prophase starts to reform to encapsulate the chromosomes (Larijani & Poccia, 2009). As the envelope reforms, the chromosomes also start to decondense, returning to their diffuse DNA form within the nucleolus. The microtubules release from the chromosomes, leaving a single centrosome with a newly formed nucleolus.

### Cytokinesis

Cytokinesis is the final stage of mitosis and the point at which the single parent cell divides completely to form two daughter cells. The equator of the cell begins to ingress to form a cleavage furrow. At this cleavage site, both actin and myosin form the actomyosin contractile ring, which constricts, resulting in a bundle of microtubules called the midzone (Green et al., 2012; C. R. Hsu et al., 2023). Cytokinetic abscission is the final stage of cytokinesis, mediated by the endosomal sorting complex required for transport (ESCRT) pathway, which generates the force required to constrict that furrow to the point of separation, resulting in two identical daughter cells (Gershony et al., 2014).

Mitosis is essential for somatic cell maintenance, while meiosis in germ cells serves the critical function of generating genetic variation, a fundamental component of sexual reproduction.

### 1.1.3. Meiosis

Meiosis is the cell replication method utilised by cells such as gametes to produce varied haploid offspring from a diploid cell (Ohkura, 2015). The cells undergo two meiotic division stages (Figure 3) after the initial spermatogonia or oogonia phase, where DNA synthesis occurs. This initial synthesis will bring the DNA content to 4C. The first stage of meiotic division will discard half of the DNA content into the Polar Body (PB), reducing the chromosome amount from 4C to 2C, resulting in the typical number of homologous chromosome pairs as seen at the beginning of mitosis (Severson et al., 2016). The second division of meiosis occurs without any further synthesis, reducing the DNA content to 1c (a haploid number of chromosomes that will form a complete set during fertilisation).

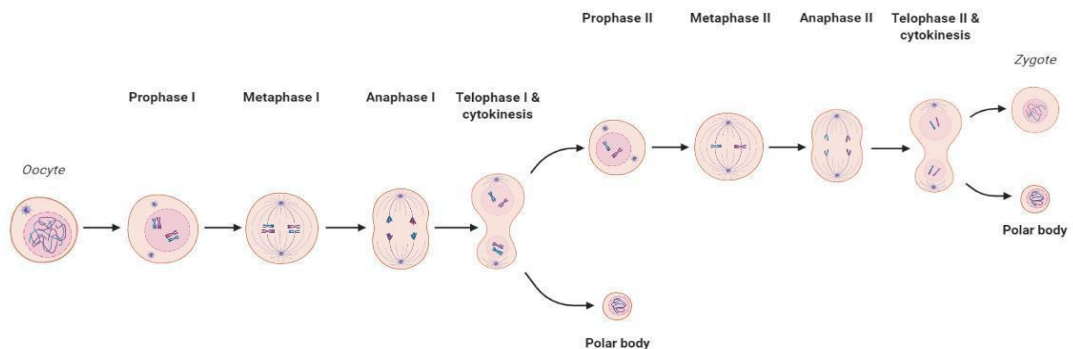


**Figure 1.3. Stages of oocyte maturation and fertilisation.** The diagram illustrates the progression of oocyte meiosis and subsequent fertilisation. Starting from an immature oocyte, the cell undergoes Prophase I, where homologous chromosomes condense. The cell progresses through Metaphase I and Anaphase I, with chromosomes aligning and segregating. In Telophase I and cytokinesis, the first polar body is extruded, and the oocyte enters Meiosis II. The process continues through Prophase II, Metaphase II, Anaphase II, and Telophase II with the extrusion of a second polar body following fertilisation. The fertilised oocyte becomes a zygote, completing the process. This is the division pathway that gametes follow in the cell cycle. (Made using BioRender).

## Prophase I

Prophase I is split into five phases: Leptotene, Zygotene, Pachytene, Diplotene and Diakinesis. During leptotene, the chromosomes condense, and the sister chromatids form, although they appear thin and 'thread-like' (Brooker & Berkowitz, 2014; Zickler & Kleckner, 1998). In zygotene, the homologous chromosomes align through synapsis, resulting in pairs of chromosomes (bivalent chromosomes) consisting of four chromatids (tetrads) (Zickler & Kleckner, 1998). Pachytene is the stage in which the genetic material is shared via crossing over, forming chiasmata, and ensuring genetic variation in the offspring. During Diplotene the chromosomes start to separate and remain connected only at the chiasmata. The oocytes arrest at this stage (diacytate arrest) and remain until the follicles have been formed for an extended time and the female reaches maturity (Nagaoka et al., 2012). Finally, during diakinesis, the chromosomes condense further, and the nuclear envelope breaks down, similar to the prophase in mitosis.

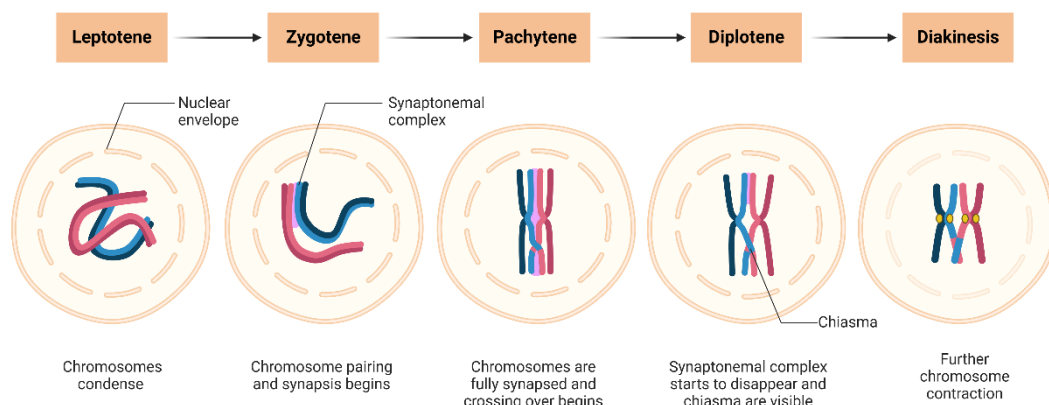


**Figure 1.4. Stages of Prophase I in meiosis.** The schematic illustrates the five stages of prophase I, including leptotene, zygotene, pachytene, diplotene and diakinesis. This is the stage in which the chromosomes introduce variation

*through crossing over and formation of chiasma to produce genetically diverse offspring.*

#### Prometaphase I

A spindle apparatus is formed, and chromosomes are attached to spindle fibres by kinetochores. Oocytes do not have centrosome structures as the sperm introduce these during fertilisation, so spindle formation and organisation are guided by the dynamic actin network, consisting of the actin nucleators, Formin-2, Spire 1, and Spire 2 (Chaigne et al., 2012; Longo & Chen, 1985; Ohkura, 2015).

#### Metaphase I

Bivalent chromosomes are arranged along the metaphase plate. The arrangement of these chromosomes along the metaphase plate, regarding the spindle poles, is random. This random organisation of paternal and maternal chromosomes is another source of genetic variation, as the number of possible arrangements results in approximately 2<sup>23</sup> combinations of chromosomal variations.

#### Anaphase

The homologous chromosomes in each bivalent are separated and move to the opposite poles of the cell.

#### Telophase

The chromosomes become diffuse, returning to DNA form, and the nuclear envelope reforms, encasing the DNA from the cytoplasm.

## Cytokinesis

The cell is segregated into two new daughter cells. However, this division is asymmetrical as only one of these 'cells will continue as an oocyte, and the other is extruded as a PB. Asymmetrical division is essential to reducing the loss of cytoplasmic content.

## Meiosis II

The stages of meiosis II are analogous to those of mitosis, with a cell produced at the end that contains 23 chromatids rather than 23 chromosome pairs as seen in somatic cells. The 'partnering' 23 chromatids will be introduced from the sperm during fertilisation, which will trigger the first mitotic division.

### 1.1.4. Oocytes

#### 1.1.4.1. Structure

Oocytes are, by volume, the largest cells in the human body that are highly specialised to support embryonic development when fertilised (Trebichalská, Kyjovská, et al., 2021). The human oocyte has a considerable influence on the development of the embryo, as the majority of aneuploid abnormalities have a maternal influence (Brooker & Berkowitz, 2014; Lu et al., 2017; Trebichalská, Kyjovská, et al., 2021). Despite the importance of oocytes in the development of embryos and, essentially, the continuation of human life, surprisingly little is understood about chromosome structure and geometry, particularly at the ultra-structural level. This is due to a myriad of technical, cost, and accessibility challenges that are long standing obstacles in this research.

Human oocytes contain cell organelles, which are also present in many other cells, such as mitochondria, smooth endoplasmic reticulum (SER), lysosomes, microfilaments, and microtubules. However, the rough endoplasmic reticulum (RER), Golgi and ribosomes are rare in these specialised cells, and centrosomes are entirely lacking (Sathananthan, 1997). The oolemma (the oocyte cell membrane) is surrounded by multiple layers, including the perivitelline space, zona pellucida (ZP), and a layer of follicle cells called the corona radiata (Tatíčková et al., 2023).

#### *1.1.4.2. Polar Body*

During oogenesis, the polar body is a small, non-functional cell that forms as a waste product of the asymmetric divisions of oocytes. In humans, two polar bodies are extruded: one following meiosis I and the second after meiosis II. This asymmetrical division ensures that the oocyte retains the majority of the cytoplasm and organelles, which are essential for early development. The first polar body contains a haploid set of chromosomes and is extruded before ovulation, in comparison, the second is released only if fertilisation occurs. While traditionally considered a waste product, the polar body may have a role as an indicator of oocyte quality. Abnormalities in polar body formation, morphology, or chromosomal content have been linked to meiotic errors and aneuploidy in the oocyte, which can result in fertilisation failure, embryo arrest, or miscarriage (Christopikou et al., 2013). However, this is currently still in debate as other large-scale studies also note that there is no significant correlation between polar-body morphology and the presence of aneuploidies (Yang et al., 2022). Furthermore, polar body biopsy has been explored as a less invasive method of preimplantation genetic testing (Verlinsky et al., 1990), although its usage is

limited, due to the fact that it only reflects the maternal DNA. Due to the limited knowledge of polar bodies, a further understanding of polar body dynamics, therefore, provides insights not only into the mechanisms of meiosis but also into reproductive success and viability.

### 1.1.5. Aneuploidy

#### 1.1.5.1. *Abnormal cell division*

As previously stated, errors can occur during cell division, leading to abnormal daughter cells. Abnormalities in the chromosome components could cause these errors and may lead to chromosomes being improperly segregated (Figure 1.5.). Errors during cell division can include misaligned chromosomes, monotelic cells, lagging chromosomes and multipolar cells, all of which could lead to daughter cells with an irregular whole chromosome number (aneuploidy) (Brooker & Berkowitz, 2014).

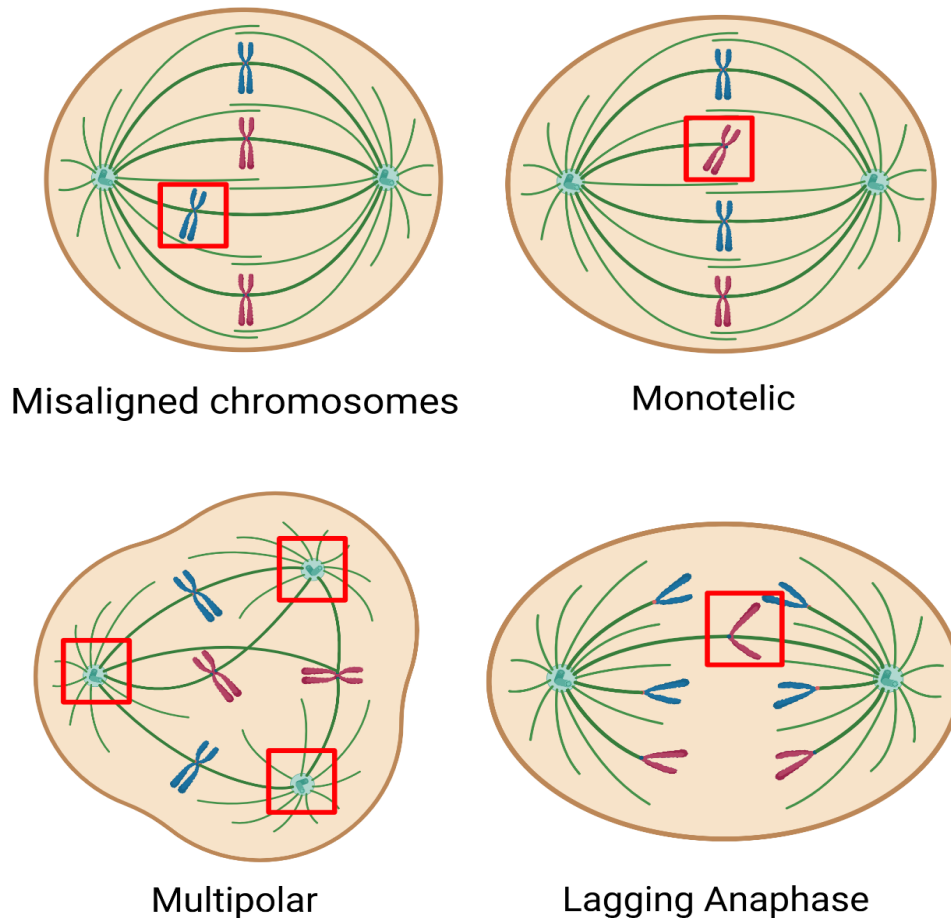


**Figure 1.5. Chromosomal abnormalities associated with aneuploidy.** Potential abnormalities that can occur during cell division and may lead to aneuploidy. (A) misaligned chromosomes – chromosomes fail to align properly on the metaphase plate leading to mis-segregation, (B) monotelic cells – a single microtubule attaches to the kinetochore resulting in abnormal segregation, (C) multipolar cells – formation of more than two spindle poles causes aneuploidy, (D) lagging anaphase division – a chromosome or chromatid lags during anaphase potentially resulting in aneuploidy. Red boxes emphasise the affected regions in each abnormality.

#### 1.1.5.2. Prevalence

Aneuploidy affects approximately 30-50% of embryos in younger women, a trend that worsens with increasing maternal age (Franasiak et al., 2014; Nagaoka et al., 2012). Despite this high prevalence of aneuploidy and the devastating effects it can have, little is known about the origin of these chromosomal abnormalities in humans.

Kubicek et al., (2019) partnered with a fertility clinic to perform 967 trophoctoderm biopsies sourced from 180 couples undergoing IVF. From the biopsies and DNA sourced from both parents, karyomapping could be performed to identify chromosomal abnormalities and the parental origin of the mutation (Table 1). From this analysis Kubicek et al., (2019) Identified that the majority of whole chromosome aneuploidies (90.1%) were maternally derived, whereas segmental aneuploidies were mostly paternally derived (70.4%) (Table 1).

**Table 1.1.** Summary of aneuploidies recorded from 967 trophoctoderm biopsies, showing each aneuploidy type's maternal or paternal origin. Recreated from Kubicek et al., 2019.

| <b>CLASS OF CHROMOSOME ABNORMALITY</b> | <b>TOTAL</b> | <b>MATERNAL</b>   | <b>PATERNAL</b>   |
|--|--------------|-------------------|-------------------|
| <b>WHOLE CHROMOSOME ANEUPLOIDY</b>     | (n)          | Chromosomes n (%) | Chromosomes n (%) |
| <b>MEIOTIC TRISOMY</b>                 | 149          | 137 (91.9%)       | 12 (8.1%)         |
| <b>MI</b>                              | 354          | 319 (90.1%)       | 35 (9.9%)         |
| <b>MII</b>                             | 45           | 38 (84.4%)        | 7 (15.6%)         |
| <b>MONOSOMY</b>                        | 205          | 182 (88.8%)       | 23 (11.2%)        |
| <b>SEGMENTAL ANEUPLOIDY</b>            | 54           | 16 (29.6%)        | 38 (71.4%)        |
| <b>TRIPLOID</b>                        | 9            | 7 (77.8)          | 2 (22.2%)         |

#### 1.1.5.3. Causes

Oocytes begin meiosis while still in female development, then enter meiotic arrest until the resumption of meiosis later in life. This resumption of meiosis may not occur for years and therefore, meiotic maturation of oocytes in females is an extended process (Hassold & Hunt, 2001). In comparison, male cells begin meiosis in puberty, and the process is continual with no prolonged pauses (Hassold & Hunt, 2001). Each meiotic cell division produces four sperm,

and the progression of cell division repeats with new cells (Hassold & Hunt, 2001).

This prolonged meiotic arrest in female cells, that may have resided in the body for 40+ years before being utilised, may be responsible for the increased maternal origins of aneuploidy. Many aneuploidy abnormalities occur due to errors that begin during the meiotic cycle; therefore, the protracted meiotic cycle in human oocytes could be responsible for increased abnormality in oocytes (Webster & Schuh, 2017).

#### *1.1.5.4. Identification*

The gold standard for identifying desirable embryos during assisted reproduction technology (ART) is assessing the embryo's morphological and developmental features (Toft et al., 2020). This is a subjective method for prioritisations and could be improved if there were a way to assess embryo suitability in an impartial and quantitative way. The need for identification of aneuploidies in embryos is clear, and improved methods of identifying and selecting against aneuploid embryos could have beneficial clinical applications. This could be solved if the causes of aneuploidy were more fully understood, e.g. if abnormal chromosome structure were responsible, identifying these abnormal chromosomes in embryos could indicate an embryo is unsuitable for implantation.

Fluorescence in-situ Hybridization (FISH) is a laboratory technique to detect specific chromosomes or genetic sequences within a cell. In the context of preimplantation genetic testing for aneuploidy, FISH is used to identify cells

with the correct number of chromosomes (euploid cells) and select them for embryo implantation, reducing the risk of miscarriage (Toft et al., 2020). However, this method did not show improved live birth rates compared to the morphological and developmental assessment already in place. Fragouli et al., (2014) indicated that the lack of success for this method could be due to the aneuploid chromosomes presenting at later stages of cell cleavage rather than during the blastocyst stage, which was when the FISH analysis was being performed, providing further support that investigation of chromosomes during all stages of meiosis is essential for understanding chromosomal abnormalities.

#### *1.1.5.5. Idiopathic*

A lot of specific data on the different types of aneuploidies has been collected from studies performing blastocyst biopsies. This allows the polar body to be biopsied without the embryonic cells being affected, and therefore, the blastocyst is still viable to continue development to form a foetus (Kubicek et al., 2019).

Despite its success for preimplantation genetic diagnosis, as previously mentioned, this technique may miss certain aneuploidies during later stages of embryogenesis, e.g., cleavage stages. Also, this technique only indicates the presence of aneuploidies and potentially traces the origin of the aneuploidy in the parental samples. However, it is currently impossible to identify the cause of most aneuploidies; therefore, most cases remain idiopathic.

Aneuploidy, the result of errors during chromosome segregation, is one of the most common causes of developmental disorders and infertility. As most

aneuploidies arise from maternal cells, especially oocytes, understanding the ultrastructure of chromosomes in oocytes is crucial for uncovering the mechanisms that lead to these errors. Understanding how cell division processes ensure the accurate division of genetic material is essential. The most fundamental components involved in these processes are the chromosomes themselves, whose proper segregation is key to the success of both mitosis and meiosis and avoiding aneuploidy.

## 1.2. Chromosomal ultrastructure

### 1.2.1. Definition and historical background

Chromosomes are small rod-shaped structures found in the nucleus of eukaryotic cells. They encase genetic data and support the efficient division of this data into daughter cells. They comprise many components, including DNA, proteins and Ribonucleic Acid (RNA) (Paulson et al., 2021). The DNA within these cells contains an individual's genetic makeup, including characteristics such as height and hair colour, metabolism, and predilection to genetic diseases. The genetic composition is almost always unique to an individual (excluding identical twins), and the transmission of this genome from one cell to another is essential for the continuation of life, the variation of a population, and the evolution of a species.

A healthy human somatic cell contains 46 chromosomes (23 pairs), all containing different DNA content and varying genetic information that create the entire human genome (Table 1.2)). The number and structure of chromosomes

varies between species. For instance, mice have only 40 chromosomes (20 pairs), and humans have 46 chromosomes (23 pairs).

**Table 1.2. Genes and DNA content in each chromosome.** (created from *Information (US), 1998; Nurk et al., 2022; Takenouchi et al., 2024*)

| <b>CHROMOSOME</b> | <b>DNA CONTENT (MILLION<br/>BASE PAIRS;<br/>HUMANS)</b> | <b>DNA CONTENT (MILLION<br/>BASE PAIRS; MBP)<br/>MOUSE OOCYTES</b> |
|-------------------|---|--|
| <b>1</b>          | >240  | 195.5  |
| <b>2</b>          | >240  | 182.1  |
| <b>3</b>          | ~200  | 160.0  |
| <b>4</b>          | ~190  | 156.5  |
| <b>5</b>          | 180   | 151.8  |
| <b>6</b>          | 170   | 149.7  |
| <b>7</b>          | 150   | 145.4  |
| <b>8</b>          | 140   | 129.4  |
| <b>9</b>          | 130   | 124.6  |
| <b>10</b>         | 130   | 130.7  |
| <b>11</b>         | 130   | 122.1  |
| <b>12</b>         | 130   | 120.1  |
| <b>13</b>         | 110   | 120.4  |
| <b>14</b>         | 100   | 124.9  |
| <b>15</b>         | 100   | 104.0  |
| <b>16</b>         | 90  | 96.2   |
| <b>17</b>         | 80  | 95   |
| <b>18</b>         | 70  | 90.7   |
| <b>19</b>         | 60  | 61.4   |
| <b>20</b>         | 60  | N/A  |
| <b>21</b>         | 40  | N/A  |
| <b>22</b>         | 40  | N/A  |
| <b>X</b>          | 150   | 171.0  |
| <b>Y</b>          | 50  | N/A  |

Chromosomes were first observed in the 19<sup>th</sup> century by Karl Wilhelm von Nageli (Fukui & Uchiyama, 2007; Nägeli & Nägeli, 1884). However, they were not identified until 40 years later when Walther Flemming identified the structures with aniline staining and drew diagrams of the chromosomes, along with the microtubules, during various stages of the mitotic process (Flemming, 1882;

Paweletz, 2001) (Figure 1.5.). The understanding of these chromosomes was expanded upon in the following years, including the naming of chromatin (Meshorer & Plath, 2020) and, consequently, the naming of chromosomes by Waldeyer (Scheuerlein et al., 2017). By the 20<sup>th</sup> century, Walter Sutton and Theodor Boveri suggested inheritance theories and that the chromosomal structures contained genetic material that resulted in Mendelian inheritance (Sutton, 1903). Genetics, which is the basis of chromosomes and DNA, was expanded on later in the 1900s by Mendel, who identified genetic inheritance. The combination of chromosome segregation and identification of heredity meant that not only was the separation of chromosomes important, but also the counting and identification of specific chromosomes. This is due to the genetic information being different for each chromosome, and the separation of chromosomes being required to produce a complete chromosome complement in the daughter cell, e.g. the separation of the 23<sup>rd</sup> chromosome pair in meiosis will determine the sex of the offspring.

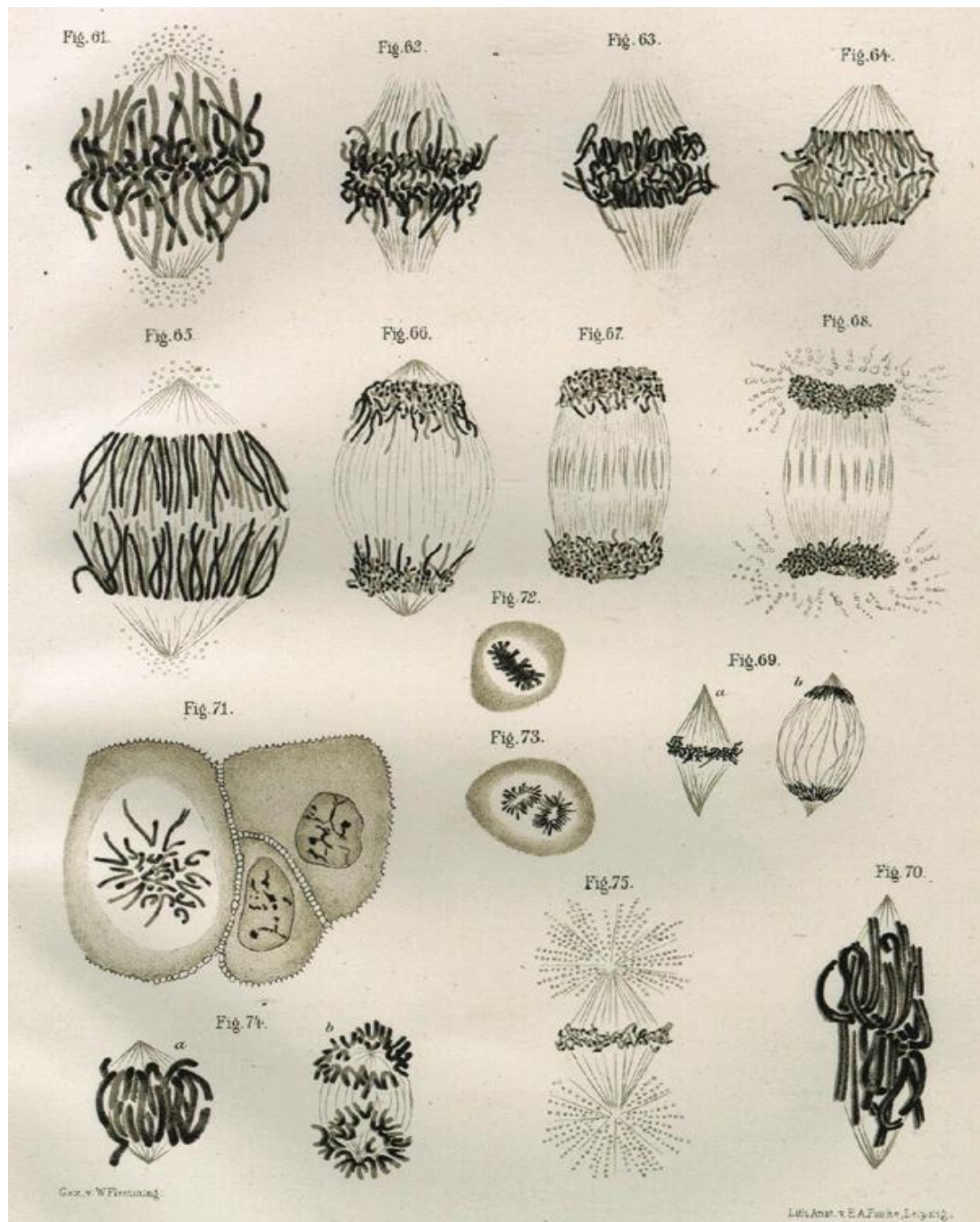


**Figure 1.5. First recorded image of chromosome structures.** Sketched images of chromosomes by Walther Flemming in 1883. This was the first image of chromosomes (Image from Flemming, 1882).

Following on from the discovery of chromosomes and their role in encasing genetic material in the mid-20<sup>th</sup> century, DNA was proven to be the genetic material within cells rather than the previously thought proteins (Avery et

al., 1944; Hershey & Chase, 1952). Franklin, Watson and Crick then further expanded on this potential role for chromosomes as gene carriers with their identification of DNA as a helical structure (Watson & Crick, 1953). Chromosome imaging advancements has enabled a greater understanding of chromosomes, their components, and their purpose. Fundamentally, chromosomes are the structures required to encase DNA and allow for successful cell division and maintenance of life (Kadauke & Blobel, 2009). For chromosomes to fulfil this purpose, many steps and structures must all work together and progress without error to ensure successful cell division. These include the initial formation of the chromosome structure, division of chromosomes throughout mitotic or meiotic stages, interaction with other components of the cell such as microtubules and successful formation of chromosome structures such as the centromeres, telomeres, and chromosome periphery (Booth & Earnshaw, 2017). The accurate formation of these structures and the appropriate division between daughter cells can sustain life (mitosis) and allow for new life (meiosis).

### 1.2.2. Basic structure and organisation of chromosomes

Chromosomes are formed primarily of DNA, histones and other none-histone proteins totalling over 4000 proteins (Ohta et al., 2010). The histones assist in organising and wrapping the DNA, compacting it into chromatin, which is used to form the typical chromosomal structure (Batty & Gerlich, 2019). This formation of chromosomes occurs during mitosis and then decondenses to DNA strands during interphase (Section 1.1). This change in structure to a cylindrical chromosome is

essential for efficient segregation of the chromosomes to produce identical daughter cells in mitosis or haploid offspring in meiosis (Batty & Gerlich, 2019).

The formation of chromosomes requires DNA to go through multiple stages of compaction, beginning with the DNA, which is complexed with eight histones (couples of H2A, H2B, H3 and H4) to aid in the formation of a nucleosome (Fyodorov et al., 2018). Histone H1 resides in the nucleosome core and connects to linker DNA, which aids in compaction into a 30nm chromatin fibre. Following this, a series of loops of chromatin form. These loops in the chromatin were identified through electron microscopy and are essential for the compaction of chromatin into chromosomes (Kadauke & Blobel, 2009). The loops are formed by linear DNA extruding through a protein to form loops and condense into more compacted chromatin (Kadauke & Blobel, 2009). Chromatids become individualised as the loops form, and separate chromosomes are formed with minimal cross-linking (Kadauke & Blobel, 2009). These chromatin loops do not overlap and are organised in a genomically related order, which allows the massive volume of genetic data to be condensed and organised, ready for efficient division. Following the formation of chromosome loops, they are folded to form a fibre, which is compressed and coiled to form a 'bottle-brush array of loops that form the well-known structure of a chromatid alongside its sister chromatid within the chromosome pair (Kadauke & Blobel, 2009; Samejima et al., 2024) (Figure 1.6.).

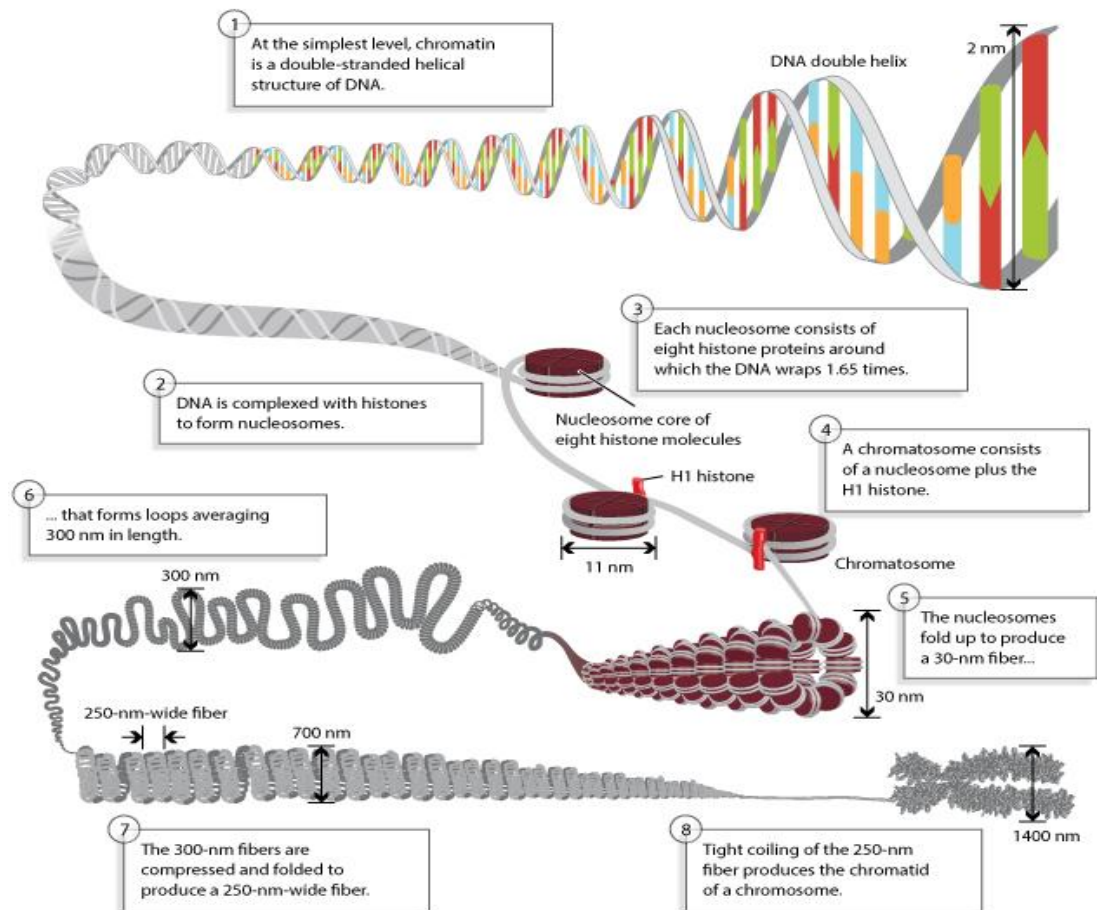


**Figure 1.6. Schematic of DNA condensation into chromosomes.** Condensation of DNA into nucleosomes, chromatin and finally chromosomes occur throughout the S phase to the M phase of the cell cycle to aid in the division of genetic data into daughter cells. (Figure by Annunziato, 2008)

### 1.2.3. Chromosome territories and positioning within the nucleus

During interphase, chromosomes are arranged throughout the cells in topologically associated domains (TADs) (Hug & Vaquerizas, 2018). These TADs were identified in 2012 as genomic blocks in which chromatin sequences reside (Beagan & Phillips-Cremins, 2020; Dixon et al., 2012). Within these TADs, the chromatin sequences interact frequently with each other, whereas they interact with sequences outside of the TAD much less frequently (Beagan & Phillips-Cremins, 2020). The presence of these domains was found to be consistent

across cell types (human and mouse embryonic stem cells) and conserved across different species, indicating that TADs are an innate component of mammalian cells (Dixon et al., 2012).

Nora et al., (2012) used transcriptome analysis over the 84 hours of mouse embryonic stem cell differentiation and found that clustering within the TADs may coordinate the gene expression patterns that occur during development. This study also confirmed that the removal of these boundaries can cause transcriptional mis-regulation and concluded that TADs are essential for transcriptional control (Nora et al., 2012).

The segmentation of chromatin into TADs is a stable feature across cell lines and is conserved across mice and humans (Dixon et al., 2012). This highly conserved feature may, therefore, be an essential principle for genome organisation in animal cells and may influence cell division (Dixon et al., 2012).

#### 1.2.4. Chromosome components

##### *Scaffold – structure and function*

The scaffold was first observed in the 1970s by Paulson and Laemmli, who identified a backbone structure within the chromosomes (Paulson & Laemmli, 1977). This backbone structure was located within the axes of the chromosomes (Figure 1.7B) and named as the chromosomes scaffold (Paulson & Laemmli, 1977).

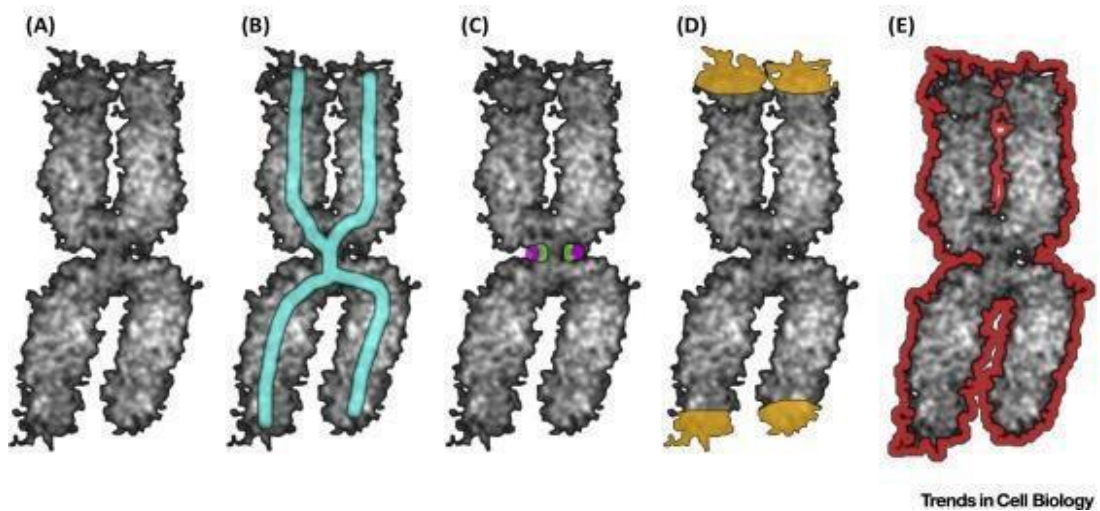


**Figure 1.7. Core components of chromosomes.** (A) chromatin - the condensed DNA. (B) The scaffold within the chromosome axis. (C) The centromere (green) and kinetochore (purple). (D) Telomeres - caps on the end of the chromosome arms. (E) The chromosome periphery contains proteins including Ki67 (Figure by Booth & Earnshaw, 2017)

At its base, DNA is organised around histones; however, the chromosome scaffold was identified as being composed of non-histone proteins (Adolph et al., 1977; Earnshaw & Laemmli, 1983). The first proteins identified in the scaffold were topoisomerase IIa (Topo IIa), condensin core subunit, structural maintenance of chromosome (SMC) proteins and kinesin superfamily member 4 (KIF4) (Earnshaw et al., 1985; Lewis & Laemmli, 1982). The scaffold proteins are arranged in a network forming the shape of a metaphase chromosome (Paulson & Laemmli, 1977). Electron microscopy images indicate this network appears to act as a support for the loops in the DNA structure; therefore, it aids in the organisation of the mitotic chromosomes, thus acting as a scaffold (Hudson et al., 2009; Samejima et al., 2012).

The scaffold structure is still not fully understood, in part due to the imaging techniques available to study this internal structure (Poonperm et al.,

2015). Light microscopy is limited by diffraction, and electron microscopy can impact chromosome preservation and requires the appropriate environment for chromosome imaging (Phengchat et al., 2019). The understanding of the chromosome scaffold has changed with the application of various techniques to investigate the structure. Light microscopy studies initially indicated a stacking structure resulting in a 'barber pole' appearance (Maeshima & Laemmli, 2003). Advances in imaging methodologies including electron microscopy alongside immunogold labelling has proven helpful for the imaging of condensin and Topo Ila (two of the proteins within the scaffold structure) (Maeshima et al., 2005). Further advances in imaging including super-resolution imaging have further improved the understanding of the scaffold structure. Poonperm et al., (2015) used three-dimensional structured illumination microscopy (3D-SIM) to image the positions of each of the scaffold proteins and overall scaffold structure. Focused-ion-beam scanning electron microscopy (FIB-SEM) was used alongside the 3D-SIM as this provides improved resolution of the proteins. These combined methods identified two strands of the scaffold within the chromosomes, supporting the concept of a double-stranded structure inside the chromosome axes (Poonperm et al., 2015).

Each of the scaffold proteins appears to be essential to supporting the formation of the scaffold structure and removing some of these proteins has been shown to cause defects in chromosome formation (Samejima et al., 2012). These mitotic defects can affect cell division and may be one of the causes of aneuploidy cells (Mazumdar et al., 2006). This shows that the alteration of the chromosome scaffold can affect chromosome organisation, and the structure is

essential for normal chromosome formation and cell division (Poonperm et al., 2015).

#### *Centromere – structure and function*

The centromere is a feature of all eukaryotic chromosomes and is essential for segregating genetic data during cell division (Schalch & Steiner, 2017). The centromere is a specialised region on the chromosome that plays a crucial role in chromosome segregation during cell division. It is where the kinetochore, a protein complex, attaches to the microtubules of the mitotic spindle, ensuring that chromosomes are pulled to opposite poles of the cell during division (McKinley & Cheeseman, 2016).

There are two distinct types of centromeres; the first is holocentric centromeres, where the centromeric DNA is diffuse along the chromosome length (McKinley & Cheeseman, 2016). Alternatively, monocentric chromosomes are the more common form of centromere (Figure 1.7.C), where the centromeric DNA is arranged into a point centromere or regional centromere (McKinley & Cheeseman, 2016).

Point centromeres consist of short sequences of DNA specific to the centromere function and are seen in yeast species (Pluta et al., 1995). In comparison, regional centromeres are formed of tandem repeats that contribute to the centromere function but are not sufficient enough to function alone and are seen in humans (Sullivan, 2013). These regional centromeres often contain a central core where the centromere protein A (CENP-A) nucleosome resides (McKinley & Cheeseman, 2016). CENP-A is a unifying aspect of the centromere

and is key in the condensation of chromatin into chromosomes. CENP-A is a highly conserved centromere protein that is essential for centromere function (McKinley & Cheeseman, 2016). It is also essential for the localisation of the spindle components to the kinetochore (Fachinetti et al., 2013). To achieve efficient segregation of chromosomes, the centromere works in collaboration with the kinetochore to form attachments to the meiotic or mitotic spindles (McKinley & Cheeseman, 2016). Due to the key role the centromere and kinetochore play in chromosome segregation during cell division, any abnormalities in their functions can have detrimental effects, leading to developmental disorders or diseases (Holland & Cleveland, 2009).

#### *Kinetochore – structure and function*

Kinetochores are a proteinaceous multi-subunit assembly that is assembled upon centromeres (Figure 1.7C) and functions to facilitate chromosome segregation from a mother cell into daughter cells during cell division (Musacchio & Desai, 2017). The kinetochore consists of two regions, the inner and outer kinetochore, which assist in the equal division of chromosomes during cell division. The inner kinetochore binds directly to the centromeric region and assembles throughout the cell cycle; in comparison, the outer kinetochore binds to KMTs and only assembles during mitosis (Navarro & Cheeseman, 2021; Ris & Witt, 1981). Therefore, the interactions between kinetochores and the spindle microtubules begins during early mitosis through the 'search and capture' action of the microtubules (Section 1.1.2.). As the connection becomes more stable throughout mitosis this connection assists in arranging chromosomes in the metaphase configuration (chromosome

congression) and separating them during anaphase (Drpic et al., 2018; Maiato et al., 2004).

The 'ideal' kinetochore varies during stages of cell division and also, across species. The structure of the inner kinetochore varies throughout the cell cycle in line with the decondensation and replication of chromosomes in the S phase and then the condensation of chromosomes during the G2/M transition. This variation in the inner kinetochore refers not only to the conformation of the protein but also to the abundance of the formative components, which varies throughout the cell cycle changes (Eskat et al., 2012).

The variation in kinetochore structure has also been shown to vary between species, and the size of the complex can impact its functionality. Drpic et al., (2018) used Indian muntjac cells to study the physiological relevance of the kinetochore size. Female Indian muntjac cells have the lowest chromosome number of any mammalian cells ( $2n=6$ ) and their chromosomes are much larger than that of humans, making them a very useful model for chromosome research (Drpic et al., 2018). Magidson et al., (2015) used computational models to determine that error prevention during spindle assembly in humans is influenced by changes in the kinetochore size and shape. These computational models were supported by (Drpic et al., 2018), who found that larger kinetochores did have more efficient chromosome orientation and congression but increased merotelic attachments and abnormal segregation. However, their electron microscopy imaging of *C.elegans* does not support the data from the Indian muntjac cells,

indicating that the optimal size varies depending on the species (Drpic et al., 2018).

The kinetochore is a key component of chromosome segregation, and abnormalities in kinetochore function could severely impact cell division and result in aneuploidy. Zielinska et al., (2019) used super-resolution microscopy to study the centromere and kinetochore in egg cells arrested at metaphase II. Their study found that centromeric chromatin de-compacts with age, and kinetochores formed on these decompacted centromeres can become fragmented, affecting 30% of human and mouse kinetochores (Zielinska et al., 2019). The microtubule-pulling actions worsened the fragmentation, which may provide an explanation for increased aneuploidy rates in mature women (Zielinska et al., 2019).

#### *Chromatin – structure and function*

Within the nucleus, the genetic information is packed into a form called chromatin (Figure 7A), which is a nucleoprotein of organised and repeated epigenetic information (Kouzarides, 2007). Chromatin is primarily composed of protein and DNA (Krude & Elgin, 1996). The sequence of DNA contributes to the structure of chromatin, and this spatial structure partitions the genome of eukaryotic cells into distinct functional domains (Kouzarides, 2007). These TADs can affect the gene expression and chromosome stability of the cell; they are also essential for processing regulatory signals and generating cellular responses (Hnisz et al., 2016; Ong & Corces, 2014).

The basic unit of chromatin is the nucleosome, and this is composed of a histone octamer with H2A, H2B, H3 and H4. Post-translational modifications to these histones can affect the accessibility and gene expression of the chromatin and, therefore, alter cell identity (Corpet et al., 2020). Although the nucleosome core (the basic unit of chromatin) structure is well documented, the 30nm fibre structure remains unclear (Tremethick, 2007). Finch and Klug (1976) proposed the solenoid model, which suggests consecutive nucleosomes are positioned beside each other within the 30nm fibre that condenses to form the chromosome structure (Tremethick, 2007). Alternatively, a second model was proposed that suggested the nucleosomes were organised into a zig-zag structure that consists of two rows of nucleosomes with linker DNA between nucleosomes (Tremethick, 2007). This was supported by (Schalch et al., 2005), who studied the crystalline structure of a tetranucleosome and confirmed there were two rows of nucleosomes and linker DNA segments.

High-frequency contacts can be used to indicate what the 3D organisation of chromatin looks like. The chromosome conformation capture (3C) method and technologies derived from this method, such as Hi-C, can shed light on the chromosome organisation and provide information on components such as chromatin organisation, TADs and loops (Naumova et al., 2013). These Hi-C studies identified chromatin composition as an array of linear chromatin loops (Naumova et al., 2013). This is further confirmed by advanced light microscopy (Liang et al., 2015). Most other chromosomal components are formed from chromatin; therefore, the correct composition of chromatin is essential for cell division.

*Telomeres – structure and function*

Telomeres are short segments of DNA present on the ends of chromosomes, ranging from 10-15kb (Figure 1.7D). These segments of DNA are formed of a tandem repeat (TTAGGG – in humans) that has a 3' G-rich overhang. This overhang invades the telomerase 5' DNA strand and forms a D-Loop (Liu et al., 2019).

The shelterin complex caps the telomeres in humans; this complex is formed of six proteins: TRF1, TRF2 (Telomere repeat binding factors), TIN2 (TRF interacting nuclear factor), POT1 (Protection of telomeres), TPP1 (Tripeptidyl peptidase 1) and RAP1 (Ras-related protein 1) (Shay & Wright, 2019; Turner et al., 2019). The shelterin complex prevents erroneous DNA repair mechanisms, and if the complex is deficient in any of its proteins, this can lead to telomere dysfunction or cellular senescence (Liu et al., 2019).

The telomere length decreases as an individual ages, and this shortening inhibits shelterin complex function (Lansdorp, 2008; Muñoz-Espín & Serrano, 2014). Eventually, the shortening is significant enough that the cells can no longer divide. This often occurs after 40-60 passages of the cell; this is termed the Hayflick limit (Turner et al., 2019). Telomerase is an enzyme responsible for maintaining the length of telomeres, the protective caps at the ends of chromosomes. This enzyme is crucial for cell longevity and stability, as it counteracts telomere shortening.

Telomeres are the most well-studied component of the chromosomes due to their role in cellular senescence and ageing. The connection between

telomerase and cellular senescence has been linked to cancer, as abnormalities in telomeres may cause chromosomal abnormalities during division.

### *Chromosome periphery – structure and function*

The chromosome periphery (CP) was identified for the first time in the late 1800s, and thought to be present in the nucleolus, but interacting with the chromosomes during division. One of the first sketches of the structure was provided in the 1920s (Figure 1.8), and has been imaged with improving technologies since then (Bolles Lee, 1920). One of the earlier studies referred to the CP as a 'sheath' and considered it to be a gelatinous layer coating the surface of chromosomes (Metz, 1934). However, the biophysical properties of the CP were not yet known at this stage and still have not yet been fully elucidated. Over the following years the CP was explored under many different names including the periphery, perichromosomal layer, chromosome coat, surface and matrix. Hsu et al., (1965) confirmed the presence of nucleolar material surrounding mitotic chromosomes in Chinese hamster cells, referring to it as a chromosome coat. Using azure B staining and brightfield imaging they successfully demonstrated removal of this 'chromosome coat' following ribonuclease digestion (T. C. Hsu et al., 1965), Hernandez-Verdun & Gautier (1994) Later showed one of the first TEM images of the CP in which a 'grainy' surface could be seen surrounding the chromosomes. These images indicated the CP was formed of chain-like structures with only parts of the periphery being in direct contact with the chromosomes and that it was not distributed evenly along the entirety of the chromosome structure. This led them to theorise that the CP played a role in mitotic organisation, but this could not yet be confirmed. However more recent

studies into the periphery used three-dimensional correlative light electron microscopy (3D-CLEM) imaging was used to investigate the chromosome periphery (Booth et al., 2014) (Figure 1.8). Booth et al., (2014) demonstrated that the CP actually makes up one third of the chromosome volume and the removal of it led to clumping of the chromosome structures. This demonstrated the function of the CP in maintaining mitotic chromosome structure and separation of sister chromatids.

The understanding of the periphery structure and composition has expanded over the years and is known to include nuclear proteins and ribonucleoproteins, but the composition is not yet fully categorised (Booth et al., 2014; Hernandez-Verdun & Gautier, 1994). Some of the key identified components include nucleolin, fibrillarin and Ki67, among others. The significant discovery of Ki67 being a significant organiser of the periphery proteins has led to a reinvigoration of this area of research, opening new avenues to explore its role in cell division.

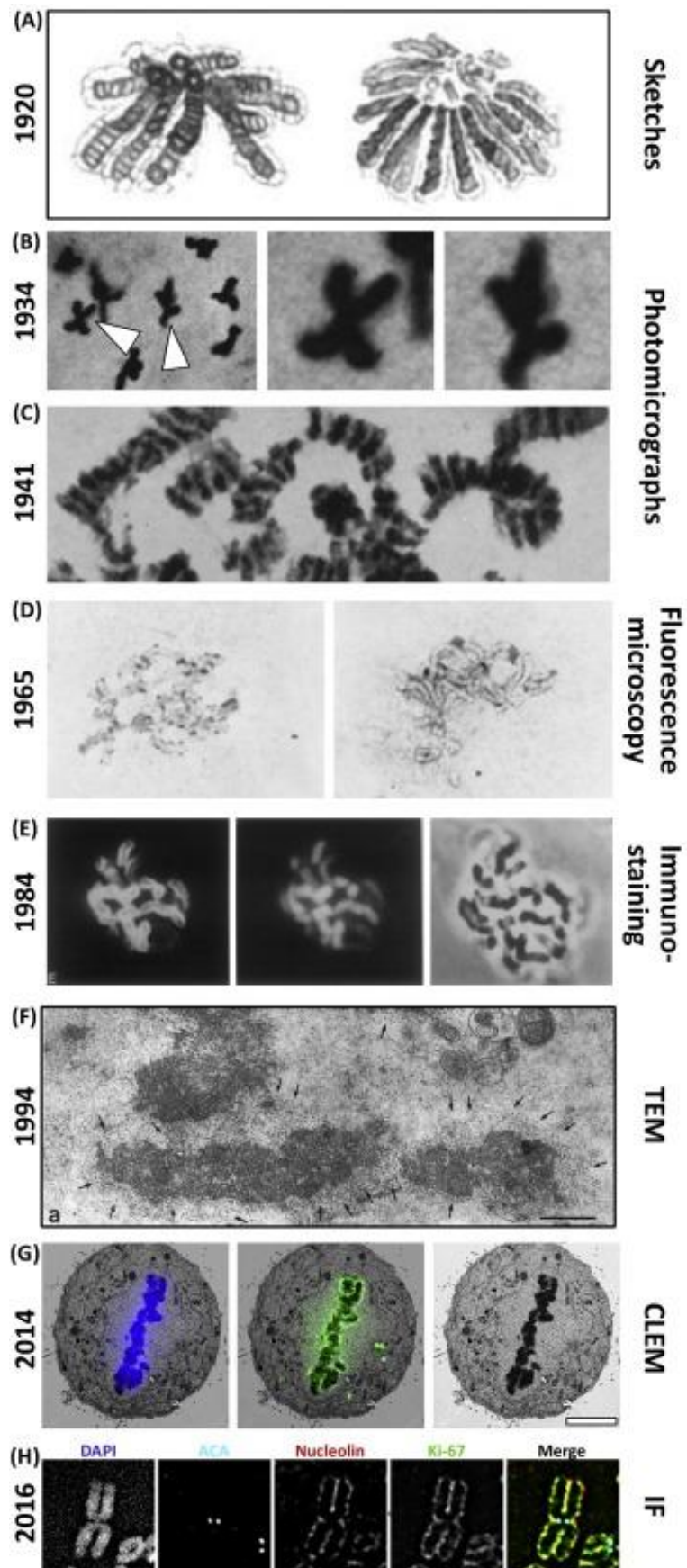


**Figure 1.8. Historical developments in the investigation of the CP.** (A) One of the first sketches depicting the chromosome periphery (Bolles Lee, 1920) (B-C) Pictomicrographs of the substance surrounding chromosomes (Coleman & Hillary, 1941; McClintock, 1934) (D) One of the earliest fluorescence microscopy images of the CP stained with pyronin-methyl green (T. C. Hsu et al., 1965) (E) immunostaining of chinese hamster ovary cells (Mckee et al., 1984) (F) TEM image showing the fuzzy appearance of the CP (Hernandez-Verdun & Gautier, 1994) (G) 3D-CLEM imaging and processing of a metaphase cell showing the DNA (blue) and the CP (green) (Booth et al., 2014). (H) High-resolution fluorescence microscopy of the CP proteins (Ki67 and nucleolin) (Booth et al., 2016).

## 1.3. Ki67

### 1.3.1. Ki67 background

Ki67 is a proliferation marker protein produced by the *MKI67* gene, located on chromosome position 10q26.2. The entire gene locus *MKI67* was sequenced by Duchrow et al., (1996), who determined that the sequence was 30,000 base pairs in size. Ki67 was identified by Ki67 monoclonal antibody that had been produced from mice immunised with Hodgkin lymphoma (cell line L428) (Gerdes et al., 1983). Schlüter et al., (1993) sequenced the cDNA of the protein, identifying two splice variants encoding for two isoforms; the first has a molecular mass of 320kD and is missing exon 7, and the second has a mass of 359kD. Three further splice variants have since been identified; however, their function is not currently known (Schmidt et al., 2004).

Within the two Ki67 proteins are a few conserved features, including a PP1 binding domain, a forkhead-associated domain (FHA) and a region of 16 tandem repeats. Ki67 utilises the PP1 binding domain to bind PP1 $\gamma$  to anaphase chromosomes and is known to regulate heterochromatin during interphase (de Castro et al., 2017; Takagi et al., 2014). The FHA domain is a common feature of

proteins associated with regulating the cell cycle and recognising phospho-threonine epitopes (Hofmann & Bucher, 1995). Finally, the 16 tandem repeats are present in all isoforms of human Ki67 and are all encoded by exon 13, each containing a highly conserved amino acid sequence, referred to as the Ki67 motif (TPKEKAQALELDLAGFKELFQTP) (Gerdes et al., 1983).

Ki67 was found to be present exclusively in proliferating cells (all stages of the cell cycle G1-M) but not in cells in G0 (senescent/quiescent cells), with the protein residing in the nucleus during interphase and relocating to the chromosome surface during mitosis (Gerdes et al., 1984). This differential expression between cycling and resting cells has made Ki67 popular as a proliferation marker, particularly in pathology, where it is considered a successful diagnostic tool for various cancers (Scholzen & Gerdes, 2000).

### 1.3.2. Use as a proliferation marker.

Ki67 is a standard marker used in immunohistochemistry for the assessment of proliferation. As pathology samples are routinely fixed and embedded in paraffin and these sample types often fail to stain with Ki67 successfully, alternative antibodies were developed to act as equivalents. MIB-1 is a monoclonal antibody against the Ki67 antigen and is the most routinely used antibody for detecting Ki67-positive cells in paraffin-embedded pathology samples (Cattoretti et al., 1992). The Ki67 index (percentage of cells positive for Ki67 staining) gives an understanding of the proliferative characteristics of tumours, providing insights into prognosis and patient outcome, which is why it is a commonly used marker in the assessment of cancer patients (Scholzen &

Gerdes, 2000; Uxa et al., 2021). For example, data suggests the level of Ki67 in breast cancer patients (<10-14% Ki67 Index score) is evidence of the patients having a higher risk prognosis, which may influence treatment options, in particular, adjuvant therapies (Yerushalmi et al., 2010).

However, despite the identification and diagnostic use of the protein over four decades ago, the function of Ki67 has only recently been explored and found to have a significant role in the formation and organisation of chromosomes (Booth et al., 2014).

### 1.3.3. Ki67 and the Chromosome Periphery

As previously stated, the localisation of Ki67 changes throughout the cell cycle, being present in the nucleus during interphase and then localising to the chromosome surface during mitosis (Figure 1.9). Booth et al., (2014) showed that Ki67 plays an essential role in the recruitment and organisation of proteins and RNAs associated with the CP. Ki67 acts as a steric and electrostatic barrier that aids chromosome individualisation during early mitosis, facilitating the transition from an interphase state to a condensed mitotic state (Booth et al., 2014). The CP also interacts with condensin complexes as part of the restructuring of chromatin into chromosomes (Hirano, 2012). This identification of Ki67 as a key organiser of the CP meant that for the first time since its initial observation in the 1880s it could now be manipulated.

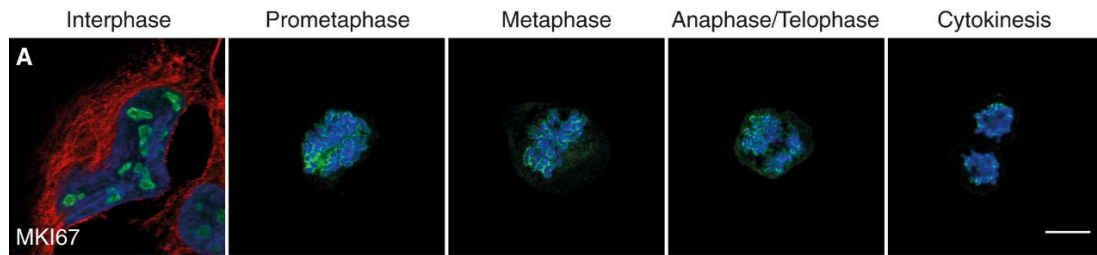


**Figure 1.9. Ki67 localisation to the chromosome periphery throughout mitosis.** Immunofluorescence staining of Ki67 shows the localisation of Ki67 to the nucleoli during interphase and the periphery during all stages of mitosis. Ki67 (green), microtubules (red) and DAPI (Blue). Scale bar – 10 $\mu$ m. (Stenström et al., 2020).

Booth et al. (2014) confirmed Ki67 was the organiser of the CP via depletion studies and imaging of the ultrastructure using electron microscopy (EM) in Henrietta Lacks (HeLa) cells (Figure 1.10). EM imaging of control (CTRL) and Ki67 knockdown (KD) cells showed the loss of the ‘fuzzy’ chromosome periphery following Ki67 depletion (Figure 1.10.A). This loss was confirmed quantitatively via line scans from the cytoplasm into the chromosomes to analyse the change in greyscale values. The Ki67 KD cells had a significantly steeper decline in density across the cytoplasm-chromosome border (Figure 1.10.B), confirming the loss of the periphery and suggesting that Ki67 is a key organiser of the periphery, without which it is unable to form successfully. This was supported by a more recent study by (Stenström et al., 2020), who performed fluorescence microscopy on HeLa cells and also found that Ki67 was essential for at least 19 of the periphery proteins to adhere to the periphery during mitosis.

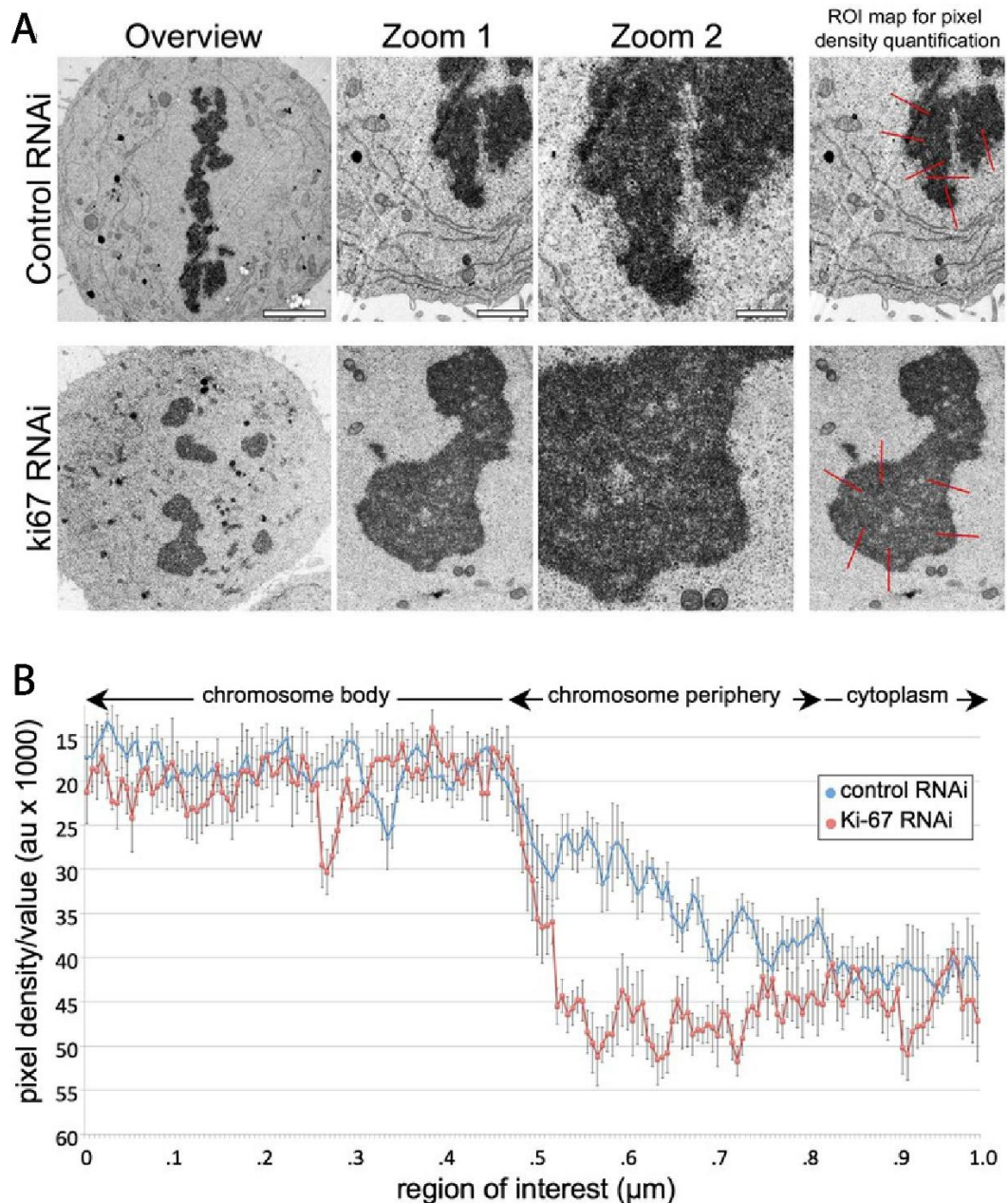


**Figure 1.10. *Ki67 identified as the organiser of the chromosome periphery.*** (A) EM of HeLa cells for control and *Ki67* knockdown cells showing the loss of the ‘fuzzy’ chromosome periphery appearance and the regions of interest for line scan analysis (red lines), (B) Greyscale analysis of control (blue) and *Ki67* knockdown (red). Image from (Booth et al., 2014).

As the CP could now be manipulated, its function could be explored.

There are four key functions that have been theorised: 1) a physical barrier between cytoplasmic proteins and chromatin protecting from DNA damage, 2)

maintenance of chromosome structure, 3) a buffer between chromosomes preventing 'sticking', and 4) a storer of nucleolar proteins during mitosis.

The first of these potential functions was proven to be unlikely by Booth et al., (2014) who observed that the protein 53BP1, a protein that localises to foci with DNA damage, was not varied between control and Ki67 knockdown cells. This indicated that there was no increased DNA damage following the loss of the chromosome periphery, and therefore, its role as a protector from DNA damage is unlikely. The second and third theorised roles, that of the maintenance of chromosome structure and preventing chromosome 'sticking', were shown to be likely, if not definite, roles of the periphery in mitotic cells by (Booth et al., 2016). Following the depletion of Ki67 and the consequent loss of the periphery, the typical structure of chromosomes was lost, and aggregates formed where the chromosomes 'clumped' together (Figure 1.11.). By forming a peripheral region surrounding the chromosomes, Ki67 supports mitotic spindle attachment and the organisation of heterochromatin (Cuylen et al., 2016; Sobacki et al., 2016). During anaphase, the periphery also helps prevent premature chromosome decondensation, ensuring accurate segregation to the daughter cells. This is done via targeting of PP1y by Ki67 during anaphase and binding to the PP1 binding domain, enabling mitotic histone phosphorylation reversal and, therefore, mitotic exit. The final role was also shown to be possible from Booth et al., (2014) and Stenström et al., (2020) who both showed that Ki67 recruits periphery proteins to the surface of the chromosomes, and they remain there throughout mitosis until mitotic exit. This suggests that the chromosome periphery doesn't

have a singular role and, in fact, has multiple functions during cell division to ensure 'normal' progression.

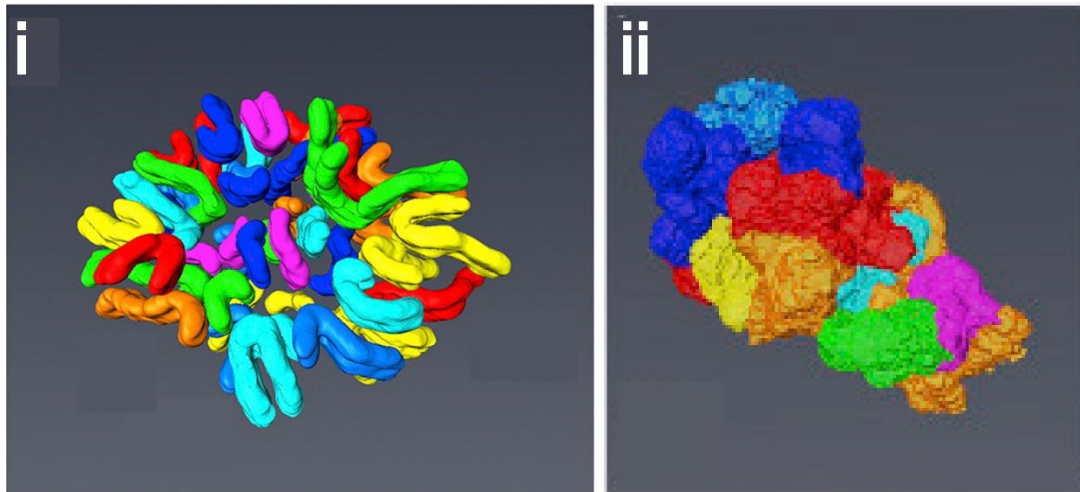


**Figure 1.11. Altered chromosome structure as a result of Ki67 depletion.** (i) AMIRA model of control chromosomes showing typical chromosome structure (ii) AMIRA model of Ki67 knockdown showing 'clumping' of chromosomes. Image from (Booth et al., 2016).

The CP is one of the least characterised components of the chromosome structure. As a result, the associated proteins within the periphery were previously thought to be fewer than 20 proteins (Hernandez-Verdun & Gautier, 1994). However, this is now known to be a significant underestimation, and more than 60 associated proteins have currently been identified, with novel proteins being identified to this day (Stamatiou et al., 2023; Stenström et al., 2020; Takata et al., 2007). There is currently no comprehensive biochemical analysis of the periphery and therefore the complete composition is still unknown.

The role of Ki67 as the recruiter of these components was shown through the inability of many known periphery proteins being unable to localise to the chromosome surface following Ki67 depletion (Booth et al., 2014; Stenström et al., 2020). Disruptions in the expression or function of Ki67 and other

chromosome periphery components during mitosis have been implicated in genomic instability, aneuploidy, and diseases such as cancer. This highlights the importance of Ki67 as a proliferation marker and its essential role in chromosome stability and segregation. The role of the periphery has thus far only been explored in mitosis and its role in meiosis is currently completely unexplored; however, its role in chromosome organisation and the individualisation of chromosomes could be vital in female gametes as they are stalled in prophase for a significant time. Understanding the role of the periphery in these cells could provide insight into the occurrence of aneuploidies, particularly the high rates that occur in mature women as their gametes have been 'paused' in meiosis for an extended period. There is also a clear need for advanced imaging pipelines to study the chromosome periphery and more widely overall chromosome ultrastructure to further understand the chromosome structure in mitosis and meiosis.

## 1.4. Advanced Imaging Techniques

### 1.4.1. Overview of imaging techniques used in chromosome research

Microscopes are split into roughly two groups: light microscopes (LM) and electron microscopes (EM). These two microscope modalities have subtypes that mean the imaging technology can be specialised to the subject (Chen et al., 2011). The light microscopes include brightfield, fluorescence and confocal, all of which can be used for chromosomal imaging but can be limited by their resolution of images, which can impact the ability to view significant features of chromosomes clearly (McNamara et al., 2017). However, LM can tag specific cellular components easily with fluorophores and can also be used for live

imaging of cells, providing a more comprehensive view of the chromosomes during cell division (McNamara et al., 2017). In comparison, electron microscopes can produce a higher-resolution image than light microscopes, allowing subcellular structures to be imaged and analysed. Due to the nature of the technique, however, the samples are placed in a vacuum for imaging. Therefore, live imaging is not possible, preventing real-time analysis during cell division.

These can and have been used for chromosomal imaging, some with better results than others. LM is limited by its resolution for chromosomal imaging. In comparison, EM offers high-resolution images of cellular structures, but its primary limitations are specificity and imaging depth. Since the technique requires samples to be placed in a vacuum, the sample must be sliced into thin sections to capture detailed images, which means that three-dimensional structures are challenging to capture completely (McNamara et al., 2017). 3D-CLEM combines light microscopy and electron microscopy on a single sample to generate three-dimensional reconstructions and may provide a new technique to investigate chromosomal ultrastructure without compromising on temporal or spatial resolution.

#### 1.4.2. Fluorescence microscopy and super-resolution microscopy

Fluorescence microscopy is an imaging technique that uses fluorescent dyes and proteins to label specific cellular components. These dyes and proteins fluoresce when excited by light or an electron is moved to a higher energy state. The fluorescent tags absorb the light from the microscope and emit that light at a

longer wavelength, allowing for visualisation of the region of interest. The technique is popular in cell biology due to its high sensitivity, specificity and compatibility with native-state imaging.

Several types of fluorescence microscopy exist, including widefield, multi-photon, and confocal microscopy. Widefield fluorescence microscopy illuminates the entire sample simultaneously, which can be beneficial when interested in larger cell components or whole cell/organoid imaging. However, this method includes a large amount of background signal, especially in thicker specimens, which could limit clarity. Multi-photon microscopy utilises two or more lower-energy photons to excite fluorescent molecules, enabling deeper tissue penetration with minimal damage. Confocal microscopy is one of cell biology's most popular fluorescence microscopy techniques. It uses a laser to scan the sample point-by-point, providing improved resolution and enabling optical sectioning of the sample, which is particularly important when imaging smaller cellular components.

### *Confocal Microscopy*

Confocal microscopy uses lasers (excitation beams) to excite fluorescent tags on a sample, detecting emissions between 400-700nm wavelengths (Combs, 2010). The excitation beam passes through a dichromatic mirror and is redirected through an objective to illuminate a specific point within the sample (Figure 1.12) (Elliott, 2020). The beam scans across the sample, facilitated by sweeping mirrors, and the emitted fluorescence is reflected through the objective and dichromatic mirror to the detector (Elliott, 2020). The detector can

then recreate the region of interest (ROI) image from each individual point illuminated during scanning. A pinhole aperture prevents any light not in the focal plane from passing through to the objective, reducing the signal-to-noise ratio (SNR). As this technique illuminates a single point of the sample at a time, it is also possible to optically section the sample, creating a stack of confocal images that can recreate 3-dimensional structures.

The resolution of the images that can be collected from the confocal is limited by numerical aperture (N.A.), refraction index and wavelength of light (Equation 1 & 2) (Combs, 2010). The pinhole can also affect resolution; for example, opening the pinhole can allow more light into the detector for low emission samples at the cost of resolution, or the pinhole can be narrowed to smaller than a single airy unit at the expense of SNR. Therefore, the best resolution that can be achieved is 0.2 $\mu$ m lateral, and 0.6 $\mu$ m axial (Combs, 2010).

$$\text{Equation 1} \quad \textit{lateral } R = \frac{0.4 \lambda}{NA}$$

$$\text{Equation 2} \quad \textit{axial } R = \frac{1.4 \lambda \eta}{(NA)^2}$$

$\lambda = \textit{wavelength}$ ,  $\eta = \textit{refractive index}$ ,  $NA = \textit{numerical aperture}$

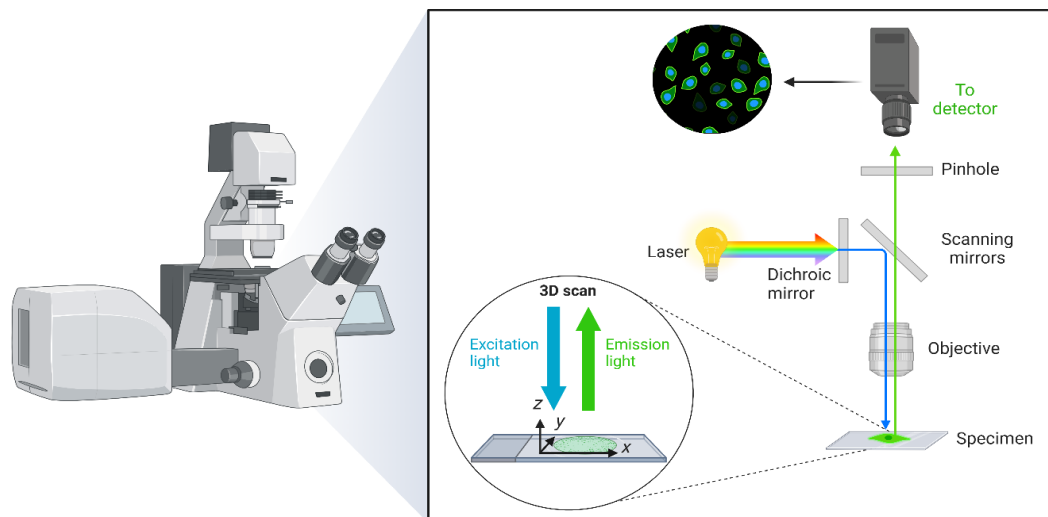


**Figure 1.12. Confocal microscope schematic.** Schematic shows the key components of a confocal microscope, including the laser, objective lens, dichromatic mirror and pinhole. The path of light from the laser to the sample and up to the detector can be seen in this figure. (Figure made using BioRender).

This method can be used on both fixed and live samples. However, due to the intensity of the excitation beam, photobleaching (damage to the fluorophore stopping fluorescence) and cell damage can occur, particularly in delicate sample types, and should be carefully considered, especially in live samples.

### *AiryScan*

Traditional confocal microscopy has a limited resolution due to light refraction. AiryScan (Zeiss) is a form of super-resolution confocal microscopy that achieves resolutions beyond the diffraction limit using a specialised honeycomb detector system.

The patented honeycomb detector system consists of 32 detectors, each collecting light from multiple points within the focal plane. The image reconstructed from this data has a higher resolution than traditional confocal

microscopy, with the lateral resolution reaching  $0.12\mu\text{m}$ . However, this microscope's axial resolution is not altered and remains  $\sim 0.6\mu\text{m}$ .

AiryScan and other 'super-resolution' confocal microscopes have become more popular in cell biology over recent years due to the increasing available options and accessibility, as well as the sample preparation remaining the same as traditional confocal microscopy.

AiryScan is also faster than many other super-resolution techniques, such as photoactivated localization microscopy (PALM) or stimulated emission depletion (STED) microscopy. Zeiss has developed a fast mode with AiryScan 2 that can increase speed imaging, which can be particularly useful during live imaging to reduce exposure to the lasers and reduce the likelihood of photobleaching or damage to the sample.

### 1.4.3. Electron microscopy

EM is a high-resolution imaging mode that generates an image of biological samples using a beam of electrons rather than a beam of light. EM enables the visualisation of subcellular structures, making it invaluable for studying cellular components such as organelles and chromosomes.

#### *Imaging System*

The main components of an electron microscope include the electron column, specimen chamber, detectors, and accompanying computer system (Ul-Hamid, 2018) (Figure 1.13). There are a few types of electron sources, including thermionic or field emission sources. Thermionic sources use a heated

filament or crystal that emits electrons when a current is applied. Field emission sources apply an electrostatic field to a tip which ejects electrons. The scattered or absorbed electrons from the sample are then detected and an image of the sample surface is recreated. Many signals can be generated including secondary electrons, backscattered electrons and x-rays.

Secondary electrons are produced at the surface of the specimen and are generally used for topological studies of biological samples. Secondary electrons are generated as a result of energy transfer from the electron beam to an atom within the sample. Back-scattered electrons are generated when the electron beam collides with the nuclei of an atom within the sample, causing high-energy electrons to be reflected off the sample (Peddie et al., 2022). the quantity of back-scattered electrons produced during these collisions is dependent on the atomic number of the sample; the higher the atomic number, the more back-scattered electrons are produced.

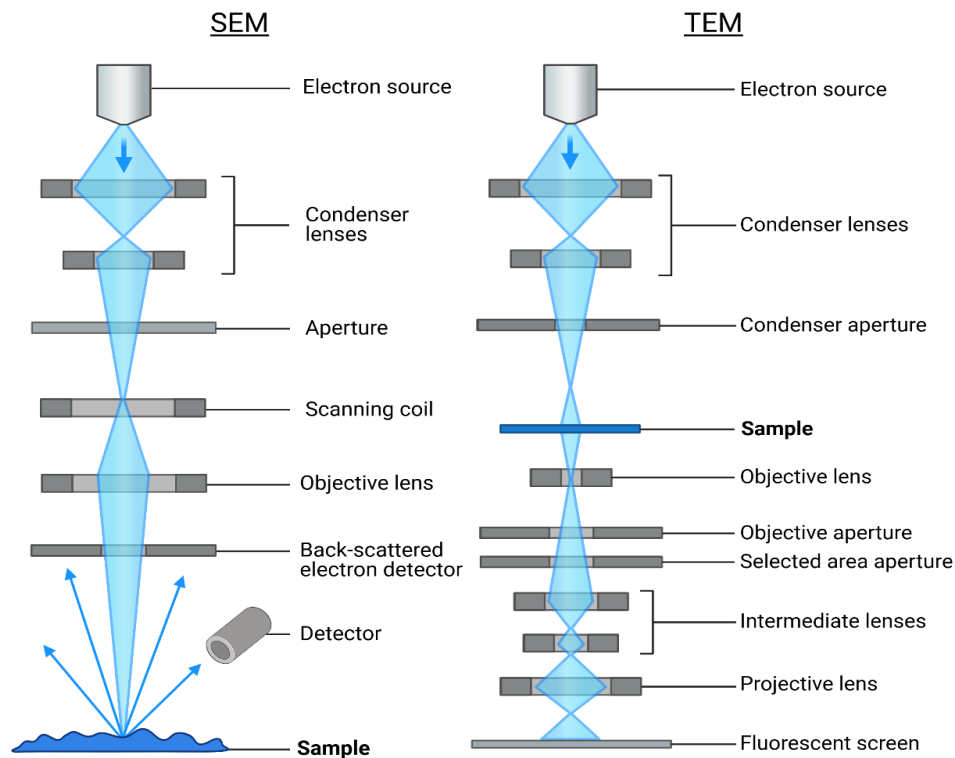


**Figure 1.13. Electron microscopy schematic.** Schematic of SEM and TEM. SEM: an electron beam is generated by the electron source and focused through condenser lenses and an aperture. The beam passes through a scanning coil and objective lens before interacting with the sample surface. Back-scattered and secondary electrons are detected to create an image showing surface details. TEM: the electron beam is focused by condenser lenses and a condenser aperture before passing through a thin sample. The beam is magnified by the objective, intermediate, and projective lenses, and the transmitted electrons are visualised on a fluorescent screen to reveal internal structure.

### Types of Electron Microscopy

There are two main types of electron microscopy: Transmission Electron Microscopy (TEM) and Scanning Electron Microscopy (SEM) (Figure 1.10). TEM is often used to study the internal structure of cells, including chromosomes, by transmitting electrons through thin sections of a specimen. This method provides exceptionally high-resolution images  $\sim 0.1$  nm, allowing the observation of minute details within cells and chromosomes. In contrast, SEM is mainly used to observe

the surface of samples and is often used to image larger structures, or sample types and has a typical resolution of around 0.5-4nm.

With TEM an electron beam passes through a thin sample slice, usually loaded on to a copper grid to generate an image of the surface. In comparison scanning electron microscopy uses the electron beam to raster scan over the surface of the sample, and the detectors recreate an image from secondary or backscattered electrons.

Within SEM, there are further subtypes, including focused ion beam (FIB) SEM and serial block face (SBF) SEM. These two techniques refer to the methods used by the SEM system to slice the sample, revealing the surface for imaging. FIB utilises a beam of ions which are sent into the sample to sputter slices of the surface, revealing a new surface for imaging (Russell et al., 2017). In comparison, SBF utilises a diamond knife that manually slices layers of the sample surface away, in situ, to reveal the next slice for imaging (Russell et al., 2017). Both techniques are destructive, as they are done inside the vacuum chamber of the SEM, and the removed slices cannot be collected for mounting to be retained.

The preparation process, including fixation, dehydration, and embedding, can introduce artefacts or alter the native state of the sample. Additionally, the contrast in the images is typically achieved by staining the sample with heavy metals, which can obscure certain fine details of the structure.

EM lacks specificity as cellular components are stained with heavy metals that target broad groups, e.g. osmium binds to phospholipid head regions,

compared to fluorescence microscopy, where individual proteins can be stained with fluorescent tags (Nagaoka et al., 2012).

### *Volume-Scanning Electron Microscopy (Volume-SEM)*

Volume electron microscopy (vEM) is a recent advancement in the microscopy field. It expands on the existing scanning and transmission electron microscopy methods and helps investigate three-dimensional structures in biological samples. Most electron microscopy techniques provide two-dimensional (2D) image data of single slices of specimens, with the development of vEM. The technique is a time-consuming and technically complex method of imaging, especially if using TEM, where the segmentation of the sample is done manually rather than by an automated system, as is often seen in SEM set-ups (Peddie et al., 2022). Due to the low-throughput nature of the technique, the number of replicates produced from this type of imaging may be limited, which can limit conclusions drawn from the data, as the sample population may not be big enough (Peddie et al., 2022).

## 1.4.4. Correlative Light-Electron Microscopy (3D-CLEM)

### *1.4.4.1. Principles and workflow of 3D-CLEM*

3D-CLEM tackles some of the drawbacks of light microscopy and electron microscopy independently and combines the best features of the two. Light microscopy allows for the tagging of fluorescent tags for specific structures (Booth et al., 2016). Although there have been developments in super-resolution microscopy allowing for higher magnification and greater resolution, confocal microscopes have a resolution of ~200nm or ~120nm in super-resolution

confocal microscopes (Elliott, 2020). In comparison, electron microscopy allows for the visualisation of fine structural details in high-resolution as small as 0.1nm, although the resolution of electron microscopes is theoretically unlimited for imaging cells and is restricted by the objective within the EM system.

Specific proteins of interest are fluorescently tagged to identify 'rare events' (stages of cell division) and then imaged with light microscopy before being stained with heavy metals and imaged with electron microscopy. Single samples can be tracked through the 3D-CLEM pipeline and the LM imaging can help identify and locate regions of interest during EM (van Rijnsoever et al., 2008). This enables the identification of the specific structures using fluorescent tags, and through correlation of light microscopy images during EM set-up, the structures can be reidentified and imaged at higher resolution. This overcomes one of the drawbacks of EM and reduces the need for extra steps in the EM processing such as immunogold labelling (van Rijnsoever et al., 2008). This technique can combine the best of both microscopy methods, allowing for specific, high-resolution imaging of cellular components. Applying this to chromosome ultrastructure can provide insight into the geometry of chromosomes and any chromosomal abnormalities that could lead to aneuploidy.

## 1.5. Research Objectives and Hypotheses

### Hypotheses

- Establishing 3D-CLEM at UoNottingham, to study dividing cells, will allow us to “Atlas” chromosomes at all stages of mitotic division to provide new insights into chromosome structure and compaction
- Advanced imaging will reveal that Ki67, and the chromosomes periphery are critical components of oocyte chromosomes in mouse and human.
- We can expand our 3D-CLEM pipeline to study, for the first time, the 3D architecture of human oocyte chromosomes.

### Aims

The overarching goal of this research project was to improve our understanding of chromosome structure mechanics during cell division – more specifically, if the chromosome periphery, the least understood compartment of chromosomes, has an essential role during female meiosis. This ambitious project required substantial development of key multi-modal imaging pipelines, such as 3D-CLEM.

Oocytes are unique in that they undergo a prolonged period of meiotic arrest and are particularly susceptible to errors in chromosome segregation, leading to aneuploidy. The role of the periphery is completely unexplored in meiosis. However, the known role in mitotic cells indicates that it could be essential for maintaining chromosome fidelity in meiosis and may have a role in aneuploidy occurrence. The findings from this research could significantly

enhance our understanding of the underlying mechanisms responsible for chromosome instability in oocytes and identify new targets to address infertility and developmental disorders.

## Significance of the Research:

### Advancing Chromosomal Understanding in Oocytes

This research will contribute to creating the first comprehensive mitotic and meiotic chromosome atlas for human oocytes. This resource can potentially deepen our understanding of chromosome architecture and organisation throughout the division processes. By characterising the structural dynamics of chromosomes in oocytes during meiosis, this research will identify key changes in chromosome behaviour and the factors that contribute to proper chromosome alignment and segregation. To date, there is no complete 3D geometry data of mouse or human oocyte chromosomes, in any stage of cell division. Thus, this work, the first of its kind, is expected to not only resonate with meiosis experts, but also the wider chromosome biology community.

### *Impact on Fertility and Developmental Disorders:*

Exploiting, amongst other tools, a 3D 3D-CLEM pipeline, this study will help to establish if and how specific components of chromosome architecture, such as the chromosome periphery and Ki67, play a role in maintaining chromosomal fidelity in oocytes. Abnormalities in these components may lead to chromosomal missegregation, which is linked to conditions such as trisomies and infertility. By focusing on these aspects, the research could contribute to

more effective diagnostic tools for identifying at-risk oocytes and potentially inform therapeutic strategies.

*Innovative Use of Advanced Imaging Techniques:*

The use of live imaging and 3D-CLEM will provide insights into the dynamic structural changes of chromosomes during meiosis. These cutting-edge imaging techniques, particularly when combined with removing the chromosome periphery, offer a novel approach to studying the mechanisms that regulate chromosome segregation. The ability to track live oocytes in real-time while also investigating ultrastructural details represents a significant advancement in cell biology.

## 2. Methods

### 2.1. Cell Biology

#### 2.1.1. Cell types used

**Table 2.1. Cells and handling conditions used.**

| CELL LINE      | SPECIES     | SOURCE                  | HANDLING   |
|----------------|-------------|-------------------------|--|
| RPE            | Human       | ATCC                    | DMEM f12, 10% FBS, 1% pen-strep, 37°C, 5% CO <sup>2</sup>    |
| MURINE OOCYTES | Mouse – CD1 | University of Newcastle | M2 medium overlaid with mineral oil, 37°C 5% CO <sup>2</sup> |

|                      |       |   |   |
|----------------------|-------|---|---|
| <b>HUMAN OOCYTES</b> | Human | Warwickshire Fertility Clinic via University of Warwick collaboration | Gx-TL media overlaid with mineral oil, 37°C, 5% CO <sup>2</sup> |
|----------------------|-------|---|---|

### 2.1.2. Cell Culture

All cell culture associated with this project was conducted in a category 2 microbiology cabinet. Retinal Pigmented Epithelial (RPE) cells harvested from the retina of a female patient and immortalised using pGRN145 hTERT expressing plasmid (MBA-141, ATCC) created the immortalised cell line hTERT RPE-1 (CRL-4000, ATCC) which were sourced from ATCC.

The suggested cell culture medium, DMEM: F12 (Gibco; 11320033), was supplemented with 10% Foetal Bovine Serum (FBS) (Sigma Aldrich; F9665) and 1% Penicillin-Streptavidin (Gibco; 15070063) to produce a complete medium. A single vial of 2,000,000 RPE cells was thawed in a water bath at 37°C and transferred into a T25 Cell Culture Flask (Thermo Fisher; 156367) containing pre-heated complete media, then immediately stored in an incubator at 37°C with 5% CO<sub>2</sub>. The cells were incubated overnight to allow for cell adherence, and the media was replaced the following day after ensuring the cells were healthy and viable. Cells were expanded into T75 flasks (Thermo Fisher; 156499) once they had reached 80% confluency in the T25 flasks. After the removal of media from the flask to remove non-adherent (dead) cells and two washes with Phosphate Buffered Saline (PBS) (Gibco; 10010023), the cells were separated from the surface of the flask using TrypLE Express Enzyme 1X (Gibco; 12604013) and

incubated for ~3 minutes at 37°C (volume of TrypLE dependent on vessel size). The reintroduction of pre-warmed complete media inhibited the TrypLE, and the resulting cell solution was used to split the cells into a fresh T75 flask at a 1:3 ratio. These flasks were then returned to the incubator at 37°C and 5% CO<sub>2</sub> until needed for an experiment or until they required splitting again to maintain optimal cell health.

### 2.1.3. Cell Storage

Stocks of cells were made up from early passage cells and stored for long periods of time in liquid nitrogen, using Cellbanker 2 (amsbio; 11914). The solution protected the integrity of the cells during long-term storage in -150°C. When stocks were required to maintain cell stocks, a low passage vial of cells was thawed and expanded in the same manner as previously stated. When sufficient cells were grown, they were detached from the surface of the flask using TrypLE, and the collected media and cells were centrifuged at 300 x g for five minutes. The supernatant was then removed, and the pellet of cells was resuspended in Cellbanker 2 media. The cryovials hold approximately 750µl, so the volume of freezing media was determined by having a concentration of approximately two million cells per 700µl. These cryovials containing the cell solution were then moved immediately to -150°C liquid nitrogen for long term storage.

### 2.1.4. Mycoplasma testing

Routine mycoplasma testing was done on any cultured cells monthly using a Plasmotest™ Mycoplasma Detection kit (InvivoGen; rep-pt1). Cells were

cultured in antibiotic-free media for a minimum of 7 days, and the collected media was incubated with the cells for at least 48 hours prior to collection and testing.

### 2.1.5. Cell counting and seeding

The RPE cells were counted using a haemocytometer. After detaching the cells from the base of the flask with TrypLE and the addition of complete media, 10 $\mu$ l of cell suspension was loaded onto the haemocytometer. The haemocytometer slide was viewed using the 10x objective on a standard inverted light microscope. The slide surface contains gridded regions for counting of various cell types. The RPE cells within each of the four corner squares of the grid were manually counted. Cells on the top and right edge of the squares were counted, whereas cells on the bottom and left were not. The total number of cells counted was then used to calculate the total cells/ml (equation 1). The number of cells per ml was then used to calculate how much cell solution was required to achieve the desired cell density during cell seeding (equation 2).

$$\text{cells/ml} = \frac{\text{total cells counted} \times 10,000 \text{ cells/ml}}{4 \text{ squares counted}}$$

$$\text{volume of cell solution needed} = \frac{\text{cells/ml} \times 1000\mu\text{l}}{\text{cell count required for each well}}$$

For this research RPE cells were seeded either into 12-well dishes (Falcon; 351143) for immunofluorescence staining or 35mm gridded dishes (MatTek; 35G-) for 3D-CLEM. 18mm round glass coverslips (Scientific Life Supplies; REF: MIC3342) were placed into the bottom of each well of the 12-well plate prior to cell seeding. The coverslips were stored in 100% ethanol for sterility

and washed three times for two minutes in PBS before placing one coverslip into each of the 12 wells on the plate. The coverslip was pushed down with tweezers to ensure they were secured to the well's base and prevent cell shearing during handling. RPE cells are adherent and require no fixative to be applied to the coverslips before seeding. The 35mm gridded dishes have a glass bottom so require no preparation prior to cell seeding. The desired quantity of cells was then seeded onto each of the coverslips, or into the gridded dishes, and the plates were incubated at 37°C for at least 24 hours.

## 2.2. Mouse Oocytes

### 2.2.1. Collection and Culture

All animal work was undertaken at The University of Newcastle. All animal handling was performed in accordance with the UK Home Office Animal Scientific Procedures Act 1986. The Project did not require Home Office licensing, so approval was given and monitored by Newcastle University's Comparative Biology Centre Ethics Committee – AWERB reference 663.

Six-to-ten-week-old female CD1 mice (Charles River; 022) were used for oocyte collection. GV oocytes arrested in Prophase were syringe collected from ovaries, and cumulus cells surrounding the oocyte were mechanically stripped by a glass pipette. Oocytes were handled and imaged in droplets of M2 medium (Sigma Aldrich; MR-051-F) under mineral oil (Sigma Aldrich; ES-005-C). Where it was required to maintain cell arrest in Prophase I, the M2 media was supplemented with 30nM 3-isobutyl-1-methylxanthine (IBMX) (Sigma Aldrich;

17018). Cells with minimal granularity, clear perivitelline space and centralised germinal vesicle (GV) were selected for. Cells for both the control and the knockdown groups were randomly selected from the same pool of oocytes.

### 2.2.2. Ki67 Knockdown

A morpholino oligo was used to knock down endogenous Ki67 mRNA. Sequence: AGAAGCCTCTCGGTGAAGCTCGCA – designed and generated by GeneTools. Manufacturer instructions were followed, and the morpholino was used at a concentration of 1nM in water and heated at 65°C for 5 minutes prior to usage. Morpholinos are DNA analogs that bind to complementary regions of targeted mRNA preventing translation of the sequence and consequently protein formation (Heasman, 2002). The oligos are stable as they are not susceptible to enzyme degradation and are soluble due to their limited Guanine content (<36%); they are also specific and have few non-antisense effects making them an ideal method of protein depletion in developmental biology studies (Moulton, 2006).

Oocytes were microinjected on an Olympus IX71 inverted microscope using a heated stage and the handling conditions described above. Microinjection needles were made from filamented glass capillaries (Harvard Apparatus) and a P-97 Flaming/Brown micropipette puller (Sutter Instruments). Morpholino injections were delivered with a PV830 Pneumatic PicoPump and MICRO-ePore (World Precision Instruments; SYS-PV830;). The injection volume was determined by cytoplasm displacement and was ~0.25% cell volume.

## 2.3. Human Oocyte collection

### 2.3.1. Donation to Research

Any research using human oocytes was conducted as part of a study approved by the NHS Research Ethics Committee (Indicators of Oocyte and Embryo Development 04/Q2802/26) and under the Human Fertilisation and Embryology (HFEA) research licence (R0155; Indicators of Oocyte and Embryo Development). Human oocytes were sourced from the Centre for Reproductive Medicine, University Hospitals Coventry and Warwickshire in collaboration with the McAinsh Lab at the University of Warwick, as described in Currie et al., (2022). Oocytes are donated by patients receiving fertility treatment as part of an egg-sharing program. Patients provide informed consent for eggs that are deemed unsuitable for in vitro fertilisation (IVF) or intracytoplasmic sperm injection (ICSI) to be donated for research purposes. Clinical embryologists verified consent during oocyte evaluation

### 2.3.1. Oocyte collection and transport

Oocytes were generally collected from the patients in the morning, and following early assessment by a clinical embryologist, they are classified as acceptable for usage or not. The oocytes were stored in Gx-TL media (Vitrolife; 10172) droplets and all handling was performed on a heated stage at 37°C. The cumulus cells of the oocyte were mechanically stripped, and the oocytes were returned to fresh media droplets overlaid with oil to transport to the research lab at Warwick Medical School. Sealed cell culture dishes were transported from the

clinical lab to the research lab in a portable incubator at 37°C before being transferred to a humidified incubator with 5% CO<sub>2</sub> until required for an experiment (same day).

### 2.3.2. Oocyte Fixation

Oocytes were handled under a stereomicroscope on a heated stage using a handling micropipette. Gridded dishes (MatTek; P35G-1.5-14-C-GRD) were pre-coated with Poly-L-Lysine (PLL) at 20µg/ml for 1 hour at 37°C to aid in the adherence of oocytes to the glass-bottomed dish. The oocyte, held inside a small media volume, was transferred from the holding dish to the MatTek dish. 2% Paraformaldehyde (PFA) (Thermo Fisher; 28908) and 2% Glutaraldehyde (GLUT) (Sigma Aldrich; G5882) fixative in sodium cacodylate buffer was made containing 1:1000 DAPI (Invitrogen; 10116287). A 20µl droplet of the fixative solution was placed onto the oocyte to chemically fix the cell. The dish was then placed into a 37°C incubator to fix for at least one hour before the fixative was removed, and the cell was washed 3 times for 3 minutes with PBS; then the entire dish was flooded with 3ml PBS for storage until IF or 3D-CLEM processing.

## 2.4. Light Microscopy

### 2.4.1. Immunofluorescence

Immunofluorescence staining is a technique used to label specific proteins of interest within a cell or tissue sample, using antibodies tagged with fluorophores. 24 hours post cell seeding and incubation, the cells were adhered and were suitable for immunofluorescence staining. The media was aspirated

from the wells, replaced with pre-warmed 3.5% PFA fixative, and incubated at room temperature for 20 minutes. The PFA acts as cross-linker of proteins, essentially killing the cell and fixing it at a specific timepoint. The fixative should maintain the cell structure without blocking epitopes and preventing antibody binding. The fixative was removed, and the coverslips were washed with PBS three times for five minutes each. 0.3% permeabilising solution made from 10% Triton (Sigma Aldrich; 9036-19-5) stocks and PBS was added to each of the wells and incubated at room temperature for 5 minutes. The triton disrupts cell membranes, improving antibody penetration and labelling of target proteins (Im et al., 2019). After the permeabilising solution was aspirated, the coverslips were rewashed 3 times for 3 minutes with PBS before pre-prepared 2% blocking solution (PBS and 10% Bovine Serum Albumin (BSA) blocking buffer stocks (Thermo Scientific; 37525) was added and incubated for 1 hour at room temperature. BSA improves antibody staining specificity by competing with the antibodies at each of the epitopes, reducing non-specific binding (Im et al., 2019).

The coverslips were removed from the 12-well plate and placed onto a parafilm-coated slide in a humid, dark box. The desired primary antibody solutions were made up in the excess blocking solution, and 90µl was placed onto each coverslip before incubating in the dark box at 4°C overnight. Following 12 hours of incubation, the coverslips were returned to the 12-well plate and 5 x 5 min washes with PBS + 1:1000 Triton were performed. The coordinating secondary antibody solutions were diluted in the remaining block solution. The coverslips were placed back into the dark box, and 80µl of secondary solution

covered the coverslips and were left to incubate for one hour at room temperature. The coverslips were returned to the 12-well plate after 1 hour and washed with PBS + 1:1000 triton 3 times for 5 minutes. The coverslips were washed with PBS twice for 1 minute each and then washed with ultrapure water once for 2 minutes. The coverslips were then mounted onto glass slides using a Mowiol mounting medium (Sigma Aldrich; 1381) containing a 1:1000 concentration of DAPI (ThermoFisher; D1306). The slides were stored overnight at room temperature to allow the mounting medium to cure and be imaged the following day.

#### 2.4.2. Confocal Microscopy

Confocal microscopy was used for the light microscopy portion of the 3D-CLEM pipeline. This technique utilises lasers and excitable fluorescent tags to identify molecular structures in fixed cells. The laser excites selected fluorescent tags within a 400–700nm wavelength range. Emissions from these fluorescent tags are focused through a pinhole, and illumination is restricted to a single sample plane. This setup improves the resolution of the sample by eliminating out-of-focus light, enabling finer structures to be visualised. Imaging a single plane with minimal background signal facilitates the generation of a 3D reconstruction of the sample by combining multiple single-plane images.

The resolution limit of a standard confocal microscope is approximately 200nm, constrained by the diffraction limit of light (Abbe's diffraction limit). Samples were fixed and stained with DAPI as previously described (2.1.6) and imaged at room temperature (RT) using the highest available magnification

objective on the confocal microscope to maximise detail in chromosome structure.

#### *2.2.1.1 Leica SPE Confocal*

The Leica SPE confocal microscope was used for standard confocal imaging throughout this project. A 63x oil immersion objective (N.A.=1.4) and a UV filter (405 nm excitation) were employed to image chromosomal structures during mitosis. Images were captured at a resolution of 4096 × 4096 pixels, with the z-slice thickness determined by the Leica software to optimise imaging quality, typically ranging from ~0.2–0.3 µm per slice. Laser power was kept consistent across all imaging sessions, and an average of 4 scans per slice was used to reduce noise and improve image quality. The pinhole was set to 1 Airy Unit (A.U.) to minimise noise while preserving the signal from the sample.

Brightfield and fluorescence imaging were used to identify cells of interest. Tile scans and z-stacks were acquired to localise and analyse the samples effectively.

#### *2.2.1.2 Zeiss LSM 900 Confocal (AiryScan 2)*

The Zeiss LSM 900 confocal microscope utilises AiryScan 2 technology, making it a 'super-resolution' confocal microscope. This is achieved through its patented honeycomb array design, which employs 32 detector elements, each acting as a pinhole to improve the SNR. The multiple detectors enable the capture of more light and spatial information, enhancing the resolution of the sample and effectively breaking the conventional resolution limit. As a result, the AiryScan confocal can achieve an increased resolution of approximately 120 nm.

Samples were imaged on the LSM 900 using a 100x oil immersion objective (N.A. = 1.518) and a UV filter (405 nm excitation). The Zen Blue software platform was used for image acquisition and the deconvolution of images into AiryScan format. Brightfield imaging and fluorescence imaging were performed to identify cells of interest. Tile scans and z-stacks were acquired to localise samples accurately. Z-stacks were captured with a slice thickness of 0.17–0.18  $\mu\text{m}$ , optimised for AiryScan resolution, achieving a spatial resolution of 24 pixels/ $\mu\text{m}$ .

### 2.4.3. Live Imaging

Live imaging of mouse oocytes through meiosis I was performed on either a DMI8 widefield microscope or an LSM 880 confocal microscope using AiryScanFAST mode, depending on the desired resolution. Oocytes were tagged with SiR-DNA to visualise the chromosomes, and all imaging was done at 37°C on a heated stage to maintain cell morphology.

Lower-resolution, high-throughput, imaging was undertaken on a 20x air lens of the widefield microscope to review the progression of cells through meiosis. These images were captured in 10 focal planes every 10 minutes.

Cells that were to be modelled with AMIRA required higher-resolution images and were imaged using a 63x water immersion lens on the confocal microscope. 132 slice z-stacks of each cell (slice size 420nm) were performed every 30 minutes per cell.

## 2.5. Electron Microscopy

### 2.5.1. 3D-CLEM protocol

#### *Cell seeding and fixation*

Cell seeding for electron microscopy processing required a seeding density of 150,000 cells per dish (MatTek). The cells/ml were counted using the haemocytometer, and the total cell count (equation 1) was used to calculate the volume required for each dish (equation 2). The calculated volume was placed into the gridded EM dishes, and this was topped up to 3ml with complete media before the dishes were put into the incubator at 37°C with 5% CO<sub>2</sub> for a minimum of 12 hours before use for electron microscopy processing.

Fixation was done at least 12 hours post-seeding to ensure the cells had sufficient time to adhere to the coverslips. A fixation solution was made from a 16% stock of PFA and 25% stock of GLUT, in 0.1M sodium cacodylate buffer (Sigma Aldrich; C0250-100G) to create a 2% PFA & 2% GLUT solution. The cell media within the dish was removed, and the prewarmed 4% PFA solution was placed into the dish for cell fixation. PFA fixative was removed from the dish after 30 minutes and washed with PBS three times for five minutes to remove all traces of the fixative. 3ml of PBS was placed into the dishes to ensure the fixed cells remained hydrated during imaging, and these dishes were then imaged using the confocal microscope.

*Staining, dehydration and embedding*

All handling and processing of samples for electron microscopy was done in a fume cupboard due to the toxicity and teratogenic nature of the reagents used.

Following light microscopy imaging, the samples were immediately prepared for electron microscopy to maintain their native state. PBS was aspirated from the dishes, and the cells were stained with reduced osmium. A 0.1M sodium cacodylate buffer was made using 0.1598g sodium cacodylate (Sigma Aldrich; C0250) in 10 ml sterile water. 0.3g of Potassium Ferrocyanide (Sigma Aldrich; 702587) was added to the cacodylate buffer, and the Potassium Ferrocyanide Buffer was filtered with a 0.2µm filter (Merck; SLGSR33SS). 4% Osmium Tetroxide (Agar Scientific; AGR1024) was filtered through a 0.2µm filter and added to the Potassium Ferrocyanide in equal parts to make a total of 20ml. The final solution was filtered again through a 0.2µm filter before 3ml of solution was added to each gridded dish and incubated for 1 hour at room temperature.

The reduced osmium solution was aspirated, and the dishes were washed with double-distilled H<sub>2</sub>O (ddH<sub>2</sub>O) five times for three minutes. After washing the cells, the mordant was made with 0.1g of tannic acid (Thermo Fisher; A17022.30) in 10 ml of sterile water. 2ml of 1% tannic acid solution, made up in sterile water, was added to each dish and incubated for 20 minutes at room temperature.

The tannic acid was aspirated, and the dishes were washed with ddH<sub>2</sub>O five times for three minutes. 2% Osmium Tetroxide (Agar Scientific; AGR1022) was filtered using a 0.2µm filter and added to the dishes to incubate for 40

minutes at room temperature. The samples were rewashed with ddH<sub>2</sub>O five times for three minutes. The dishes were incubated in 1% uranyl acetate in ddH<sub>2</sub>O (Electron Microscopy Science; 22400) overnight at 4°C (~12 hours).

After overnight incubation, the uranyl acetate was aspirated, and the samples were washed five times for three minutes with ddH<sub>2</sub>O. Waltons Lead Aspartate (WLA) was made up prior to the washes. To make the WLA 0.399g of L-Aspartic acid (ThermoFisher; 043317.36) was dissolved in 100ml of ddH<sub>2</sub>O. The solution was adjusted to pH 3.8 using 1M potassium hydroxide (KOH) solution to enable the aspartic acid to fully dissolve into solution. 0.066g of Lead Nitrate (ThermoFisher; A16345.36) was dissolved into 10 ml of the aspartic acid solution. This was adjusted to pH 5.5 using 1M sodium hydroxide (NaOH) solution. This was added one droplet at a time and mixed using a magnetic flea. A milky precipitate forms when the NaOH is added but disappears immediately. If the precipitate didn't disappear the solution was made again. The WLA solution was incubated at 60°C for thirty minutes and should not have formed precipitate during this incubation period.

Following the aspiration of the tannic acid solution and five three-minute washes with ddH<sub>2</sub>O, the solution was added to the dishes and incubated at 60°C for 30 minutes.

Gradual dehydration of the samples was done using graded ethanol solutions at 30%, 50%, 70% and 90% each for five minutes. Two 100% ethanol washes were done for five minutes each before the ethanol was aspirated,

ensuring the dishes were as empty as possible to avoid interference of the alcohol with the curing of the resin.

Epoxy resin (Agar Scientific; AGR1140) was diluted in ethanol to create three concentrations of hard resin for gradual resin infiltration. A 1:1, 2:1 and 3:1 resin: ethanol solution was made, and the dishes were incubated in each of these solutions for 40 minutes each. The hard epoxy was then added directly to the dishes to incubate for an hour. The final hard resin was added to fill the dishes by 3mm. This was then cured at 60°C for 48 hours to ensure the resin had cured fully and would be suitable for microtomy.

#### *Resin Block Preparation*

Once fully cured, the resin needs to be separated from the dishes for preparation. Pliers are used to remove the plastic edges of the dish from the resin. A razor blade removes the base of the dish and the glass coverslip from the resin. The surface of the resin in contact with the glass coverslip was removed carefully with minimal contact to avoid damaging the embedded cells and the imprinted gridded references.

Using a stereomicroscope, the grid references identified during light microscopy were relocated, and the cells of interest were identified. The region around the cell was marked with a pen for visibility, and then the marked area was cut from the resin using a coping saw while being held stable in a mitre block.

The small block of resin was cut further using a razor blade to trim the block down to contain the cell of interest in the centre of the block.

Sample resin blocks were fixed to EM stubs using a conductive epoxy. The conductive epoxy (CircuitWorks; 2400) was mixed at a 1:1 ratio to create an epoxy resin that could be used to glue the samples to the stubs. A small amount of the conductive epoxy was put onto the stubs to act as glue for the resin blocks. The excess epoxy was spread over all the sides of the resin blocks up to but not covering the top surface and put into the oven at 60°C for 20 minutes to cure the epoxy securing the resin to the stub. Once the resin block was secured to the stub it was placed into the microtome and the resin sample was trimmed down leaving a projection containing the cell.

The ultramicrotome was used to trim down embedded samples in resin using a glass blade. The glass knife strips (Agar Scientific; AGG336) were cut using a glass knifemaker (Electron Microscopy Sciences; GKM-2). The glass strips were placed into the knifemaker up to the preset stop, which is set to cut a square on the end of the glass strip, and secured in place with the clamp. The glass was then scored with the glass knife and by applying pressure from below, a balanced break was completed. The process was repeated diagonally to create two triangular glass blades. Once the blades were produced, they had an arc on the surface that met the corner of the blade indicating it was sharp enough for ultramicrotomy. If there were any chips or the edge wasn't sharp enough the blades were discarded.

The glass blades were positioned against the top surface of the resin block and each of the four edges was manually trimmed to remove the excess resin around the cell of interest. The sample was then finely trimmed using a fresh

blade which was positioned against one of the edges of the resin blocks and set to run at a speed of 100mm/s to a depth of 1000nm. Once the first side was completed, the sample was turned 180°C and the blade was aligned with the cut edge before moving the sample across 300µm and the fine trimming process was repeated. This was then replicated on the remaining two sides of the resin block which produced a projection of resin that was 300µm x 300µm with the cell of interest in the centre of this area.

Following trimming the entire surface of the resin block (excluding the cell surface) was coated with silver paint (Agar Scientific; AGG3692) and air-dried at room temperature for a few minutes. The samples were then coated with a 10nm layer of platinum using a sputter coater (Quorum; Q150V) and were ready for imaging with the electron microscope.

### 2.5.2. SBF-SEM microscope set up

SBF-SEM imaging was conducted with the 3View system (Gatan) integrated with an FEI Quanta 250 FEG SEM (FEI Company). Prior to loading the sample into the SBF the x, y, and z positions were zeroed, and the software was restarted to ensure proper calibration. The pin holder stage was unscrewed and pushed down as far as possible to ensure the pin would be below the blade during set up. The pin holder was removed from the SEM, and the pin was mounted securely. The sample was visualised under a tabletop microscope and the holder rings were adjusted to centre the block face. Once correctly aligned, the holder was secured around the pin and inserted into the SEM, secured in place by a screw to prevent any movement during slicing and imaging.

The tabletop microscope was attached to the side of the EM to facilitate sample alignment. Coarse adjustments were done to position the block as close to the knife as possible. Fine adjustments were made to bring the block face up to the knife without making contact. This was checked by manually moving the knife carefully over the top of the sample, ensuring the sample was central and not at risk of being cut before imaging was started.

Once positioned correctly, the knife was set to perform 100 cuts at 200 nm increments. The sample was monitored closely using the attached microscopy to stop the process immediately once the knife encountered the block face. After the first cut was made, the microscope was removed, and the chamber drawer was closed. The chamber was then pumped to create a vacuum chamber pressure of 70Pa, and the electron high tension (EHT) beam was turned on with an accelerating voltage of 4kV.

The live feed of the block face was used to centre the sample and locate the cell of interest. This was done by increasing the accelerating voltage to 15kV for a single image to increase the electron penetration so that the embedded cells could be visualised. Increasing the voltage increases penetration of electrons for an increased imaging depth, however this can damage the sample over a long period of time, risking charging of the sample (electron build up within the sample that can distort the sample) so is only done for a very short time. The light microscopy images obtained earlier in the pipeline were used to locate the ROI, and the magnification and position adjusted to centre the cell and fill the field of view. 100nm slices were cut with low resolution images taken every slice

to reach the surface of the cell. Once the first slice with the surface of the cell was visible, the contrast, focus and stigmator were adjusted to obtain the clearest possible image. Serial sections were then acquired with 70-80nm slices to take images throughout the cell for high-resolution 3D reconstructions. The imaging was monitored throughout to ensure there were no issues with the SEM or software until the entirety of the cell had been imaged.

When the lossless acquisition was completed, the raw DM4 files were exported and saved, as well as converted TIFF files, these were then ready for analysis.

### 2.5.3. FIB-SEM microscope set-up

FIB-SEM imaging was acquired using a Crossbeam 550 FIB-SEM (Zeiss). The prepared sample was inserted into the sample holder within the SEM chamber before the chamber was pumped to create a vacuum. Once the sample was secured, the EHT was activated.

Before imaging the sample, the alignment of the beams was checked and adjusted as required using an empty sample stub to avoid damaging the cell of interest during adjustments. Both XY and XZ views were utilised to position the stage closer to the detector with a working distance of 5.0mm. The magnification, focus, and contrast were adjusted to acquire an initial image of the block face surface. Once the image was clear, a small feature was selected, and the focus, magnification, wobble, and aperture were fine-tuned to optimise image quality.

The working distance was monitored throughout the process and was maintained at approximately 5.0 mm. Adjustments were made to the z-position

as necessary during image fine-tuning to ensure this distance remained consistent. When the image quality for the chosen feature of the sample was optimised and the working distance was confirmed as 5.0 mm, the stage was tilted incrementally, beginning with 1° movements. The image was readjusted using the *m* control to maintain the correct position. Tilt increments were gradually increased, with ongoing monitoring and adjustments to the working distance as needed. The final tilt angle was 54°. At this point, tilt compensation was activated to ensure the imaged surface was accurate and not distorted. The accelerating voltage was increased to 20kV for visualisation of the block surface and localisation of the ROI similarly to the process described for SBF-SEM.

The FIB was then turned on, allowing the current to reach 2.1  $\mu$ A. A gas injection system (GIS) was prepared for coating the ROI with 10nm platinum. Outgassing of the platinum gas line was performed with the EHT turned off. Once outgassing was completed, the GIS was brought in. Brightness and contrast were adjusted as needed to visualise the ROI. A platinum coating was applied to the area of interest with the probe set to an accelerating voltage of 30 kV, a chamber pressure of 1.5nA and an ion dose factor of 1.000. After coating with platinum, the GIS was parked, and brightness and contrast were adjusted accordingly.

With the GIS removed, the field of view was adjusted to visualise the entire milling area. Rough milling was initially done to remove the bulk of the resin around the sample of interest, using an accelerating voltage of 30 kV, chamber pressure of 7nA and ion dose of 5.00. Such high voltage, pressure and dose could

be used as the sample wasn't being imaged during this time, so it wouldn't be damaged.

After the bulk of the area before the sample had been milled, 'rough' serial section imaging (SSI) was performed with 200nm slice cuts used to locate the edge of the cell. In comparison to SBF the sectioning of the FIB samples was done along the X or Y axis rather than the Z axis, essentially imaging the cell from front to back rather than top to bottom. Once the start of the cell came into view, SSI imaging was set up to image throughout the cell, using the most appropriate voltage, pressure and dose settings for high-quality imaging.

#### 2.5.4. EM Imaging of mouse oocytes

For serial block-face SEM, samples were imaged using the Gatan 3View system (Gatan) integrated with an FEI Quanta 250 FEG SEM (FEI Company). Two nested ROIs were defined: ROI\_1 (full cell overview) was captured at a resolution of 4096 x 4096 pixels with a magnification of 3.6K, while ROI\_2 (chromosome region) was imaged at a higher resolution of 8192 x 8192 pixels and a magnification of 5.4K. Imaging was performed under a chamber pressure of 70Pa and an accelerating voltage of 4kV. Serial sections were acquired at a slice thickness of 80nm to generate high-resolution 3D reconstructions.

#### 2.5.5. Greyscale analysis

To quantitatively assess the effect of tannic acid concentration on chromosomal staining, greyscale values of chromosomes were measured using ImageJ. Images of cells stained with either 0.1% or 1% tannic acid were imported

into ImageJ), where masks were generated to isolate individual chromosomes. Approximately 15 chromosomes were selected across multiple cells for each condition, and the mean greyscale intensity was measured for each chromosome. These greyscale values were then used to assess the relative staining contrast. To determine whether the difference in staining between the two concentrations was statistically significant, a Mann-Whitney test was performed, comparing the distributions of greyscale values obtained from the two conditions.

## 2.6. AMIRA Modelling

### 2.6.1. Analysis of Light Microscopy Data using AMIRA

LM images were initially processed in ImageJ to convert raw image files into TIFF format for subsequent analysis. The processed TIFF images were imported into AMIRA software (Thermo Fisher Scientific) for detailed 3D analysis. Live imaging videos were separated to individual stacks per timepoint and processed in AMIRA as individual cell models. Each image stack was saved as an image sequence, and the image stacks were imported into AMIRA as a single object.

### 2.6.2. Analysis of Electron Microscopy Data Using AMIRA

Raw EM data files in DM4 format were processed to enhance visualisation and prepare them for 3D analysis. The raw DM4 files were binned at a 2 x 2 x 1 (x, y, z) ratio to optimise image resolution while maintaining data integrity. The contrast was uniformly enhanced by 0.35% across all images to improve

greyscale differentiation. The adjusted DM4 files were then exported as TIFFs for analysis in AMIRA (Thermo Fisher Scientific).

### 2.6.3. Generating Surfaces

#### *Chromosome identification*

In AMIRA, imported images were visualised with the Ortho Slice module, which allowed the visualisation of a single slice of the images, which were aligned using the *Align Slice* module to correct for any positional shifts, ensuring accurate 3D reconstruction. This could be done automatically by identifying landmarks, or manually by aligning each successive slice.

Auto-thresholding of the images was applied to differentiate chromosomes from the cytoplasm of the cell based on greyscale variations, as the chromosomes are stained darker and therefore should be recognisable separately from the background. In the Segmentation tab, the highlighted regions (chromosomes) were then added to a material, creating a surface in the software that could be edited if required. As thresholding was an automatic process based on greyscale values and cells are dynamic structures containing many other components that would also be stained, it was essential to do refinement of these 'chromosome' surfaces. The surfaces were manually refined, using various other tools such as the lasso and brush to remove any excess selections and create accurate chromosome models.

In the Project tab, *Generate Surfaces* was then applied to the newly created 'object' with the labelled surfaces. Smoothing was applied at this stage but only for clearer visualisation of the chromosome structures and the

geometric data from the models was not affected by this. The *256.labels* colourmap was used on the segmented chromosome models to label each material with different colours for easy cross-referencing.

### *Chromosome segmentation*

The whole chromosome complement was further processed using *the separate objects* module, using a marker extent of 1-4. The marker extent controls the marking of objects to be separated, and a higher number reduces separation, which in some cases was required e.g. prophase chromosomes required a higher marker extent to avoid excessive separation because of less compacted structured, whereas anaphase chromosomes required a lower marker extent to separate the chromosomes that were close neighbours. A new object was created from this separation and then the *labelling* module could be applied with 3D interpretation settings, including 26-neighbourhood voxel connectivity and a 4-marker extension. This tagged each individual 'object' as a new material. Following these automated processes, manual refinement was used to ensure the chromosomes were appropriately separated and labelled. Materials were selected and fused if the chromosome had been excessively separated, or the brush tool was used to manually separate chromosomes that hadn't been segmented by the *Separate Objects* module. This was done until all obvious chromosome structures were labelled, and a set of individual chromosomes was generated.

### *Extracting quantitative data*

The whole complement of chromosomes and each individual chromosome material was analysed with the *Label Analysis* module. The preset label analysis included Volume and Surface Area. This provided basic data on each of the chromosomes and complements. Width, Length, Thickness and Sphericity were also manually added using the appropriate equations to extract more geometric data from the models.

### *Displacement*

Bounding boxes were applied to both the entire chromosome complement and individual chromosomes to define the area of coverage and determine centroids. This method enabled the quantification of chromosomal movement between time points and calculations of total displacement and spatial dispersal of chromosomes. Additionally, the directionality of chromosome displacement and subsequent polar body extrusion were analysed using centroid data and trajectory assessments.

## 2.7. Statistical Analysis

Throughout the project the data was subjected to statistical analysis, often the mean (average) was sufficient. To measure statistical significance t-tests and Mann-Whitney tests were applied where appropriate using GraphPad Prism software. A statistical significance value was set at  $P \leq 0.05$ . Statistical tests used are referred to in text or figure legends throughout this thesis.

### 3. Establishing 3D-CLEM for chromosomal investigation

## of somatic cells and generating the first “mitotic chromosome atlas”

#### 3.1. Introduction

Investigating chromosomal ultrastructure is challenging due to the technical obstacles, which have historically limited progress in this area of research. E.g. the use of unimodal imaging has highlighted the capabilities of various approaches, whilst also demonstrating their limitations. Combining methodologies via correlative techniques enables the mitigation of some of these limitations. Chromosomes are complex, dynamic structures whose architecture is intricately linked to their function, yet the finer details of their organisation, particularly the role of the chromosome periphery, remain poorly understood. This gap in knowledge is largely due to the limitations of conventional imaging techniques, which have been unable to achieve the spatial resolution required to capture chromosomal structures in their native, three-dimensional context.

To overcome these limitations, a 3D-CLEM pipeline was established, using an existing approach previously established in our lab (Booth et al., 2016). 3D-CLEM is a technique that has been developing since the first attempts to combine light and electron microscopy in the late 1970s, early 1980s (Bucana et

al., 1976; Wouters & Koerten, 1982). This was used to investigate the geometry of all chromosomes, at nanometre precision, during all stages of mitotic division.

LM, using a DNA marker, guided us to cells at desired stages of mitosis, and specifically to the chromosomes within those cells. Light microscopy enables specific imaging of chromosomes. Advances in confocal technology, such as super-resolution microscopy, have improved the resolution from ~200 nm to ~120 nm. While this offers enhanced specificity, it lacks the nanometre precision of electron microscopy required to investigate chromosomal geometry. Conversely, electron microscopy provides ultrastructural detail but is limited to fixed cells and labour-intensive tagging processes. Combining these methods through 3D-CLEM bridges this gap, providing novel insights into chromosome structure. The added advantage of 3D reconstruction enables researchers to examine chromosomes in a volumetric context, revealing spatial relationships that are otherwise obscured in two-dimensional projections.

To achieve high-resolution 3D reconstructions of chromosomal structures, it was first necessary to adapt and compare the two most commonly used volume EM techniques; FIB-SEM and SBF-SEM, which incorporated into the 3D-CLEM pipeline to determine the most appropriate approach for chromosomal investigation. The vEM field is largely divided in which approach is best suited for cell biology, Remarkably, however, a direct comparison between the two modes of imaging remains elusive.

FIB-SEM uses a focused ion beam to 'burn' layers of the sample away for imaging, whereas SBF-SEM uses a diamond knife to cut samples for imaging.

Both processes are destructive; however, a 3D reconstruction of the ROI post-imaging will be available by incorporating sequential imaging throughout the sample.

This chapter explores the establishment and optimisation of a 3D-CLEM workflow, specifically tailored for investigating chromosomal structure, but over a collection of cell division stages. The development of this technique was driven by the need to achieve high-resolution insights into the chromosomal organisation, but also, for later chapters, to investigate the role of the chromosome periphery, already known to have a critical role during mitosis, specifically in meiosis. By applying 3D-CLEM to chromosomal study, this work aims to overcome previous limitations to provide a deeper understanding of the architecture underlying chromosomal organisation and regulation and its implications for aneuploidy research. Therefore, this work is important from both a fundamental biology and a translational research perspective.

## 3.2. Hypothesis and Aims

### Hypothesis

Establishing and optimising a 3D-CLEM workflow will enable 3D visualisation of chromosomal ultrastructure. This method will be reproducible and adaptable, providing a reliable framework for investigating chromosome organisation and dynamics in various cell types, including mitotic and meiotic cells.

## Aims

- Establish 3D-CLEM as a robust method for chromosomal investigation:  
Develop a comprehensive workflow that integrates high-resolution fluorescence imaging with electron microscopy to enable detailed visualisation of chromosomal ultrastructure in 3D. Including assessing between FIB-SEM and SBF-SEM.
- Optimise the method for chromosomal ultrastructure investigation:  
Systematically refine the sample preparation, imaging, and correlative alignment protocols to maximise resolution and minimise sample distortion.
- Establish a reproducible framework for future chromosomal ultrastructure studies. Providing a robust methodology that can be adapted for investigating chromosomal dynamics in different cell types and contexts, including meiosis.
- Validate the technique using mitotic cells as a proof of concept: Apply the optimised 3D-CLEM approach to mitotic cells, demonstrating its efficacy and generating new insights into chromosomal organisation and geometry. This proof-of-concept study validates the technique before applying it to more challenging and precious samples, such as oocytes.

### 3.3. Results

#### 3.3.1. Optimisation of the pipeline

Establishing 3D-CLEM required specific focus on various aspects of the pre-existing technique for it to be established. This included; (1) comparing the optimal imaging methodologies available and the cost appropriateness of these techniques for the 3D-CLEM pipeline (2) improving contrast of chromosome components compared to the surrounding cell for improved identification (3) optimising the FIB-SEM imaging parameters, including imaging resolutions and dwell times to achieve the best imaging for serial sectioning imaging (SSI) on an unfamiliar system, (4) comparing the optimised FIB-SEM imaging and previously established SBF-SEM imaging to determine which technique would be the most appropriate for volume imaging of chromosomes within mitotic and eventually meiotic cells, (5) AMIRA segmentation optimisation to determine the best tools and process for creating the 3D chromosome models. Through optimisation of these stages, a clearly defined and reproducible 3D-CLEM workflow for chromosome analysis was established at UoN that could be applied to both mitotic and meiotic cells.

#### *Seeding densities*

The seeding density of cells is crucial in 3D-CLEM due to the need to identify a single cell of interest and track it throughout the entire process. When applying 3D-CLEM to mitotic cells, the cells need to be sufficiently confluent to support healthy cell division and ensure the presence of mitotic cells in the natural population without resorting to cell cycle synchronisation drugs.

For the advanced imaging of cells in mitosis, it is preferable for the cells to naturally progress through the cell cycle and enter mitosis, rather than risk interfering with cell division mechanics using drugs to enrich specific stages. This allows for the imaging of chromosomes at different stages of mitosis in their unaltered state, minimising interference with cell structure or disruption of the cell cycle. For example, using Nocodazole to synchronise cells could increase the proportion of RPE cells arrested at the prometaphase or metaphase stage; however, this drug functions by impairing the assembly and disassembly of microtubules, preventing cells from progressing to anaphase and telophase. Extended periods of arrest in nocodazole are known to impact chromosome structure, relating to chromosome fatigue. Therefore, prolonging the metaphase stage could lead to abnormal chromosomal structures that would not accurately represent the typical state of chromosomes during mitosis. Additionally, since the 3D-CLEM protocol requires capturing cells at all stages of mitosis, Nocodazole synchronisation would only be beneficial for increasing the abundance of prometaphase and metaphase cells, which does not align with the aim of imaging the entire range of mitotic stages.

Therefore, it was essential to achieve a high level of confluency to support successful cell division. If the confluency is too low for RPE cells, they struggle to thrive, resulting in reduced cell division rates and signs of cellular stress. However, for 3D-CLEM, the cells must not be overly confluent, as this would obscure the visibility of the grid references engraved onto the cell culture dishes, which are necessary for correlating light and electron microscopy images. Therefore, four different seeding densities were tested to balance the cells' need

for high confluency with the requirement for space to visualise the grid references.

Seeding 50,000 or 100,000 cells into 13mm MatTek dishes resulted in insufficient confluency, causing the cells to struggle to divide successfully. In contrast, seeding 150,000 or 200,000 cells supported the cells' requirement for higher confluency. However, at a density of 200,000 cells, the cultures began to form a more solid monolayer, which reduced the visibility of the engraved grid references (Figure 3.1.). Thus, the optimal seeding density was identified as 150,000 cells, providing a balance between supporting cell division and maintaining visibility for 3D-CLEM imaging.

Different fixative agents were also tested to compare the adherence of cells to the coverslips under different conditions. RPE cells are adherent, but the 3D-CLEM process requires lots of stages that could disturb the cells from the surface of the coverslip, particularly mitotic cells that are rounded and have a smaller surface area attached to the surface. The fibronectin-coated coverslips adhered more cells to the surface after staining with DAPI and washing. However, sufficient cells were retained on the surface of the uncoated coverslips, which indicated that a fixative was not required for the processing of RPE cells. This also removed another variable that, although unlikely, could potentially interfere with the later stages of the 3D-CLEM pipeline.

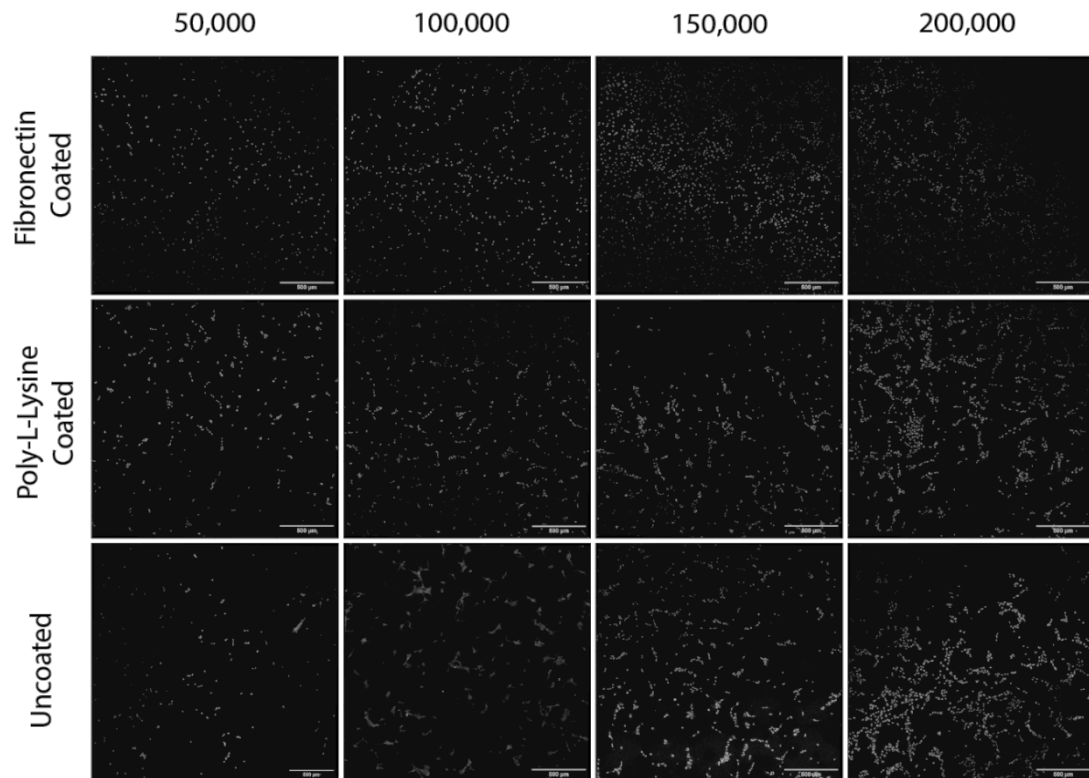


**Figure 3.1. Optimisation of seeding density and substrate coating for Correlative Light and Electron Microscopy (3D-CLEM).** Different surface coatings and seeding densities were tested to optimise cell adhesion and fixation for 3D-CLEM. Fibronectin and Poly-L-Lysine coatings were compared to uncoated surfaces, with no significant differences in cell retention following immunofluorescence processing. Seeding densities ranging from 50,000 to 200,000 cells per dish were evaluated. A density of 50,000 cells resulted in insufficient mitotic cells, while 200,000 cells led to excessive confluence, obscuring the grid references required for sample identification. A density of 150,000 cells provided an optimal balance. Cells were stained with DAPI and imaging was performed using a Leica SPE confocal microscope with a 20× objective. Scale = 500 µm.

#### 3.3.1.1. Leica SPE vs Zeiss AiryScan

The purpose of developing this pipeline was to develop a technique that could explore chromosome ultrastructure in 3D at a high resolution to obtain as much geometric data as possible. This was not limited to the EM and therefore two confocal methods were compared in order to achieve the best quality imaging possible at every stage of the process. To do this, chromosomes at all stages of mitosis (prophase, prometaphase, metaphase, anaphase, and

telophase) were imaged using both systems with their highest available objectives and best N.A. The Leica confocal microscope, equipped with a 63x oil objective, was compared to the Zeiss LSM900 with AiryScan using a 100x oil objective, representing the maximum resolution for each respective system.

As shown in Figure 3.2, the AiryScan system provided significantly enhanced resolution compared to the conventional confocal microscope, allowing for clearer visualisation of chromosomal structures without requiring additional imaging time or adjustments to the existing sample preparation process. Despite using the highest magnification available on each system, the AiryScan images revealed considerably more detail, including the ability to distinguish sister chromatids during prometaphase and metaphase; features that were less discernible with the standard confocal system (Figure 3.2, yellow arrows).

The improved clarity and definition provided by the AiryScan system enabled more precise characterisation of chromosome morphology and less ambiguous to confidently select mitotic stages. Importantly, this increase in detail was achieved without extending acquisition times or complicating the imaging workflow, demonstrating that the AiryScan system offers a superior resolution advantage for chromosomal investigations, even when using comparable high-magnification objectives.

In order to distinguish details of interest and improve the correlation between LM and EM datasets, the LM images needed to be as high resolution as possible. Using the super-resolution method gave clearer visualisation of the

chromosomes and cells of interest and aided in the localisation of the EM later in the pipeline. Using the Zeiss AiryScan confocal required the same sample preparation and acquisition time as the standard confocal, so didn't require any extra work to incorporate into the pipeline, making it a seamless incorporation into the imaging pipeline.

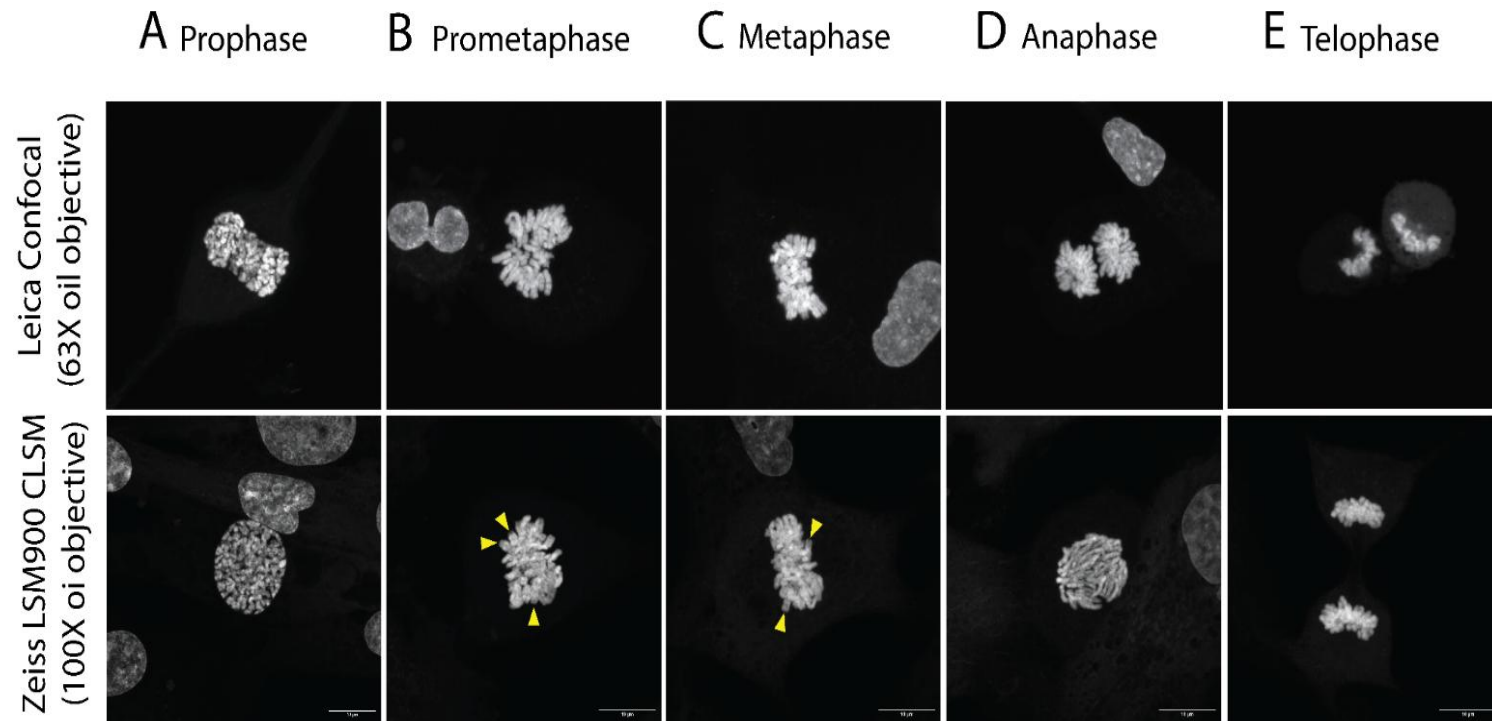


**Figure 3.2. Comparison of confocal and super-resolution microscopy for mitotic imaging.** Confocal imaging using the Leica SPE, and super-resolution confocal imaging using the Zeiss LSM900 AiryScan, were compared to determine the most suitable method for the experimental pipeline. Mitotic cells at various stages were stained with DAPI and imaged with both systems to assess image quality and resolution. Confocal imaging was performed with a 63× oil objective, providing clear images, whereas AiryScan super-resolution imaging was conducted with a 100× oil objective, offering enhanced resolution. AiryScan processing further improved image clarity, allowing for the visualisation of individual chromosomes with greater detail. In some instances, sister chromatids (yellow arrows) were distinguishable in AiryScan images, a level of detail not as visible with the standard confocal microscopy. Scale = 10µm.

### 3.3.1.2. *Optimising contrast*

To improve the quality of staining for electron microscopy the tannic acid concentration was adjusted. Tannic acid acts as a mordant aiding in the staining of cells, creating a stabilising matrix between the osmium and cell membranes (Simionescu & Simionescu, 1976). Adjusting the tannic acid concentration could aid in the binding of osmium to the cell structures enhancing contrast of different cellular components during imaging. The standard protocol recommended a concentration of 0.1% tannic acid (Booth et al., 2016; Figure. 3.3.A), but it was hypothesised that increasing this concentration could enhance chromosomal visualisation by improving binding of the stains. Increasing the tannic acid concentration to 1% resulted in visibly improved staining as seen in Figure. 3.3.B, with chromosomes appearing significantly darker and more distinct.

A quantitative analysis of greyscale values was conducted to confirm this observation. Using ImageJ, masks were created to isolate chromosomes, and greyscale values were measured for approximately 15 chromosomes in each condition. Statistical comparison using a Mann-Whitney test revealed that chromosomes stained with 1% tannic acid had significantly higher greyscale values ( $p \leq 0.0001$ ), indicating darker staining than those treated with 0.1% tannic acid (Figure 3.3.C). Therefore, increasing the tannic acid concentration to 1% improves chromosomal contrast, providing clearer visualisation for further ultrastructural studies, which in turn should improve the segmentation analysis later in the workflow.

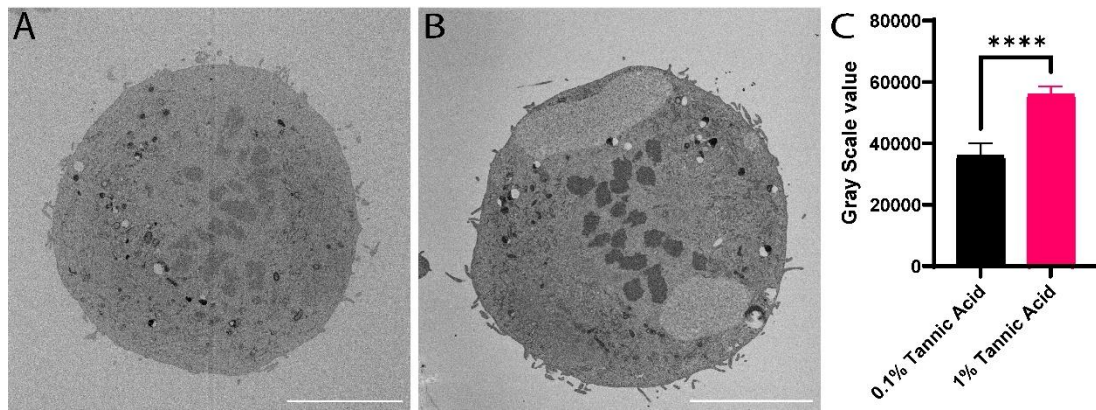


**Figure 3.3. Optimisation of tannic acid concentration for electron microscopy staining.** (A) EM image of a mitotic cell processed using the existing staining pipeline with 0.1% tannic acid. (B) EM image of a mitotic cell stained using an optimised protocol with 1% tannic acid. (C) Quantification of grayscale intensity in chromosomal regions shows significantly darker staining in cells treated with 1% tannic acid compared to 0.1% (\*\*\*\*,  $p \leq 0.0001$ , unpaired t-test). Increased chromosomal contrast enhances the visibility of structural details and improves focusing on regions of interest. Scale =  $10\mu\text{m}$ .

### 3.3.1.3. FIB-SEM preparation parameters

The set up of FIB-SEM was optimised for serial sectioning imaging of an entire cell. The technique had a few extra steps for set up when compared to SBF due to the directionality of the slicing, secondary platinum coating and the tilting of the sample.

An overview of the entire block surface was located and centred for imaging (Figure 3.4.A). Using a higher accelerating voltage (15kV), the monolayer of cells could be visualised (Figure 3.4.B), 15kV provided a deep enough penetration into the resin block to visualise the cell without causing damage to the surface. This visualisation of the cell was then used to locate the cell of interest through correlation with the LM images obtained earlier in the pipeline. With the increased electron penetration, the full cell could be visualised and was measured to correlate with the LM data to confirm the cell of interest (Figure

3.4.C). The embedded grid references in the resin could also be compared to the LM to orient the cell for imaging, this was especially important as the imaging of the cell with the FIB was not in the same orientation as the LM and confirming the direction of the FIB milling made registration easier later on in the process.

As FIB-SEM imaging is performed on a sample tilted to a 54° angle the images are acquired in a different orientation to the SBF-SEM, and as a result the entire cell area that is yet to be imaged is exposed to the electron beam throughout the entirety of the imaging. The beam is focused on the surface for imaging, but there is secondary exposure during the serial sectioning which could lead to charging of the sample, potentially leading to imaging artefacts. To combat this, an extra layer of platinum was coated over the cell surface to provide protection and prevent damage to the cell or resin that could have altered the structure and quality of the sample (Figure 3.4.D). The FIB mills down into the surface of the block, meaning that slices are removed laterally through the resin block. To visualise this surface, an area of resin in front of the sample was removed at an angle to clear a pathway for the electron beam to reach the cell surface and reflect electrons back to the detector to produce an image (Figure 3.4.E). The clearance of the region was adjusted to produce an optimal image without interference from remaining resin. The width of the clearance area was limited to the width of the cell region, but the length was adjusted to be double that of the cell region, which ensured no resin was left in the path of the electron beam that could potentially block the sample surface. If the length of this region was not long enough, the edge of the resin surface could be visible in the field of view, which could interfere with the early imaging of the cell. During this stage, it

was evident that the milling of the resin was not consistent, most likely due to the nature of the resin curing being variable throughout the surface. This resulted in portions of the resin remaining during the milling as the FIB dose was not sufficient for removal of the denser regions of resin (Figure 3.4.E). To combat this, a rough milling at a high dose and kV was done initially to clear the area quickly and effectively. Following this, a smaller region was milled at a lower dose and kV to produce a smoother surface, which aided in the focus and stigmation adjustment to produce the clearest image for the serial sectioning imaging (SSI).

Once the fine milling of the clearance area was completed, a surface at the edge of the cell was revealed and this was used to adjust the magnification, contrast, brightness, focus and stigmation to produce the clearest image of the cell (Figure 3.4.F). Adjusting these imaging parameters at this point was essential as these needed to remain consistent throughout the SSI for successful reconstruction of the 2D slices post imaging. The earlier optimisation of orientation and resin clearance ensured that the settings used at the beginning of imaging would be sufficient throughout the SSI for whole-cell imaging and reconstruction.

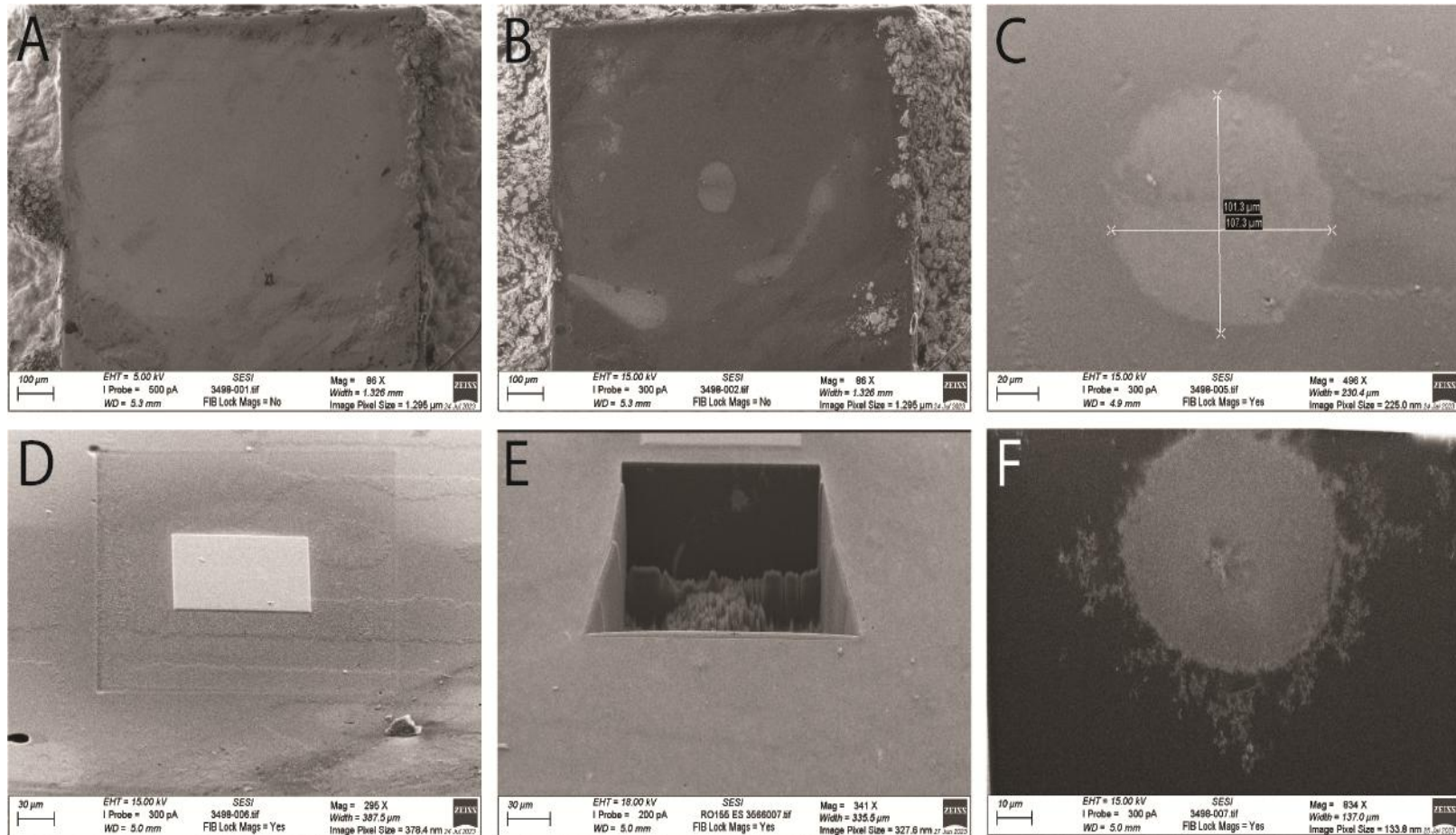


**Figure 3.4. FIB-SEM imaging setup pipeline using the Zeiss Crossbeam 550.** (A) Overview of the entire block face after optimising the working distance, focus, and brightness/contrast for the specific sample. (B) The electron high tension (EHT) was increased to 15 kV to enhance penetration depth and improve visualisation of the cell of interest. (C) Measurements of the cell were compared with light microscopy (LM) data to confirm cell identity and orientation using grid references. (D) A 10 nm platinum coating was applied over the cell region using the gas injection system (GIS) to protect the sample during imaging. (E) The region

*in front of the cell was sputtered away using the focused ion beam (FIB) to expose the imaging surface. Peaks of residual resin in this area indicate variability in FIB milling. (F) Final view of the exposed cell after tilting the stage and applying tilt compensation. Fine adjustments were made before initiating serial section imaging (SSI). Imaging was performed using the Zeiss Crossbeam 550 FIB-SEM. Scale = 100–10 $\mu$ m.*

#### 3.3.1.4. *FIB-SEM imaging optimisation*

The imaging of the sample was optimised to determine which parameters would be the most suited for SSI of a full cell for 3D reconstruction. The FIB-SEM can potentially produce high resolution images, which can exceed the SBF-SEM capabilities due to the ability to achieve smaller slice sizes (down to 5nm slice size limit compared to SBF-SEM 15nm limit). However, achieving this z-resolution on such a large sample would be incredibly time-consuming and limit the sample diversity significantly. This high-resolution setting on the FIB would extend the acquisition time to become prohibitively long and expensive – indeed, such imaging is best suited to small regions of imaging, e.g. imaging a single organelle. This was in addition to the already increased SSI timing for the FIB which took longer to mill each slice than the SBF diamond knife and increased dependent on the size of the surface to be removed. The axial resolution of the image acquisition was also significantly longer for the FIB-SEM when compared to the SBF-SEM and to determine the best resolution achievable within a ‘reasonable’ time-frame, various conditions were applied to a single slice of a sample.

Three different pixel resolutions were compared to determine which could provide the best quality image whilst keeping the overall imaging time within a reasonable range. The first attempts used a shorter dwell time of 200ns and a line average of 11 (Figure. 3.5.A). This was used to attempt quicker imaging of the cell and determine whether the quality would be sufficient for chromosomal imaging. No matter the resolution used for these parameters the image produced was highly granular which would limit the modelling of the sample at later stages, potentially resulting in the loss of geometric data as a result. Therefore, it was

determined that the dwell time and averaging should be increased to attempt to produce a clearer image.

The dwell time is the amount of time the electron beam is focused on a specific spot during scanning and increasing this parameter was determined to be the best way to improve image quality. Various scan speeds were tested with live detection until a clearer image was produced while keeping the overall imaging time at a reasonable duration. In the next set of imaging the dwell time was increased to 1600ns (Figure. 3.5.B). These images were much less granular and the organelles within the sample were much clearer, with cristae of the mitochondria even being easily identifiable. This was determined to be a sufficient resolution for chromosomal imaging. However, at these settings the pixel resolution of 3072x2304 took >5min to image a single slice which when imaging an entire cell with >300 slices would take an extremely long time, without even factoring in the time taken to mill each of the slices using the FIB on top of that.

In an attempt to increase the resolution while keeping overall imaging time down, the dwell time was reduced back to 200ns, and the line averaging was increased to produce a faster image while maintaining image quality (Figure. 3.5.C). This was found to improve the quality of imaging from the first group however the images still had a granular appearance and the increased scanning per line darkened the image, indicating possible charging of the sample which could lead to damage over time. Therefore, it was determined that imaging at 2048x1536 pixel resolution with a dwell time of 1600ns and a line average of 11

was found to be the optimal imaging parameters. This produced a clear image of the cell structures whilst keeping the imaging time low per slice and was used in future SSI set ups for chromosomal imaging.

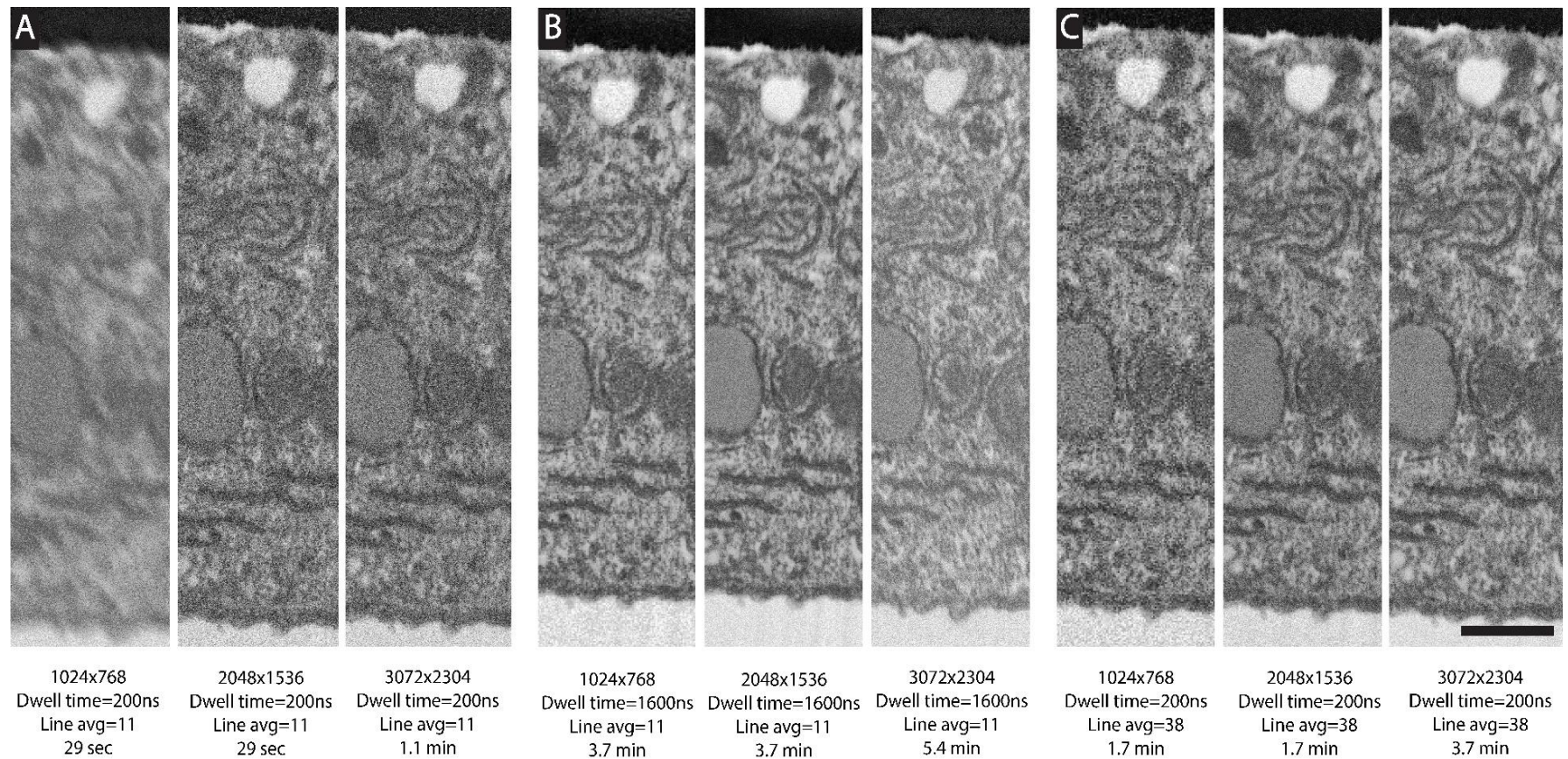


**Figure 3.5. Optimisation of FIB-SEM imaging parameters.** (A) Pixel resolutions of 1024×768, 2048×1536, and 3072×2304 were tested with a dwell time of 200 ns and a line average of 11. Images were acquired rapidly but showed significant granularity, reducing organelle visibility. (B) Increasing the dwell time to 1600 ns while maintaining a line average of 11 improved image clarity but increased acquisition time, with 3072×2304 resolution requiring 5.4 minutes per

*slice. (C) A dwell time of 200 ns with a higher line average of 38 was tested to reduce acquisition time while maintaining image quality. However, images appeared more pixelated compared to (B), indicating that a longer dwell time with a lower line average provided better results. Imaging at 2048×1536 resolution was optimal for balancing resolution and acquisition time. Imaging performed using the Zeiss Crossbeam 550 FIB-SEM. Scale = 1µm.*

### 3.3.1.5. *Half and Half comparison of FIB and SBF*

The two most commonly used modes of volume EM (SBF-SEM and FIB-SEM) proved capable of imaging dividing cells in sufficient detail to make 3D reconstructions, however, both methods had their own unique drawbacks. To optimise this pipeline even further, two types of SEM were compared to determine which would be the best for chromosomal imaging and 3D reconstruction of mitotic cells and for future proofing, which might be better for studying oocytes in later chapters. To truly test each method and compare them directly, the only way to achieve this is imaging the same cell – on half with SBF-SEM and the other half of the same cell with FIB-SEM. To the best of our knowledge, confirmed by Zeiss, this type of absolute-direct analysis had never been performed (Figure 3.6.).

To do this effectively, the SBF-SEM was the most logical method to do first, as it would slice through the sample, leaving a smooth surface similar to that of the block face, making preparation for the FIB-SEM virtually unaffected compared to normal. In comparison, if FIB-SEM had been imaged first, because of its lateral imaging style it would have left a hole in the same which would have been potentially problematic when preparing the sample again, e.g. sputter coating filling the hole and affecting the imaging parameters; also the cell would be on the edge of the block surface which when sliced with the SBF could have resulted in warping of the sample due to the lack of support from surrounding resin.

The single cell was prepared following the optimised 3D-CLEM pipeline and the cell was first imaged with the SBF. 90 slices of 70nm thickness were imaged axially with the SBF before the imaging was stopped and the sample was removed and sputter coated again to then be imaged with the FIB. The sample was then imaged laterally with the FIB which required 305 slices of 70nm thickness (Figure 3.7.). Each of these image stacks were then modelled with the AMIRA software using a combination of thresholding and the brush tool, and the two models were combined to create a whole model. During transportation between the SBF-SEM (University of Liverpool) and the FIB-SEM (University of Nottingham) some damage occurred during the platinum coating from the GIS, however this was minimal with only a few nm of the sample affected.

This gave insight into the best technique for chromosomal imaging. The SBF technique was a simpler technique that produced more consistent slice and therefore cleaner images. The imaging of the same orientation also made the imaging process smoother as correlation between the LM images and the EM sample could be easily done during the imaging process, whereas with the FIB imaging, the correlation couldn't be done until post imaging where the images could be resliced, and registration could be done. The FIB had capabilities to produce a higher quality image, however, when imaging such a large area, this was compromised to keep the imaging time reasonable. Thus, overall, a qualitative assessment of both approaches indicated no tangible benefit for either approach, however, the relative ease and application of SBF-SEM make this the more desirable option.

These features all indicated that SBF-SEM would be the best method for volume EM, especially when applied to larger samples, e.g. oocytes are five-fold bigger than these cells. Also, the oocytes are a much more precious sample type so the inconsistency that was seen in the slices with the FIB would not be an acceptable risk for these samples. However, if imaging of specific components was required, e.g. imaging of the kinetochores, the FIB-SEM would have been the better choice due to the increased resolution options.

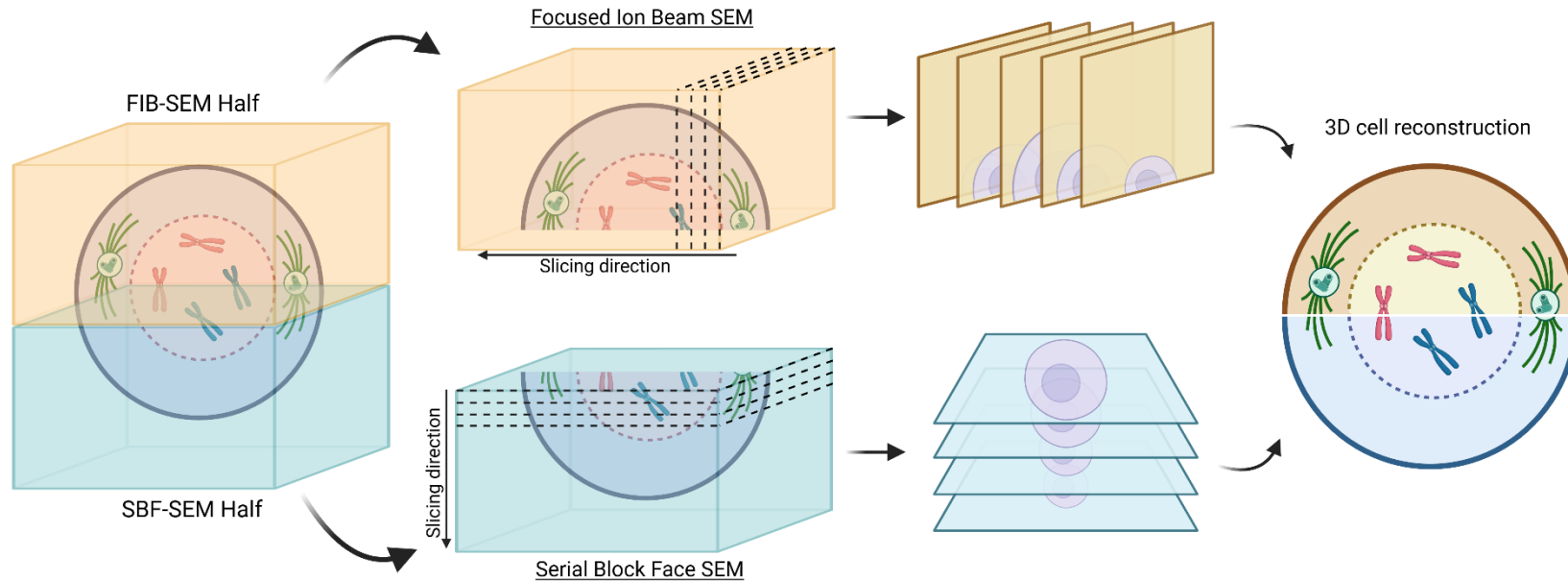


**Figure 3.6. Comparison of FIB-SEM and SBF-SEM for whole cell imaging.** A single cell was imaged using both Serial Block-Face SEM (SBF-SEM) and Focused Ion Beam SEM (FIB-SEM). SBF-SEM was used to acquire images from the top half of the cell, stopping approximately at the midpoint. The remaining half was imaged using FIB-SEM. The two datasets were combined to generate a complete 3D cell model, enabling geometric analysis and direct comparison of the two EM techniques. (Figure created using BioRender.)

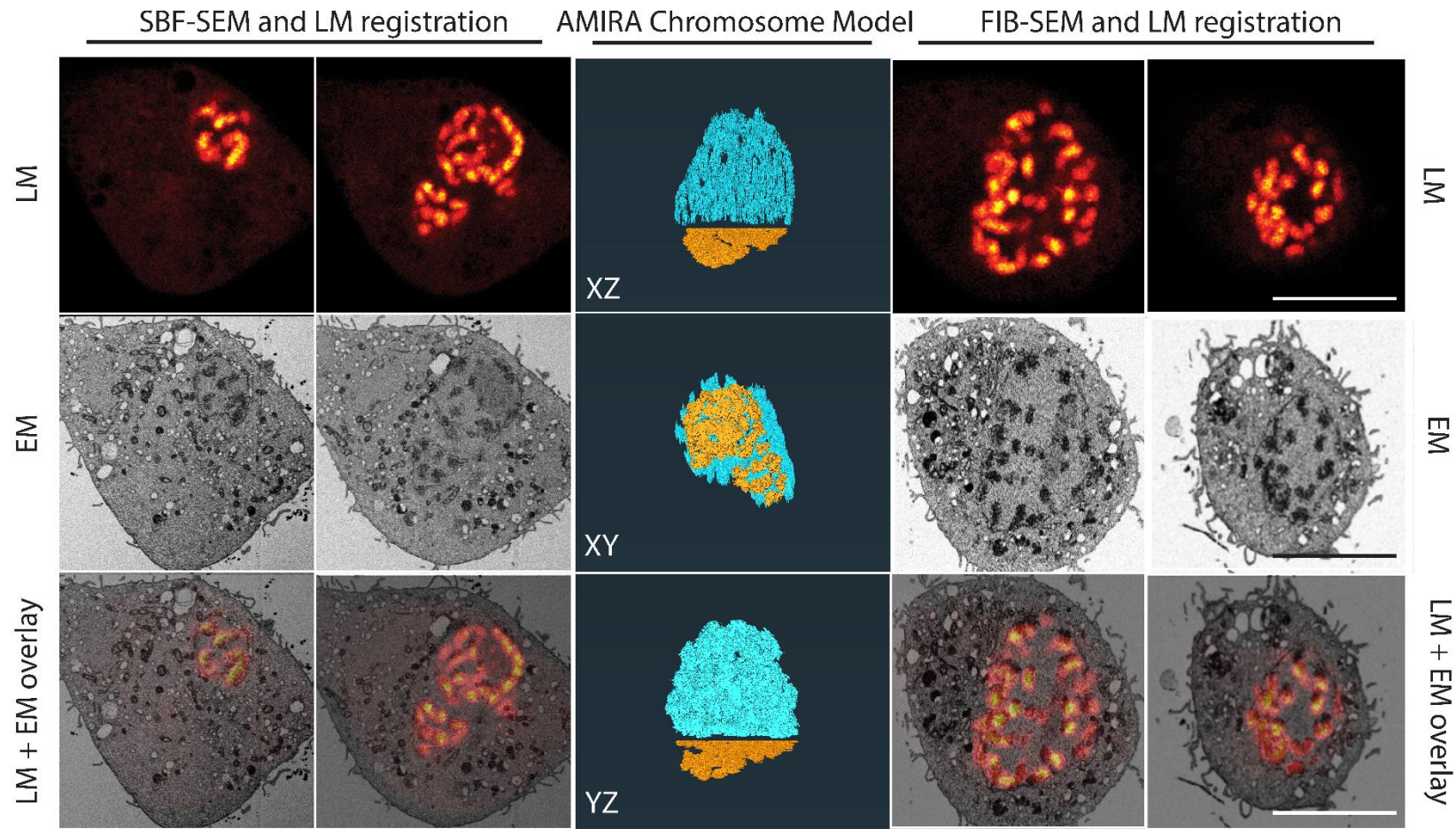


**Figure 3.7. Correlative LM and EM chromosome reconstruction using SBF-SEM and FIB-SEM.** Light microscopy (LM) and corresponding electron microscopy (EM) slices of a single prophase cell demonstrate continuity throughout the 3D-CLEM workflow. LM-EM overlays confirm that the same cell was imaged in both modalities. FIB-SEM images were adjusted using the Volume Viewer plugin (ImageJ) to facilitate LM registration. AMIRA models show individual chromosome reconstructions from SBF-SEM (orange) and FIB-SEM (blue), which were aligned to generate a complete chromosome complement for the cell. Imaging performed using Zeiss LSM 900 100x objective, Zeiss Crossbeam 550 FIB-SEM and FEI 250 Quanta FEG-SEM.

#### 3.3.1.6. *Modelling techniques for 3-dimensional models*

Following imaging, 3D modelling was done to produce quantitative data from the various tools available in the AMIRA software for segmentation of surfaces. These tools range from mostly automated to entirely manual, allowing for increased control over selection of the chosen material.

A single stack of LM images for a prometaphase cell was imaged with each of these methods to determine which technique would be best suited for the modelling of chromosomes (Figure 3.8.). This included the blow tool, thresholding tool, lasso tool and the brush tool. Each of the techniques was compared for the time it took to image, the accuracy of the method and the potential bias that could be introduced (Table 1).

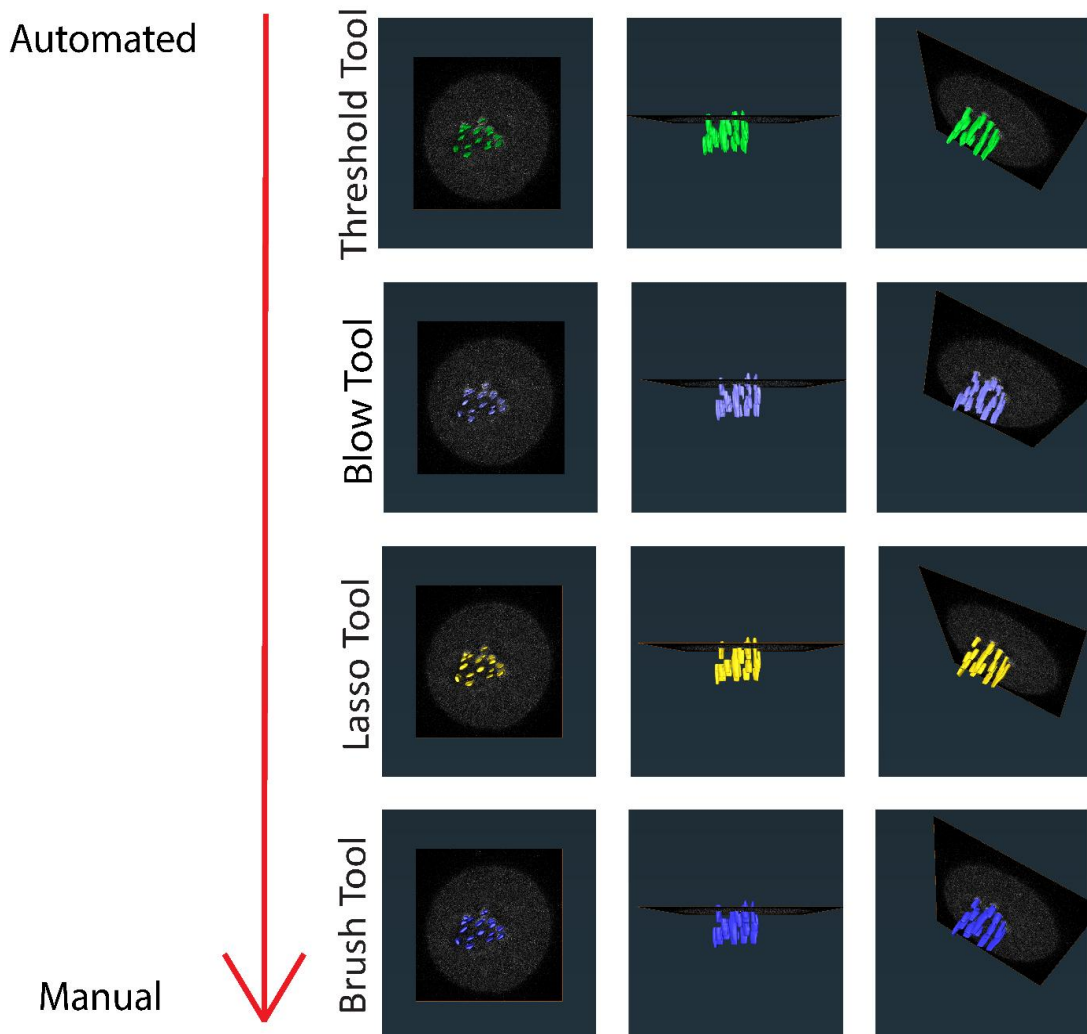


**Figure 3.8. Comparison of segmentation tools in AMIRA.** Different AMIRA segmentation tools were applied to the same cell model. The Threshold Tool (green) is fully automated, selecting pixels based on grayscale intensity within a defined range. The Blow Tool (purple) uses pixel saturation to identify and segment regions of similar intensity. The Lasso Tool (yellow) is a manual method requiring the user to outline the region of interest, which is then filled. The Brush Tool (blue) is also manual but allows for more precise selection by painting directly onto the material, offering greater flexibility. Segmentation ranges from fully automated to fully manual approaches.

The thresholding tool was the most automated of the tools, using auto-thresholding the pixels of a specific range were selected using the masking range slider. As this range was adjusted, the selected pixels were highlighted in blue which enabled precise selection of the chromosomes. These chromosomes were visualised with a 3D projection and the slices could be monitored to adjust

the selection to fit the chromosomes as closely as possible. This technique took only about two minutes to model the chromosomes and was almost completely unbiased as the majority of material selection was done through the greyscale selection (Figure 3.8.). However, it was less accurate than some of the other more manual selection methods, this could be improved by post-selection refinement with some of the other tools. This technique could be applied to the entire cell and thresholding the entire chromosome complements at once, however, to improve accuracy applying the thresholding to individual slices was employed (Table 1).

The blow tool acts with the same principle by selecting material based on the greyscale of the pixels. However rather than applying this selection to the entire slice, a region of the material was manually selected and the area was expanded by dragging the selection across the area of interest. The contour of the selected area selected nearby pixels with homogenous grey values and stops when the grey values change. The tolerance values of this tool were adjusted to increase edge sensitivity, with a Gaussian filter of 8 and a threshold limit of 1. This produced the strictest selection of the material producing the most accurate selection (Figure 3.8.). Despite this, the technique was limited in accuracy due to the nature of the chromosomes, which often have varying grey scales throughout the structure, and with the individual selections, it was laborious and took a long time to select the material to produce essentially the same result as the threshold tool (Table 1). As it was a more manual tool, it also introduced more bias to the models, making it a less successful technique for the modelling of chromosomes.

The lasso tool was also used to model the chromosomes. The chromosome region was drawn around with the lasso tool, and when the contour was closed, the area was filled automatically (Figure 3.8.). This required each individual chromosome on each slice to manually be drawn around, which took a prolonged time (15 minutes per cell; Table 1). This was quicker than the blow tool and the brush tool; however, the accuracy of this tool was somewhat limited by the auto-filling, which assumed the selected area was completely uniform. In comparison the blow tool and the thresholding tool compensated for this by basing the selections on the grey values. This is especially important for Prophase cells as the chromosomes are not yet completely condensed so there were often gaps in the chromosome which were not accounted for using the lasso tool.

The brush tool was the most manual of the tools used, this used a paintbrush method to highlight the region of interest for selection (Figure 3.8.). This technique gave the most flexibility; however, it was also the most time-consuming of the methods (25 minutes per cell; Table 3). Despite this being the most accurate of the techniques due to the detailed selection of the material, it was also the most biased as it was entirely dependent on user selection.

Based on the assessment of each technique, it was determined that the best option was to combine multiple techniques to reduce the time taken, preventing a bottleneck, in an already low throughput method, whilst also maintaining accuracy. Therefore, the thresholding technique was used first to select the materials based on the grey values producing a quick and unbiased

model. Following this, the brush tool was used to refine this model, removing excess selections and improving edge specificity, which gave the model more accuracy.

**Table 3.1. Comparison of AMIRA segmentation tools.** *The time required to segment a single light microscopy (LM) image of a cell was recorded for each AMIRA tool, with the Brush Tool taking the longest (25 min) and the Threshold Tool the shortest (2 min). These values were extrapolated to estimate the time required to model a timelapse video consisting of 70 timepoints. The volume of each segmented model was measured, assuming the Brush Tool provides the most accurate representation. Accuracy was assessed by comparing each method to the Brush Tool, with the Blow Tool being the least accurate. Method bias was also evaluated, with manual techniques introducing higher potential bias, while the Threshold Tool, being fully automated, had minimal bias.*

| TECHNIQUE                            | TIME TO MODEL ONE CELL | TIME TO MODEL ONE CELL WITH 70 TIME POINTS | VOLUME $\mu^3$ | ACCURACY | BIAS |
|--------------------------------------|------------------------|--|----------------|----------|------|
| <b>THRESHOLD TOOL</b>                | 2 minutes              | 140 minutes                                | 768.872        | +++      | X    |
| <b>BLOW TOOL</b>                     | 18 minutes             | 1260 minutes                               | 628.677        | +        | XX   |
| <b>LASSO TOOL</b>                    | 15 minutes             | 1050 minutes                               | 962.565        | ++       | XXXX |
| <b>BRUSH TOOL</b>                    | 25 minutes             | 1750 minutes                               | 831.729        | ++++     | XXXX |
| <b>THRESHOLD-ING THEN BRUSH TOOL</b> | 8 minutes              | 560 minutes                                | 743.633        | ++++     | XX   |

### 3.3.1.7. *Smoothing optimisation*

To ease the segmentation of chromosomes, one of the adjustments that could be applied was smoothing. This is a technique that uses a Gaussian filter to average the voxel intensities of the model, reducing harsh variations and smoothing transitions between surfaces. As the purpose of applying 3D-CLEM to the samples was to gain geometric data on chromosomes, the smoothing adjustments effects on the models was measured to quantify data lost. Figure 3.9.A shows the models for each of the smoothing levels with a visible change in the texture of the chromosomes. From these images applying a smoothing level 8 did make the chromosome structures more defined and made the segmentation of chromosome easier with fewer projections interacting.

However, applying this smoothing adjustment caused a loss of data like that of binning. Figure 3.9.B indicates that the smoothing adjustment has minimal effects on the volume of the chromosome complements, with the most intense smoothing parameter only losing 2.55% of its volume. However, Figure 3.9.C indicates that the surface area was much more drastically affected by the smoothing adjustment. With even the mildest of the smoothing adjustments causing the chromosome complement to lose 28.7% of its measured surface area. To gain the improved segmentation of smoothing, one of the highest settings would need to be used, which would result in losing >50% of the surface area, which was not acceptable for the geometric analysis. As a result, it was determined that no smoothing would be applied to the models post-segmentation, in the same way no binning was done to the binning pre-

segmentation. The ease of segmentation through smoothing was not enough of a benefit to accept the loss of data in this manner.

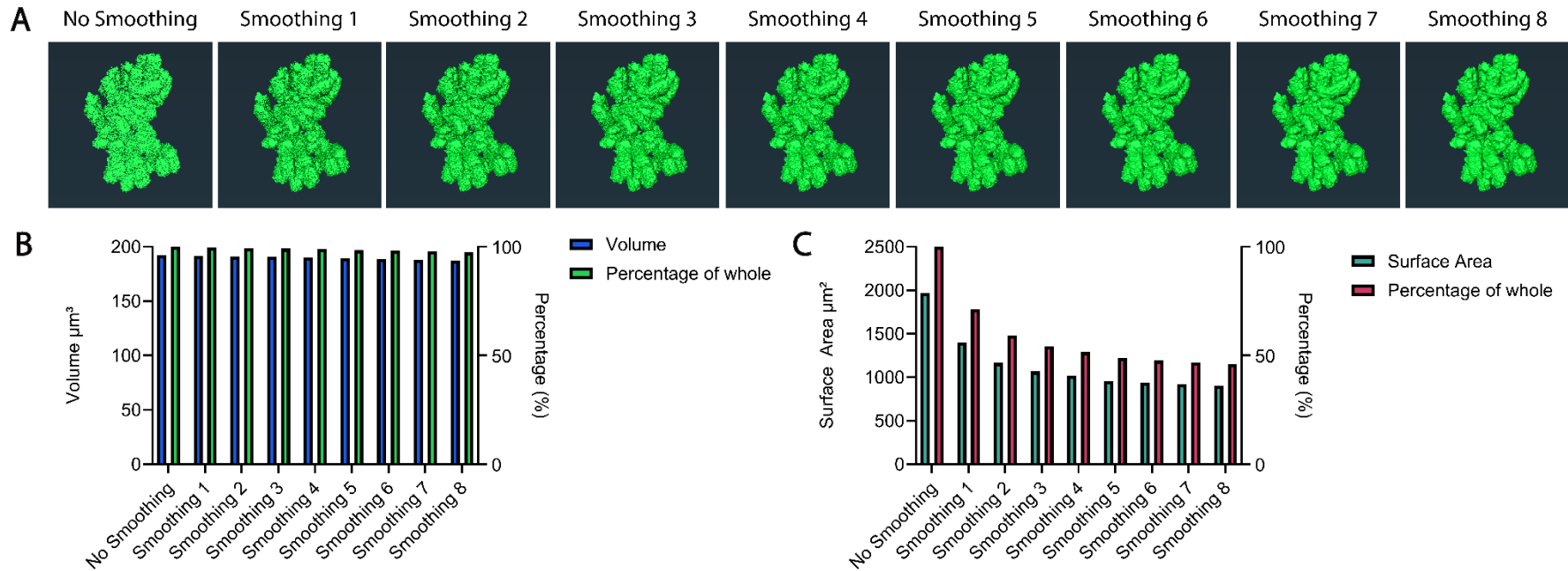


**Figure 3.9. Effect of smoothing on chromosome model geometry.** (A) 3D models of a single cell with increasing levels of smoothing applied, showing progressive loss of surface texture and refinement of chromosome structures. (B) Volume measurements indicate minimal change across smoothing levels, with values remaining consistent relative to the unsmoothed model. (C) Surface area measurements show a significant reduction with increasing smoothing. At Smoothing 1, the surface area decreased to 71.3% of the original ( $1402.62 \mu\text{m}^2$  vs.  $1966.9 \mu\text{m}^2$ ), and by Smoothing 6, it was reduced to less than 50% of the original surface area.

### 3.3.1.8. *Automated Deep Learning Modelling*

The 3D-CLEM pipeline is a low throughput technique, and one of the largest bottlenecks of the full process is post-acquisition modelling of the chromosomes – a long-standing issue in the field of vEM. The AMIRA software has a deep learning prediction module; this has been established and used already for the modelling of more simplistic organelles such as mitochondria (Garza-Lopez et al., 2021). Whilst there have been some advances in AI-led segmentation of vEM data, this has been exclusively for simple, uniform and generally symmetrical structures with very little deviation across structures of the same classification. E.g. clathrin coated vesicles can range between 70-150nm, however they are consistently spherical. Chromosomes, although having some defined limits (in general, width is thought to be constant), can occupy a wide range of flexible conformations. Our attempts, in collaboration with ThermoFisher, would be the first of its kind to apply AI/machine learning to segment whole chromosomes.

To attempt to use this for chromosomes it required deep learning (DL) training from an existing model. The prometaphase cell was modelled manually using the thresholding technique followed by refinement with the brush to remove excess as described in section 3.4.1.8.

The manual model was used with multiple parameters to train the deep learning module and improve the prediction made through the software (Table 2; Figure 3.10.A ii-v). The automated suggestions of the software were used for the first training attempt, but this introduced a lot of background selections, and the chromosomes were not easily definable (Figure 3.10.A ii). The patch size (pixel

sampling size) was lowered to attempt to reduce the excess selections, and the epochs (number of iterations through the training program) were raised to improve the quality. This did improve the model with the chromosomes becoming more visible however, there was still a lot of excess selections (Figure 3.10.A iii). The patch size was increased again, but the patches per image were reduced, and the epochs returned to the original amount, which further improved the quality of the model (Figure 3.10.A iv). The patches per image were increased again to improve specificity, and this produced the clearest model of chromosomes, with few excess selections (Figure 3.10.A v). These excess selections were removed using the brush tool, and the model was compared to the original manual model.

**Table 3.2. Deep learning parameters for chromosome modelling training.** Deep learning models were trained with varying parameters to optimise chromosome segmentation and reconstruction. The table summarises the patch size, images per batch, patches per image, and number of training epochs used in each training attempt. Different patch sizes (96–320px) and patches per image (4–8) were tested to assess their impact on model accuracy and performance. The results corresponding to each training attempt are shown in Figure 3.10 (ii–v).

| TRAINING ATTEMPT      | PATCH SIZE | IMAGES PER BATCH | PATCHES PER IMAGE | NUMBER OF EPOCHS |
|-----------------------|------------|------------------|-------------------|------------------|
| 1 (FIGURE 3.10.A II)  | 320        | 8                | 4                 | 25               |
| 2 (FIGURE 3.10.A III) | 96         | 8                | 8                 | 30               |
| 3 (FIGURE 3.10.A IV)  | 128        | 8                | 4                 | 25               |
| 4 (FIGURE 3.10.A V)   | 128        | 8                | 8                 | 25               |

The manual model and the DL model were compared to determine the accuracy of the training module (Figure 3.10.B); in these models, it is evident there are losses of data in the DL model. This is supported by the geometric data, which shows the surface area of the DL model was reduced to 1692.46 $\mu\text{m}^2$

compared to the control model,  $2849.65\mu\text{m}^2$ , a loss of ~41% of the surface area (Figure 3.10.Ci). The volume of the DL model was also reduced from  $255.145\mu\text{m}^3$  for the control to  $187.583\mu\text{m}^3$  which is a loss of ~27% of the overall volume (Figure 3.10.C ii). This indicated that the DL training module was not able to provide the level of detail that could be achieved with the manual modelling technique already established.

The DL training was also attempted on another sample (Figure 3.10.D) but was unable to successfully identify the majority of the chromosomal region within the image. It was determined that the DL prediction could be a useful and promising technique in the future to reduce the bottleneck in the 3D-CLEM pipeline. However, the software would have required a significant amount of optimisation and expertise to apply to chromosomal modelling, to a time-level well beyond the scope of this PhD project. Therefore, going forward AI was not applied to any of our data sets during this project.

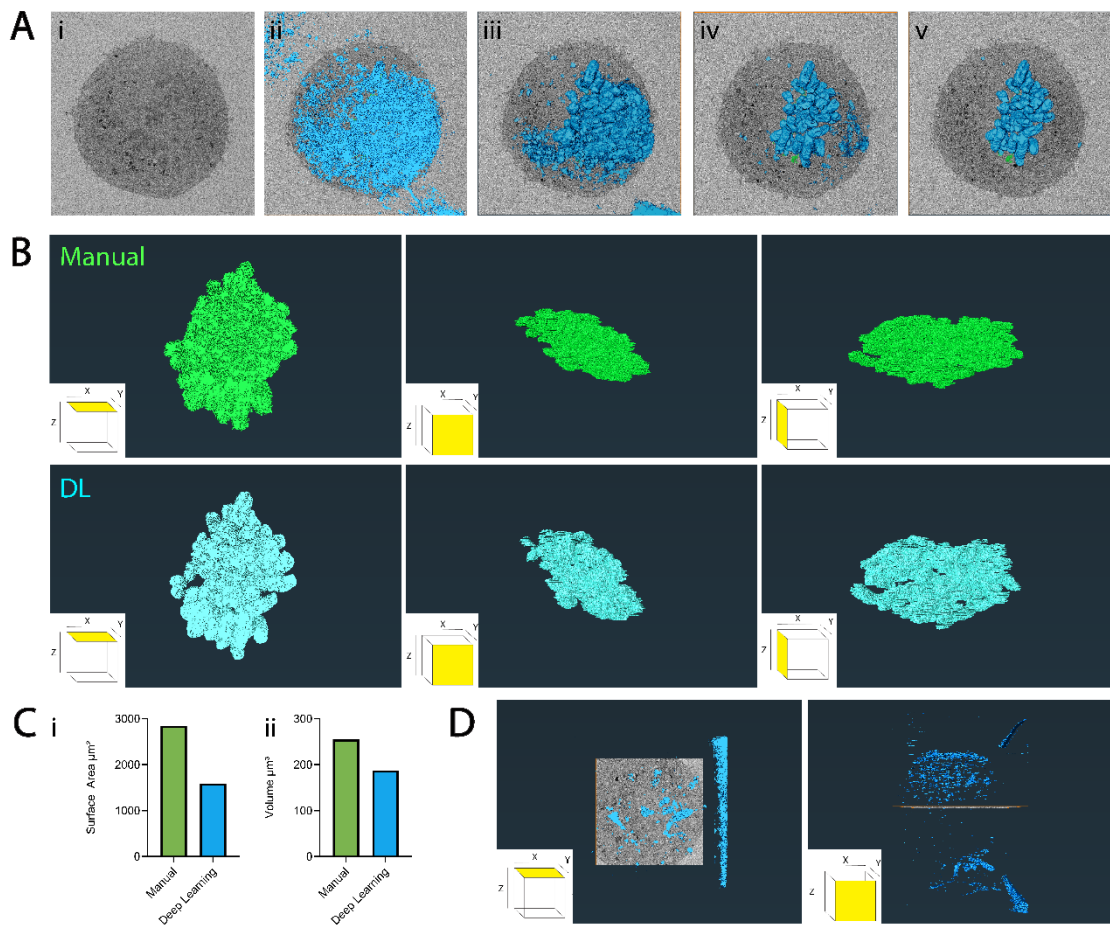


**Figure 3.10. Deep learning training for chromosome modelling.** (A) Sequential models generated by AMIRA training from a prometaphase EM stack, showing progressive improvement in segmentation accuracy. (B) Comparison of manually segmented (green) and deep learning generated (blue) chromosome models in XY, XZ, and YZ views. The DL model exhibits missing data and underestimation of chromosome regions, with visible gaps in segmentation. (C) Quantitative comparison shows that the DL model underestimates both surface area and volume relative to the manual model. (D) The optimised DL model was applied to a separate prometaphase EM stack, but the prediction failed to capture most chromosome structures, rendering it unsuitable for further analysis.

### 3.3.1.9. *Final optimised pipeline*

The combination of these optimised steps resulted in refinement and production of a reproducible pipeline for chromosomal ultrastructure analysis. Figure 3.11. shows the overall pipeline developed for this work from cell seeding and fixation through to 3D model generation and geometric analysis. Each of these individual steps was optimised for chromosomal study and the complete pipeline was successful when applied to trial samples.

The next step of optimising this technique was to apply this pipeline to a specific question to confirm the success of the pipeline for analysis of samples to produce novel data. Therefore, the workflow was applied to mitotic cells. Previous work had shown the success of using 3D-CLEM on a single metaphase cell (Booth et al., 2016). Therefore, expanding on this existing data and investigating each stage of mitosis to generate a mitotic atlas of chromosome ultrastructure seemed the most logical next step.

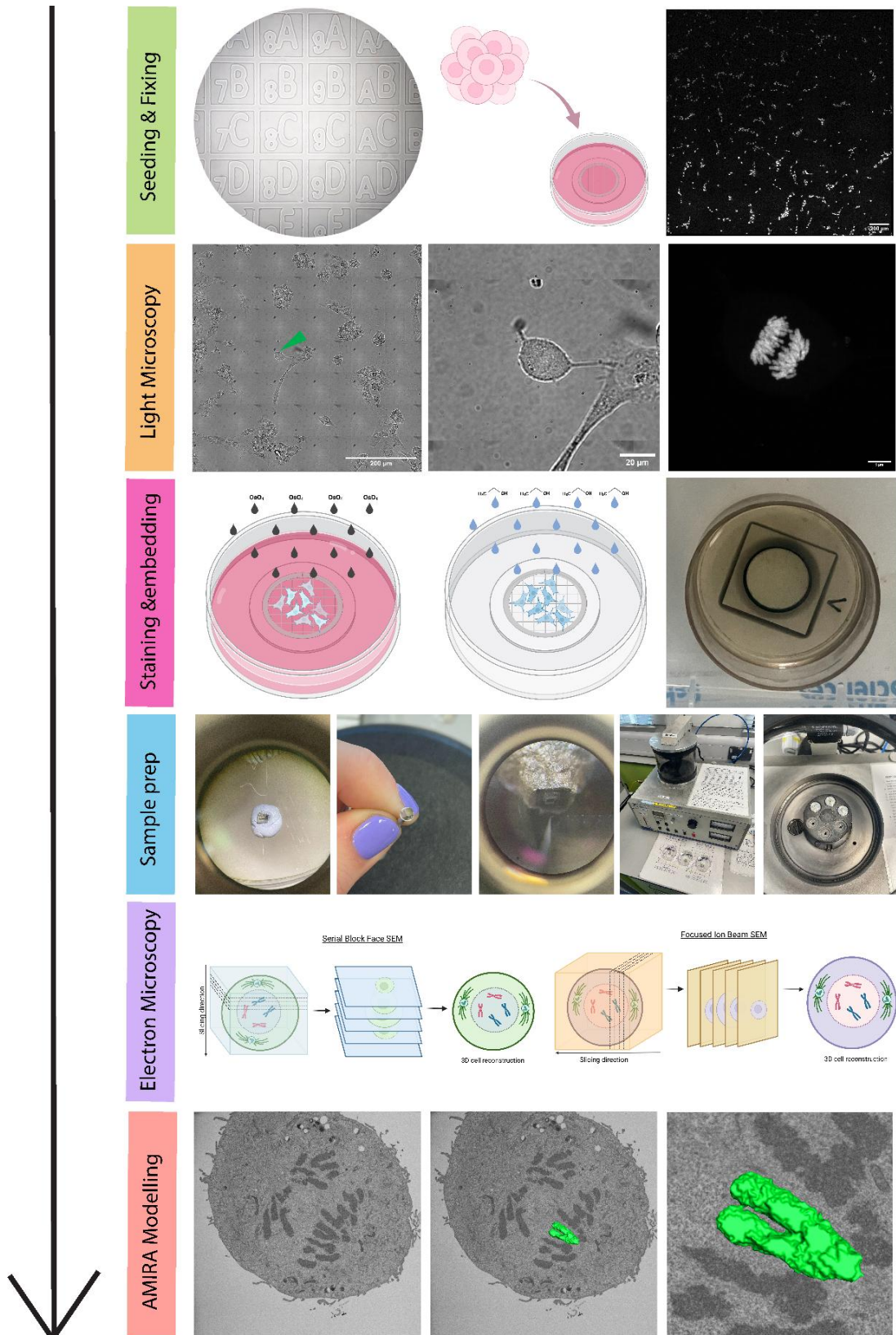


**Figure 3.11. Optimised 3D-CLEM pipeline.** A schematic overview of the optimised Correlative Light and Electron Microscopy (3D-CLEM) workflow. *Seeding & Fixing:* Cells were seeded at the optimal density (150,000 cells per dish) onto a gridded dish and cultured for 24 hours before fixation with 2% paraformaldehyde (PFA) and 2% glutaraldehyde (GA) in the presence of 1:500 DAPI. *Light Microscopy:* Phase contrast imaging and fluorescence z-stacks were acquired to locate the cell of interest and visualise the chromosome region. *Staining & Embedding:* Samples were stained with heavy metals and mordants, including osmium tetroxide ( $\text{OsO}_4$ ), tannic acid, and uranyl acetate, followed by multiple washing steps before resin embedding. *Sample Preparation:* Cells were manually trimmed with a razor blade, mounted onto a cryo-pin with conductive epoxy resin, and further trimmed using an ultramicrotome to a 300×300 nm surface. The sample was coated with silver DAG paint and sputter-coated with platinum to enhance conductivity and prevent electron charge buildup. *Electron Microscopy:* Imaging was performed using FIB-SEM or SBF-SEM, depending on the experimental requirements. *AMIRA Modelling:* 3D reconstructions were generated from light and electron microscopy datasets using AMIRA software, enabling geometric data extraction and analysis.

### 3.3.2. Mitotic Chromosome Atlas

To ensure the success of this pipeline, it was applied to somatic RPE cells, a readily available cell line that could be relatively easily prepared and handled. This was also an opportunity to expand on existing data that had used volume EM on a single mitotic cell (Booth et al., 2016). The pipeline was applied to cells from each stage of mitosis both to ensure the method was useful at all stages of mitosis and to build a mitotic atlas to expand on existing data on chromosomal ultrastructure. This work resulted in a publication in collaboration with The University of Edinburgh on the compaction of mitotic chromosomes (Cisneros-Soberanis & Simpson et al., 2024).

#### 3.3.2.1. Mitosis stage parameters

To ensure the cells selected for each stage were consistent, parameters were put in place to define each stage (Figure 3.12.). Mitosis is a dynamic

process, so defining specific stages requires these parameters for a consistent selection of cells for each group.

Prophase cells were defined as having chromosomes that weren't completely condensed and clearly defined and that still covered the area of the nucleus, confirming that the nuclear envelope breakdown (NEBD) was either partially or very recently broken down (Figure 3.12.A). Prometaphase cells had chromosomes that were clearly defined and visible but not yet aligned along the metaphase plate (Figure 3.12.B). Metaphase cells showed chromosomes that had congressed and were clearly aligned along a metaphase plate (Figure 3.12.C). Anaphase cells showed two chromosome regions, with finger-like projections towards the centre of the cell, indicating directional pulling towards the poles (Figure 3.12.D). The cells also remained, mostly spherical/oval, indicating they were not yet approaching cytokinesis. Telophase cells had two chromosomes like that seen in anaphase. However, the chromosomes no longer had defined structures, indicating decondensation. Also, the cell clearly had a cleavage furrow that has not yet fully separated indicating the cell was approaching cytokinesis (Figure 3.12.E).

Despite these parameters being put in place, it was important to keep in mind that the mitotic process is dynamic, therefore it was expected that there would be variation within the stages. The longer stages would likely have more variation e.g. Prophase is the longest stage that can last 30-60 minutes and therefore the geometric data of these stages was expected to have greater geometric variation

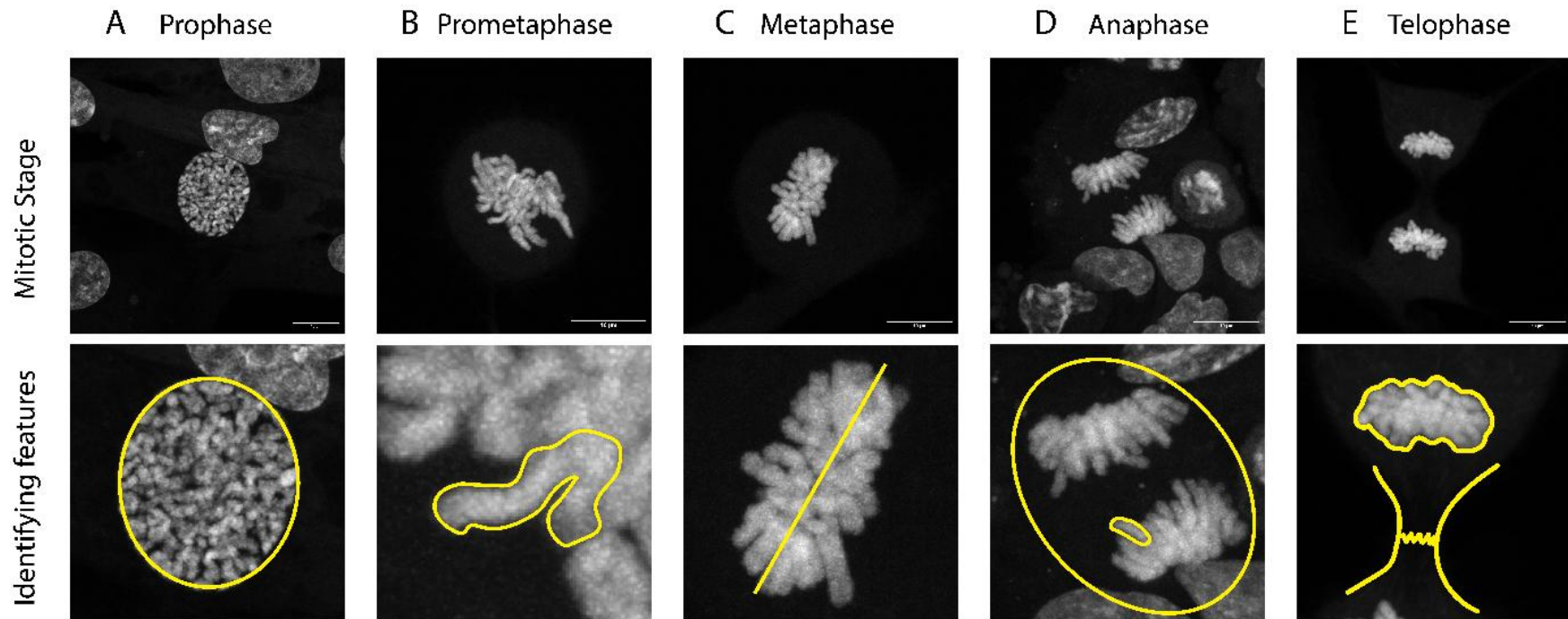


**Figure 3.12. Identification of mitotic stages using fluorescence microscopy.** Representative fluorescence images show the defining characteristics of each mitotic stage. In prophase, chromosomes begin to condense but remain loosely structured within the nuclear region. By prometaphase, chromosomes are fully condensed but not yet aligned, appearing disorganised. In metaphase, chromosomes align along the metaphase plate, forming a well-defined structure. During anaphase, sister chromatids separate into two distinct groups, moving toward opposite poles, while the cell remains intact with no visible cleavage furrow. In telophase, chromosomes begin to decondense, and the cleavage furrow forms, initiating cytokinesis. Cells were stained with DAPI and imaging was performed using a Zeiss LSM 900 confocal microscope with a 100× oil objective.

### 3.3.2.2. *3D-CLEM of mitotic cells*

Each of the cells was imaged with LM, EM and then modelled using the AMIRA software. Figure 3.13. shows the correlation between these modalities for a single example cell. Z-Stacks using EM (Figure 3.13.A) and LM (Figure 3.13.B) were taken for each cell, and these could be correlated throughout the cell to confirm the same cell had been processed through the pipeline.

For registration of EM with LM, the slices were binned to be equivalent to that of the LM, e.g. LM slices were 140nm and the EM slices were 70nm, so the EM images were binned along the A axis by 2. This allowed for improved correlation between the images. Registration throughout the cell could be completed, showing the correlation between the LM and EM images throughout the entire cell structure, as seen in Figure 3.13.C. This confirmed the cell identity, ensuring any data from LM and EM could be either combined or compared. From these z-stacks, the chromosomes were modelled with AMIRA as defined in Section 2.6, and from this, quantitative geometric data could be extracted from the qualitative images (Figure 3.13.D).

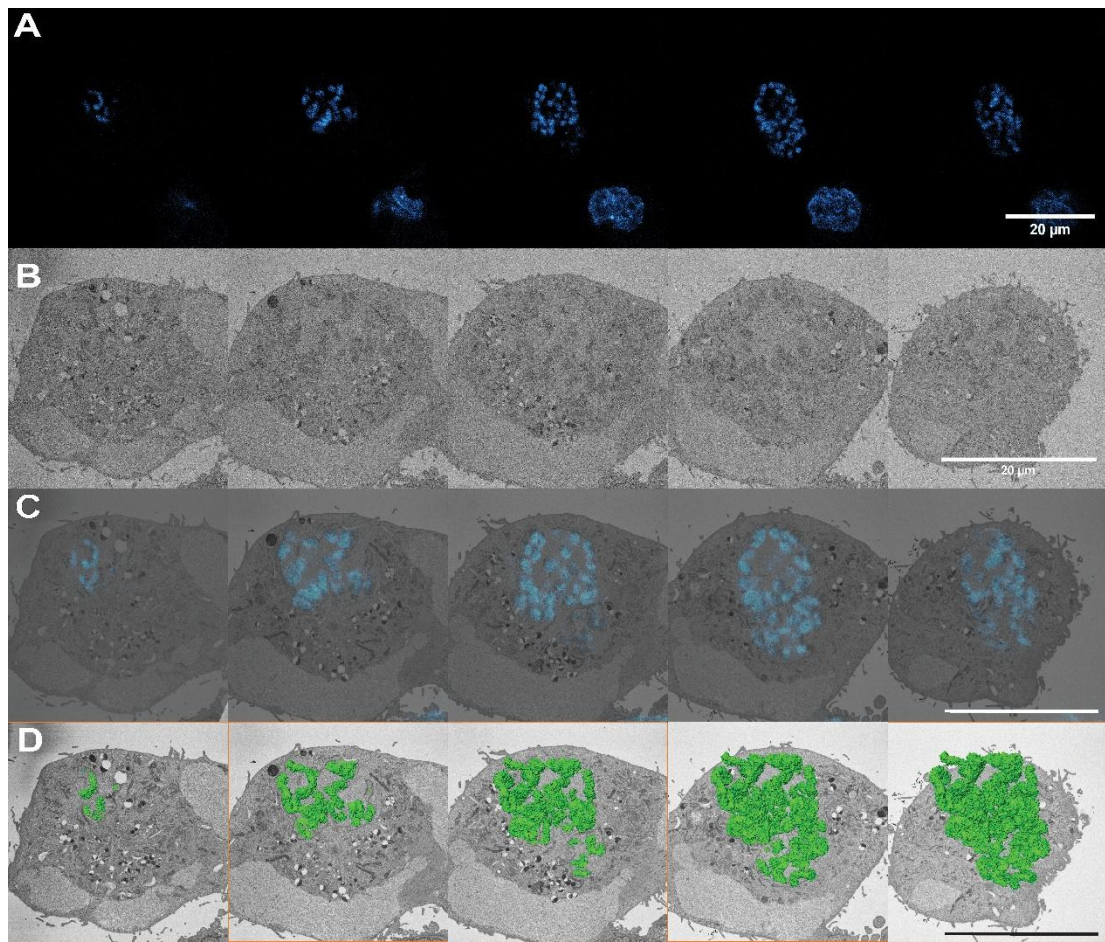


**Figure 3.13. 3D-CLEM processing of cells.** Representative correlation of a single prophase cell applied to all mitotic cells. (A) EM images show sequential slices through a prophase cell, from the initial visibility of chromosomes to the midpoint and final slice where chromosomes remain identifiable. (B) LM images of the same cell capture chromosome positions across corresponding slices. LM imaging was performed using a Zeiss LSM 900 with a 100× oil-immersion objective on cells stained with DAPI. (C) Overlay of LM and EM images confirms alignment and verifies that the same cell was imaged in both modalities. EM imaging was conducted using an FEI 250 Quanta FEG-SEM. (D) AMIRA-generated chromosome models (green) illustrate the progressive segmentation of chromosome structures, culminating in a full chromosome complement in the final image. Scale = 20μm.

### 3.3.2.3. Mitotic Chromosome Atlas

To validate the optimised pipeline, it was applied to mitotic cells at each stage of mitosis. For this purpose, RPE cells were used. These cells had a stable karyotype and were chosen to provide data on the standard 23-chromosome-pair complement. This made them the ideal reference cell for generating fundamental

biological data on mitotic chromosome ultrastructure, as it reduced variability between cells and could be used as a reference for future research.

The cells were seeded into gridded dishes and were grown for 24 hours (methods 2.2, etc.). They were not synchronised with any chemical agent, such as nocodazole (an anti-neoplastic agent that disrupts microtubule organisation). This was to keep the cells as close to their native state as possible and avoid any chemically induced cell or chromosome structure abnormalities.

A total of 16 naturally occurring mitotic cells were examined across the mitotic stages (four prophase, four prometaphase, two metaphase, one anaphase, five telophase) based on the parameters for each stage of mitosis as defined in section 3.4.2 (Figure 3.14.). After LM, the cell of interest was then processed using the optimised 3D-CLEM pipeline and re-located for electron microscopy imaging.

3D models of the reconstructed chromosomes were created from the resulting LM and EM datasets. This included whole-chromosome-complement models and from these, individual chromosomes were segmented. In addition to examining overall chromosome organisation, the models allowed for the extraction of geometric data such as volume and surface area, which could provide quantitative insights into structural variation across mitotic stages. Together, these results confirmed that the 3D-CLEM pipeline could reliably model and segment chromosomes at each stage of mitosis (Figure 3.14.). This robust approach set the stage for future studies seeking to compare 'normal' versus

altered mitotic chromosomes (e.g. aneuploid, knockdown, drug-treated cells) or investigate the chromosomal ultrastructure of meiotic cells.

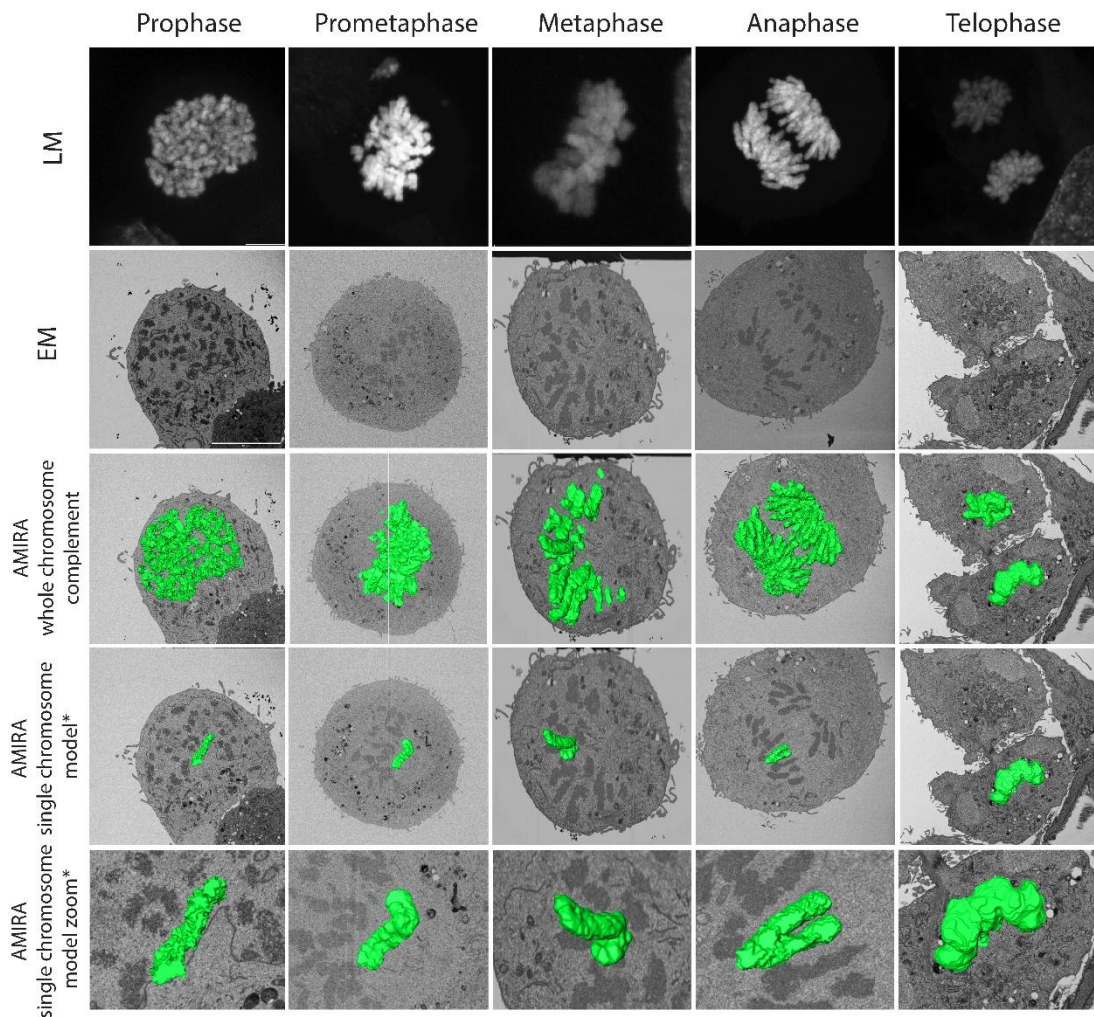


**Figure 3.14. Representative 3D-CLEM models of mitotic stages.** This figure presents LM, EM, and 3D models of RPE cells at different mitotic stages (prophase, prometaphase, metaphase, anaphase, and telophase). Each column represents a single cell at a specific stage, illustrating the complete imaging and modelling workflow. LM imaging was performed using either a Leica SPE (63× oil-immersion objective) or Zeiss LSM 900 (100× oil-immersion objective) on DAPI stained cells. EM imaging was conducted using a Zeiss Crossbeam 550 FIB-SEM or an FEI 250 Quanta FEG-SEM. Chromosomes were segmented using AMIRA Thermo Fisher software, where thresholding was applied to isolate chromosomal regions, followed by manual refinement with the brush tool to remove background material. The rows display EM images, the whole chromosome complement model, an isolated single chromosome, and a zoomed-in view of the individual chromosome. This pipeline enables high-resolution 3D segmentation and structural analysis of mitotic chromosomes.

#### 3.3.2.4. *Quantitative data analysis*

To investigate mitotic chromosome morphology, chromosome volume, surface area, and chromatin compaction were analysed across different mitotic stages (prophase, prometaphase, metaphase, anaphase, and telophase) using 3D-CLEM.

Chromosome volume and surface area were quantified from 3D reconstructions obtained through light and electron microscopy (Figure 3.15.A-B). The chromosome volume remained relatively stable throughout mitosis, with a slight increase observed but not statistically significant variation between the stages (Figure 3.15.A). In contrast, surface area exhibited greater variability, with the largest values detected in prophase, followed by a general decrease as mitosis progressed (Figure 3.15.B). These trends support chromosomal reorganisation throughout cell division, with the chromosomes becoming smoother and more clearly defined throughout mitosis.

To assess the differences in chromosome geometry between the two imaging modalities, the volume and surface area from LM and EM models were compared (Figure 3.15.D-E). The volume measurements were significantly lower in EM for prophase ( $p = 0.0025$ ) and prometaphase ( $p = 0.0045$ ), while no significant differences were observed in metaphase, anaphase, or telophase (Figure 3.15.D). Surface area also appeared lower in electron microscopy measurements across all stages; however, these differences were not statistically significant ( $p > 0.05$ , Figure 3.15.E). These results suggest that light microscopy overestimates chromosome dimensions.

Chromatin compaction density was calculated as the total DNA content per unit volume ( $\text{Mbp}/\mu\text{m}^3$ ) using EM volume measurements (Figure 3.15.C). Chromosomes displayed the highest compaction levels in prophase, followed by a gradual decrease towards telophase. However, the variation between the different mitotic stages was not significant, indicating the variation is due to individual cell organisation rather than a specific chromosomal trend.

This quantitative analysis highlights mitotic chromosome remodelling, with subtle changes in volume, surface area, and compaction across various mitotic stages. The observed differences between LM and electron EM highlight the importance of high-resolution imaging for accurate chromosome structure quantification.

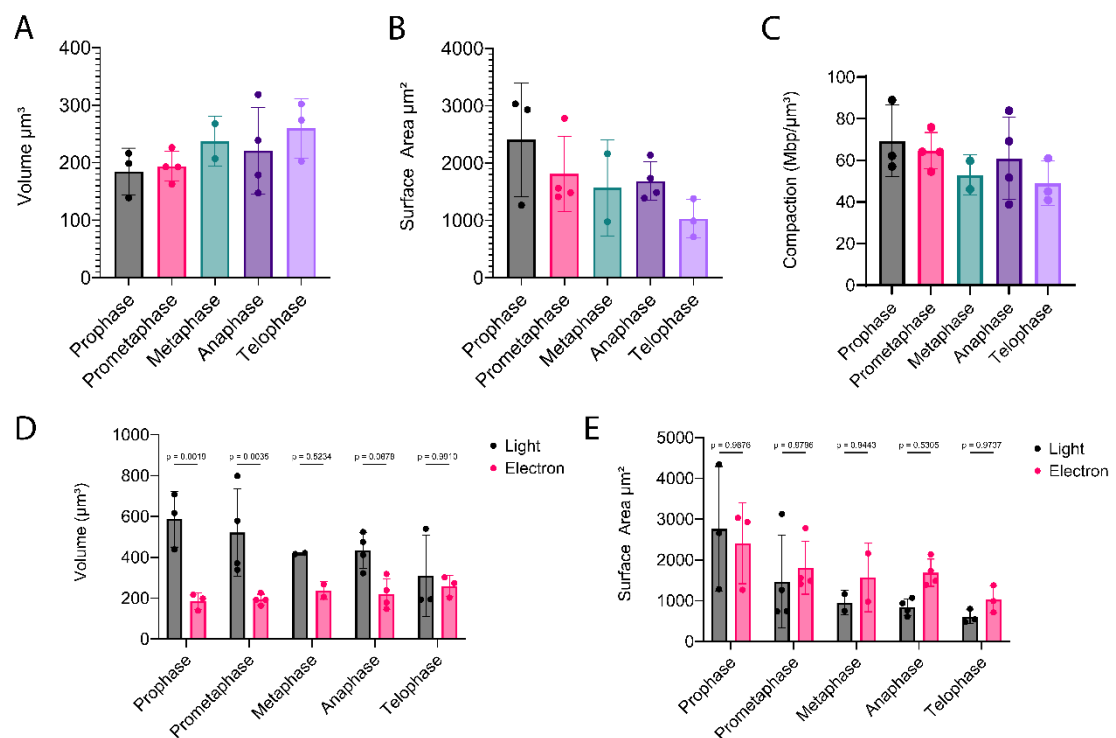


**Figure 3.15. Quantification of mitotic chromosome ultrastructure using 3D-CLEM.** (A, B) Chromosome volume and surface area were measured across mitotic stages using electron microscopy. Chromosome volume remained relatively stable, with a slight increase in anaphase and telophase, while surface

*area showed greater variability, decreasing after prophase. Data are presented as mean  $\pm$  SD, with individual data points shown. (C) Chromatin compaction density ( $\text{Mbp}/\mu\text{m}^3$ ) was highest in prophase and gradually decreased toward telophase, reflecting progressive structural changes in chromosome organisation during mitosis. (D, E) Comparisons of chromosome volume and surface area between light and electron microscopy. Volume measurements were significantly lower in electron microscopy for prophase ( $p = 0.0019$ ) and prometaphase ( $p = 0.0035$ ), while no significant differences were observed in later stages. Surface area differences were not statistically significant across mitotic stages, except for anaphase ( $p = 0.0305$ ).*

#### *3.3.2.5. Nucleosome concentration plateaus during mitosis*

The combination of this 3D-CLEM data with that of the Edinburgh group enabled a higher-powered analysis of chromosome ultrastructure. This enabled the identification of a compaction plateau following prometaphase. The total volume of the metaphase cells was relatively consistent ( $140 \pm 4.8 \mu\text{m}^3$ ). Using the assumption that each nucleosome within the chromosomes has 195bp of DNA (Tate & Philipson, 1979), the concentration of nucleosomes per micron<sup>3</sup> could be determined. The analysis of this chromosome compaction and nucleosome compaction showed that from late prometaphase to mid anaphase the nucleosome density plateaued at  $74 \pm 27.6\mu\text{M}$ , supporting a phase separation mechanism for chromosome compaction.

### Nucleosome concentration ( $\mu\text{M}$ ) in human mitotic chromosomes

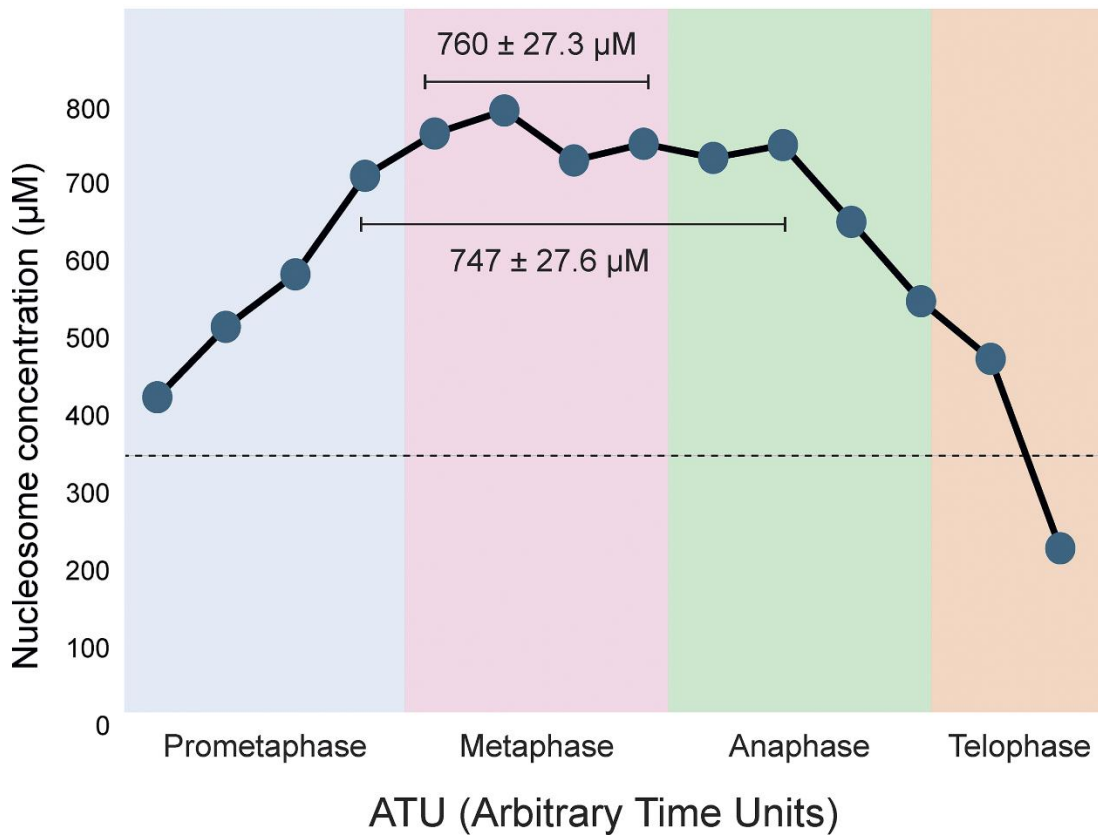


**Figure 3.16. Nucleosome density plateaus from prometaphase to anaphase.** Each circle represents the nucleosome concentration of a single cell. The temporal position of each cell was determined by measuring the centrosome separation (this could not be done with the metaphase cells). (Cisneros-Soberanis & Simpson et al., 2024)

### 3.4. Discussion

This chapter aimed to establish and optimise 3D-CLEM as a pipeline for investigating chromosomal ultrastructure, improving on existing methodologies. The hypothesis was that the 3D-CLEM pipeline could be successfully developed for high-resolution imaging of chromosomal ultrastructure to produce quantitative geometric volume data that would be otherwise unattainable.

This required the optimisation of existing 3D-CLEM workflows for the application to dividing cells in order to produce a pipeline that would be transferrable and reproducible across various different sample types. It also required the technique to be established at the University of Nottingham, where this type of work had not been done previously. The optimisation of seeding densities and fixation methods ensured consistent results across experiments that allowed for the visualisation of dividing cells without the need for chemical synchronisation. This reduced the likelihood of induced abnormalities caused by any chemical alterations to the cell (Worrall et al., 2018). It also ensured there were enough dividing cells to visualise and image all stages of mitosis, allowing for investigation into chromosomal ultrastructure during each stage of division. The use of a chemical synchronisation drug such as nocodazole would have made this impossible as its microtubule interruption mechanism would have synchronised the cells at metaphase, making later stages such as anaphase and telophase impossible to source, as well as potentially altering the validity of the results due to structural changes that may have occurred as a result of drug-induced synchronisation (Attia et al., 2015; Dalton et al., 2007).

The comparison of the standard confocal images and those produced by super-resolution microscopy allowed for increased resolution of light microscopy images. This is particularly useful for the correlation of data with EM as the improved structural clarity and decreased difference in resolution allowed for more accurate registration between the images. The resolution gap between LM and EM is one of the key limitations of the technique and incorporating super-resolution LM reduces this gap with the individual chromosomes being

approximately 1-10 $\mu$ m in size, the use of super-resolution confocal microscopy allowed for improved identification of chromosomal structures, e.g. sister chromatids, as well as any abnormalities such as misaligned chromosomes. This was particularly important as the mitotic atlas required phenotypically normal cells to create a reference for standard chromosomal ultrastructure, and future work with this pipeline would require the resolution to identify abnormalities associated with the research focus, e.g., Ki67 depletion and altered chromosome structure. This higher resolution LM eased the later stages of the 3D-CLEM pipeline, making it a valuable addition to the workflow that should be utilised in future studies of cellular components, requiring little to no alteration to the existing LM protocols.

A further development of the pipeline in the future could be to include alternative super-resolution techniques such as PALM and stochastic optical reconstruction microscopy (STORM) where applicable. Matsuda et al., (2010) applied PALM to study mitotic chromosomes in drosophila and were able to use the technique to measure chromatin filaments of  $\sim$ 70nm, thus supporting the efficacy of PALM for chromosomal investigation. However, these techniques require alternative methods for preparation (photoactivatable fluorophores) and increased processing following imaging, which could increase the resolution of the LM technique ( $\sim$ 20nm) but also increase the labour required for the already laborious 3D-CLEM pipeline.

Optimisation of the tannic acid staining to improve greyscale variation between chromosomes and cytoplasm was also an important adjustment to the

pipeline. As the quantitative data produced from models generated from EM imaging relies on the contrast between the greyscale values, it was an essential step of the pipeline to optimise. One of the causes of artefacts within chemically fixed samples comes from the heavy metal stains applied to the samples (Griffith & Bonner, 1973; Kopáni et al., 2019). Therefore, to reduce the increase of any sample artefacts the tannic acid was increased to improve the binding of the heavy metals rather than directly increasing the heavy metal concentration. By increasing tannic acid, which acts as a mordant, the binding efficiency of the heavy metals used for staining (e.g. uranyl acetate) was improved producing an increased greyscale value when compared to the previous method (Afzelius, 1992; Simionescu & Simionescu, 1976). This increased contrast between structures and improved the overall visualisation and clarity of the chromosomes, which in turn enabled a more precise selection of chromosomal structures. This improved the reliability of the geometric data produced from these results, as there were clear distinctions between the components of the cell and, therefore, fewer wrong selections made during modelling.

All these optimisation steps of the pipeline improved the overall processing of samples and images to produce the most accurate volume reconstructions of the chromosomes. Optimising these steps of the pipeline before any imaging or reconstruction was done was essential for producing the clearest possible image to make the next stages of the pipeline as smooth as possible.

The optimisation of EM imaging primarily focused on FIB-SEM due to its potential for high-resolution volume imaging. Establishing a precise method for locating the sample in the FIB-SEM ensured the sample of interest was processed through the entire pipeline without fail. Due to the tilting requirements of the FIB-SEM and tilt adjustments put in place, it was essential to overestimate the area of interest prior to reaching the sample to adjust for any misalignments. This both increased the imaging time of samples and reduced the resolution of the cell as the ROI often included extra background in the imaging that was not required reducing the nm/px resolution of the cell region.

Despite the optimisation of imaging for the FIB-SEM to achieve the best resolution possible within what was considered a reasonable timeframe, the resolution that could be achieved from the FIB-SEM was significantly reduced when compared to the SBF-SEM. This was due to the increased imaging time for each slice, but also more significantly the increased milling time required for larger and deeper surface areas, but at a low enough charge to retain the smooth surface of the revealed slice. This indicated that the method would be more suited to smaller components e.g. imaging of a single chromosome in comparison to an entire chromosome complement/cell. Luckner & Wanner, (2018) used FIB-SEM to successfully model mitotic HeLa cells and proved that the technique could be applied to whole cells, whilst also acknowledging the limitations of the techniques relative to the size of the sample, summarising that larger sample types would be better suited to 3View SBF-SEM imaging. Therefore, applying FIB-SEM to specific components of cells, e.g. single chromosomes

rather than whole cells, would enable the resolution capabilities of the FIB-SEM to be maximised whilst maintaining reasonable experimental times.

The SBF-SEM was able to achieve higher resolutions for the larger sample types in this pipeline as more time could be devoted to the imaging due to the consistent and fast slicing of the sample regardless of the surface size that needed to be removed. Despite this confirmation that SBF-SEM provides better imaging parameters for large samples, 3D-CLEM remains a low-throughput technique, requiring significant time for sample preparation and imaging. Additionally, fixation and staining steps, while optimised, could still introduce potential artifacts affecting chromosomal structure.

The utilisation of both methods for a single sample did confirm that each method was relatively equal in their estimation of chromosomal volume regardless of the variation in resolution. This indicated that both methods were equal in their capabilities of serial imaging whole cells, however the true deviation between the methods was the timing and consistency of the results. The FIB-SEM took significantly longer to process the sample, not only in the imaging and milling but also in the preparation required prior to the set up. As the FIB mills the slices directly down into the surface, the areas surrounding the cell of interest needed to be removed prior to imaging. This introduced extra hours of preparation and introduced a possible disturbance to the imaging if the area could not be sufficiently cleared and created physical blockages in the way of the sample surface. In comparison the SBF-SEM removed the entire block surface with the diamond knife which was consistent in its removal and only caused

problems if a slice was caught on the block during imaging, however, this would only last one or two slices before being removed by the action of the knife and required no user interference. Comparatively, if shelves occurred in the FIB-SEM during imaging this required manual intervention and the interruption of serial sectioning imaging which although possible is incredibly technically difficult to ensure return of SSI to the exact spot of imaging following adjustments. Also, as the imaging often had to run overnight due to the amount of time required for imaging, it was possible the 'shelving' was not identified immediately and blocked the imaged surface for multiple slices. As the technique is destructive there is then no way to recover those faulty images and therefore the sample is lost as a whole complement reconstruction. This lack of consistency made the FIB-SEM technique unfavourable for volume studies of cells and chromosomes. In an already low throughput technique, the potential loss of a sample after a prolonged period of processing and preparation was considered unacceptable and when considering the future precious samples that would be investigated (oocytes), it was determined that the SBF-SEM should be used in the future for volume studies. This application of both techniques to chromosomal study was particularly important as much of the existing research that utilises EM for ultrastructural analysis focuses on the topology, or single slice viewing of the chromosomes (Dwiranti et al., 2021). Developing the volume 3D-CLEM pipeline for the work is a promising advancement in techniques to explore whole organelle ultrastructure.

These accurate reconstructions were the basis of all the geometric data, ensuring these processes were optimised, which improves the validity of any

quantitative data extracted from this work. By applying all the available modelling techniques to a single cell this geometric data could be further improved. This comparison of modelling tools highlighted the importance of balancing accuracy and efficiency of modelling modalities. The brush tool provided the best accuracy when modelling the chromosomes but was time-consuming and prone to user bias. In comparison, the thresholding tool was faster and less biased but often overestimated the chromosomal selections. A hybrid approach, combining the brush tool and thresholding tool, was used to combine the best features of each technique – the speed of thresholding and the accuracy of the brush tool, while reducing the drawbacks of each technique, the excess selections from thresholding and the prolonged time and bias of the brush tool.

Attempts to use deep learning to automate the modelling were made to try and reduce the bottleneck that occurs during segmentation. The initial attempt using a pre-modelled cell showed some promise following refinement of the DL parameters. However, when this was applied to further samples the DL was unable to transfer the learning in a way that could produce a usable model. This DL module does show potential for the application to chromosome modelling and has already been established and used for more simplistic structures such as mitochondria. However, it would require significant development for suitable applications to this work and was not yet ready to be applied to this pipeline. Although the data from this work could be used to teach the AMIRA DL software in the future advancing this technique further for future use.

Having established and validated the 3D 3D-CLEM pipeline, we applied it to mitotic cells to generate novel biological insights into chromosomal ultrastructure. The application of the pipeline to mitotic RPE cells validated the effectiveness and reproducibility of the technique. By applying this to all stages of mitosis it demonstrated the pipeline as a tool for generating novel biological data. The mitotic chromosome models were created in combination with The University of Edinburgh and the combination of the data produced by us and them resulted in a publication on the ultrastructure of chromosomes in mitotic cells (Cisneros-Soberanis et al., 2024). The images generated by this technique could be correlated throughout the slices, proving the successful analysis of the same cell throughout the process. From this the surface area, volume, compaction and spread of the chromosomes could be determined for each stage of mitosis. There was no significant difference between the groups, which is what would be expected from the data, as the DNA content does not change throughout the different stages, and therefore the volume and surface area of the chromosomes should not change between stages. This provides a basis for comparison when investigating other biological questions. For example, this data can act as a reference for control cells if you were to investigate biological changes that may affect the chromosome structure, e.g. removal of the chromosome periphery. With this reference data any changes to the chromosomal ultrastructure can be easily compared and identified, indicating the importance of this mitotic atlas as fundamental biological data. This analysis not only validates the pipeline but also provides valuable data on mitotic chromosome organisation. Our findings contribute to the growing body of

literature on chromatin dynamics and compaction throughout mitosis, aligning with recent studies that have used advanced imaging techniques to explore chromosome structure.

The modelling of chromosomes from LM and EM could be compared to review the effectiveness of each technique for chromosome analysis. The surface area was not significantly different between the two methods despite there being a trend in the LM underestimating the surface area of the chromosomes. In comparison, the LM did significantly overestimate the volume of the chromosomes in both the prophase and prometaphase chromosomes, and the volume was overestimated in the other stages, despite this not being significantly different. However, this lack of specificity from the LM compared to the EM does indicate that LM does not provide sufficient resolution to produce reliable quantitative data on chromosome size. This significant difference in volume measurements is also important for compaction studies on chromosomes, as the measurement is dependent on the measured volume of the chromosomes. The reliance on fluorescence and reduced resolution of LM in comparison to EM results in imprecise measurements that can provide a rough estimate of the geometry of chromosomes but cannot be relied upon for precise analysis of ultrastructure, further solidifying the need for more advanced imaging modalities for the accurate analysis of chromosome structure. Nedela et al., (2024) applied advanced environmental scanning electron microscopy (A-ESEM) to mitotic chromosomes and were able to image the chromosomes in their native state, revealing details of the topology of the chromosomes. This technique doesn't provide volume reconstructions of the entire chromosomes but applying

this technique in the future could provide even more detail into the chromosome structure, particularly the composition in the native state, that could then be combined with the volume data from whole chromosome reconstructions. This could provide a pipeline with the fast-paced localisation of LM, native state topographical analysis of A-ESEM and volume reconstruction from SBF-SEM, providing a comprehensive analysis of chromosome ultrastructure that has not yet been explored.

Beyond the mitotic cells used in this chapter, this pipeline is well-suited for application to meiotic cells, where chromosomal missegregation is a key driver of aneuploidy. Given that human oocytes exhibit high rates of aneuploidy, applying 3D-CLEM to meiotic samples presents an opportunity to investigate the ultrastructural changes associated with chromosome missegregation. By establishing a mitotic atlas as a reference dataset, future work can directly compare normal chromosome behaviour with the structural anomalies seen in aneuploid cells.

This chapter presents the establishment and optimisation of a 3D-CLEM pipeline as a significant advancement in the study of chromosomal ultrastructure. By integrating the specificity of high-resolution light microscopy with the ultrastructural detail of electron microscopy, this workflow overcomes the limitations of traditional imaging methods. The resulting pipeline provides a robust and versatile framework for investigating the complex architecture and organisation of chromosomes in three dimensions. This is evidenced by the combination of this data with that of Fernanda Cisneros-Soberanis at the

University of Edinburgh to generate the mitotic atlas from which geometric data was extracted (Cisneros-Soberanis & Simpson et al., 2024). This data highlighted that the volume of chromosomes remained consistent from late prometaphase through to anaphase which may have implications for the mechanisms of chromosome condensation that occurs throughout mitosis. It also showed that the width of chromosomes following anaphase varied depending on the chromosome size, with larger chromosomes being significantly wider than the smaller chromosomes, indicating a potential variance in the organisation of chromatin within the different-sized chromosomes, or the effect of the chromosome position during separation and the resultant impact of the microtubule forces (Cisneros-Soberanis & Simpson et al., 2024).

In conclusion, the establishment of the 3D-CLEM pipeline represents a significant contribution to the field of chromosome biology. This workflow provides a powerful tool for dissecting the molecular and structural basis of chromosomal organisation, enabling researchers to address fundamental questions about genome stability, cell division, and the mechanisms driving chromosomal abnormalities. By bridging the gap between imaging modalities, this pipeline sets the stage for discoveries in cell and molecular biology. Moving forward, integrating automated segmentation approaches, including deep learning-based modelling, could improve efficiency and throughput. Additionally, applying this technique to more complex biological questions, such as chromosome periphery function in aneuploid oocytes, will further enhance its impact in cell and reproductive biology.

## 4. Role of Ki67 in meiotic cells

### 4.1. Introduction

The mitotic chromosome periphery is by far the least understood chromosome compartment, but in meiosis it remains completely unexplored. In mitotic cells four main functions have been proposed; maintenance of intrinsic chromosome structure, protection against DNA damage, support chromosome isolation, and finally a scaffold to “piggyback” nucleolar components. This suggests that, while the finer details of function are yet to be fully confirmed, the chromosome periphery is likely a multifunctional compartment.

In meiotic cells however, the role of the periphery is completely explored. Exploring for a function in meiosis could give insight into how chromosomes are correctly or improperly segregated during meiosis and by extension a possible new pathway linked to miscarriage and infertility. Embracing a multi-institutional collaboration between Newcastle, Warwick, Liverpool and Nottingham, has allowed us to exploit both mouse and human oocytes, integrating fixed imaging, live imaging and electron microscopy to study the chromosome periphery, for the first time, in female meiosis. This work is currently in pre-print (Simpson et al., 2024) and under review in Nature Communications.

The findings of this chapter, in the first instance, was to determine if an oocyte periphery exists and if so, does it provide an essential meiotic function. If it has a critical function, how does this compare to that of mitotic division – i.e. are their key differences? This understanding could provide a foundation for

future research into therapeutic strategies for conditions associated with aneuploidy.

## 4.2. Hypothesis and Aims

### Hypothesis

A meiotic chromosome periphery exists in oocytes. Removal of a meiotic chromosome periphery, via Ki67 depletion, reveals that it has a critical novel function ensuring chromosome fidelity.

### Aims

- Confirm the presence of the chromosome periphery in meiotic cells: Investigate and validate the existence of the chromosome periphery in mouse oocytes using fixed imaging.
- Investigate the effects of Ki67 depletion in mouse oocytes during Meiosis I via live imaging: Examine how the absence of Ki67 influences chromosome dynamics, organisation, and segregation fidelity during the first meiotic division. This will help determine whether Ki67 is critical for maintaining chromosome periphery integrity in meiosis.
- Investigate the ultrastructural changes in mouse oocytes following Ki67 depletion using 3D-CLEM: Employ 3D-CLEM to visualise structural alterations at high resolution. This approach will clarify the specific morphological impact of Ki67 depletion on meiotic chromosomes and provide insights into the mechanism underlying potential segregation errors.

## 4.3. Results

### 4.3.1. Ki67 is present on the periphery of meiotic chromosomes

Previous research undertaken by the lab group identified Ki67 as a key organiser of the chromosome periphery in mitotic chromosomes. Therefore, the initial aim was to determine whether there was a chromosome periphery in oocytes and whether Ki67 maintained its role in meiotic chromosomes. There is currently only one existing publication that suggests the presence of a periphery in meiotic chromosomes, however the visual evidence is inconclusive (Traut et al., 2002).

The chromosome periphery was stained in mouse oocytes using Ki67 and the cell were fixed at various stages from germinal vesicle breakdown (GVBD) to MII show the localisation of the periphery throughout MI (Figure 4.1.). The imaging indicated that Ki67 was recruited to the chromosome surface throughout all stages of MI with some chromosomes being completely encapsulated (Figure 4.1.B, blue arrows) and others appearing only partly surrounded (Figure 4.1.B, yellow arrows). This suggested that there is definitely a chromosome periphery in oocytes and that it forms similarly to that seen in mitotic cells.

However, a surprising localisation of Ki67 was seen during anaphase, where the Ki67 was separated unequally between the oocyte and the polar body, with the majority being retained within the oocyte (Figure 4.1.F). Fluorescence intensity measurements showed that the separation of Ki67 between these two oocyte components was statistically significant ( $P < 0.05$ ) with 63.6% ( $\pm 4.3$ ) of

Ki67 remaining within the oocyte, and the remaining 36.4% ( $\pm 4.3$ ) was extruded into the polar body (Figure. 4.1.F, graph). Importantly, the Ki67 chromosome periphery was not altered in MII following this unequal separation and the chromosomes were all coated completely (Figure 4.1.G).

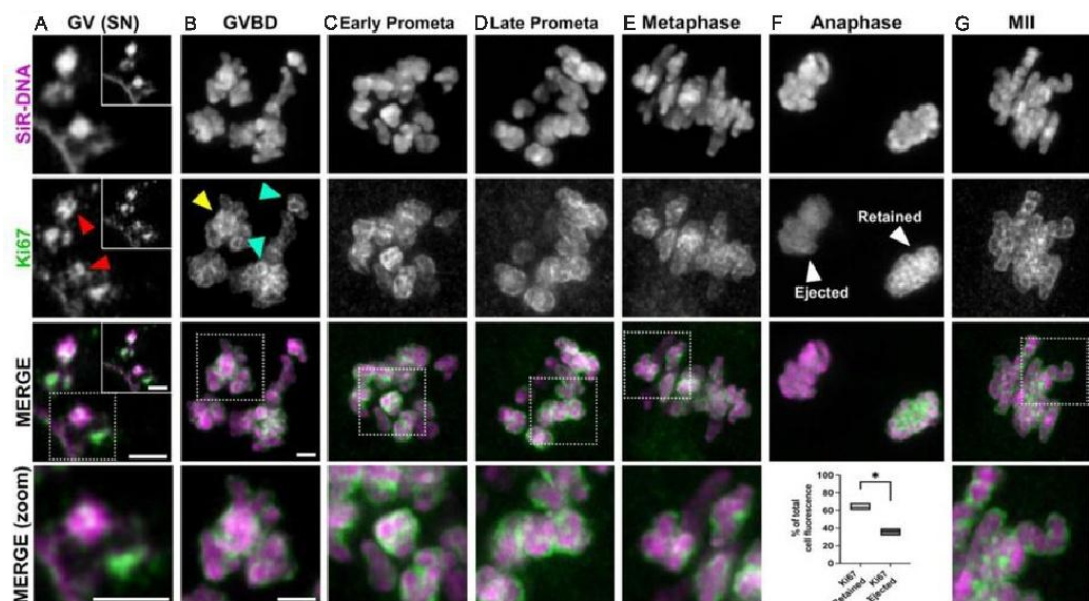


**Figure 4.1 Ki67 distribution during Meiosis I confirms chromosome periphery and reveals novel distribution.** (A-G) Mouse oocytes released and fixed at each given stage of division. Each panel shows sirDNA (magenta) and Ki67 (green) staining, with resultant merged images. Arrows point to varying Ki67 coatings: potential enveloping (red), complete enveloping (cyan) and partial enveloping (yellow). Graph in K shows the fluorescence intensity measurements for Ki67 during anaphase.  $N=3$  oocytes. (This work was performed by Ben Wetherall – University of Newcastle)

#### 4.3.2. Ki67 Live Imaging Phenotypes

Live imaging of mouse oocytes, both control and knockdown, allowed for investigation of the role of Ki67 during meiosis in native-state oocytes (i.e. none fixed). The live imaging revealed a significant increase of multiple aberrant phenotypes that were present in Ki67 Knockdown cells compared to controls. A qualitative analysis of these phenotypes (Figure 4.2.) included ‘stalled’

chromosomes, which appeared to progress through the initial stages of meiosis successfully and even form a clean metaphase plate (Figure 4.2. red arrow). Still, the process was delayed and could not be completed before the end of imaging (1040 minutes), which should have been ample time for the first meiotic division to have been completed as this is timed as 520 minutes in “healthy” division. ‘Misaligned’ chromosomes are those that attempted to progress through meiosis. Still, during the alignment of the metaphase plate, the chromosomes could not align successfully, and chromosomes were lagging and misaligned, affecting their ability to progress through the remaining stages of meiosis (Figure 4.2. green arrows). ‘Mis-segregated’ cells are those that progressed through the early stages of meiosis well, but during PB formation, the chromosomes did not separate equally (Figure 4.2. blue arrow). In some cases, all of the chromosomes

were extruded into the PB. These defects suggest a key role for Ki67 in ensuring chromosome alignment and faithful segregation during meiosis.

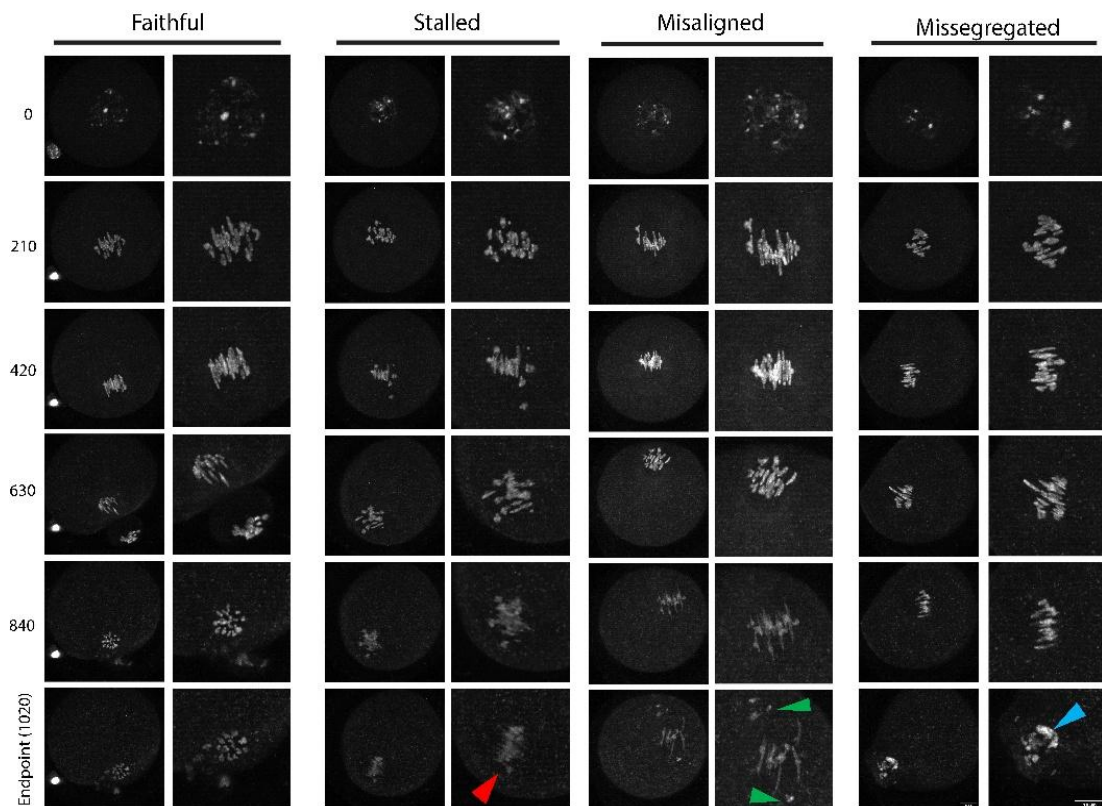


**Figure 4.2. Imaging of chromosome segregation phenotypes following Ki67 knockdown.** Time-lapse imaging of mouse oocytes, stained with SiR-DNA during meiosis illustrates distinct phenotypes observed in CTRL and KD conditions. The 'Faithful' column represents a CTRL oocyte that successfully progressed through meiosis, forming a metaphase plate and extruding a polar body (PB) with equal chromosomal segregation. In KD oocytes, three phenotypic categories were identified: *Stalled*: Oocytes initiated meiosis but failed to complete division within the imaging period (1020 minutes) despite sufficient time for progression through the first meiotic division (red arrow). *Misaligned*: Chromosomes failed to align correctly into a metaphase plate, resulting in an inability to progress through further stages of meiosis (green arrows). *Missegregated*: Oocytes extruded all chromosomal content into the PB during division, resulting in aneuploidy (blue arrow). Time stamps (in minutes) indicate the progression of meiosis, starting at 0 (prophase/metaphase onset) and ending at 1020 minutes. Scale bar = 5 $\mu$ m.

#### 4.3.2.1. *Quantitative Analysis of Phenotypes*

To confirm the phenotypes observed (Figure 4.2.) quantitative assessment of live imaging data was performed (Figure 4.3.). The overall success rate of the cells and their ability to progress through meiosis was quantified by investigation of various aspects of meiosis. For example, the ability to form a metaphase plate was quantified (Figure 4.3.Bi) and showed that 88.9% of control cells were able to reach metaphase in Meiosis I. In contrast, only 50% of knockdown cells reached metaphase, suggesting that the removal of Ki67 protein has a detrimental effect on the ability of cells to progress through meiosis.

To investigate this potential effect of Ki67 removal, the ability to progress through Meiosis I and successfully produce a PB was quantified (Figure 4.3.Bii). This showed that 85.7% of control cells progressed through meiosis and formed a polar body, whereas only 47.7% of knockdown cells were able to do so. This opened up further investigation into the quality of the divisions that did occur. As the Ki67 knockdown appeared to impact meiotic progression, the next step was to assess cell division outcome. Of those that *did* manage to divide (Ctrl=18, KD=10) they were categorised as either 'faithful' segregation – meaning the chromosomes were apparently split evenly between the PB and oocyte, or 'Unfaithful' segregation – meaning the chromosomes were either apparently split unequally between the PB and oocyte, or in fact all the DNA content was extruded into the PB. The results showed that 75% of the control oocytes underwent 'faithful' segregation and only 62.5% of knockdown oocytes.

Of the cells that were able to divide, the timing for the two groups from GVBD to anaphase was compared to determine if there was a delay in meiosis that might result in the phenotypes seen. When comparing all the cells that divided, regardless of whether the division was ‘faithful’ or ‘unfaithful’, there was a slight decrease in the time spent in meiosis for Ki67 KD cells (CTRL=520.8, KD=471.3, Figure 4.3.v). However, when reviewing only the cells that ‘faithfully’ divided, the timing for GVBD to anaphase did not differ (CTRL=532.8, KD=512.0, Figure 4.3.iv), which seems to be in line with expectations that when the division is successful, the cells spend a comparable amount of time in meiosis to pass all of the progression checkpoints successfully.

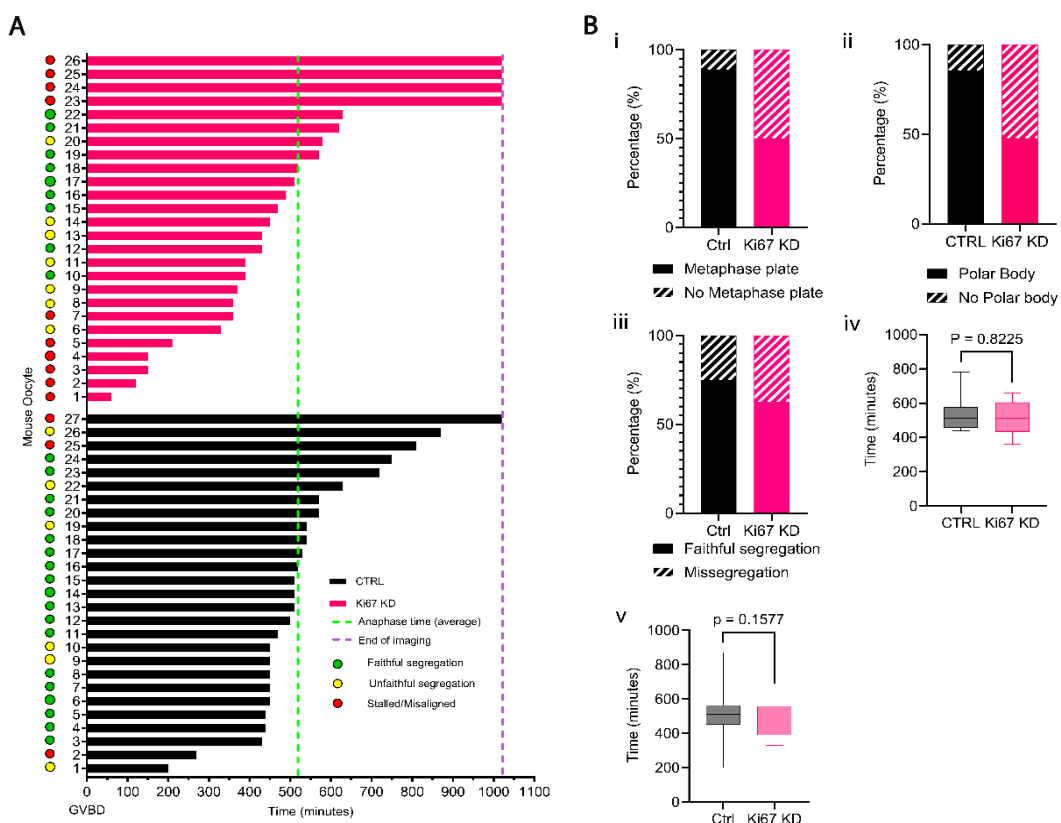


**Figure 4.3. Quantitative analysis of meiotic progression phenotypes following Ki67 knockdown.** (A) Live imaging analysis showing the progression of mouse oocytes through meiosis. The time from germinal vesicle breakdown (GVBD) to polar body (PB) extrusion or imaging endpoint (1020 minutes) is plotted

for each oocyte (CTRL, black; Ki67 KD, pink). Cells are classified as: Faithful segregation: Green circles. Unfaithful segregation: Yellow circles. Stalled/misaligned: Red circles. The green dotted line indicates the average timing of anaphase onset (calculated from CTRL 'faithful' cells), and the purple dashed line marks the imaging endpoint. (B) Quantitative analysis of meiotic progression phenotypes: (i) Bar plot showing the percentage of cells forming a metaphase plate. 89% of CTRL oocytes achieved metaphase, compared to 50% in Ki67 KD oocytes (CTRL N = 27, KD N = 26). (ii) Percentage of oocytes extruding a PB. 85% of CTRL cells successfully formed a PB, compared to 48% of KD cells. (CTRL N= 18, KD N=10) (iii) Comparison of chromosomal segregation during PB extrusion. 75% of CTRL cells exhibited faithful segregation, while 62.5% of KD cells showed missegregation (CTRL N=18, KD N=10). (iv) Box plot showing the time from GVBD to PB formation for successfully dividing cells (CTRL N = 18, KD N = 10). No significant difference was observed ( $p = 0.8225$ ). (v) Box plot showing the time from GVBD to PB formation for all dividing cells (faithful or unfaithful; CTRL N=27, KD N=26). No significant difference was observed ( $p = 0.1577$ ). Error bars in (iv) and (v) represent the interquartile range, and statistical significance was determined using a two-tailed unpaired t-test.

#### 4.3.2.2. 3D segmentation of live-imaging data to assess meiotic defects

A course-grain analysis of live-imaging data revealed a significant impact of Ki67 depletion on meiotic progression. We next applied 3D segmentation to better study potential oocyte defects. The chromosomes from live-imaging data were modelled using AMIRA software to determine, quantitatively, whether the depletion of Ki67 influenced chromosome microenvironment.

To assess chromosome number as accurately as possible, prometaphase was selected as the point of chromosome modelling as this was demonstrably the stage where chromosomes were most dispersed and readily quantified in control cells (Figure 4.4.A). The knockdown oocytes showed a significant decrease in the number of individual chromosomes present at this stage, with control cells having an average of  $15.75 \pm 3$  chromosomes visible compared to only  $7 \pm 8.5$  in knockdown cells (Figure 4.4.B). We assume that ploidy is intact (as

this is a pre-division analysis), however, a decreased ability to count, could indicate that depletion of Ki67 does affect the formation of individualised chromosome structures similar to that seen previously in mitotic cells, indicating an increased tendency to ‘clump’ into abnormal structures (Booth et al., 2016; Cuylen et al., 2016). It was considered that an impact to chromosome geometry could also contribute to these findings (such as changes in volume), however this was beyond the resolution capabilities of standard confocal and therefore addressed with advanced imaging approaches (Section 4.3.4).

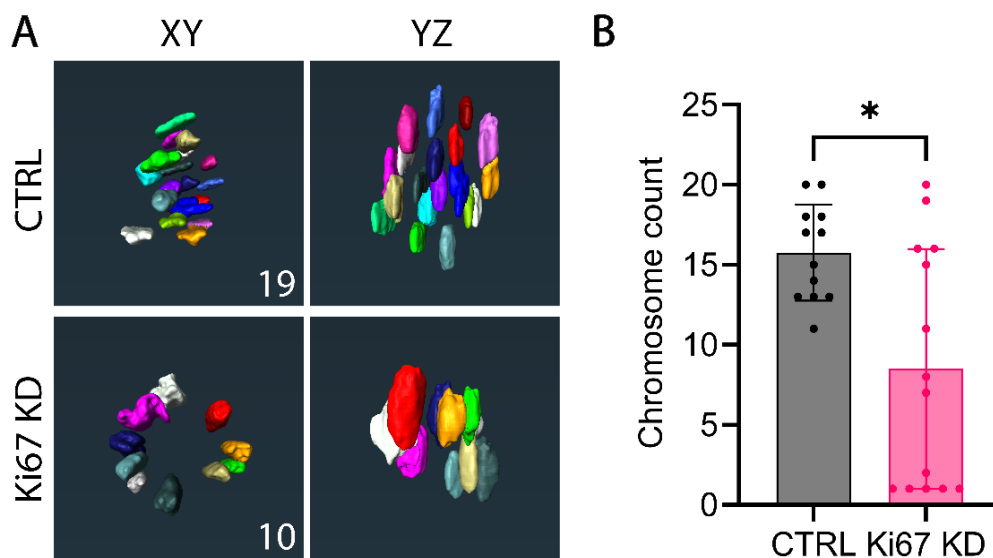


**Figure 4.4. Quantification of chromosome count in control and Ki67 knockdown oocytes.** (A) 3D-rendered chromosome models from control (CTRL, top) and Ki67 knockdown (KD, bottom) oocytes, visualised in two orientations: XY (left) and YZ (right). Chromosomes are colour-coded to distinguish individual structures. The total chromosome count for each condition is displayed in the bottom right corner of the panels (19 for CTRL and 10 for KD). (B) Bar plot showing the quantification of chromosome count in CTRL and Ki67 KD oocytes (CTRL N=12, KD N=14). Each dot represents an individual oocyte. The average chromosome count was significantly reduced in Ki67 KD oocytes compared to controls ( $p < 0.05$ , unpaired t-test). Error bars represent the standard deviation.

#### 4.3.2.3. *Chromosome dynamics*

The reduced chromosome quantity and delayed progression through meiosis suggested that there may be changes in chromosome organisation and dynamics. Live imaging data provided an opportunity to investigate the chromosome displacement throughout meiosis, modelling the whole chromosome complement and tracking the centroid of the complement over time (Figure 4.5.A).

With the chromosome complements modelled, the centroid of this area could be identified and measured over each time point to monitor the distance the chromosomes were displaced throughout imaging. Interestingly, issues seen with chromosome individualisation (Figure 4.4.) didn't appear to have any effect on overall chromosome dynamics in the cells that managed to progress past metaphase. Dynamic analysis of the cells that arrested during meiosis was uninformative as the chromosomes did not progress and therefore clearly did not move during imaging. Displacement of chromosomes was measured in all of the cells that managed to divide within imaging time regardless of any abnormalities (Figure 4.5.Bi), which showed no significant difference between the two groups in terms of cumulative distance travelled from NEBD to PB formation. When only the cells that 'faithfully' divided were compared, there was an increase in the average distance travelled by the chromosomes through Meiosis I. However, this difference between control ( $41.18\mu\text{m} \pm 15.84$ ) and knockdown ( $50.75\mu\text{m} \pm 20.80$ ) cells was still not significantly different. This showed that the structural abnormalities that affect chromosome segregation did not affect the movement of the chromosomes throughout the oocyte.

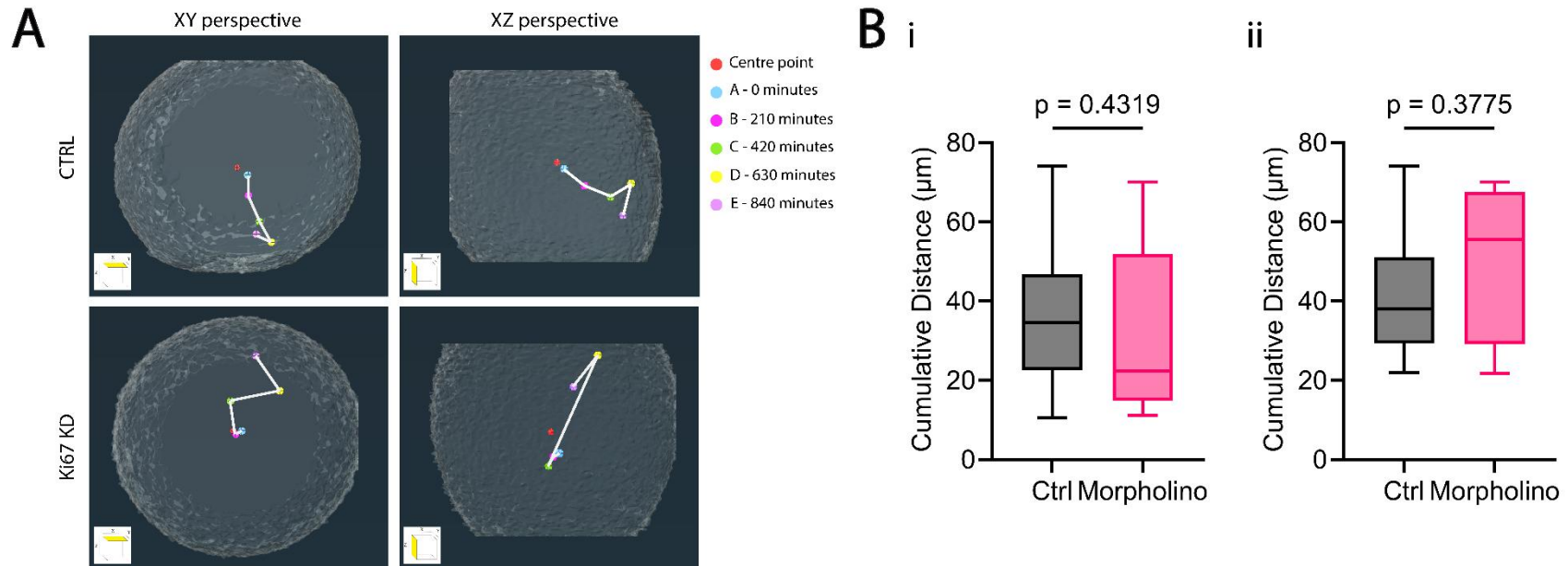


**Figure 4.5. Chromosome displacement analysis in control and *Ki67* knockdown oocytes.** (A) Representative 3D tracks of chromosome complement displacement in control (CTRL, top) and *Ki67* knockdown (KD, bottom) oocytes, visualised from two perspectives: XY (left) and XZ (right). Tracks represent the movement of the chromosome centroid over time, with colour-coded markers indicating time points: red (0 minutes), blue (210 minutes), green (420 minutes), yellow (630 minutes), and purple (840 minutes). The centre point is marked in red at the start of imaging. Scale bars: 10  $\mu\text{m}$ . (B) Cumulative chromosome displacement measurements: (i) Box plot of cumulative displacement in all oocytes that successfully underwent meiosis. (ii) Box plot of cumulative displacement in only the oocytes that exhibited faithful chromosome segregation. No significant differences were observed between CTRL and KD groups in either case ( $p = 0.4319$  and  $p = 0.3775$ , respectively; unpaired t-test). Error bars represent the interquartile range

#### 4.3.2.4. *Abnormal polar body extrusion following Ki67 depletion*

Although there was no significant variation in overall chromosome dynamics, there was a specific abnormality that was noted - the directionality of the polar body extrusion (Figure 4.6.B). In control cells, the polar body was mostly extruded from the side of the oocyte (80%), with only 12% being extruded through the bottom (against the glass dish) and 8% through the top (Figure 4.6.A). In comparison, when the knockdown cells were analysed, only 57% of PBs were extruded from the side of the cell, and 37% were extruded through the top and 6% through the bottom.

Therefore, it's possible that the removal of the periphery and consequential abnormalities in the chromosome structure causes issues in the spindle organisation. However, this is contradictory to the displacement data, which showed no change in the amount of movement by the cells. Therefore, this abnormal PB extrusion has no identifiable reason for being altered due to chromosome periphery removal. Consequently, it's possible that Ki67 specifically is the cause of this abnormality rather than the periphery, and the interaction of Ki67 with other proteins and complexes is what caused this PB extrusion abnormality. Additionally, it could be that gross abnormalities to chromosome morphology, or indeed other defects, unobservable and beyond the resolution of the present confocal imaging techniques could be impacting polar body directionality. This could only be explored using more advanced imaging approaches.

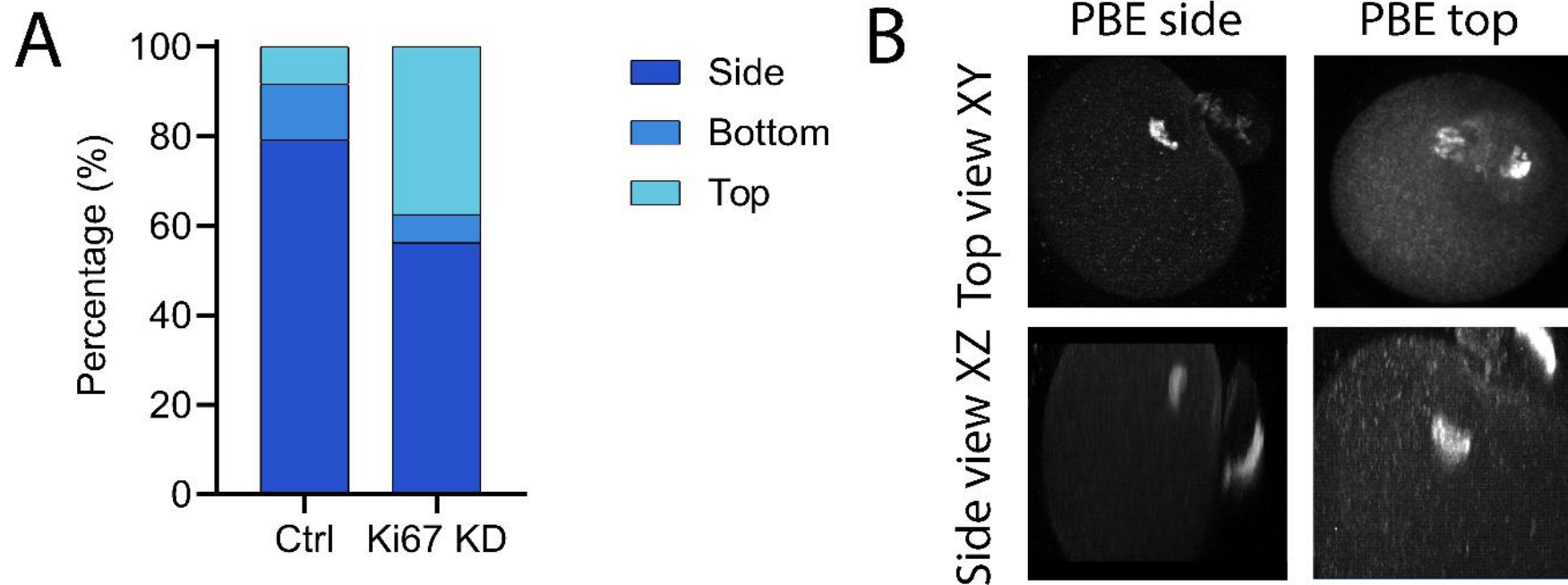


**Figure 4.6. Polar Body extrusion directionality in control and Ki67 knockdown oocytes.** (A) Stacked bar graph showing the percentage distribution of polar body extrusion (PBE) directionality in control (CTRL) and Ki67 knockdown (KD) oocytes. Extrusion through the side (dark blue) was the predominant direction in CTRL oocytes (~80%), while KD oocytes exhibited increased extrusion through the top (light blue) and bottom (medium blue) of the oocyte. (B) Representative images illustrating PBE directionality in CTRL and KD oocytes, stained with SiR-DNA. PBE Side: Images (top: XY view; bottom: XZ side view) show polar body extrusion occurring laterally (side). PBE Top: Images (top: XY view; bottom: XZ side view) show polar body extrusion occurring through the apical (top) region of the oocyte. Scale bars - 10  $\mu$ m. These findings highlight abnormal polar body extrusion directionality in Ki67 KD oocytes, with a reduced preference for lateral extrusion compared to CTRL oocytes.

### 4.3.3. Super-resolution light microscopy to investigate chromosome changes following Ki67 depletion

#### 4.3.3.1. *Super-resolution light microscopy of fixed mouse oocytes confirms altered phenotypes following Ki67 knockdown*

To investigate the role of Ki67 in maintaining chromosomal organisation during meiosis, high-resolution light microscopy was performed as the initial step in the correlative light and electron microscopy (3D-CLEM) workflow. Mouse oocytes from both CTRL and KD groups were observed using sir-DNA to monitor meiotic progression and fixed when the control samples reached metaphase (7 hours post release). The oocytes were then stained with DAPI for optimal chromosome visualisation and imaged using super-resolution confocal microscopy.

As shown in Figure 4.7.A, max projection images reveal the chromosomal organisation differences between the CTRL and KD oocytes. In the CTRL group, chromosomes appeared compact and evenly distributed, forming well-defined metaphase plates (which was confirmed with 3D projections of the LM data to view the chromosomes from all angles). In contrast, the KD oocytes display irregular chromosomal arrangements. In two of the cells, there was a misaligned chromosome; in one, there was obvious clumping of chromosomes, and of all five, only one cell was able to achieve metaphase alignment supporting the 'stalled' phenotype witnessed in the live imaging (Figure 4.7.B). These abnormalities are consistent with the hypothesis that Ki67 is crucial for chromosome periphery formation and ensuring chromosomal fidelity.

The use of high-resolution LM enabled the visualisation of individual chromosomes and the identification of positions within the cell. This was essential for correlating with the EM data, as it allowed for imaging the chromosomes with high spatial resolution to investigate the phenotypic variations between the two groups. This LM dataset confirmed the presence of the abnormalities that occur in oocytes when the periphery is depleted, reiterating the findings via live imaging. This approach allowed us to sample and select specific cells of interest with a representative phenotype, to be imaged using EM and modelled for ultrastructural investigation.

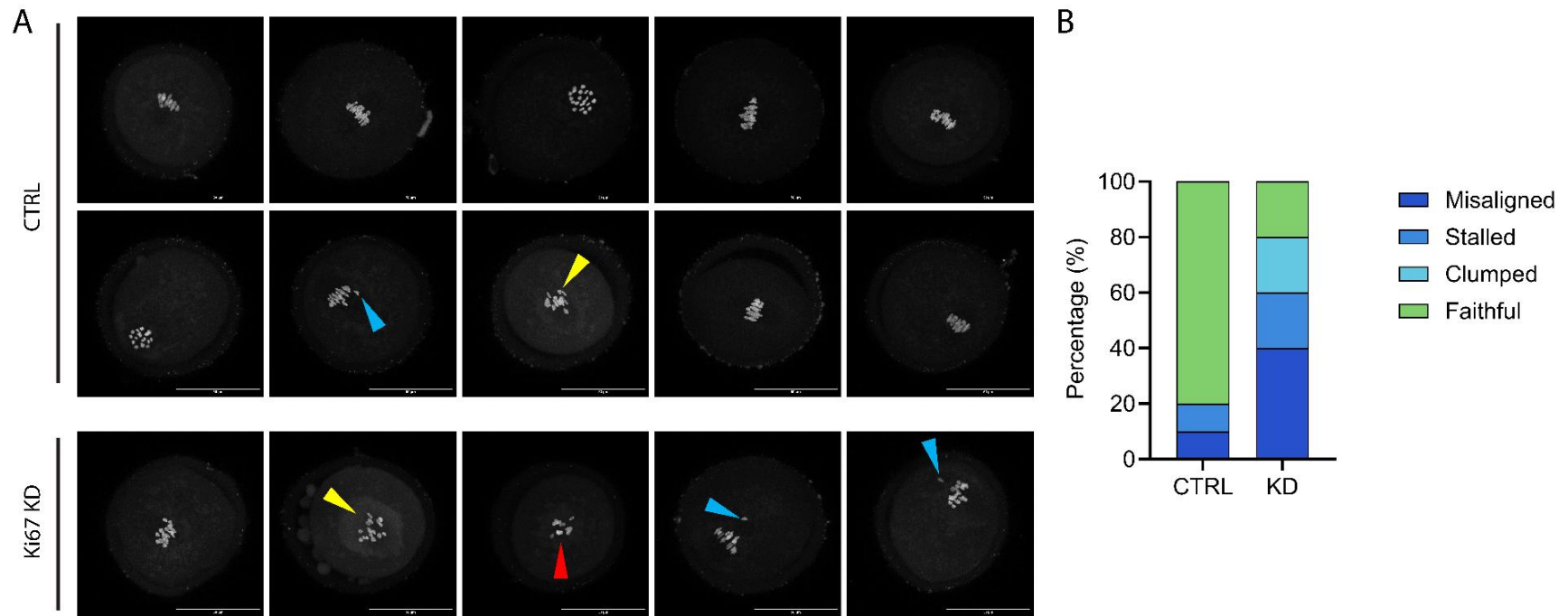


**Figure 4.7. Maximum projection images of chromosomes in mouse oocytes under control and *Ki67* knockdown conditions.** (A) Representative maximal projection images of mouse oocytes stained with DAPI to visualise chromosomal DNA. Oocytes from control (CTRL, top panels) and *Ki67* knockdown (KD, bottom panels). LM was imaged using a Zeiss LSM 900 (100× oil immersion objective). The images illustrate chromosomal organisation and alignment at metaphase. In CTRL oocytes, chromosomes appear compact, evenly distributed, and aligned along a well-defined metaphase plate. In KD oocytes, chromosomes exhibit abnormalities, including misaligned (blue arrow), stalled (yellow arrow) and clumping (red arrow), consistent with disrupted chromosomal structure and organisation. Scale bars - 10  $\mu$ m. (B) Graph showing the percentage of oocytes that displayed abnormal phenotypes (CTRL N=10, KD N=5).

#### 4.3.3.2. *Super-resolution LM Fixed Modelling reveals structural chromosome changes following Ki67 depletion*

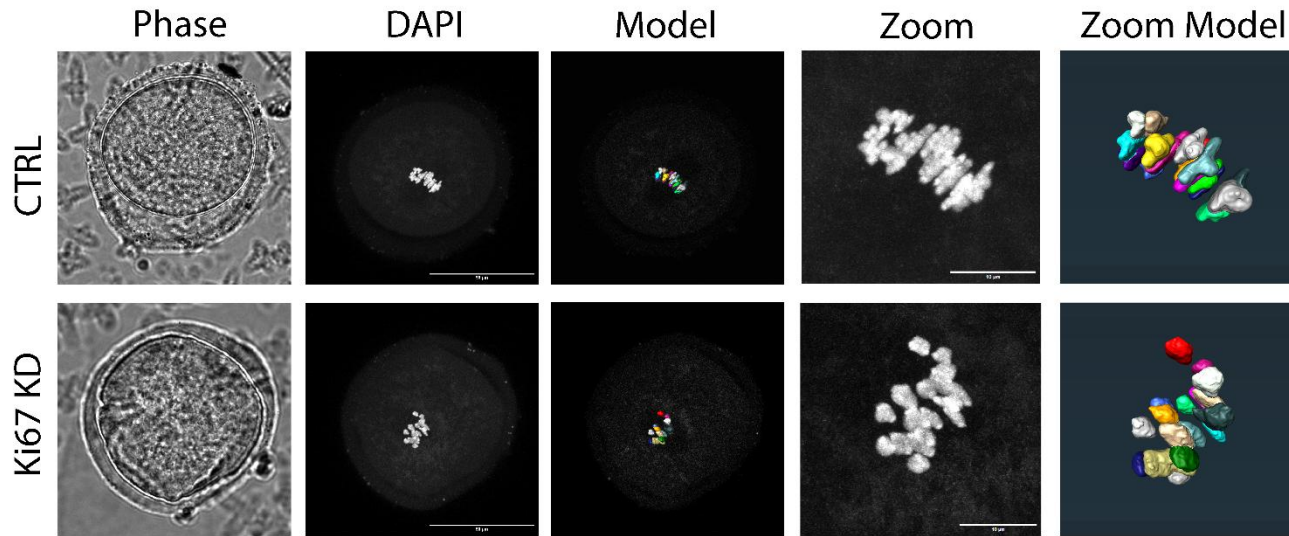
To investigate the ultrastructure of chromosomes in these meiotic cells, the 3D-CLEM pipeline was also applied to CTRL and KD cells. These cells were fixed at metaphase, as the live imaging data indicated that the majority of both cell conditions would at least progress to this stage. This was, therefore, considered a late enough stage to see abnormalities that may arise from the Ki67 depletion whilst also ensuring the cells were still 'alive'. The cell was synchronised with their release using a washout (methods 2.2.2) and the staging was monitored and determined from the control group of cells.

Z-stacks of the cells were taken using the LSM900 for super-resolution, and from these images, the chromosomes were modelled and segmented (Figure 4.8.A). This gave some initial insight into the effect of periphery removal on chromosome morphology. Geometric analysis of the chromosomes showed that there was no significant difference between the CTRL vs KD for chromosome sphericity (0.527 vs 0.546), mean width (2.5 $\mu\text{m}$  vs 2.6 $\mu\text{m}$ ), mean volume (12.7 $\mu\text{m}^3$  vs 13.6 $\mu\text{m}^3$ ), or mean surface area (46.9 $\mu\text{m}^2$  vs 49.56 $\mu\text{m}^2$ ) (Figure 4.8.C ii-v). However, the mean length of the chromosomes did vary significantly between the two groups (5.1 $\mu\text{m}$  vs 4.4 $\mu\text{m}$ ; Figure 4.8.Ci). This statistically significant variation ( $p < 0.001$ ) in chromosome length indicates that the loss of the chromosome periphery does disturb the standard chromosome morphology; however, the lack of significant differences in any of the other geometric measurements, particularly the width and volume of the chromosomes, doesn't support the theory that the chromosomes are clumping and forming aggregates.

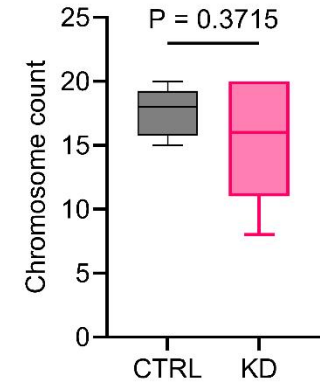
This was also supported by the chromosome counts from the segmented 3D models, which showed no significant difference between CTRL and KD sample types (Figure 4.8.B). This could be in part due to the shorter incubation time with the Ki67 morpholino, which was applied to enable the imaging of the chromosomes during metaphase and prior to cell death, which would have been much more difficult with a longer Ki67 KD. However, this reduced Ki67 KD, while less harsh, to enable imaging while cells were still alive, may have also been less informative.

Despite super-resolution LM providing further insights into the chromosome structure for both CTRL and Ki67 KD oocytes, precise geometry quantifications of the chromosome ultrastructure could not be achieved without EM. In order to understand these variations in further detail and to gain precise geometric data on the individual chromosomes, relative to one another and indeed potentially other cell structures, the oocytes were retained and processed for 3D-CLEM and reconstructions of the EM images were analysed.

**A**



**B**



**C**

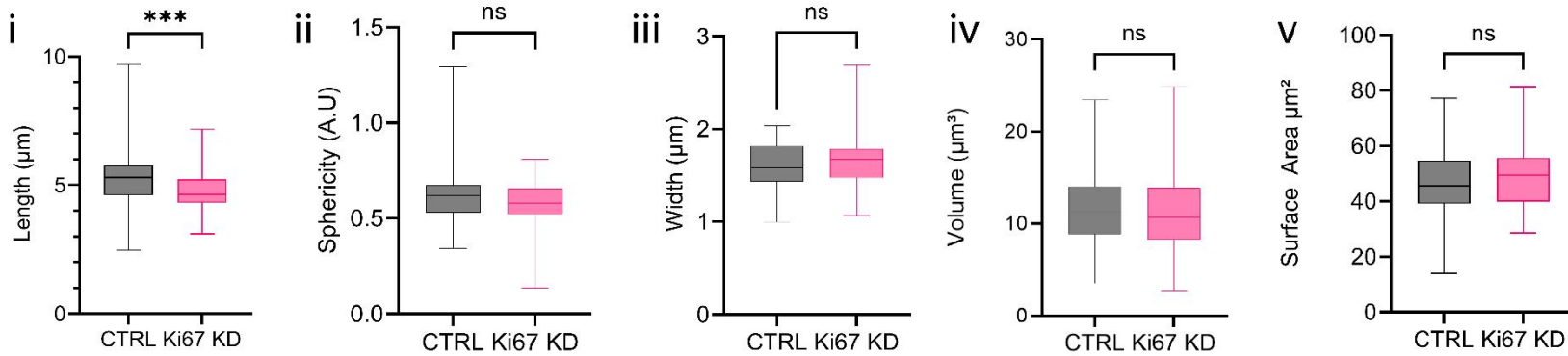


**Figure 4.8. Super-resolution microscopy of fixed oocytes.** (A) Representative images of fixed mouse oocytes imaged using phase contrast and fluorescence imaging with the Zeiss LSM900 to visualise the chromosomes stained with DAPI. Overviews of the whole oocyte and zooms of the chromosome regions along with the segmented chromosome complement models. (B) Chromosome counts from AMIRA models of LM z-stacks. (C) Geometric analysis of chromosome segmentation data, including length, sphericity, width, volume and surface area of individual chromosomes, comparing control (N=7 oocytes) and Ki67 KD (N=7 oocytes) cells. Scale bar = 10 $\mu$ m.

#### 4.3.4. Electron microscopy to study ultrastructural chromosome changes following Ki67 depletion

##### 4.3.4.1. *EM imaging confirms the removal of the chromosome periphery following Ki67 depletion*

Representative SEM images of CTRL and KD oocytes (Figure 4.8.A) reveal differences in chromosomal ultrastructure. In the CTRL oocytes, the chromosomes have a relatively uniform appearance, whereas in KD oocytes, the chromosomes have a more irregular appearance. Although the periphery is not visible to the eye with SEM resolution, this suggests a disruption of the periphery. To test if, like our lab's previous EM work has shown (albeit using TEM), periphery loss is detectable, greyscale intensity analysis was employed as an indirect method for assessment.

Greyscale intensity measurements were taken using line scans extending from the cytoplasm into the chromosome (Figure 4.9.Ai-ii). This approach enabled the quantification of greyscale density changes (Figure 4.9.B). Normalised greyscale intensity profiles revealed a significantly steeper gradient in KD oocytes than seen in the CTRL sample (CTRL slope= -2.221, KD slope= -2.788,  $p < 0.0001$ ). This steeper decline in intensity indicates a more sudden transition in the greyscale values between the chromosome and cytoplasm, supporting the loss of chromosomal peripheral density in KD oocytes. This indicated that Ki67 depletion from the oocytes removed the periphery from the chromosome surface, confirming the role of Ki67 in periphery formation in meiosis.

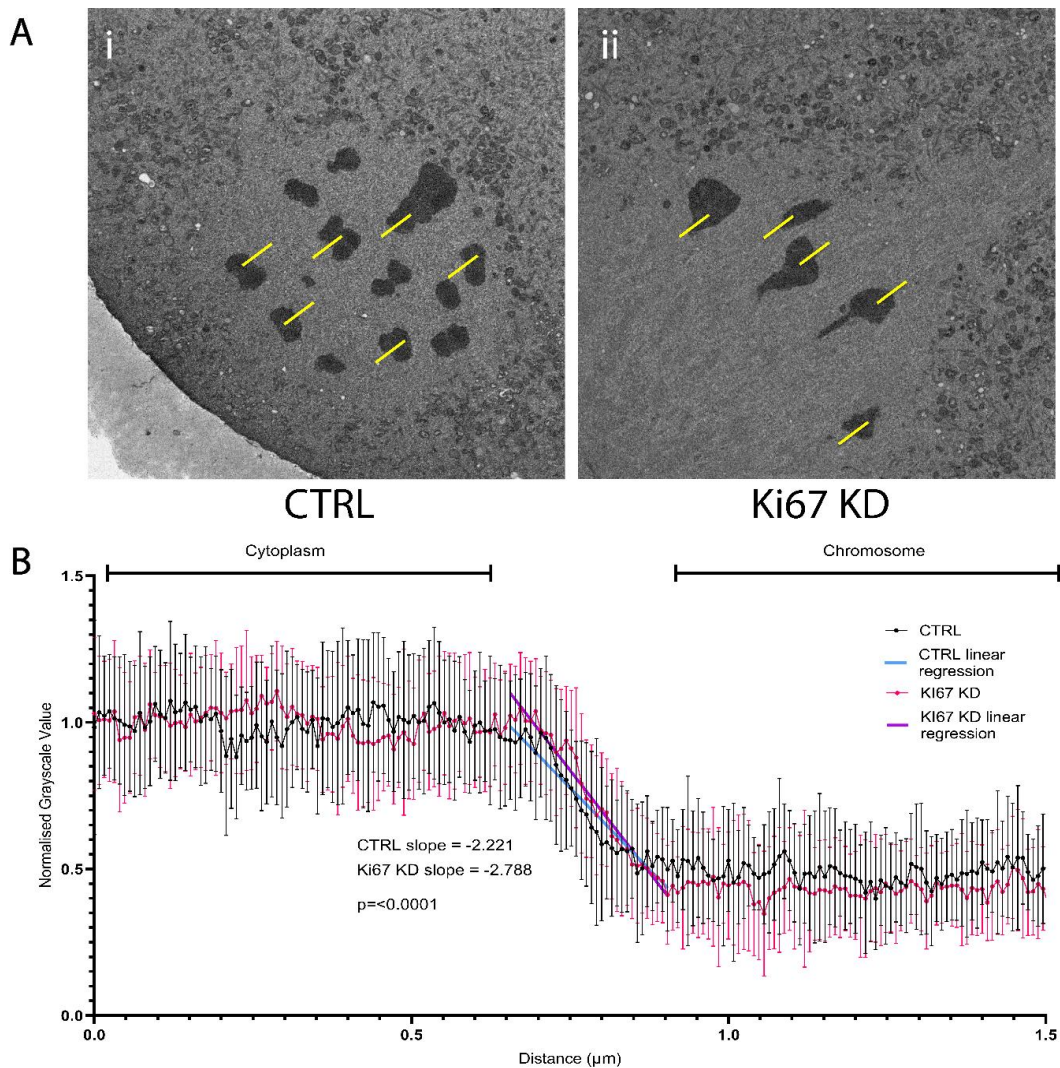


**Figure 4.9. Comparative line scan analysis of chromosomal periphery in control and Ki67 knockdown oocytes.** (A) Representative SE images of control CTRL (Ai) and Ki67 KD (Aii) oocytes. Yellow lines indicate representative line measurements taken from the cytoplasm into the chromosome for greyscale intensity analysis. (B) Greyscale intensity plots generated from 25 line-measurements per condition were normalised to cytoplasmic values. Linear regression analysis revealed a significantly steeper gradient in Ki67 KD cells (slope = -2.788) compared to control cells (slope = -2.221;  $p < 0.0001$ , ANCOVA), indicating effective removal of the chromosome periphery in Ki67 KD oocytes.

#### 4.3.4.2. *Segmentation of 3D chromosome structures*

To investigate the impact of Ki67 knockdown on chromosome morphology and organisation in meiotic cells, the complete 3D-CLEM pipeline was applied to the mouse oocytes that had been fixed and imaged using super-resolution light microscopy (Section 4.3.2.).

The CTRL and KD cell were successfully imaged using LM and EM and correlated to confirm the tracking of the same cell through the 3D-CLEM pipeline (Figure 4.10.A/B i-vi). The EM datasets were used to generate high-resolution 3D reconstructions of the chromosome complements in both CTRL and KD oocytes (Figure 4.10.C-D). Figure 4.10.C-Dii-iii displays the full chromosomal reconstructions and segmentations of individual chromosomes. Segmentation was colour-coded to distinguish between chromosomes, providing insights into their spatial arrangement and organisation and matching with the karyotype image for specific referencing (Figure 4.11). The models are shown in multiple orientations to display the alignment of the chromosomes from various perspectives, Figure 4.10.C-Dii displays the metaphase alignment. Figure 4.10.C-Diii shows the birds-eye view of the metaphase plate, and Figure 4.10.C-Div-v show the side perspectives of the models.

In the CTRL oocytes, chromosomes appeared compact, clearly defined, and evenly aligned along a single plane, consistent with expected metaphase organisation. In comparison, KD oocyte chromosomes appeared less uniform, were misaligned, and clumped, indicative of structural abnormalities (Figure 4.7.D). The KD chromosomes also appeared to be not yet fully aligned along the

metaphase plate, indicating a delay in meiotic progression similar to that observed during live imaging.

Magnified views of individual chromosomes (Figure 4.10.C-Dvi-viii) revealed differences in surface morphology. KD chromosomes often showed irregular structures, suggesting a loss of structural integrity following periphery loss. The combination of LM and EM data enabled a comprehensive analysis of chromosomal morphology and organisation in oocytes. From these 3D chromosome reconstructions, geometric analysis of the chromosome structures in the two groups could be performed.

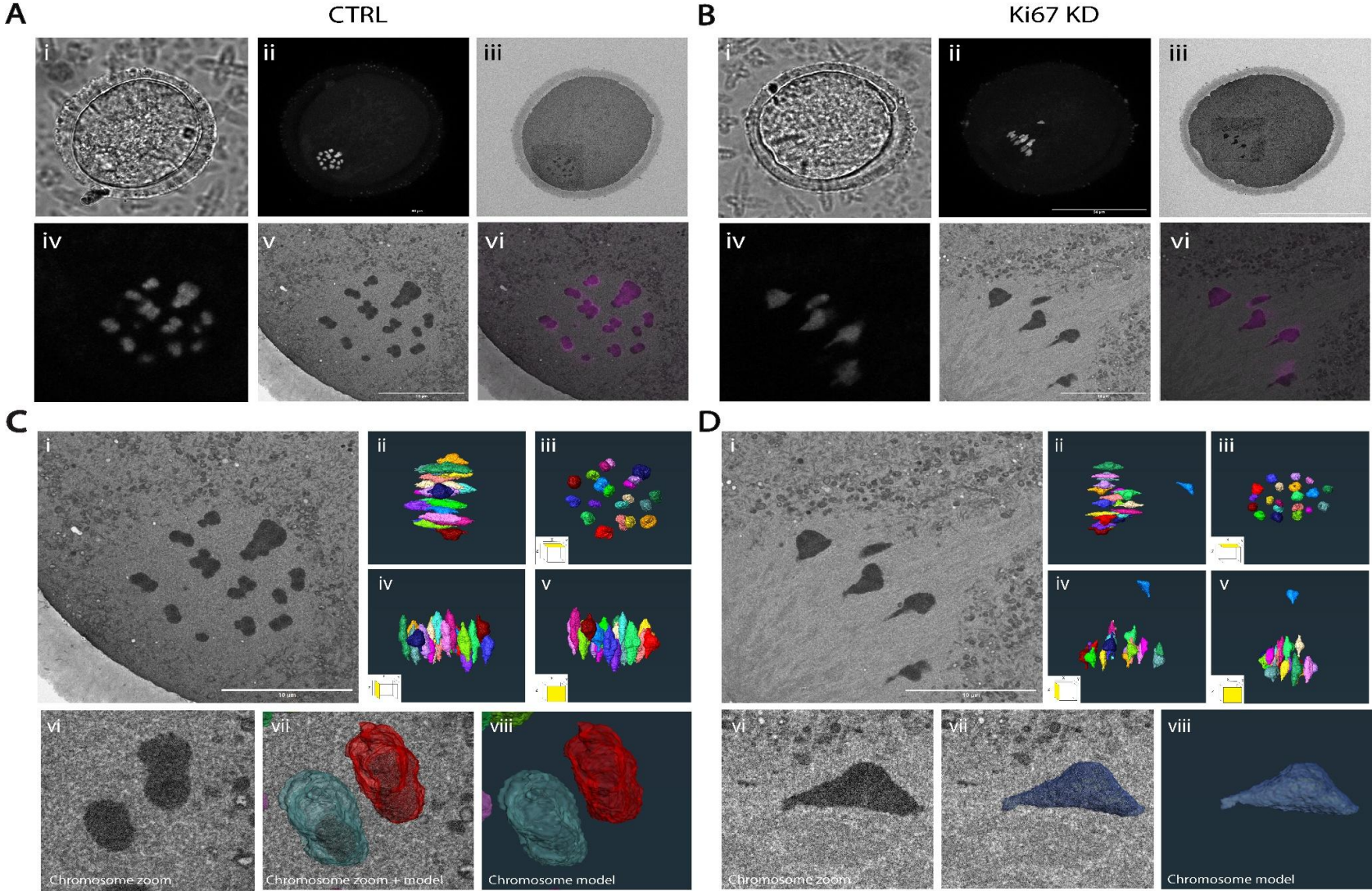


**Figure 4.10. Impact of Ki67 knockdown on chromosome morphology and organisation.** (A-B) Representative images of control (CTRL; A) and Ki67 knockdown (KD; B) oocytes at metaphase. Panels (i-iii) show differential interference contrast (DIC) imaging (i), light microscopy (LM) imaging of chromosomes stained with DAPI (ii), and correlative electron microscopy (EM) (iii). Higher-magnification views of the chromosomes are shown in fluorescence (iv), EM (v), and correlative fluorescence and EM overlays (vi). (C-D) 3D chromosomal reconstruction from control (C) and Ki67 knockdown (D) oocytes. Panels (i) show representative EM slices used for 3D reconstruction. Panels (ii-iii) illustrate reconstructed 3D chromosome models in full (ii) and individual chromosome segmentation (iii). Panels (iv-v) highlight chromosome segmentation in 3D models with colour coding to denote individual chromosomes. Chromosome zoom-ins show raw EM data (vi), EM overlaid with 3D models (vii), and isolated 3D chromosome models (viii). These results demonstrate distinct chromosomal ultrastructural differences between control and Ki67 knockdown oocytes, particularly in terms of chromosome compaction and surface morphology. Scale bars, where present, represent 10  $\mu\text{m}$ .

#### 4.3.4.3. *Quantitative Data from 3D chromosome models enables generation of meiotic chromosome karyotype*

The relationship between DNA content and chromosome structure was assessed by comparing chromosome volumes, compaction levels, and 3D karyotype reconstructions in CTRL and KD cells.

Scatter plots of chromosome volume against DNA content were generated for both CTRL and Ki67 KD cells (Figure 4.11.A-B). This was done under the published knowledge that Mbp and volume should be positively correlated in chromosomes as shown with 3D-CLEM modelling of prophase chromosomes (Booth et al., 2016). Therefore, the chromosome number could be estimated based on the relationship between the volume and Mbp. A linear correlation was observed in both conditions, as indicated by the regression lines and the  $R^2$  values, supporting the relationship. From this a karyotype of the CTRL and KD chromosomes could be determined. However, the similar volume and DNA content of the middle chromosomes meant that only the largest and smallest chromosomes could be confidently identified.

Chromosomal compaction was quantified as the ratio of DNA content to chromosome volume ( $\text{Mbp}/\mu\text{m}^3$ ). Box plot analyses (Figure 4.11.C) showed no significant difference in compaction between CTRL and Ki67 KD cells. These results indicated that overall chromosomal DNA density was maintained following Ki67 knockdown. However, the variation of compaction in the KD group was larger than that of the CTRL cells, which could indicate abnormalities in chromosome compaction following the loss of the periphery.

Chromosome models were colour-coded consistent with those seen in the whole chromosome complement and arranged in descending order of volume (Figure 4.11.D). The chromosome identities were assumed based on the identified relationship between volume and known DNA content. This data indicated that the relationship between chromosome volume and DNA content was preserved in CTRL and KD cells. Furthermore, chromosomal compaction remained consistent despite the increased variation in the KD group, indicating that Ki67 depletion did not significantly alter chromosomal DNA density or structural integrity. However, there were visible variations in the morphology between the two groups. Due to this analysis being conducted on a single CTRL and KD cell, it couldn't be conclusively attributed to the Ki67 depletion and require further investigation to be explored fully.

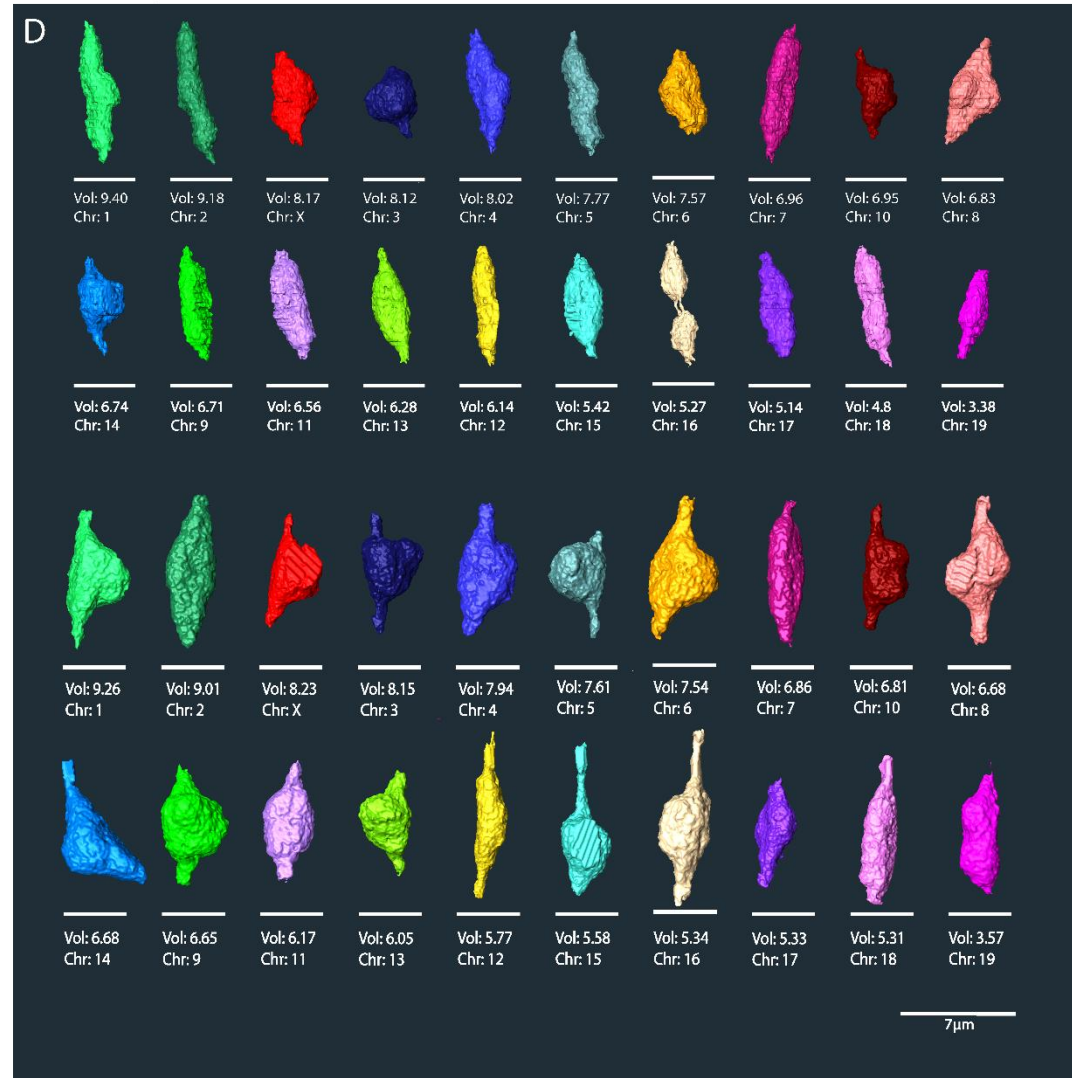
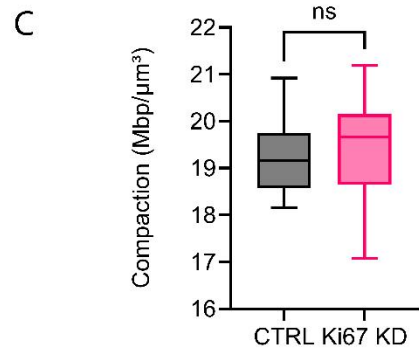
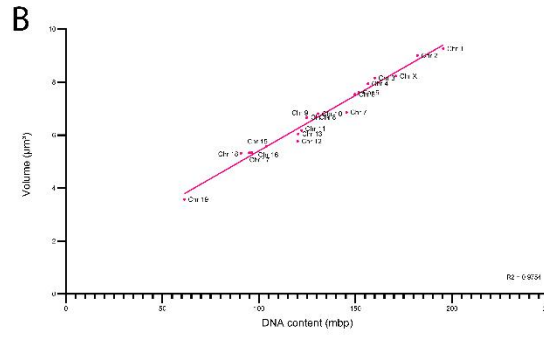
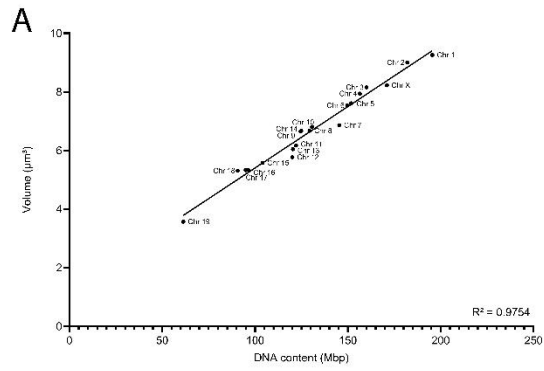


**Figure 4.11. Chromosome volume, DNA content, and 3D karyotype reconstruction in control and Ki67 knockdown cells.** (A, B) Scatter plots showing the relationship between DNA content (megabase pairs, Mbp) and chromosome volume ( $\mu\text{m}^3$ ) in control (CTRL; A) and Ki67 knockdown (KD; B) cells. Linear regression lines illustrate a positive correlation between DNA content and chromosome volume in both conditions, with  $R^2$  values indicating the consistency of this relationship. (C) Box plots comparing chromosomal compaction (measured as  $\text{Mbp}/\mu\text{m}^3$ ) between CTRL and KD cells. Data are presented as median, interquartile range, and minimum/maximum values. Statistical analysis reveals no significant difference in chromosomal compaction between conditions (ns: not significant). (D) 3D-rendered chromosome models from CTRL and KD cells, colour-coded by chromosome number and arranged by descending volume (Vol;  $\mu\text{m}^3$ ). The corresponding chromosome number is annotated beneath each model. The reconstructions reveal morphological differences and variations in chromosome volume between individual chromosomes. Scale bar =  $7 \mu\text{m}$ .

#### 4.3.4.4. *Spatial distribution of chromosomes altered in Ki67 depleted oocytes*

Following the successful segmentation and identification of individual chromosomes, the vEM data was then used to explore the spatial distribution of chromosomes within the oocyte. The individual chromosome models were analysed to evaluate the impact of KI67 KD on the relative positioning of chromosomes based on size. Chromosomal distances from the epicentre of the metaphase plate were measured in both 2D (X/Y) and 3D (X/Y/Z) perspectives, as shown in Figure 4.12. These analyses were informed by previous studies that report a general trend in mammalian cells, where smaller chromosomes tend to localise closer to the centre, while larger chromosomes are typically positioned towards the periphery, reflecting a size-dependent spatial organisation (Booth et al., 2016; Mosgöller et al., 1991; Takenouchi et al., 2024).

Metaphase chromosomes modelled using AMIRA and from the extracted geometric data were colour-coded by volume, with the largest 6 chromosomes depicted in red, and the smallest 6 chromosomes in blue, and the remaining chromosomes in grey. Concentric rings spaced 2 $\mu$ m apart were overlaid to facilitate the assessment of chromosome positioning (Figure 4.12.A). In CTRL cells, both large and small chromosomes exhibited a consistent radial distribution relative to the metaphase plate centre (Figure 4.12.Ai). In KD cells, however, small chromosomes appeared to be positioned further away from the centre compared to large chromosomes (Figure 4.12.Aii).

The distance from the chromosome centroid to the centre of the metaphase plate was measured in both 2D and 3D for each chromosome to

determine whether there was a statistical variation in the organisation of chromosomes. For both the 2D and 3D measurements, the large chromosomes showed no significant difference in radial positioning between CTRL and KD cells (Figure 4.12.Bi). In contrast, small chromosomes in KD cells were positioned significantly further from the metaphase plate centre compared to their counterparts in CTRL cells in both the 2D and 3D measurements, indicating a redistribution of these chromosomes towards the periphery of the metaphase plate periphery removal ( $p < 0.05$ , Figure 4.12.Bii).



*metaphase plate in CTRL and KD cells. Large chromosomes showed no significant difference in radial distribution (ns), while small chromosomes were positioned significantly further from the centre in KD cells compared to CTRL (\*,  $p < 0.05$ ). (C) Quantitative analysis of chromosome-to-centre distances for each individual chromosome in CTRL and KD cells. Bar plots represent the mean distance ( $\mu\text{m}$ ) for CTRL (i) and KD (ii) chromosomes, demonstrating consistent positioning for large chromosomes and an outward redistribution for small chromosomes in KD cells.*

#### 4.3.4.5. *Loss of the chromosome periphery pushes the limits of the exclusion zone*

Within dividing cells, the chromosomes and spindle are positioned within an exclusion zone (EZ) (Ferrandiz et al., 2022). The EZ is an area of the cell that is mostly free of intracellular organelles and membranes, and previous studies suggest that this EZ must be cleared for spindle formation and 'normal' functionality (Champion et al., 2019; Schlaitz et al., 2013; Schweizer et al., 2015). An observed anomaly in the oocyte 3D-CLEM images was the penetration of the chromosomes into the membranes surrounding the EZ. Figure 4.13 presents an ultrastructural analysis of chromosomes and associated mitochondria in CTRL and KD oocytes. In CTRL oocytes, chromosomes appear compact and well-defined, with no evidence of exclusion zone penetration, despite bordering the edge closely. In contrast, KD oocytes exhibit irregular chromosome morphology, with some chromosomes penetrating the exclusion zone boundary.

In CTRL oocytes, the chromosome does not encroach upon the exclusion zone with the membranes forming a linear surface that came close to but did not touch or surround the chromosome. However, in KD oocytes, the membranes appear disrupted, and the chromosome penetrates the exclusion zone's boundary with the membranes surrounding the chromosome, adjusting to the shape of it (Figure 4.13.). This indicated an abnormal interaction between the chromosome periphery and surrounding cytoplasmic membranes.

These findings suggest that Ki67 could be essential for maintaining the structural integrity of the chromosome periphery and its interactions with

surrounding membranes, indicating not only is the periphery essential for maintaining chromosome structure and preventing clumping but also acts as a surfactant to prevent ‘sticking’ to other organelles. The disruption of the periphery in KD oocytes likely contributes to the observed changes in membrane organisation and exclusion zone penetration. The combined EM imaging and 3D modelling defined the ultrastructural changes in chromosomes and the association with cytoplasmic membranes following Ki67 knockdown. The observed abnormalities highlight the essential role of Ki67 in preserving chromosomal organisation and cellular architecture during meiosis.

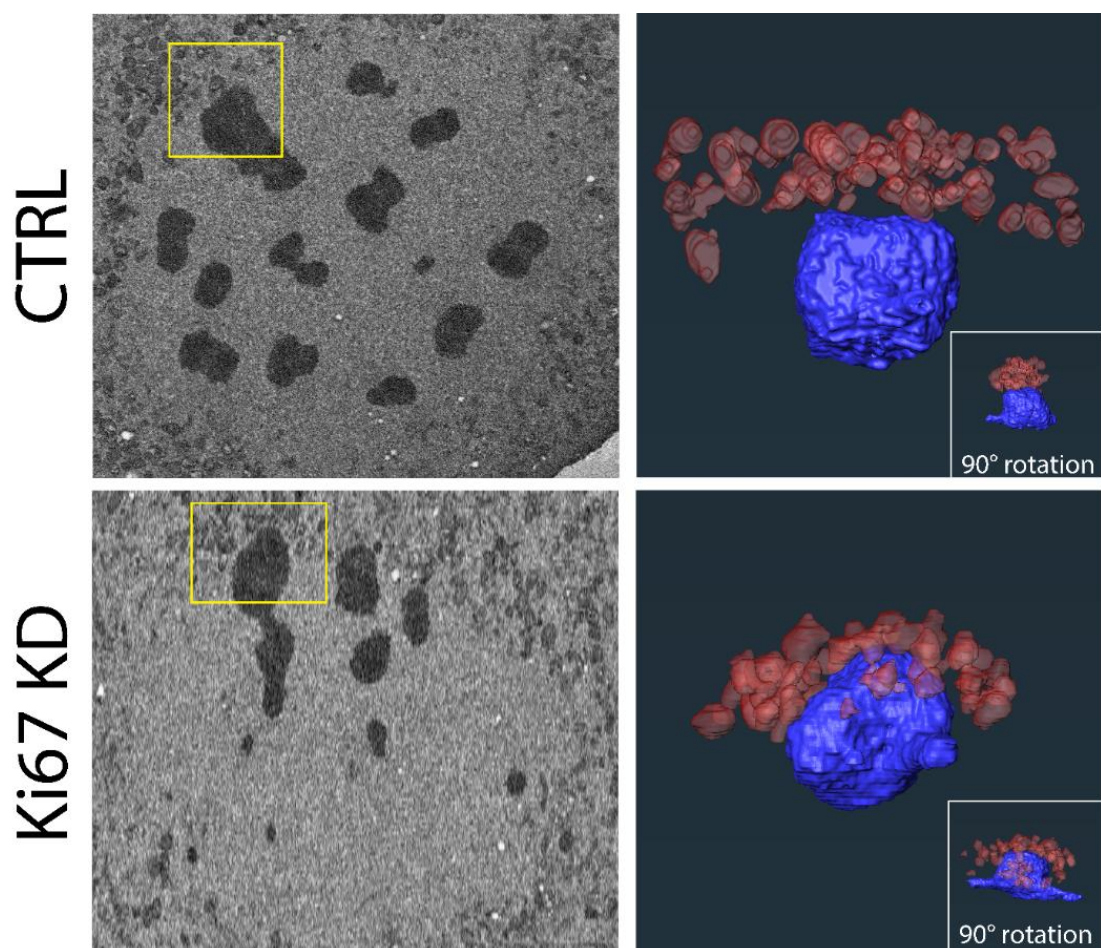


**Figure 4.13. Chromosomal positioning at the edge of the exclusion zone in control and Ki67 knockdown oocytes.** Left Panels: Representative electron microscopy (EM) images showing the chromosome closest to the exclusion zone edge in mouse oocytes from control (CTRL, top) and Ki67 knockdown (KD,

bottom) conditions. Yellow boxes highlight the regions of interest. Right Panels: Corresponding AMIRA 3D models of the highlighted chromosomes, with chromosomes represented in blue and membranes in red. Insets show 90° rotated perspectives of the models for better spatial visualisation. In Ki67 knockdown oocytes, chromosomes are observed penetrating the exclusion zone edge, a phenomenon not seen in control oocytes. These results suggest that Ki67 knockdown disrupts the spatial positioning of chromosomes relative to the exclusion zone, potentially impacting chromosome-membrane interactions.

#### 4.3.4.6. Comparison of LM and EM segmentation data reveals variations in quantitative results

Following the ultrastructural analysis, the LM and EM data were directly compared to assess the quality of the geometric data that could be extracted from each technique. Although this did not provide further insight into the effect of Ki67 on oocyte phenotypes, it did highlight the differences between the two datasets, further emphasising the need for ultrastructural and multi-modal imaging to quantify organelle geometry reliably. Figure 4.14 presents a quantitative analysis of chromosomal dimensions in CTRL and KD oocytes measured using LM and EM. Key parameters such as volume, sphericity, length, surface area, and width were evaluated to assess the effects of Ki67 depletion on chromosome morphology.

In the LM datasets, KD chromosomes displayed significant differences in several parameters compared to CTRL chromosomes. Chromosome volume and length were moderately increased in KD cells ( $p < 0.05$ ), while surface area also showed a significant increase ( $p < 0.01$ ). Conversely, chromosome width was reduced in KD cells ( $p < 0.001$ ). Sphericity measurements revealed no significant differences, suggesting that overall chromosomal shape was not drastically altered despite the size variations. These findings from the LM data indicate that

Ki67 knockdown affects chromosomal size and dimensions during meiosis, with changes that are detectable at the resolution of LM imaging.

EM provided a nm-resolution assessment of chromosomal dimensions. KD chromosomes displayed reduced sphericity compared to CTRL chromosomes ( $p < 0.0001$ ), indicating a significant deviation from the regular, rounded morphology observed in controls and contradicting the results observed by LM. The surface area was also significantly increased in KD chromosomes ( $p < 0.0001$ ), aligning with the LM findings. However, no significant changes were observed in chromosome volume, length, or width, suggesting that certain features identified by LM may be a result of limitations in resolution. The sphericity and surface area differences highlight structural abnormalities caused by Ki67 depletion. This was consistent with the hypothesis that the chromosome periphery plays a key role in maintaining chromosomal structure.

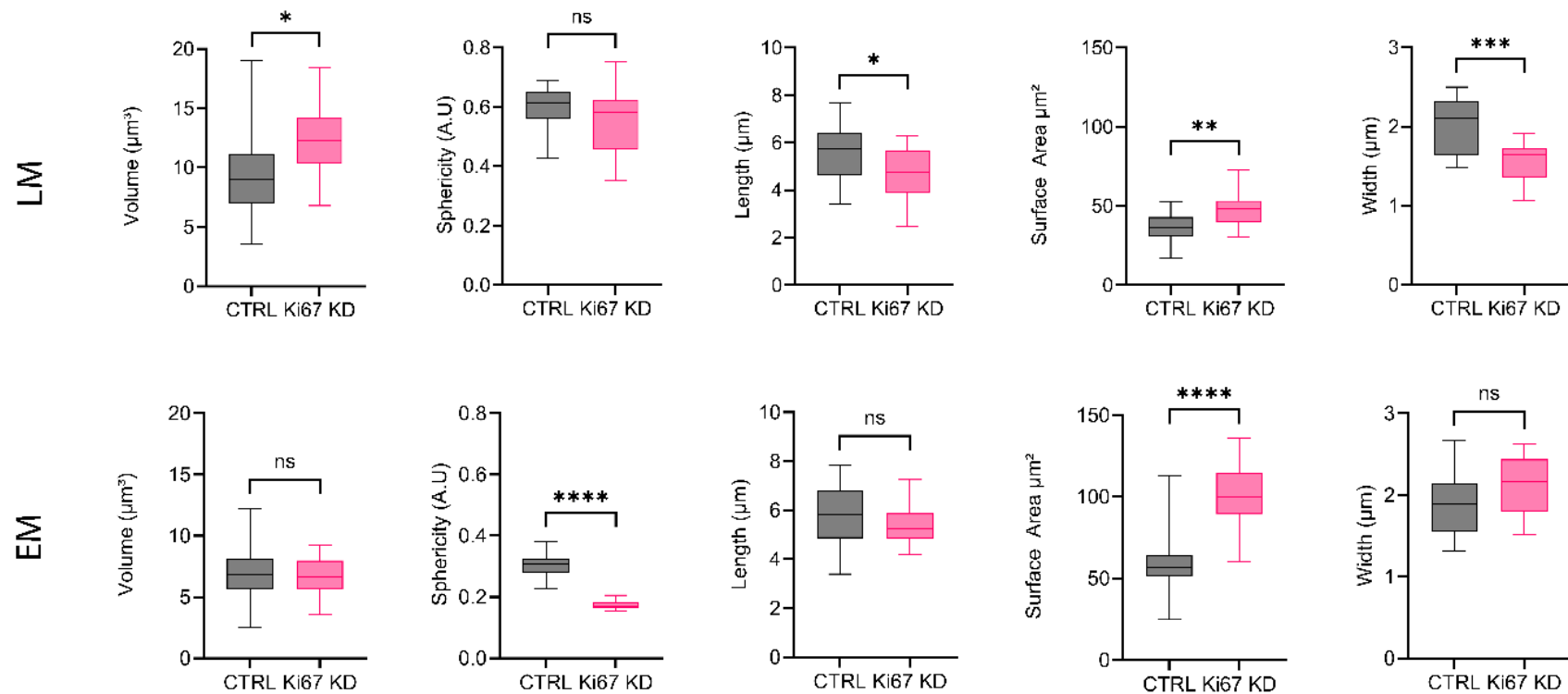


**Figure 4.14. Quantitative comparison of chromosomal dimensions in control and Ki67 knockdown oocytes.** Boxplots displaying key chromosomal parameters measured in control (CTRL, grey) and Ki67 knockdown (KD, pink) oocytes using light microscopy (LM, top row) and electron microscopy (EM, bottom row). (Top Row: LM Measurements). Chromosomes in KD oocytes exhibit increased volume ( $p < 0.05$ ), length ( $p < 0.05$ ), and surface area ( $p < 0.01$ ) compared to controls, alongside a significant reduction in width ( $p < 0.001$ ). No significant difference (ns) was observed in sphericity, suggesting that despite changes in size, the overall chromosomal shape remains largely consistent in LM analysis. (Bottom Row: EM Measurements). EM measurements reveal a significant reduction in sphericity ( $*p < 0.0001$ ) and an increase in surface area ( $*p < 0.0001$ ) in KD oocytes, indicating a loss of chromosomal structural integrity. No significant differences (ns) were detected in volume, length, or width between CTRL and KD groups at the higher resolution of EM imaging. These findings highlight the morphological abnormalities in KD

*chromosomes and underscore the complementary nature of LM and EM analyses in evaluating chromosomal structure. Statistical significance is indicated as follows: \* $p < 0.05$ , \*\* $p < 0.01$ , \*\*\* $p < 0.001$ , \*\*\*\* $p < 0.0001$ .*

## 4.4. Discussion

This chapter aimed to first and foremost confirm the presence of a chromosome periphery in oocytes and then explore the role of this periphery during meiosis. The periphery was confirmed to be present via immunofluorescence microscopy, which showed that Ki67 localises around the surface of meiotic chromosomes (Figure 4.1). This imaging also highlighted the novel asymmetric distribution of Ki67 in meiosis, which involved the retention of ~ two-thirds of the Ki67 within the oocyte. This was in contrast to the equal distribution of Ki67 observed in mitosis (Booth et al., 2014), and potentially identifies a mechanism in meiotic cells which retains Ki67 in the oocyte for future divisions following fertilisation rather than discarding it into the PB with the excess DNA content.

The role of Ki67 was then explored further within this chapter through functional analysis of Ki67 during meiosis via depletion studies. To achieve this goal mouse oocytes were analysed using, live imaging, super-resolution light microscopy and an adapted version of the 3D-CLEM pipeline, established in Chapter 3. Here, it was used as a method of exploring the role of Ki67 and the periphery during cell division. Our hypothesis was that the loss of Ki67 would result in periphery loss, consequently leading to altered chromosome fidelity. By applying advanced imaging, this chapter explored the structural and functional consequences of Ki67 knockdown in mouse oocytes, providing novel data that can be used to understand the poorly characterised chromosomal component.

This data supported the theory that Ki67 remained the organiser of the chromosome periphery in meiosis, and the periphery played an essential role in chromosome organisation. Live imaging was utilised to assess the progression of the oocytes through meiosis following loss of the CP. The live imaging was done as a separate component of the investigation into the meiotic chromosomes, as the oocytes were particularly sensitive to LM and required staining with antibodies (Ki67), meaning they had to be permeabilised, which is incompatible with the processing of samples for chemical EM fixation and embedding. The live imaging data displayed evident phenotypic variations between the control and Ki67 knockdown groups, which was then further supported by the quantitative analysis of meiotic progression. The phenotypes observed included missegregation, misalignment and stalled progression, all consistent with aneuploidy.

3D models of these oocytes were used to quantify chromosome number during metaphase (Figure 4.4) and showed a significant reduction in chromosome counts, indicating 'clumping'. This data supported the theory that the CP acts as an organiser of the chromosome structure, preventing 'clumping' of the chromosomes in the same way it does in mitotic cells (Booth et al., 2016). These abnormalities observed in the KD group also led to significantly fewer oocytes progressing past metaphase I (Figure 4.3.B), indicating that CP loss contributes to the halting of meiosis. This 'clumping' is something that has been shown to naturally occur in human oocytes, although the mechanism behind this has not yet been identified (Bongso et al., 1988). The 'clumping' of chromosomes was also observed in a few of the control mouse oocytes, although this may be in

part due to the variation in native Ki67 within the oocytes, as some of the control cells had such low levels of Ki67 that they were comparable to the KD oocytes. This also could have affected the efficacy of the morpholino KD as those with higher starting Ki67 KD levels may have shown a weaker phenotypic change. However, as mouse oocytes are more karyotypically stable than human oocytes, this observation is clearly a result of CP loss.

It is also important to be aware that the control cells of this study were not injected during this process, whereas the Ki67 KD samples were microinjected with morpholinos. This does make it difficult to directly compare the two groups as they were not treated in the same way. The purpose of this was to determine the behaviour of chromosomes in control cells that had not been altered in any way. This allowed for a comparison of CTRL cells in their natural state but did mean that the samples had been treated somewhat differently. Despite this, it is one of the first studies to explore the impact of Ki67 depletion in meiosis and even the preliminary data collected from this lays the foundation for future studies, which should aim to utilise missense morpholino injections into the control cells for more direct comparison. It's also necessary to consider that morpholino injections can be quite difficult to repeat consistently due to the problematic nature of injecting precise volumes into the oocyte. The morpholino could have detrimental effects and potentially lose activity when stored in aqueous solutions and used multiple times, as well as the injection itself, potentially damaging the oocyte and leading to improper divisions (Ebner et al., 2001; Rosen et al., 2006). There were variations in the phenotypes witnessed within the oocytes, potentially as a result of the levels of native Ki67 or the morpholino

injections introducing variability due to inconsistent uptake or potential off-target effects. Therefore, future studies employing alternative knockdown strategies, such as CRISPR-based approaches, would provide further validation of these findings.

The quantitative analysis of these phenotypes also supported this association with aneuploidy, providing evidence of the Ki67-depleted oocytes struggling to progress through meiosis I to form the first polar body. With most meiotic aneuploidies occurring as a result of abnormalities in Meiosis I, this stunted or altered progression is evidence of the potential role of periphery alterations causing the occurrence of aneuploidy (McCoy, 2017). Unequal division of the chromosomes between the oocyte and polar body could lead to aneuploidy that causes death of the oocyte, or potentially, the oocyte could survive, leading to fertilisation of an abnormal oocyte, resulting in spontaneous abortion or a foetus with developmental disorders. The correlation between Ki67 depletion and meiotic failure highlights a direct mechanistic link between periphery integrity and chromosome segregation.

Interestingly, chromosome movement prior to PB formation was not significantly altered following the depletion of Ki67 and consequential loss of the chromosome periphery (Figure 4.5). This indicated that the periphery does not alter chromosome motility within the oocyte. Instead, its role appears to be confined to structural integrity and spatial organisation. This is consistent with the idea that chromosome movement is primarily governed by microtubule-associated forces while periphery-associated factors contribute to chromosome

stability. However, despite the movement within the oocyte appearing unaltered, something that did change was the directionality of the polar body extrusion (PBE). In the CTRL group, the majority of PBE occurred on the side of the oocyte (over 80%) (Figure 4.6). In contrast, in the KD group, only approx. 50% of PBE occurred at the side of the oocyte, with a significant increase in the number extruded through the bottom of the oocyte (towards the glass dish). There is currently no literature on the relevance of the direction of the PBE, with most publications focusing on the relationship between the two polar bodies following fertilisation (Yang et al. 2022). Therefore, it is not currently possible to draw a conclusion from this data; however, the distinct variation between the two groups does indicate a potentially abnormal phenotype that should be explored further to determine the mechanistic role of PBE directionality. The abnormal positioning of polar body extrusion in knockdown oocytes raises intriguing questions about the broader role of Ki67 in cellular organisation. While there is limited literature on the implications of polar body extrusion directionality, these findings suggest that Ki67 may influence spindle positioning and may play a role in the spindle asymmetry observed in oocytes (Akeru et al., 2017). Future studies should explore whether Ki67 interacts with key spindle-associated proteins during meiosis.

Following on from the live imaging analysis, mouse oocytes were imaged with super-resolution confocal microscopy and then SBF-SEM using the established 3D-CLEM pipeline, in order to investigate the chromosome ultrastructure in increased detail. 3D-CLEM proved to be an invaluable method for studying chromosomal ultrastructure following the removal of the periphery

as it showcased the abnormalities that occurred in the oocytes following Ki67 removal that would have otherwise been missed. These segmented chromosome models identified an abnormal distribution of the smaller chromosomes within the metaphase plate (Figure 4.12). This could indicate that Ki67 and the periphery have a role in the positioning of chromosomes within the complement during cell division. Although the significance of this redistribution remains unclear, a recent study identified a prometaphase pathway that moves chromosomes closer to the epicentre of the metaphase plate, and therefore, it's possible the loss of the periphery interferes with this pathway, altering this optimal alignment (Takenouchi et al., 2024).

The quantitative analysis of the chromosome ultrastructure showed little variation between the two groups other than surface area. This could be due to the noted elongated appearance of the KD chromosomes increasing the surface area. Alternatively, the surface area may be increased due to the 'rougher' surface of the chromosome following the removal of the periphery, which may provide a smoothing effect over the surface. Therefore, the loss of the chromosome periphery and the consequential 'rough' and exposed chromosome surface may result in an increased 'stickiness,' altering the interactions with other components of the oocytes. Increased 'stickiness' could provide an explanation for the reduced number of chromosomes visible in the KD live imaging. It could also provide an explanation for the knockdown chromosomes embedded into the organelles at the edge of the exclusion zone; the loss of the periphery makes the surface rougher and gets stuck to organelles. In contrast, it could be that the periphery provided some repelling buffer to the organelles at the edge of the

exclusion zone, and the loss of the periphery results in a reduced repelling action between the chromosomes and other cellular components. This interaction with the cytoplasmic organelles is also particularly important as 'membrane ensheathing' was linked to increased segregation errors (Ferrandiz et al., 2022) To truly understand this, the periphery would need to be characterised in its entirety, and the interactome would need to be mapped to understand the relationship between the periphery and its components and the other components of the oocyte. However, the observed differences in surface area and chromosome morphology suggest that the periphery plays a role in maintaining chromatin compaction, but further molecular characterisation of periphery-associated proteins will be necessary to understand these interactions fully.

The technical analysis of the two imaging modalities that was possible from this data also revealed significant changes in chromosomal surface area and morphology, and volume and length measurement discrepancies, which suggested that the two imaging modalities identify different aspects of chromosomal structure. Despite this comparison not providing further information regarding the structure of chromosomes and the impact of Ki67 loss, it did provide evidence for the need for advanced imaging techniques to investigate these cellular components. LM was a suitable technique for capturing broader trends in size, while EM provided insights into irregularities at the ultrastructural level. It was also evident that LM overestimated volume and surface area measurements, indicating that LM is not an optimal method for the quantitative analysis of chromosomes as is commonly used in the field. This quantitative analysis demonstrated that Ki67 knockdown leads to significant

alterations in chromosome morphology, particularly in surface area and sphericity. The combination of LM and EM highlights the need for multi-modal imaging to understand chromosomal abnormalities comprehensively. However, the low sample number used for the 3D-CLEM analysis limits the conclusions that can be drawn from this data, and a larger sample size would be needed for conclusive results. These results emphasise the importance of multimodal imaging approaches in chromosome research. While LM provides valuable insights into chromosomal dynamics, EM is essential for capturing high-resolution ultrastructural details.

Chromosome length measurements obtained by LM and EM were largely consistent in control oocytes, suggesting that LM provides reasonably accurate estimates of chromosome morphology. However, in knockdown cells, measurements derived from LM consistently underestimated chromosome length compared to EM, indicating a reduction in accuracy. This underestimation is likely due to the limitations of light microscopy, such as resolution.

Published data from Walther et al., (2018), using STED super-resolution microscopy to examine mitotic chromosomes in human somatic cells, reported chromatid lengths ranging from 7.2 to 10.2  $\mu\text{m}$ . Although these values differ from those measured in this work, they are within a comparable range to the lengths obtained by LM measurements. This slight variation could be due to differences in chromatin compaction and organisation between mitotic somatic cells and meiotic oocytes. Nevertheless, the similarity between STED-based measurements and the confocal LM data presented here under control

conditions supports the validity of the light-based approach when chromatin structure is preserved.

Volume measurements also show broad agreement with published work, e.g. a study by Nagasaka et al., (2016) reported a metaphase chromosome volume of  $\sim 230 \mu\text{m}^3$  in RPE cells. This is within  $\sim 10\%$  of the volume measured by light microscopy in this study ( $\sim 242 \mu\text{m}^3$  in a metaphase mouse oocyte), further supporting its precision. However, EM measurements showed lower volumes ( $\sim 180 \mu\text{m}^3$ ), suggesting that LM may slightly overestimate chromatin volume, likely due to the point-spread function and resolution limits. These comparisons underscore the strengths of LM for morphological investigations. However, it also highlights its limitations when quantification of ultrastructure is required. The variation between LM and EM measurements highlights the limitations of relying on a single imaging modality and emphasises the need for correlative techniques to explore chromosomal architecture.

This chapter demonstrates that Ki67 is definitely involved in the formation and maintenance of the periphery in female meiosis. Moving forward, analysis of the role of Ki67 in human oocytes should also be explored for direct clinical translations. However, the technical and legal ability to do this would make it very difficult to achieve, and therefore, mouse oocytes proved a useful model. The genetics of mouse oocytes are well studied, and the use of mouse oocytes as a model for meiosis is a well-established and commonly used representation in meiotic research (Marin et al., 2018). The optimal model for aneuploidy analysis would be human oocytes as mouse oocytes have a significantly more stable

karyotype (95% stability in selected young oocytes) compared to human oocytes (50% stability); however, for the analysis of Ki67 depletion, mouse oocytes are the best and most readily available model (Greaney et al., 2018; Nagaoka et al., 2012; Nakagawa & FitzHarris, 2017; Pan et al., 2008).

In conclusion, the disruption of the chromosome periphery following Ki67 knockdown provides further evidence for its essential role in ensuring meiotic accuracy. Loss of periphery integrity was associated with altered chromosomal morphology, increased surface area, and irregular shapes, as well as mislocalisation of smaller chromosomes within the oocyte. These findings suggest that the chromosome periphery, maintained by Ki67, plays a central role in protecting chromosomal architecture, supporting proper spatial organisation, and facilitating accurate segregation. Furthermore, the observed defects in polar body extrusion suggest that Ki67 may influence cytoskeletal dynamics beyond its structural function.

Overall, this chapter demonstrates that Ki67 is indispensable for ensuring chromosomal fidelity during meiosis and highlights the need for advanced imaging pipelines to investigate this role. By integrating advanced imaging techniques and quantitative analyses, these findings provide a detailed understanding of the structural and functional importance of the chromosome periphery.

## 5. Advanced Imaging of Human Oocytes and the First

### Whole Oocyte 3D Model

#### 5.1. Introduction

Defects of human oocytes, such as aneuploidy, contribute to 40-60% of early pregnancy losses (Brosens et al., 2022). Despite the increasing knowledge in this area, the molecular mechanisms of these difficulties are still poorly understood. This is partly due to the lack of available data on chromosome ultrastructure, even in “healthy” cells, where almost nothing about cell division machinery is known, e.g. there is still yet to be a complete 3D reconstruction of human oocytes. Therefore, to expand on this knowledge and produce novel data on oocyte ultrastructure, the aim of this chapter was to apply the established 3D-CLEM pipeline to human oocytes following its successful application to mitotic cells and mouse oocytes (Chapter 3 and 4). This data should reveal unknown chromosome architecture in human meiosis, and provide the basis for long-term research into the role of Ki67 in human oocytes.

The unique features of human oocytes, characterised by their prolonged arrest in meiosis and susceptibility to errors in chromosome segregation, makes them an ideal model for investigating chromosomal organisation and stability (Pincus & Enzmann, 1935; Sagata, 1996; Tripathi et al., 2010). Oocytes are also a preferred model for investigating the relationship between ultrastructure and aneuploidy in human meiosis as the majority of aneuploidies occur in the female gametes rather than the male ones (Kubicek et al., 2019).

To build on the methodologies developed in earlier chapters, this study applies the optimised 3D-CLEM pipeline to human oocytes to investigate chromosomal ultrastructure. The imaging of human oocytes was done to attempt to generate an atlas of human meiotic chromosomes to provide a reference of 'control' chromosome ultrastructure. Despite extensive studies on oocyte ultrastructure, previous analyses have primarily focused on single-slice organelle imaging, leaving chromosome geometry largely unexplored (Trebichalská, Kyjovská, et al., 2021). The first volume analysis using electron microscopy has been applied to human oocytes, however, the focus of this study was on the mitochondria of the cell, and currently there is no comparable study that has analysed chromosomal ultrastructure (Trebichalská, Javůrek, et al., 2021).

Given the translational importance of human oocytes, this chapter focuses on addressing the specific challenges of applying advanced imaging techniques to these cells, including their size, fragility, and limited availability. Despite the constraints posed by sample accessibility, this chapter presents the first three-dimensional ultrastructural model of chromosomes in human oocytes. This model offers novel insights into the ultrastructural geometry of chromosomes, and it establishes a framework for future studies aiming to explore the ultrastructure of meiotic chromosomes in a clinically relevant context.

By optimising and validating the 3D-CLEM pipeline for human oocyte research, this work demonstrates the potential of advanced imaging techniques to address longstanding questions in reproductive biology. The findings provide a

critical foundation for further exploration of chromosomal segregation mechanisms in human gametes and contribute to a deeper understanding of the origins of aneuploidy.

## 5.2. Hypothesis and Aims

### Hypothesis

The development of a 3D-CLEM pipeline to work with human oocytes, is feasible. This approach will provide novel insights into the ultrastructure of chromosomes in human oocytes. 3D reconstructions of the meiotic chromosomes will generate geometric data that can be used as a reference for healthy oocyte chromosome structure, assisting future investigations into oocyte mechanics, in both health and disease.

### Aims

- Optimise the 3D-CLEM pipeline for human oocytes and adapt imaging techniques to account for cell fragility, size, and sample preparation constraints.
- Establish a methodological workflow for future studies by validating the applicability of the optimised 3D-CLEM pipeline for broader studies of meiotic chromosome ultrastructure and its potential clinical applications.
- Generate the first 3D ultrastructural model of chromosomes in human oocytes, using high-resolution 3D reconstructions of chromosomal organisation, to investigate chromosomal organisation in meiosis.

## 5.3. Methods

Our collaborators at Warwick University (Aleksandra Byrska) and Warwick Medical School, assisted in preparing the human oocytes up until the stage of fixation, at which point they were transferred, under a material transfer agreement (MTA) agreement, to Nottingham. The rest of this chapter is dedicated to the novel protocol development, establishing 3D-CLEM for imaging human oocyte cell division machinery.

### 5.3.1. Fixation

Oocytes were washed in pre-warmed PHEM buffer consisting of 60mM PIPES (Thermo Fisher; J62494-AP), 25mM HEPES (Thermo Fisher; J61017-AK), 10mM EGTA (Merck; 324626), 4mM MgSO<sub>4</sub>·7H<sub>2</sub>O (Merck; 63138), pH 6.9 with 0.25% Triton X-100 (Sigma-Aldrich; X100RS). They were then incubated in 3.7% formaldehyde (Merck; 252549) diluted in PHEM for 30 minutes at room temperature, then incubated in 0.5% BSA (Merck; A5611) in PBS (PBB). The cells were then permeabilised by 0.25% Triton in PBS for 15 minutes before incubating in a 3% PBS with 0.05% Tween-20 (Sigma-Aldrich; P6585) blocking solution at 4°C overnight.

### 5.3.2. Immunofluorescence

Human oocytes were incubated for one hour at room temperature in 25µl droplets of blocking solution containing the primary antibodies for Ki67 and CREST (Table 4.1). The cells were then washed with PBB solution for fifteen minutes at RT. They were then incubated in blocking solution containing

secondary antibodies for one hour at 37°C. After washing, the oocytes were then placed in 5µl drops of PBS in a glass-bottom dish (MatTek; P35G-1.5-14-C) and overlaid with mineral oil until imaging.

**Table 5.1. Immunofluorescence antibodies used for oocyte staining.**

| Primary antibodies |                     |                                       |       | Secondary antibodies |     |       |
|--------------------|---------------------|---------------------------------------|-------|----------------------|-----|-------|
| <b>Ki67</b>        | rabbit              | Abcam;<br>Ab16667                     | 1:100 | Anti-rabbit          | 594 | 1:200 |
| <b>CREST</b>       | human               | Antibodies<br>Incorporated;<br>15-234 | 1:50  | Anti-human           | 647 | 1:200 |
| <b>DAPI</b>        | Direct<br>conjugate | Invitrogen;<br>62248                  | 1:500 | N/A                  | N/A | N/A   |

### 5.3.3. Fixed Oocyte Imaging

Oocytes were imaged using a spinning disk confocal (3I, intelligent imaging innovations) equipped with 2x photometric 95B Prime sCMOS cameras and controlled with Slidebook software. The temperature was maintained at 37°C throughout imaging using a stage-top incubator (Okolab). Z-stacks with 200nm slices were imaged using the 100x oil immersion objective lens (Numerical aperture: 1.46) with 500ms exposure and 30-35% laser power for 561 and 405nm wavelengths and 100ms exposure time and 10% power for 647nm wavelength.

## 5.4. Results and discussion

### 5.4.1. Ki67 and the Periphery in Meiosis

Ki67 presence was confirmed and shown to have a significant role in mouse oocytes (Chapter 4). Immunofluorescence staining was performed to investigate its presence and localisation in human oocytes. The results confirmed that Ki67 was present in human oocytes and specifically localises to the periphery of the chromosomes (Figure 5.1). This supported the hypothesis that Ki67 contributes to the formation of the chromosome periphery in human oocytes and, therefore, may have a role in chromosomal organisation and stability similar to that seen in mouse oocytes. This further supported the need to develop 3D-CLEM for human oocytes to investigate Ki67 depletion in human meiosis.

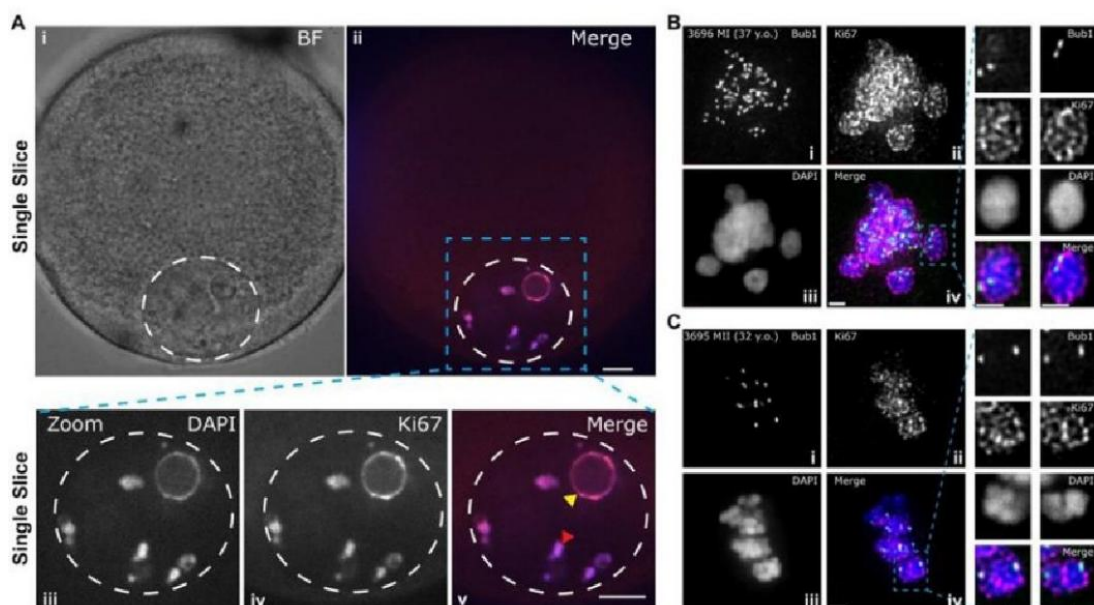


**Figure 5.1. Ki67 in human oocytes immunofluorescence.** **A)** A fixed human GV stage oocyte imaged using spinning disc confocal microscopy. Images show brightfield (i) and merge of DAPI and anti-Ki67 (ii). Dashed circle represents the location of the nucleus. Zoom images show DAPI (iii), anti-Ki67 (iv) and a merge (v).

(v). The arrows indicate partially condensed chromosomes (red) and nucleolar rim (yellow). Scale bar = 10 $\mu$ m. **(B & C)** Fixed human oocytes stained for Bub1 (green), Ki67 (magenta), and DAPI (blue) with merge (iv). **(B)** Representative Metaphase I oocyte **(C)** shows Metaphase II oocyte Scale bar = 2 $\mu$ m. (Imaging performed by Aleksandra Byrska – University of Warwick).

#### 5.4.2. Human oocyte samples for 3D-CLEM

Human oocyte samples were donated by patients seeking fertility treatments such as IVF or ICSI. Samples deemed unsuitable for progression to fertility treatment were donated to research with informed consent. The age and diagnosis associated with the patient were provided and the stage of the cell at the point of collection was noted (Table 5.1).

**Table 5.2. Human oocyte samples for 3D-CLEM.** The stage of the sample at the point of collection, as well as the age and diagnosis of the donor, are listed in the table.

| SAMPLE | STAGE  | AGE               | DIAGNOSIS         |
|--------|--------|-------------------|-------------------|
| 3566   | MII    | 31                | PCOS              |
| 3498   | 2 x MI | N/A frozen sample | N/A frozen sample |
| 3568   | 2 x MI | 35                | Tubal             |
| 3572   | GV     | 38                | PCOS              |
| 3573   | GV     | 41                | Endometriosis     |
| 3574   | GV     | 35                | DOR/MFI           |

#### 5.4.3. 3D-CLEM abnormalities in Human oocytes

Due to the previous success seen in Chapter 4 which applied 3D-CLEM to mouse oocytes, it was assumed that the same protocol would also work with human oocytes and therefore the technique was applied without modification to

test this assumption. The sample was fixed, imaged, stained, and embedded for EM, following the same protocol as previously described.

#### 5.4.3.1. *Vacuoles within the oocyte*

The initial samples showed abnormalities in the phase imaging of the oocyte (Fig 5.2.B). The high FIB charge required (30kV) to reach the appropriate depth to mill through the entire oocyte structure, resulted in uneven slicing and reduced resolution. Although the FIB-SEM successfully milled through the sample, generating a complete image stack, the reduced resolution likely compromised chromosome visibility, rendering segmentation data inaccurate and unreliable.

However, additional issues with this sample prevented meaningful chromosome analysis. The DAPI staining appeared more intense than in the previous sample despite the concentration remaining the same and both samples being processed simultaneously. This excessive DAPI staining obscured chromosome visualisation during LM imaging (Figure 5.3.A). Although phase imaging showed a smooth, rounded oocyte—with some air bubbles present (Figure 5.2.B), EM imaging revealed multiple vacuoles within the cytoplasm, suggesting cellular distress during fixation and staining (Figures 5.2.C-D). Furthermore, vacuoles were also observed in the perivitelline space, further indicating potential structural damage. Due to this abnormal morphology, chromosomes could not be clearly identified, suggesting that certain oocytes may be more sensitive to specific stages of the 3D-CLEM processing pipeline. For instance, the fixation protocol used may be too harsh for some human oocytes.

As a result, further optimisation of fixation conditions was attempted in subsequent samples to improve cell preservation for accurate volume imaging and reconstruction.

*Table 5.3. Sample 3498 A imaging parameters*

| SAMPLE        | RESOLUTION | PIXEL TIME  | PIXEL SIZE | SLICE SIZE |
|---------------|------------|-------------|------------|------------|
| <b>3498 A</b> | 4096×4096  | 3.0 $\mu$ s | 25 nm      | 70 nm      |

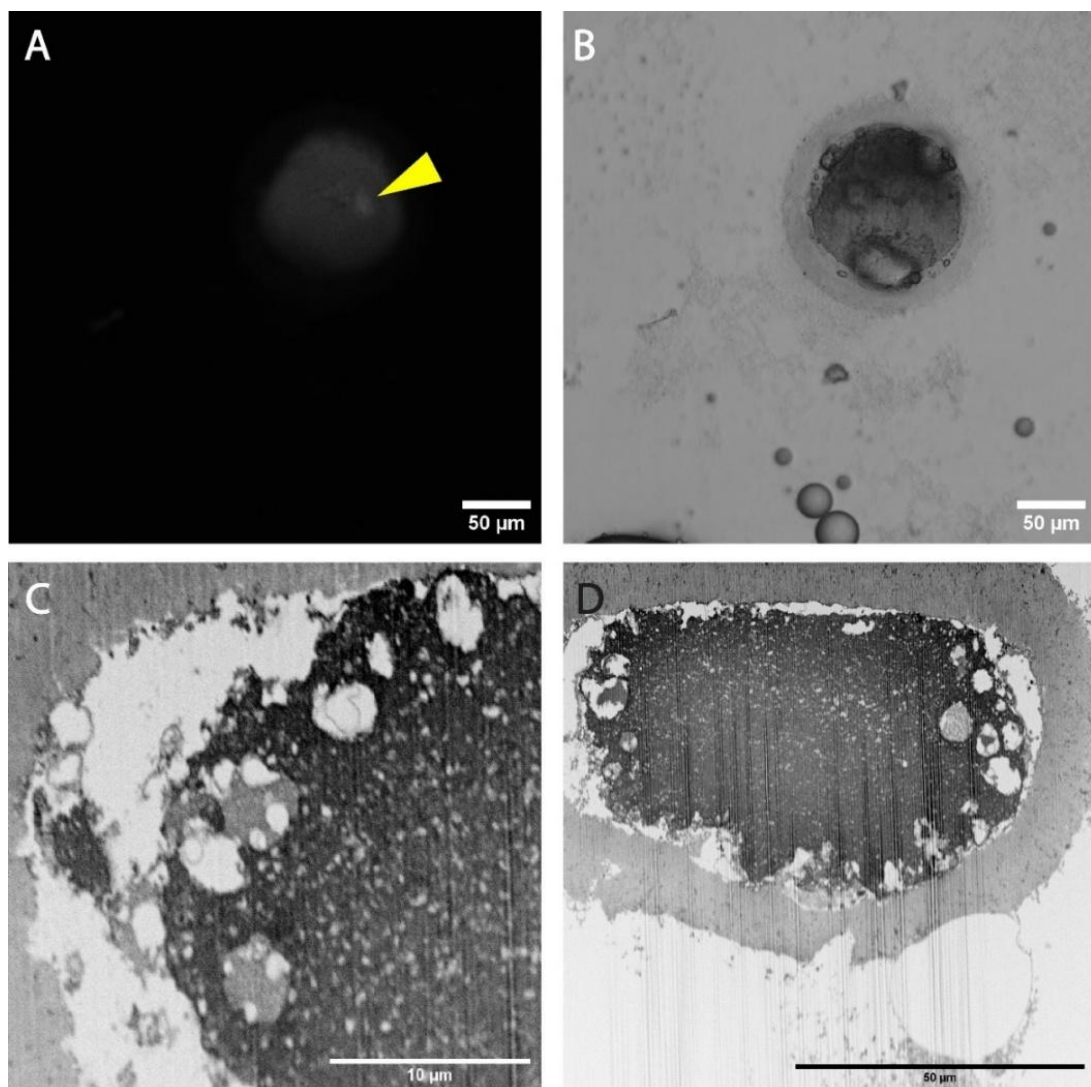


**Figure 5.2. FIB-SEM imaging of a human oocyte.** (A) Maximum projection of a human oocyte stained with DAPI, imaged using a Zeiss LSM 900 with AiryScan 2 100 $\times$  oil objective. (B) Brightfield phase imaging showing overall oocyte

*morphology. (C) Magnified EM image highlighting vesicles present within the cytoplasm and perivitelline space. (D) Single EM slice demonstrating the rough surface produced by FIB milling. EM imaging was performed using a Zeiss Crossbeam 550 FIB-SEM. Sample 3498 A. Scale = 10-50 $\mu$ m.*

#### 5.4.3.2. *Dense ZP-pellucida staining*

Following the problems that arose from using the FIB-SEM for samples of such a large size, all following oocyte samples were imaged using SBF-SEM. Similar to previous observations, excessive DAPI staining prevented chromosome visualisation (Figure 5.3.A). Additionally, phase imaging revealed the presence of air bubbles on the cell surface and surrounding area; this again indicated that the fixative caused issues that may introduce artefacts to the sample (Figure 5.3.B). However, the abnormalities observed in this sample varied from the previous ones. No vesicles were visible in the sample, as seen in Figure 5.3. The ZP displayed dark-stained patches not observed in previous samples, indicating artefacts in the sample, such as accumulation in the ZP that prevented penetration into the cytoplasm. Furthermore, the cytoplasm appeared smooth and almost solid, lacking the expected organelle structures observed in previous samples. Despite imaging the entire oocyte, no chromosomes were visible, which suggested potential alterations in oocyte morphology as a result of the processing methods.

SBF-SEM proved to be a better, more consistent imaging method than FIB-SEM, producing clearer and more consistent slices, as seen in Chapters 3 and 4. The improved sectioning reduced imaging time, allowing for increased resolution and better structural analysis of the oocyte.

These results highlight the advantages of SBF-SEM for imaging oocyte samples. However, it also indicates the need to optimise sample preparation techniques further to preserve chromosomal structures and cellular morphology.

*Table 5.4. Sample 3498 B imaging parameters*

| <b>SAMPLE</b> | <b>RESOLUTION</b> | <b>PIXEL TIME</b> | <b>PIXEL SIZE</b> | <b>SLICE SIZE</b> |
|---------------|-------------------|-------------------|-------------------|-------------------|
| <b>3498 B</b> | 4096×4096         | 3.0 $\mu$ s       | 25 nm             | 70 nm             |

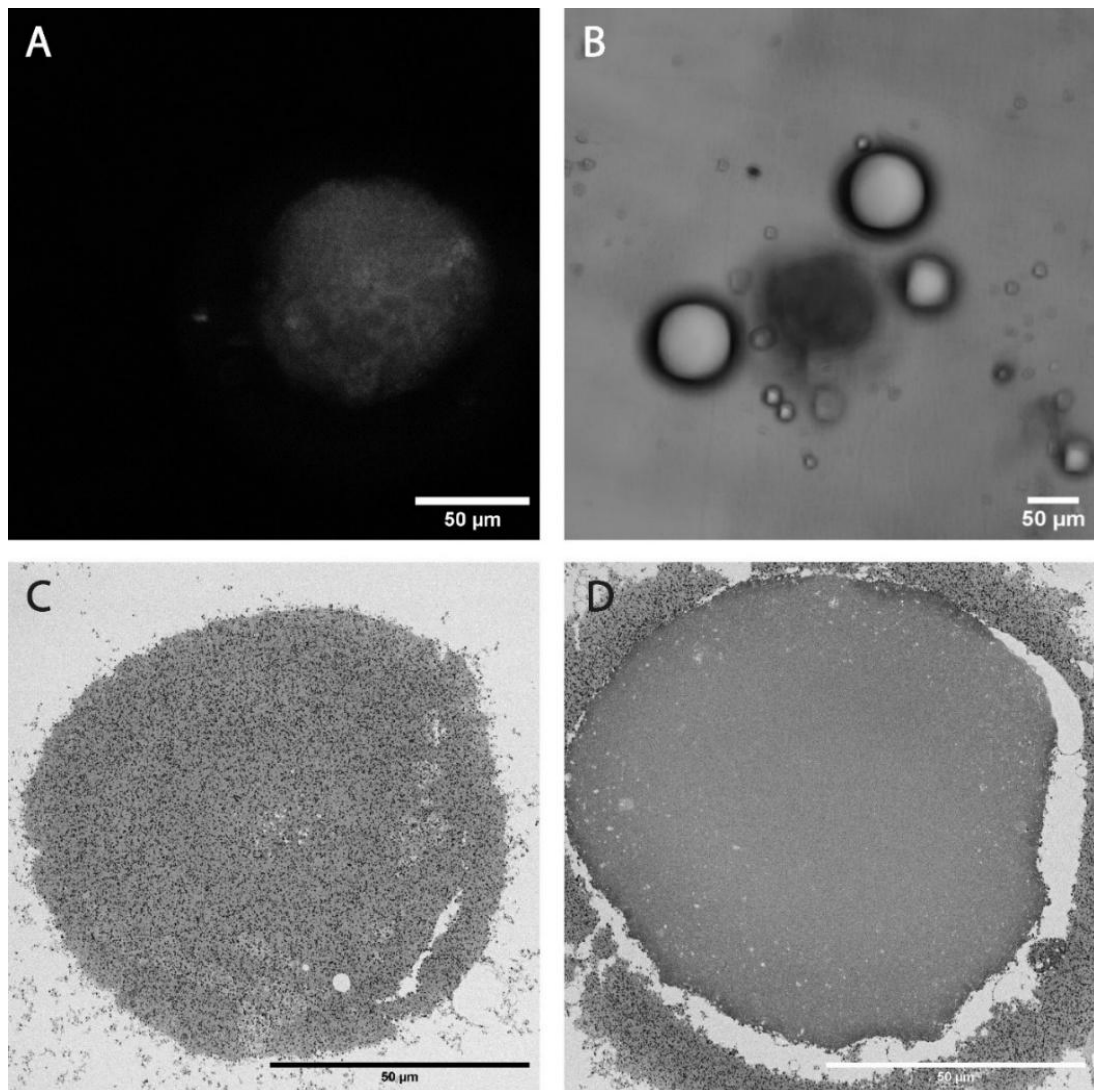


**Figure 5.3. SBF-SEM imaging of a human oocyte.** (A) Maximum projection of a human oocyte stained with DAPI, showing excessive fluorescence that obscures chromosome visualisation. (B) Brightfield phase imaging revealing the overall oocyte morphology with visible air bubbles. (C) EM slice showing dense staining spots in the ZP, a feature not observed in previous samples. (D) EM slice of the cytoplasm, showing a lack of visible organelles compared to previous samples and no identifiable chromosomes. LM imaging was performed using a Zeiss LSM 900 with AiryScan 2 100× oil objective, and EM imaging was conducted using a Zeiss Crossbeam 550 FIB-SEM. Sample 3498 B. Scale = 50µm.

#### 5.4.3.3. Absent Chromosomes

The fixative was modified to 2% PFA and 2% GLUT to improve cell morphology and preserve organelle structures. Fixation was also performed at

37°C to maintain the cells in an optimal environment until fixation was complete. This adjustment aimed to enhance structural integrity and potentially improve chromosome visualisation. However, despite these changes, the same issues persisted.

Phase imaging continued to reveal the presence of bubbles on the cell surface and surrounding area, suggesting that fixation artefacts remained a challenge (Figure 5.4.A). The organelles appeared more defined in this sample compared to previous attempts, indicating that the modified fixation may have improved overall cellular preservation. However, despite this, the chromosomes remained absent in the EM images (Figure 5.4.B). The cytoplasm appeared structurally intact, although slightly misshapen and constricted. This reinforced the theory that processing either altered the chromosome structure or the stains were unable to successfully penetrate into the oocyte and stain them due to alterations that occurred earlier in the pipeline.

These findings suggest that while the adjusted fixation protocol improved organelle preservation, additional modifications may be required to ensure chromosomal visibility.

*Table 5.5. Sample 3568 A&B imaging parameters*

| <b>SAMPLE</b> | <b>RESOLUTION</b> | <b>PIXEL TIME</b> | <b>PIXEL SIZE</b> | <b>SLICE SIZE</b> |
|---------------|-------------------|-------------------|-------------------|-------------------|
| <b>3568 A</b> | 4096x4096         | 3.0µs             | 22nm              | 70nm              |
| <b>3568 B</b> | 8192x8192         | 4.0µs             | 15nm              | 70nm              |

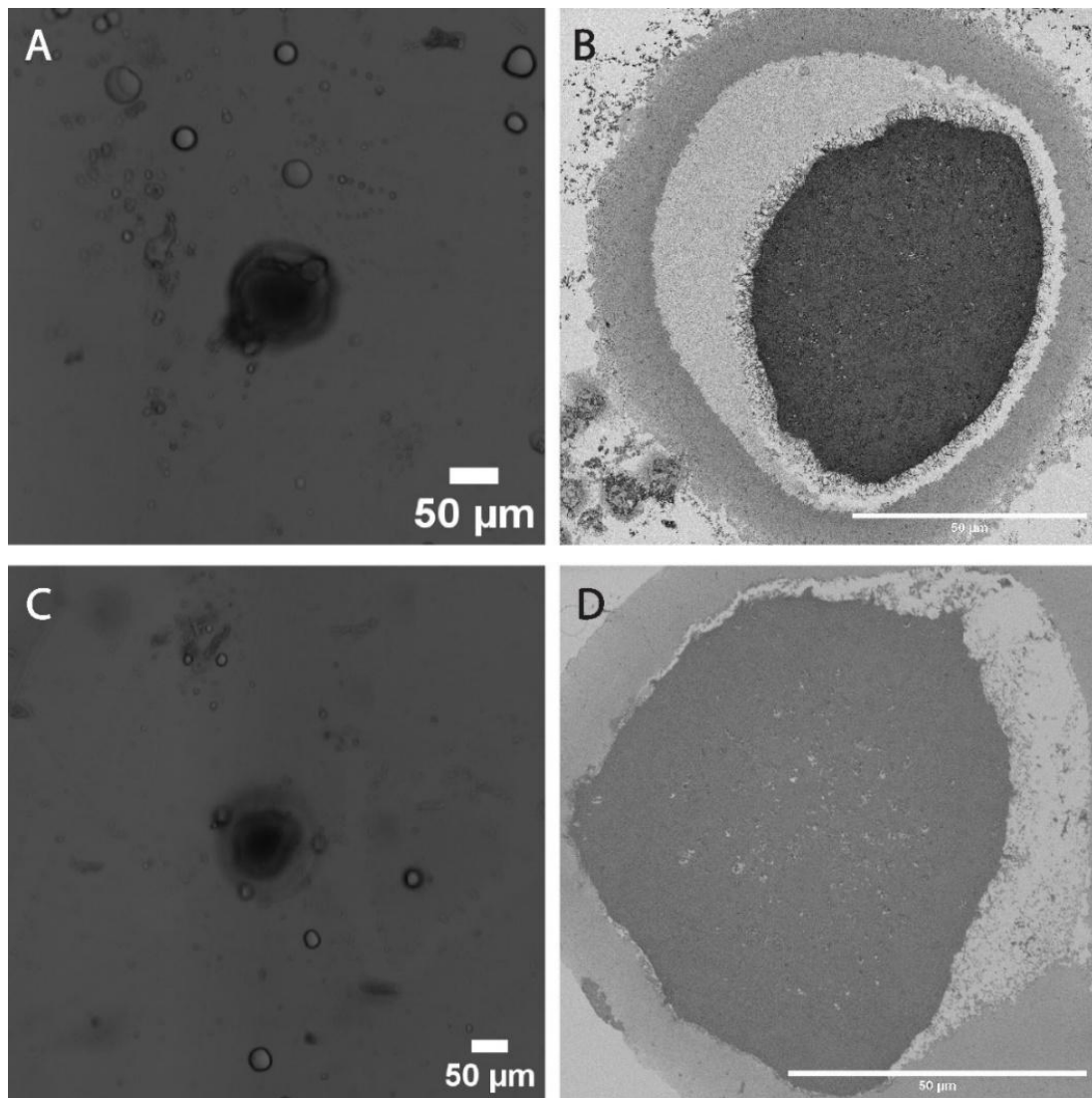


**Figure 5.4. SBF-SEM imaging of human oocytes showing a lack of chromosomes.** (A) Brightfield phase imaging of an oocyte corresponding to the EM slice shown in (B). (B) EM slice of the oocyte, showing the absence of visible chromosomes within the cytoplasm. (C) Brightfield phase imaging of a second sample corresponding to the EM slice shown in (D). (D) EM slice of another sample in which no oocyte is present. Light microscopy (LM) imaging was performed using a Zeiss LSM 900 with AiryScan 2 100× oil objective. Sample 3568 A and B. Scale bars = 50 µm.

#### 5.4.3.4. Altered ZP

Following previous experiments where excessive DAPI staining prevented chromosome visualisation, the next oocyte was stained with a lower

concentration of DAPI (1:2000). This adjustment was successful, as chromosomes were now clearly visible within the cell during LM (Figure 5.5.B-C). However, despite improved staining, the morphology of the oocyte appeared abnormal (Figure 5.5.A). Instead of maintaining a typical spherical shape, the cell exhibited a "folded" appearance, and the chromosomes clustered into large aggregates. Nevertheless, a few individual chromosomes were visible (Figure 5.5.C), prompting further processing to optimise the 3D-CLEM pipeline for chromosome visualisation.

However, the abnormal shape and structure of the oocyte negatively impacted the success of the 3D-CLEM process. The ZP appeared to collapse around the cytoplasm, accumulating significant staining (Figure 5.5.D-E). The region where chromosomes were observed using LM was imaged at a higher resolution as a secondary nested ROI. Unfortunately, chromosomes were not identifiable in this region, and only two dark areas were visible, containing structures resembling pieces of the endoplasmic reticulum (ER) or potentially mitochondria (Figure 5.5.D). Additionally, no clear exclusion zone was observed in the cytoplasm.

The intense staining of the ZP and the abnormal structural collapse (Figure 5.5.E) suggested that the staining process may not have sufficiently penetrated the cytoplasm to effectively define chromosome structures. These findings indicate that maintaining a structurally intact ZP before 3D-CLEM processing is critical for successful imaging. Future samples will be assessed to ensure that ZP morphology remains as close to 'normal' as possible before imaging.

Table 5.6. Sample 3572 imaging parameters

| SAMPLE | RESOLUTION | PIXEL TIME  | PIXEL SIZE | SLICE SIZE |
|--------|------------|-------------|------------|------------|
| 3572   | 4096×4096  | 3.0 $\mu$ s | 32 nm      | 70 nm      |

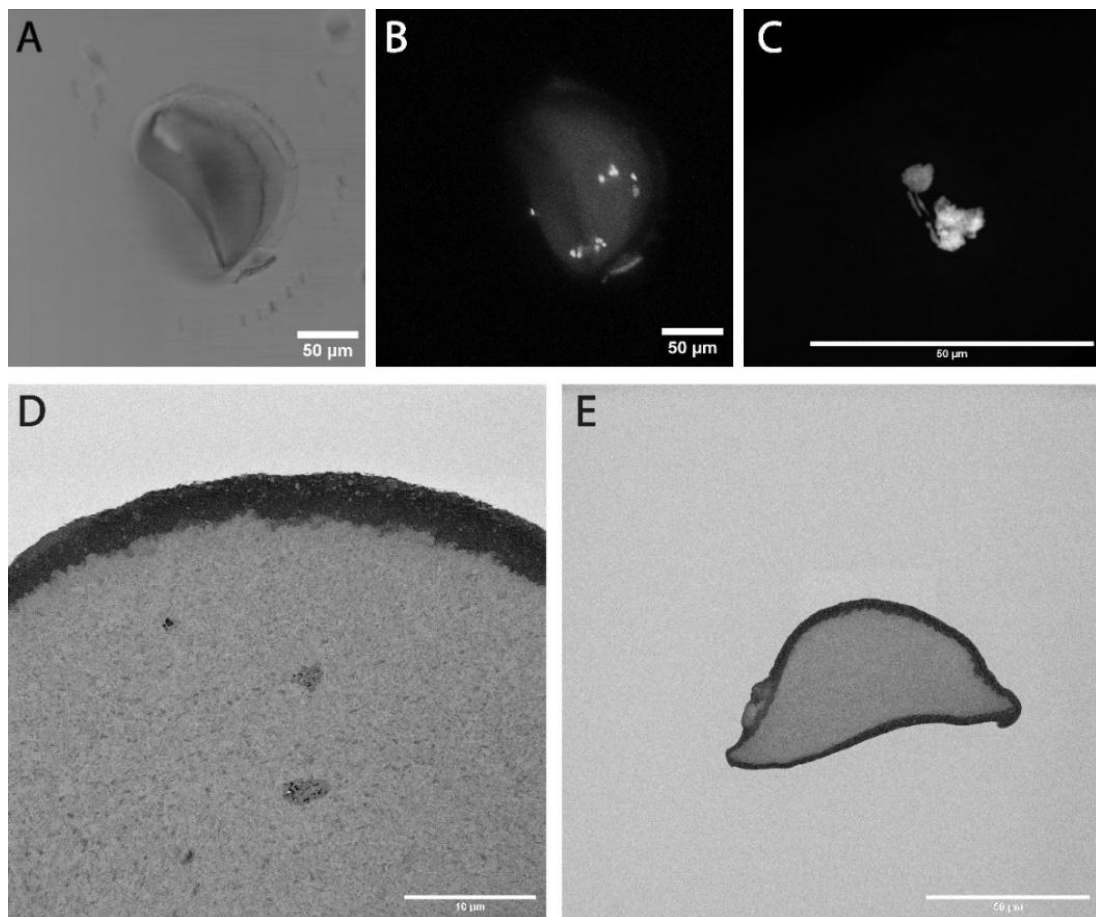


**Figure 5.5. Structural abnormalities in the ZP and their impact on chromosome visualisation.** (A) Brightfield phase image of the oocyte, showing a folded morphology rather than a typical spherical shape. (B) Maximum projection of the oocyte stained with DAPI (1:2000), revealing improved chromosome visibility compared to previous samples. (C) Higher-magnification LM image showing chromosome clustering, with a few individual chromosomes visible. (D) EM image of the region previously identified for chromosome visualisation, showing two dark-stained structures resembling ER or mitochondria but no discernible chromosomes. (E) EM image highlighting the abnormal collapse of the ZP and intense staining accumulation. Sample 3572. LM imaging was performed using a Zeiss LSM 900 with AiryScan 2 100× oil objective, and EM imaging was conducted using a FEI 250 Quanta FEG-SEM.

#### 5.4.3.5. *Cytoplasmic Abnormalities*

Within the same group of cells processed for EM, an oocyte with a smooth ZP and visible chromosomes was also imaged. The chromosomes again appeared clumped within the cell; however, as they had split into two groups, this was considered a potentially normal chromosome morphology during anaphase I. The ZP of this oocyte was more spherical and rounded, as expected in a healthy oocyte. However, phase imaging revealed that the cytoplasm appeared misshapen and granular (Figure 5.6.B).

Due to the visibility of the chromosomes and the limited availability of human oocytes for analysis, the cell was imaged to maximise data collection. However, EM imaging produced results similar to those of the previous sample (Figure 5.6.D-E). The ZP appeared compressed around the cytoplasm and displayed a darkened appearance (Figure 5.6.D). Despite the successful localisation of the chromosome region using LM image correlation, no chromosomes were visible in the EM images, preventing further analysis.

These findings further emphasise the importance of maintaining overall cell morphology before processing. Both the ZP and the cytoplasm must remain structurally normal, as observed in the mouse oocytes in Chapter 4, to ensure successful imaging and chromosome visualisation. This reinforces the need for further optimisation of fixation and processing protocols to preserve cellular structures in human oocytes.

Table 5.7. Sample 3574 imaging parameters

| SAMPLE | RESOLUTION | PIXEL TIME  | PIXEL SIZE | SLICE SIZE |
|--------|------------|-------------|------------|------------|
| 3574   | 5120       | 3.0 $\mu$ s | 12 nm      | 70 nm      |

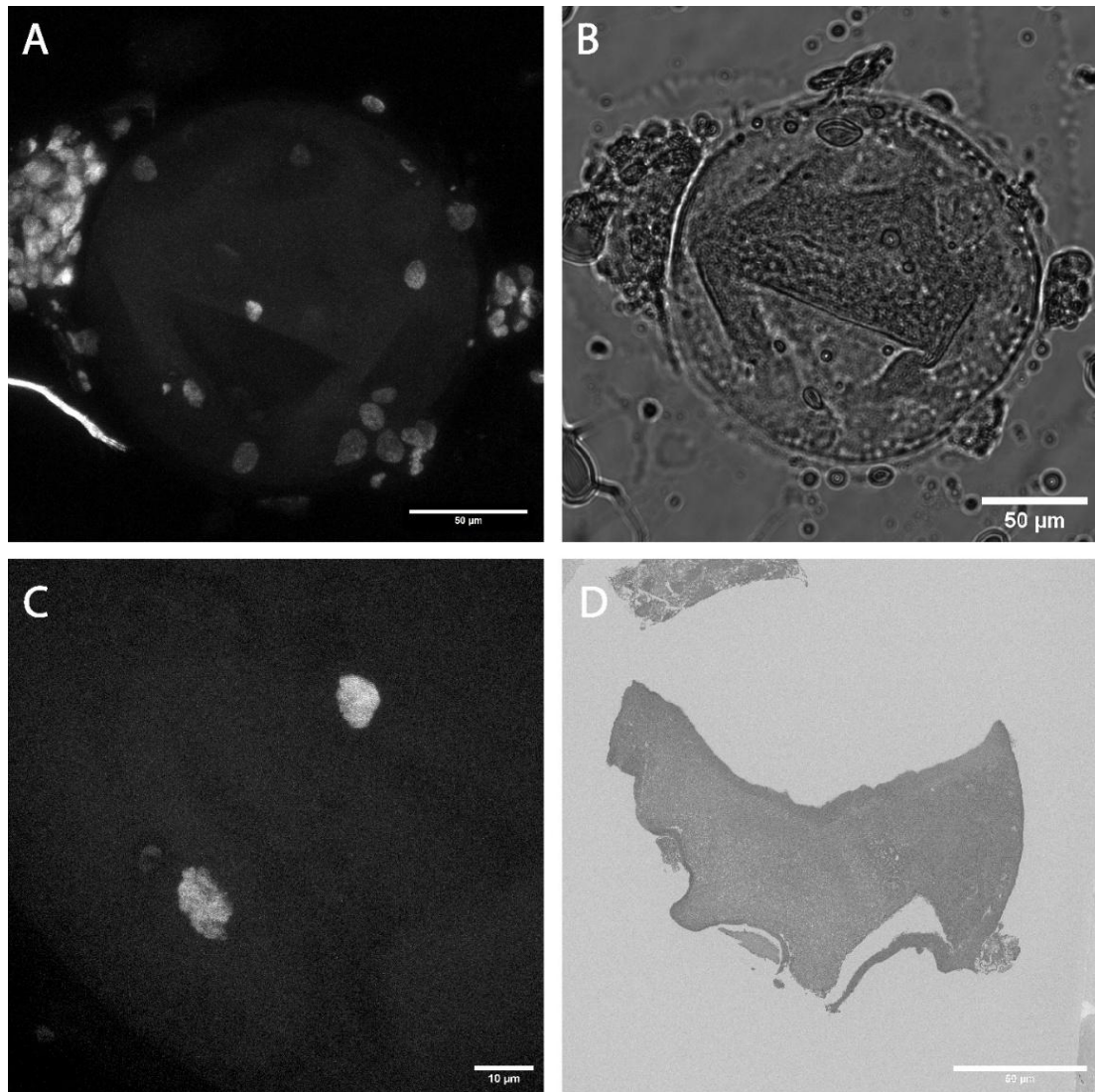


**Figure 5.6. Cytoplasmic abnormalities in human oocytes.** SBF-SEM imaging of an oocyte with a morphologically normal ZP but failed chromosome visualisation. (A) Maximum projection of the oocyte stained with DAPI. (B) The brightfield phase image of the oocyte shows a rounded ZP but granular cytoplasm. (C) DAPI stain of chromosomes that appear clumped yet split into two distinct groups, resembling anaphase I. (D) EM image of the cytoplasm, where no chromosomes were visible despite LM correlation. Sample 3574. LM imaging was performed using a Zeiss LSM 900 with AiryScan 2 100 $\times$  oil objective, and EM imaging was conducted using a Zeiss Crossbeam 550 FIB-SEM. Scale = 10-50 $\mu$ m.

#### 5.4.4. Visible chromosomes and kinetochores

Phase imaging of the oocyte showed a smooth cytoplasm, without granularity, and that the ZP remained spherical and rounded post-fixation (Figure 5.7.A). This indicated that the human oocytes withstood the fixation process without significant structural alterations. LM imaging of DAPI-stained chromosomes revealed a clear chromosome bundle, suggesting that the cell was entering metaphase alignment (Figure 5.7.B). The maximum projection showed a well-defined cytoplasmic region, and, as this was an MII oocyte, the chromosomes had already divided, with the polar body visible in the perivitelline space between the ZP and cytoplasm, containing the extruded DNA content (Figure 5.7.C). The LM data suggested that the oocyte was of high quality and at an optimal stage for electron microscopy analysis of the chromosomes.

The cellular structure was well-preserved during processing, and EM imaging successfully resolved the ZP, perivitelline space, cytoplasmic projections, and organelles within the oocyte, as expected (Figure 5.7.E). The chromosomes were distinctly stained, and both microtubules and kinetochores were visible within the cell (Figure 5.7.F).

This study represents the first volume EM analysis of human oocyte chromosomes with visible kinetochores and spindle structures, demonstrating the reproducibility of the 3D-CLEM pipeline for investigating chromosomal ultrastructure in human oocytes. However, the chromosomes were positioned at the deepest part of the resin block, making FIB sectioning challenging. The milling process struggled to reach the necessary depth, resulting in inconsistent slice

thickness. Additionally, imaging was conducted over five days, but despite this extended period, only approximately half of the cell was imaged—although this did encompass the entire chromosome region. Due to the inconsistencies in FIB milling, successful segmentation of the chromosomes for 3D reconstruction was not possible, as slices were occasionally skipped, and larger sections were removed at once. Despite these challenges, this data confirms the successful application of the 3D-CLEM pipeline for human oocyte imaging.

*Table 5.2. Sample 3566 imaging parameters*

| <b>SAMPLE</b> | <b>RESOLUTION</b> | <b>PIXEL TIME</b> | <b>PIXEL SIZE</b> | <b>SLICE SIZE</b> |
|---------------|-------------------|-------------------|-------------------|-------------------|
| <b>3566</b>   | 3078 x 2304       | 3.0 $\mu$ s       | 25 nm             | 70 nm             |

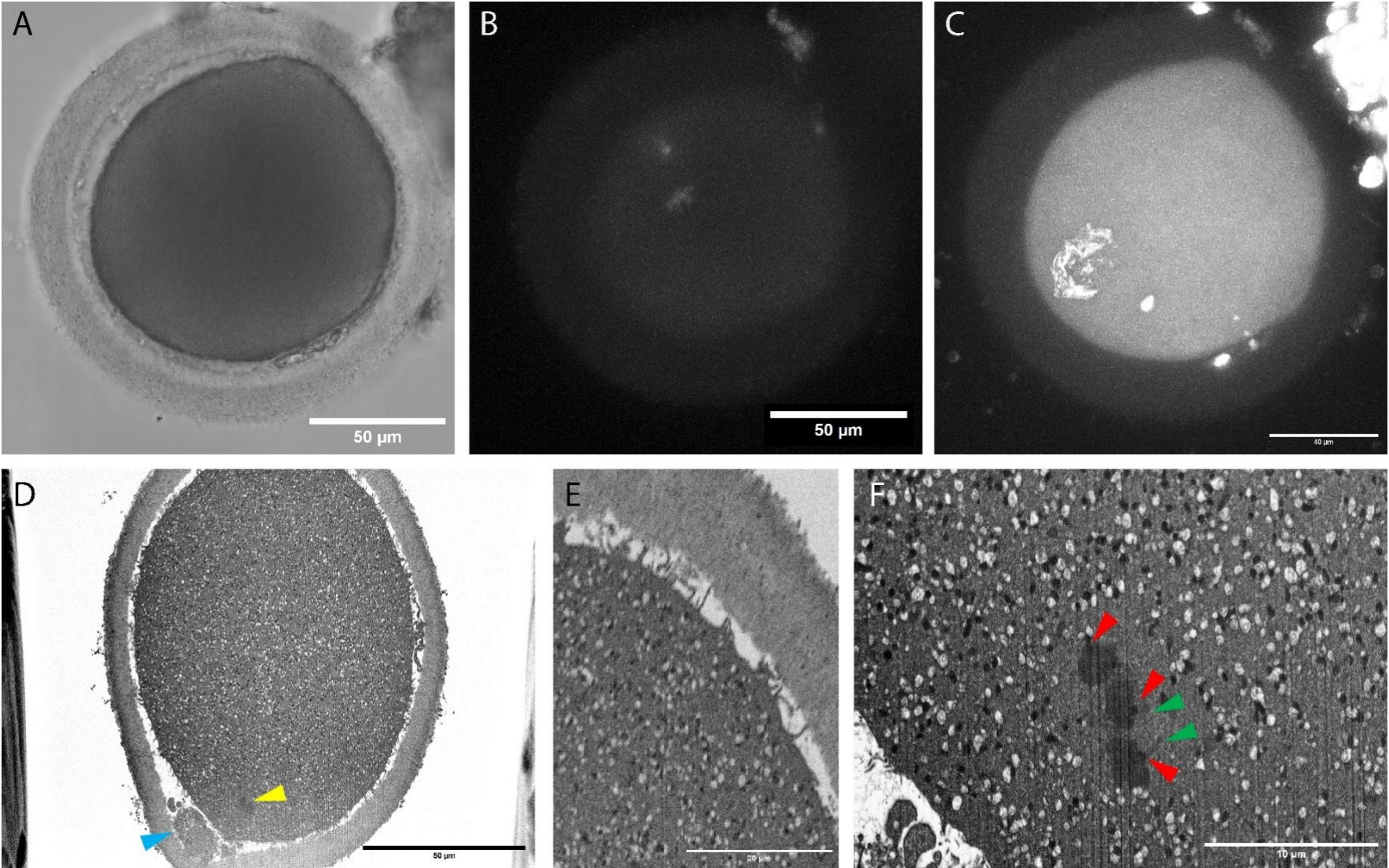


**Figure 5.7. Successful 3D-CLEM processing of an MII oocyte.** <sup>1</sup>(A) Phase imaging of the oocyte showing smooth cytoplasm and round shape. (B) Max-projection of chromosome region showing oocytes aligned in metaphase plate – stained with DAPI. (C) Max-projection of oocyte showing cytoplasmic region and a few remaining cumulus cells. (D) Single EM slice showing polar body (blue arrow) and chromosomes (yellow arrow) within the oocyte. (E) Zoom showing the cytoplasmic projections of the oocyte demonstrating the unaltered structure of the oocyte following EM processing. (F) Single slice showing the chromosomes and visible spindle structures (green arrows) and kinetochores (red arrows). LM was performed using the Zeiss LSM 900 with AiryScan 2 100x oil objective and EM was performed with the Zeiss Crossbeam 550 FIB-SEM. Sample 3566. Scale = 10-50 $\mu$ m

#### 5.4.5. Whole oocyte chromosome modelling

Following the success of the previously imaged oocyte that was not live-imaged, the final cell was fixed immediately upon collection without prior imaging. This sample maintained a spherical structure with a clearly defined ZP and visible chromosomes, as observed in LM images (Figure 5.8.A-B).

Given that SBF-SEM had been identified as the most suitable method for large-volume imaging and previous attempts with FIB-SEM had produced unsatisfactory results (Figures 5.2. and 5.7.), this sample was processed using SBF-SEM. Imaging included a complete oocyte overview and a nested ROI focused on the chromosome region (Figure 5.8.C). The entirety of the oocyte was successfully imaged, and chromosomes were clearly identifiable, enabling segmentation using the established AMIRA modelling technique.

Figures 5.8.D-F show the segmented models derived from the EM images—figure 5.8. Ei-ii displays the segmented chromosome ROI models. However, due to a slight misalignment, the tops of the chromosomes were not fully captured at this resolution. Despite this limitation, both chromosomes and microtubules were visible and could be partially modelled, figure 5.8.Fi-iii presents the complete chromosome complement modelled from the chromosome overview, revealing an abnormally structured chromosome arrangement. Instead of discrete, well-defined chromosomes, the structures formed a single non-uniform shape, deviating significantly from the distinct chromosome morphology observed in mouse oocytes (Chapter 4; Figure 4.10.).

Table 5.8. Sample 3573 imaging parameters

| SAMPLE     | RESOLUTION | PIXEL TIME  | PIXEL SIZE | SLICE SIZE |
|------------|------------|-------------|------------|------------|
| 3573 ROI_0 | 5120×5120  | 3.0 $\mu$ s | 19 nm      | 70 nm      |
| 3573 ROI_1 | 8192×8192  | 3.0 $\mu$ s | 2.0 nm     | 70 nm      |

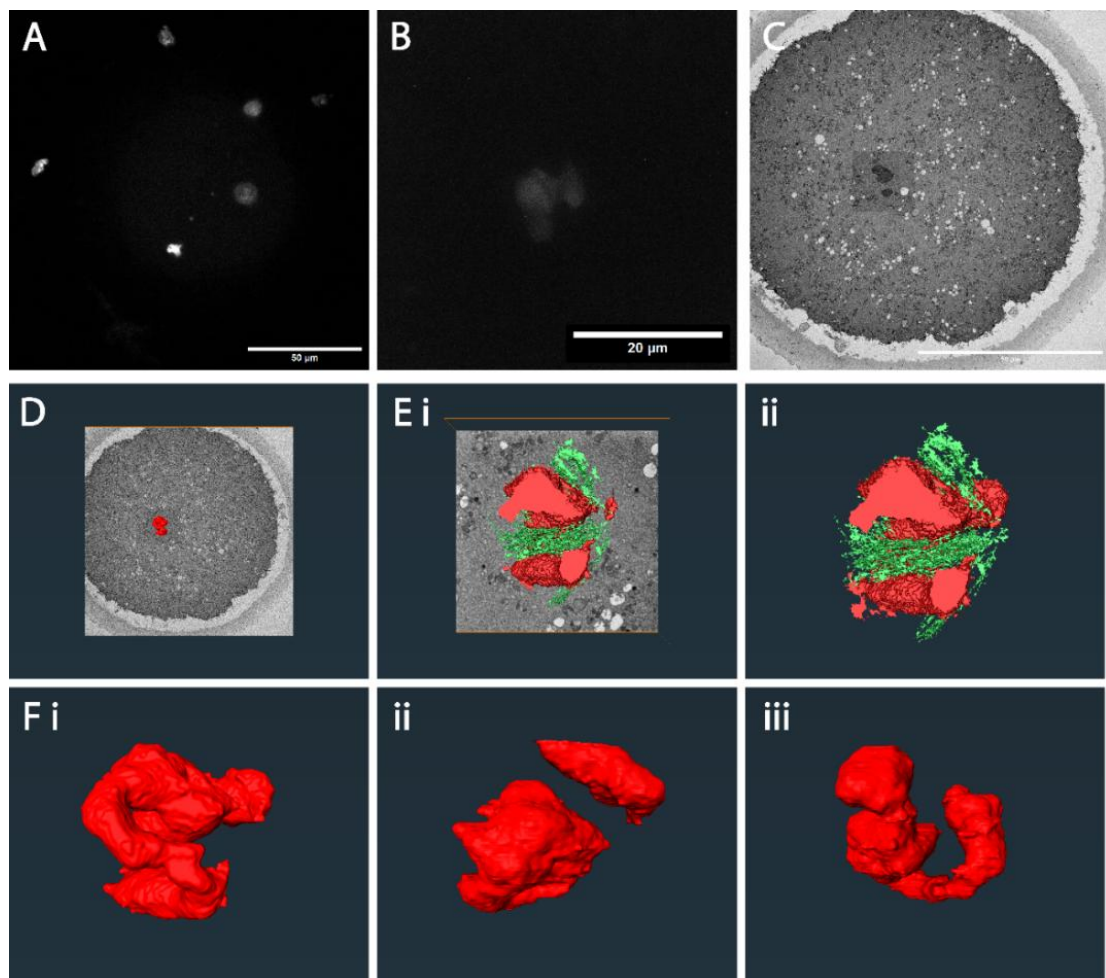


**Figure 5.8. SBF-SEM whole oocyte chromosome modelling.** (A) Max-projection of the oocyte stained with DAPI, showing little visible structure. (B) Max-projection of chromosome region. (C) Overview of the full oocyte imaged using SBF-SEM, with a nested ROI focusing on the chromosome region. (D-F) Segmented models derived from EM images showing chromosome structures. (E i-ii) Segmented chromosome ROI models, where the tops of the chromosomes were not fully captured due to slight misalignment. Chromosomes (red) and microtubules (green). (F i-iii) A complete chromosome complement was modelled from the full oocyte overview, displaying an abnormally structured

*chromosome arrangement that formed a single non-uniform shape rather than distinct chromosomes as observed in mouse oocytes—sample 3573. LM imaging was performed using a Zeiss LSM 900 with AiryScan 2 100× oil objective, and EM imaging was conducted using a Zeiss Crossbeam 550 FIB-SEM.*

#### 5.4.6. Optimisation for Human Oocytes

The imaging of human oocytes revealed specific requirements necessary for selecting cells that would be suitable for 3D-CLEM processing (Figure 5.9.). The EM results were inconsistent, and following a review of the trends observed in LM images, optimal selection parameters were defined.

Notably, many of these selection criteria could be determined using phase-contrast imaging, allowing for the identification of suitable oocytes with a standard benchtop widefield microscope. Table 5.9 summarises the key observations from LM imaging and their corresponding outcomes in EM.

This highlighted the importance of selecting round and non-granular oocytes in the LM images, as these characteristics were consistently associated with ZP and cytoplasmic abnormalities in the EM images. Additionally, chromosomes must be clearly visible in LM images—oocytes with indistinct chromosomes (presumably due to excessive DAPI staining) also exhibited poorly resolved chromosomes in EM images (Figure 5.9).

Furthermore, samples should be free of bubbles after fixation, as bubbles, despite appearing superficial, were associated with vacuoles within the cell and structural abnormalities. These defects were often not apparent in phase-contrast images, making the selection of appropriate cells more challenging.

Oocytes that met the following criteria—a well-defined round shape, a distinct ZP, a homogeneous (non-granulated) cytoplasm, and an absence of bubbles—were successfully imaged in EM.

**Table 5.9. Key characteristics observed in LM imaging and their corresponding impact on EM outcomes. Cells meeting the optimal selection criteria demonstrated superior structural preservation and imaging quality.**

| <b>SAMPLE</b> | <b>IF ISSUES IDENTIFIED</b>  | <b>EM – OUTCOME</b>  | <b>SELECTION CRITERIA</b>  |
|---------------|--|--|--|
| <b>3566</b>   | DAPI stain has a lot of background and IF is blurry                    | Cell appearance good, chromosomes visible, FIB-SEM not smooth        | Select round cells, cytoplasm not granular in phase                                      |
| <b>3498 A</b> | DAPI stain too dense to pick out chromosomes, bubbles visible in phase | Vacuoles inside the cell and FIB-SEM not smooth                      | No bubbles in phase, chromosomes must be visible   |
| <b>3498 B</b> | DAPI stain too dense to pick out chromosomes                           | Cell appearance good, chromosomes not visible                        | Chromosomes must be visible  |
| <b>3568 A</b> | Cell abnormally shaped   | ZP and perivitelline space not equal, no chromosomes                 | Select round cells, the chromosomes must be visible                                      |
| <b>3568 B</b> | Cell cytoplasm dark and grainy   | Cytoplasm only covers half of the cell space                         | Cytoplasm should not be granular   |
| <b>3572</b>   | Cytoplasm appears granular and folded                                  | Cytoplasm is folded and ZP is thin and dense, no chromosomes visible | Select round cells, cytoplasm should not be granular                                     |
| <b>3574</b>   | Cell is round but cytoplasm appears segmented                          | ZP appears to have been removed, no chromosomes                      | Cytoplasm should be round and not granular; the ZP should be evident in the phase images |

|             |   |   |  |
|-------------|---|---|--|
| <b>3573</b> | DAPI stain has a lot of background, chromosomes appear blurry | Cell structure looks good, chromosomes appear abnormally shaped | Chromosome structure in IF should be clearly defined |
|-------------|---|---|--|

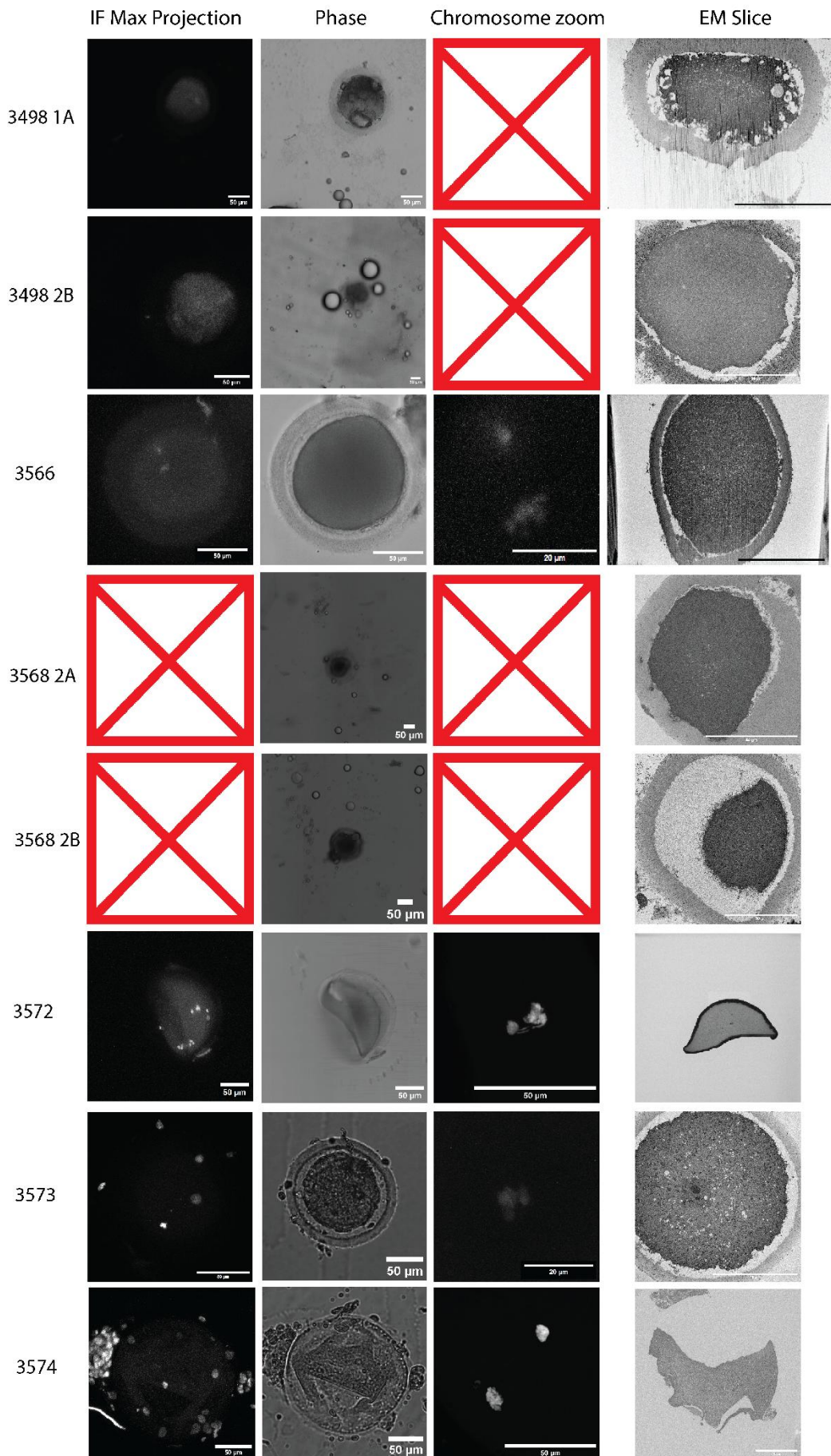


**Figure 5.9. A summary of oocyte imaging highlights the selection criteria for successful imaging.** *IF max projections, Phase overview of oocytes and chromosome zooms are shown for each cell with a single representative EM Slice. (red crosses refer to images that were corrupted).*

## 5.5. Discussion

This chapter aimed to apply the established 3D-CLEM pipeline to human oocytes to provide insight into human meiosis and generate novel three-dimensional geometric data of human chromosomes. The 3D-CLEM process, despite proving successful on both mitotic and mouse oocytes, presented new, unexpected challenges in the human oocytes that made the imaging less successful.

Live imaging was incorporated directly into the pipeline to provide temporal resolution of the chromosomes before fixation. This was done using a spinning disk microscope, and the intention was to observe the chromosomes during division to observe the nature of the chromosomes during meiosis I and identify the division stage to assist fixation. Unfortunately, it appeared that the long-term imaging of the oocytes caused damage to the cells and often led to chromosomal abnormalities.

The DAPI stain of the oocytes was one of the first issues that arose with the human oocytes. Despite the same concentration of the mouse oocytes being used, there was increased staining of the whole cell with that of the human oocytes. The excessive staining obscured the chromosomal structures, making localisation of the chromosome region more challenging. The cause of this excessive staining in some of the samples remains unclear, as DAPI stain has proven successful in previous publications (Cavazza et al., 2021; Gruhn et al.,

2019; Van Blerkom, 1990). Variations could be related to membrane permeability or DNA accessibility dependent on oocyte structure.

Additionally, the original fixation conditions appeared too harsh for the human oocytes. This was potentially the cause of some of the morphological changes that occurred in the samples. To mitigate this, the fixation protocol was adjusted from 2% PFA and 3% GLUT to a slightly milder 2%/2% formulation and performed on a heated stage to improve preservation. This was in an attempt to reduce the fixation time of the samples, preventing any alterations to the structure, as glutaraldehyde fixes samples using cross-linking to preserve ultrastructure, but this also results in extended fixation times. (Rhodes, 2013). However, despite these alterations, the morphological abnormalities remained, thus indicating that the fixation was not the cause of the observed issues.

### Patient-derived oocyte variations

The most crucial point to consider when reviewing this data was that the cells had been collected from patients seeking fertility treatment. This included issues such as polycystic ovarian syndrome (PCOS), endometriosis, diminished ovarian reserves and Tubal issues. This raised an important question: are the observed abnormalities direct consequences of the patient's condition, or do they represent natural variability? Given that the ultrastructure of human oocytes from patients with these conditions has not been well-characterized, this study highlights the need for a reference dataset of 'normal' oocytes imaged at this resolution. Establishing a baseline would enable the characterisation of disease-associated changes in oocyte morphology.

### *PCOS*

Sahu et al. (2008) conducted a retrospective study on 204 oocytes comparing PCOS, PCO-only and control oocytes and found no variation in the quality of the oocytes between the three groups. This was further supported by Uk et al. (2022), who conducted a cohort study on 1496 MII oocytes with various PCOS conditions and determined that the PCOS phenotype did not significantly alter the morphology of oocytes compared to the control group. Both studies used widefield microscopy to assess the morphology of the oocytes and, therefore, did not investigate the ultrastructural morphology of the cells. However, Sahu et al. (2022) did identify that the PCOS sample group had significantly higher rates of miscarriage than the PCO-only group, indicating an increased rate of aneuploidy within these cells, which may be due to chromosomal structure abnormalities. However, the 'normal' morphology of PCOS patients was supported by sample 3566 (Figure 4.1), an oocyte donated from a patient with PCOS. The chromosomes in this cell were the best quality of all the samples and were clearly defined, and even the kinetochores were visible. This provides supporting data to Sahu et al. (2008) and Uk et al. (2022) that oocyte morphology and, in fact, ultrastructure are not altered by PCOS.

### *Endometriosis*

Kasapoglu et al., (2018) examined 1568 oocytes split into endometriosis and control groups. The oocytes in the endometriosis group were found to have significantly higher abnormal morphology than the control group. This included variations such as darker cytoplasm, darker and thinner ZP and misshapen polar

bodies. This was in agreement with the EM images of the sample provided by a patient with endometriosis (sample 3572; figure 4.5), which showed a thin and intensely stained ZP. However, a later study conducted by Robin et al. (2021) contradicted this data. The group conducted a survey of 6000 oocytes in IVF/ICSI patients to determine the effect of endometriosis on oocyte morphology. The cell quality was quantified using the average oocyte quality index (AOQI) and metaphase II morphological scoring system (MOMS). Despite observing reduced MII oocytes during collection and fewer resultant pregnancies when compared to the control group, the AOQI and MOMS scores did not significantly differ from the controls. This indicated that endometriosis did not affect the oocyte morphology and therefore suggests that any abnormalities observed during 3D-CLEM imaging of oocytes from patients with endometriosis were not a result of disease-associated changes. Despite this disagreement, a recent systematic study of endometriosis effect on morphology concluded that it did, in fact, decrease oocyte quality and therefore suggests that abnormalities in these sample types may be genuine to the native state of the oocyte and not a result of artefacts due to processing (Fan et al., 2025).

In some cases, the pipeline was successful for human oocytes and, therefore, provides the basis for future analysis of human oocyte chromosome geometry. However, the inconsistency with the results indicates that this would need further optimisation. Using healthy oocytes from egg-sharing programs would be ideal for generating a standard chromosome atlas. However, studying oocytes from patients with reproductive disorders remains crucial for understanding disease-specific chromosomal abnormalities. This would require

oocytes that would be considered suitable for IVF, which would only be accessible through an egg-sharing program. This would be a slow process due to the nature of egg-sharing donation, but it would provide the best samples for a reference chromosome atlas. Furthermore, for improved morphology and reduced artefacts in the sample, removing live imaging from the pipeline should help reduce stress on the samples, providing the most accurate data to the native state cells. Despite the issues that arose, 3D-CLEM of the human oocytes did produce the first 3D model of chromosomes and clearly identified both microtubules and kinetochores, highlighting the potential of this method for the investigation of meiotic chromosome geometry. Overall, this work provides the foundation for future investigations into human oocyte meiosis, with potential implications for understanding aneuploidy, infertility, and assisted reproductive technologies.

## 6. Discussion

### 6.1. Summary of Research Aims

The purpose of this study was to interrogate three main hypotheses: (1) Developing and using a 3D-CLEM pipeline at UoN, to study entire mitotic progression and “atlas” the chromosomes at all stages (2) Ki67 is a critical component of the chromosome periphery in oocytes (3) the 3D-CLEM pipeline can be applied to human oocytes to study 3D architecture of human oocyte chromosomes to reveal novel aspects of the human oocyte division machinery. To address these hypotheses, three key research aims were defined,

corresponding to the major chapters of the thesis: (1) optimise the 3D-CLEM pipeline for chromosome analysis and use it to create the first ever mitotic chromosome atlas, (2) study the chromosome periphery in oocytes, undertaking the first study of its kind to explore the role of Ki67 in meiosis, exploiting the development of 3D-CLEM from aim 1, (3) develop imaging tools to generate the first 3D EM images of human oocyte chromosomes. All of these aims were achieved, and the degree of success and aspects that require further development are discussed below.

The first aim, to optimise the pipeline and create a mitotic atlas, was successfully achieved in collaboration with the University of Edinburgh. The 3D-CLEM pipeline was optimised for imaging dividing cells and then applied to human mitotic cells. This effort resulted in the creation of a detailed 3D mitotic chromosome atlas and yielded novel data about chromosome geometry during the mitotic stages. The results presented in Chapter 3 (and the associated publication produced from this data; Cisneros-Soberanis and Simpson et al., 2024) demonstrate the feasibility and robustness of the 3D-CLEM technique and its ability to generate novel biological insights that are impactful to the scientific community. The successful completion of this aim provides a strong proof-of-concept for using correlated light and electron microscopy in chromosome research.

The second aim was to investigate the role of Ki67 and the chromosome periphery in meiosis to determine whether the periphery plays a similar role to that already defined in somatic cells and explore this role using ultrastructural

analysis and Ki67 depletion. This aim was also largely accomplished, primarily through studies on mouse oocytes as a model for meiosis (Simpson et al., 2024). The methodology was applied to meiotic cells, confirming the presence of Ki67 at the chromosome periphery in oocytes and revealing a key role for Ki67 in meiotic chromosome organisation. The ultrastructural analysis of chromosomes using the 3D-CLEM pipeline allowed comparative investigation of chromosome morphology, progression, and organisation in both control and Ki67 KD oocytes. The comparison between these groups demonstrated the importance of Ki67 for multiple aspects of chromosome behaviour and highlighted that loss of Ki67 has a detrimental effect on oocyte cell-cycle progression. By exploring the impact of Ki67 loss in this high-resolution volume context, the role of Ki67 in meiosis has begun to be defined, potentially providing insights into one of the causes of the aneuploidies known to occur in oocytes and laying a foundation for future studies in oocyte biology and fertility. These findings resulted in a pre-print publication in collaboration with researchers at the Universities of Newcastle and Warwick. This work highlights both the successful development of the 3D-CLEM technique for meiotic cells and the new understanding of Ki67's role in meiosis as significant contributions to existing knowledge in the field.

The final aim of this study was to apply the established 3D-CLEM pipeline to human oocytes with a long-term view to generate a meiotic chromosome atlas. While a complete meiotic atlas could not be achieved within this project, significant progress was made that lays the foundation for future work to expand upon. This research identified several technical challenges and highlighted the optimisation necessary to build a meiotic atlas. Despite the dataset not being

complete, valuable results were obtained, including the visualisation of kinetochores in meiotic cells and the first volume 3D segmentation of meiotic chromosomes. These results provide crucial groundwork for subsequent research to create a more comprehensive meiotic chromosome atlas.

In summary, the outcomes of this thesis indicate that the primary research objectives were largely met: the 3D-CLEM pipeline was established and proven effective for chromosomal ultrastructure studies, a novel role for Ki67 in meiosis was uncovered, and significant strides were taken toward mapping meiotic chromosomes in human oocytes. This study highlights the value of improving imaging techniques and furthering knowledge of meiotic chromosome structure and behaviour to address fundamental questions in cell division biology.

## 6.2. Mitotic Atlas:

One of the key results from this study was the 3D mitotic chromosome atlas, which provides an essential reference for future chromosome research. The ability to resolve mitotic chromosomes in three dimensions at such high resolution offers a novel workflow for studying chromosome compaction and investigating mitotic abnormalities that may be linked to aneuploidy and consequently disease. This atlas explores fundamental aspects of cell division biology by capturing chromosome ultrastructure in control cells, creating a reference for normal human chromosome architecture during mitosis. It lays the groundwork for comparative studies, e.g., investigations of abnormal

chromosome ultrastructure in experimental studies that can use the atlas as a comparison for what normal chromosome organisation looks like.

### 6.3. Ki67 in Meiosis

This study confirmed the presence of Ki67 in meiotic cells at the chromosome periphery and identified a novel role for this protein during female meiosis, highlighting its potential involvement in chromosome organisation during meiosis (similar to its known role in organising the mitotic periphery; Booth et al., 2014). Ki67 has been extensively studied in mitotic cells as a proliferation marker, where it plays critical roles in chromatin organisation and nuclear envelope reformation (Booth et al., 2014; Cuylen et al., 2016). However, Ki67's function in meiosis remains almost completely unexplored. The results reported in this thesis are among the first to suggest that Ki67 also contributes to chromosome stability and organisation during meiosis. This bridges a gap in the literature by extending knowledge of Ki67 from mitotic cell division into meiotic cell division.

The presence of Ki67 in oocytes suggests that it may help maintain meiotic chromosomal structure, similar to its established functions in dividing mitotic cells. Given Ki67's known association with chromatin condensation in mitosis, its involvement in meiosis could directly influence chromosome separation and aneuploidies that occur in oocytes. These findings suggest Ki67 is a potentially fundamental factor in meiotic chromosome maintenance. Further research is warranted to determine if variations in Ki67 intensity lead to increased errors in meiotic division and to understand the mechanisms in which Ki67 functions to

organise the periphery. Addressing this could validate the role of Ki67 in ensuring accurate chromosome segregation and pinpoint Ki67 as a possible biomarker or therapeutic target in the context of aneuploidy-related infertility.

## 6.4. Volume Imaging of Human Oocytes

Another aim of this thesis was to develop volume EM methods for analysis of human oocytes. Although a meiotic atlas was not completed, the project resulted in important insights and highlighted clear directions for future efforts. Methodological challenges, particularly in sample preparation and imaging, limited the production of an atlas, but novel findings were still produced. In particular, this work achieved the first successful volume 3D segmentation of human meiotic chromosomes and enabled direct visualisation of kinetochores and microtubules within human oocytes. These accomplishments are significant because they demonstrate the feasibility of applying advanced 3D imaging to meiotic cells, and they provide proof-of-principle data that can be built upon to eventually map all chromosomes throughout meiosis.

Previously analysis of meiotic chromosome behaviour has relied on techniques like immunofluorescence microscopy (Bellou et al., 2024; Wynne & Funabiki, 2016) and traditional electron microscopy (Sezen & Cincik, 2003; Tatičková et al., 2023). While these methods have produced essential information on oocyte structure and behaviour, they each have limitations: immunofluorescence is constrained by optical resolution. It typically provides only 2D or limited 3D information, whereas conventional EM often requires destructive sample preparation and produces 2D data. In comparison, the 3D-

CLEM approach used in this thesis allows for 3D imaging and reconstruction of cells and offers a more detailed volume analysis of meiotic chromosome architecture. By doing so, this study was able to capture specific features such as kinetochores, as well as overall chromosomal geometry, that might have been less identifiable in traditional imaging techniques.

The partial success in creating a meiotic atlas also highlighted the challenges inherent in working with this specific sample type. For instance, preservation of meiotic structures proved difficult, some loss of native structure can occur during sample processing, underscoring the need for protocol optimisation, however, the variation in the impact of the sample processing on the oocyte structure indicated it was not the only factor to consider. Despite the challenges, the ability to visualise kinetochores within meiotic cells was an important validation of the approach. It confirmed the success of the pipeline for human oocytes and presented the opportunity to explore these chromosome ultrastructures in 3D in future work. This insight provides a starting point for deeper investigations into how chromosomes attach to and are moved by the meiotic spindle, an area crucial for understanding why errors in chromosome segregation are so prevalent in human oocytes. Therefore, although the comprehensive meiotic atlas was not completed, the optimisation and initial results represent a significant step forward. The insights gained lay a strong foundation for refining imaging methodologies for meiotic research. Segmenting and analysing meiotic chromosomes in 3D provides a method of investigating chromosome ultrastructure in a high-resolution and quantitative manner. This is a significant development towards eventually mapping the complete 3D

architecture of meiotic chromosomes during each stage of division, which remains an important goal for future research.

## 6.5. Limitations

### Throughput and Sample Size:

One primary challenge was the low throughput nature of the correlative imaging technique. Although the 3D-CLEM approach produces nanometre precise data, the process of preparing and imaging each sample is time-consuming and technically advanced. This limited the number of oocytes and cells that could be analysed within the project's timeframe. The relatively small sample size means that, although significant observations were noted, statistical power is limited, and trends in phenotypic variations might have gone undetected. In an attempt to mitigate this issue, deep learning-based segmentation and analysis were explored to improve segmentation. However, applying deep-learning to this 3D-CLEM pipeline required expertise and time beyond the scope of this project. In the future, collaborations with computational scientists to develop these pipelines should be a priority to improve data acquisition and sample throughput. Enhancing the throughput in this way would allow for analysis of a larger population of cells, strengthening the robustness of conclusions drawn from 3D-CLEM data. Applying deep learning to cell segmentation is not new, but it is a significant trend in all areas of image acquisition as the low-throughput of analysis is a significant bottleneck in many pipelines (Kamentsky et al., 2011; Stylianidou et al., 2016).

## Stage Variability in Meiosis:

A second limitation relates to the dynamic nature of meiotic progression. Meiotic cells can show variations in how they progress through stages, and our understanding of defined stages (prophase, metaphase, anaphase, etc.) in oocytes is still expanding. This study observed some variability (for example, unexpected chromosomal configurations in metaphase; Figure 4.2.), suggesting that a more defined approach to classifying meiotic stages is needed. Live-cell imaging could address this limitation by allowing continuous observation of meiotic events. Incorporating live fluorescence imaging before fixing and processing cells for electron microscopy could enable the correlation of dynamic events with ultrastructural outcomes. However, this introduces its own challenges, particularly when working with sensitive cells as the exposure to live-imaging at the resolution required for chromosomal identification can cause cell stress resulting in structural changes prior to fixation for EM (Icha et al., 2017). However, methodologies have been developing to combat these issues, and this should be explored further and optimised for this pipeline, as such an approach would provide a more complete overview of meiotic chromosome behaviour (Campbell et al., 2022; Zielinska & Schuh, 2018).

## Technical Difficulties

Another important consideration is the potential for the introduction of artefacts during sample preparation and imaging, a common and high-priority occurrence during EM sample processing. The preparation protocols for electron microscopy, including chemical fixation, dehydration, resin embedding, and

heavy metal staining, can introduce structural distortions or obscure certain details. Although this method was optimised to preserve native structures, we cannot rule out that some observations were influenced by processing. Expanding on this workflow and utilising alternative techniques for comparison should be explored to confirm that our observations reflect native-state structures. For instance, incorporating cryo-electron microscopy (cryo-EM) in future studies would allow imaging of vitrified samples in a near-native state, thereby reducing artefacts.

Another approach, such as array tomography, could also be considered; this method involves serial slicing and immunostaining while retaining the ability to revisit the same sample, enabling non-destructive 3D imaging at high resolution. This would enable the sample to be imaged and reconstructed, while also allowing further investigation (i.e. revisiting) into ROIs at a later date. This method could result in increased data output from a single sample as multiple areas could be investigated in high resolution, which would be particularly useful when handling rare or precious sample types such as oocytes. Using emerging technologies such as multibeam SEM (mSEM) could also improve throughput when applied to an array tomography method, by utilising 91 beams instead of a single beam it can image multiple areas simultaneously, thus reducing the overall imaging time required for a single cell (1mm<sup>2</sup> at 4nm pixel size can be imaged in a few minutes) (*ZEISS MultiSEM*, n.d.). Each of these methodological improvements addresses a specific limitation of the current pipeline e.g. preserving native ultrastructure or speeding up data collection. Incorporating

them into the existing pipeline could further improve the outcomes of 3D-CLEM studies.

## Biological Sample Constraints

Lastly, the source and condition of biological samples impose limitations on the conclusions that can be drawn from this data. The human oocytes examined in this study were donated from patients undergoing fertility treatments and were deemed unsuitable for IVF procedures. These oocytes likely represent samples with underlying quality issues, which means the chromosomal abnormalities observed might not be representative of healthy, typical oocytes. It remains unclear whether certain irregularities seen (for example, misaligned chromosomes or spindle defects) were purely a result of our experimental manipulation or partly due to the intrinsic poor quality of these oocytes. Ideally, to distinguish between these possibilities, control oocyte samples known to be of high quality (such as donated surplus oocytes from an egg-sharing program) should be included to provide the most optimal reference. Unfortunately, obtaining such samples can be ethically and logistically challenging and would significantly slow down the research pipeline. Without access to “normal” oocyte controls, it is challenging to fully validate that our imaging technique and findings are free from sample-related bias. Future work should involve further optimising sample preparation to minimise stress on sensitive oocytes and broadening the samples to include multiple species e.g. bovine and porcine, to ensure the observations are consistent and biologically relevant. In summary, the findings from this data are novel and proves the

methodology will be applicable to this sample type with further improvement, and understanding of human meiotic chromosome ultrastructure will only improve with increased samples. Further optimisation and validation with higher-quality oocytes will confirm the techniques reliability as well as eventually producing a meiotic atlas as a reference for the ultrastructure of human chromosomes during meiosis.

## 6.6. Significance and Future Directions

Despite the challenges outlined above, this study clearly demonstrates the value of advanced 3D-CLEM imaging techniques in exploring chromosome organisation and meiotic progression. The ability to reconstruct chromosome ultrastructure in 3D provides a high-resolution method for understanding meiotic chromosomal behaviour, with direct implications for understanding the origins of aneuploidy and related fertility disorders. This work opens up new questions about how subtle structural differences might influence fertility outcomes.

One of the key findings of this research was the identification of Ki67's role in meiosis, a previously unexplored aspect of meiotic chromosomes. This data provides novel insights into Ki67's role in maintaining chromosomal structure and preventing aneuploidy, or an abnormal number of chromosomes. To expand upon this further and fully understand the nature of Ki67's role during meiotic division, future studies should investigate Ki67's molecular interactions with chromatin and cell-cycle checkpoints to better understand its function in this process. Determining how Ki67 affects events like chromosome condensation, spindle attachment, or DNA repair in oocytes could offer further insight into its

mechanism of action during meiosis. Such research will not only expand on existing scientific knowledge about the regulation of meiosis, but may also have practical applications, such as evaluating Ki67 as a potential target for therapeutic intervention to improve oocyte quality or as a biomarker for assessing egg viability in clinical settings.

More broadly, the outcomes of this thesis highlight the importance of a collaborative approach that combines correlative imaging pipelines, live-cell imaging, and computational analysis to tackle research into meiotic cell biology. Combining multiple technologies can adjust for the limitations of a single method e.g. live-cell imaging adds temporal resolution, 3D-CLEM imaging adds ultrastructural detail, and computational image analysis increases the throughput and consequently the sample size. By exploring meiotic errors, it lays the groundwork for further investigation into chromosome structure that could potentially translate into direct clinical applications.

In conclusion, the findings of this discussion strongly connect to the original research objectives and hypotheses. This thesis has advanced knowledge in significant ways: it established new technical workflows for 3D chromosome analysis, discovered a novel role for Ki67 in meiotic fidelity, and made initial steps toward comprehensive mapping of meiotic chromosomes. These contributions address the questions posed at the outset of the project and open several pathways for future investigation. Continuing research into chromosome ultrastructure and continuing to advance imaging techniques for more detailed investigation will further expand the understanding of

chromosome behaviour during cell division, particularly meiosis, with the future goal of producing direct clinical applications to identify and potentially even reduce chromosome abnormalities that contribute to infertility and healthy development.

## 7. Appendix

### 7.1. Professional Industry Placement

As part of the BBSRC PhD training programme each student is required to undertake a placement away from their project to explore other areas of interest and gain an understanding and appreciation of different types of work outside their research project. Having the connections through my supervisory team I chose to undertake this placement with The University of Warwick to gain some hands-on experience with human oocytes and the Fertility Clinic.

I previously had experience in a fertility clinic prior to starting this PhD however, that work was clinical and involved shadowing rather than direct hands-on work. This placement allowed me to go into the clinics and see the process of performing research with patient samples, as well as giving me hands on experience with live human oocytes which was not something I had previously been able to do.

The experience I gained from this placement was invaluable. It gave me the opportunity to see 'behind the scenes' of fertility research as well as giving me the chance to go into the fertility clinics myself and interact with the clinicians

and embryologists undertaking this work. Through this placement I was exposed to career options I had never before known existed as well as the complexities of obtaining and handling such precious sample types. I knew prior to this placement that I wanted to pursue a career in a laboratory setting and this opportunity gave me even more options to consider for the future. It was also extremely rewarding to be able to see the direct implications of the work. Academic research can often seem very detached from the people who will benefit from the work, and often those benefits will not be seen for years to come. Working alongside, patients, clinicians, embryologists and research scientists allowed me to see the 'big picture' of academic research and renewed my motivation to pursue a career in this area.

I was initially reluctant to take time away from my PhD especially after the complications that had delayed work in the first years due to equipment failures and covid impacts. However, I am incredibly grateful to have had the chance to leave the research project and explore other areas of interest (despite how similar the areas of research were). I thoroughly enjoyed my placement and feel that it gave me some reassurance about what kind of future career I want following on from this PhD.

## 7.2. Mitotic Atlas Images

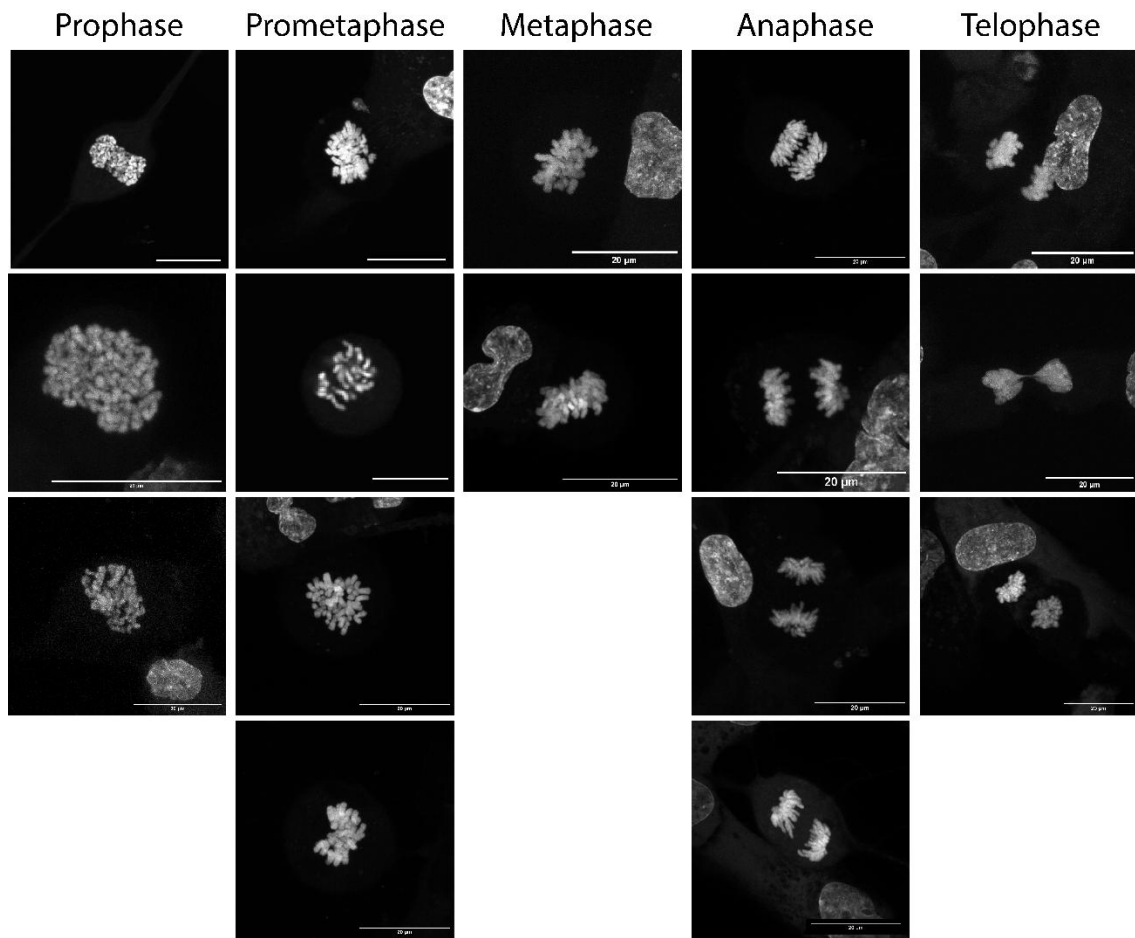


*Figure 7.1. Light microscopy max projection images of the chromosomes processed with 3D-CLEM for the mitotic atlas data.*

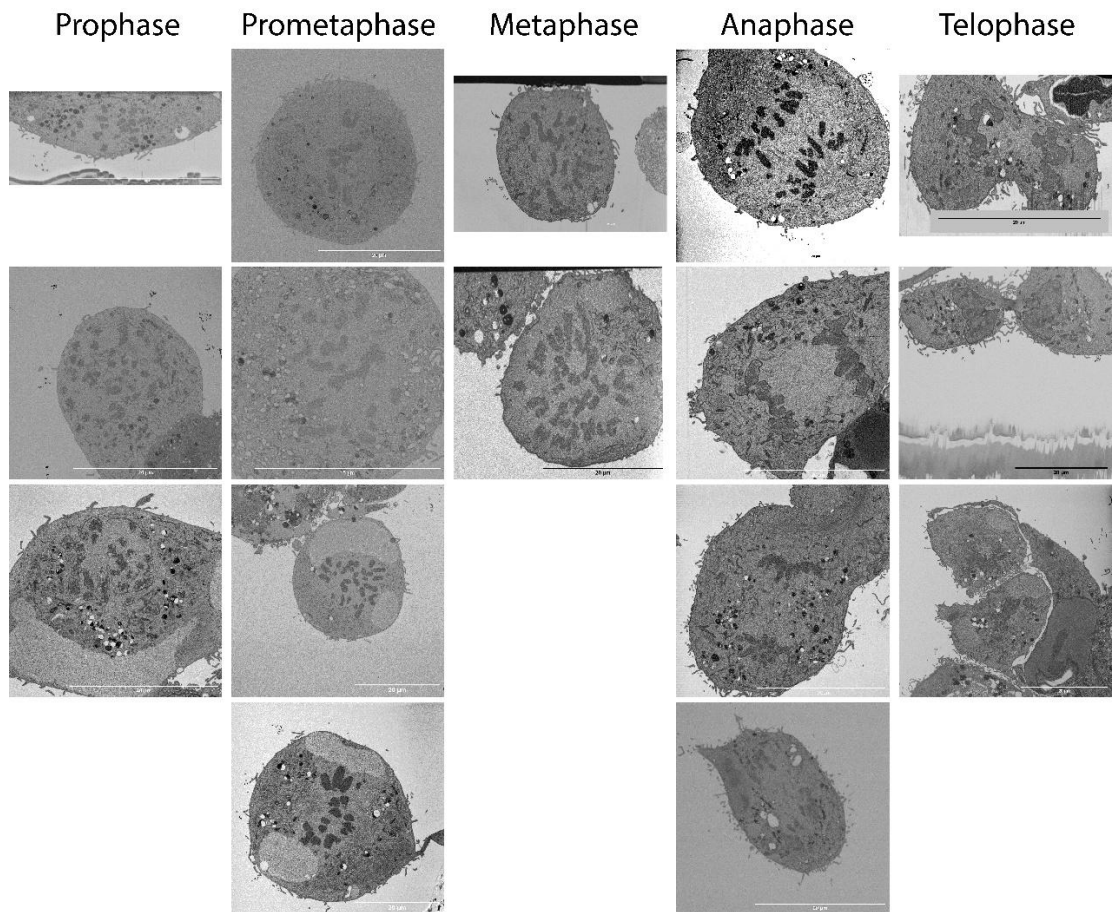


Figure 7.2. Electron microscopy single slice representative images of the chromosomes processed with 3D-CLEM for the mitotic atlas data.

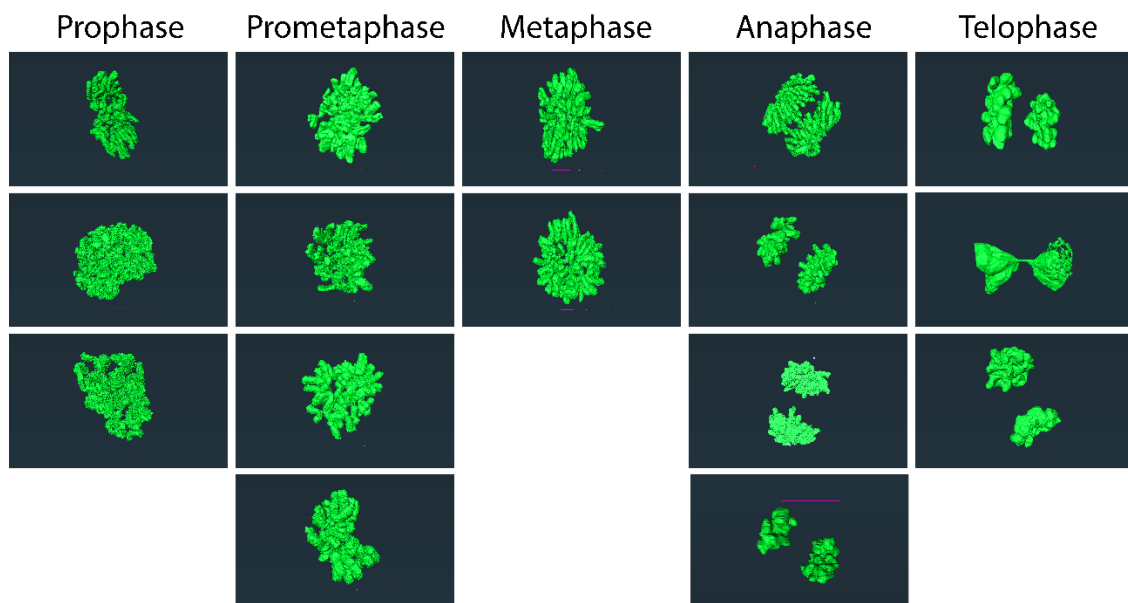


Figure 7.3. AMIRA segmented 3D models of the chromosomes processed with 3D-CLEM for the mitotic atlas data.

### 7.3. Mitotic Atlas Quantitative Data

Table 7.1. Surface Area measurements for each of the cells processed for 3D-CLEM in the mitotic atlas.

SURFACE AREA  $\mu\text{M}^2$

| STAGE        | Light   |         |         |         | Electron |          |          |          |
|--------------|---------|---------|---------|---------|----------|----------|----------|----------|
| PROPHASE     | 1284.37 | 4342.0  | 2659.7  |         | 1267.06  | 2930.62  | 3031.62  |          |
| PROMETAPHASE | 735.334 | 1263.93 | 3126.14 | 746.76  | 1412.39  | 2779.995 | 1483.281 | 1561.64  |
| METAPHASE    | 1163.36 | 747.12  |         |         | 975.39   | 2161.399 |          |          |
| ANAPHASE     | 1071.06 | 606.248 | 939.161 | 765.714 | 2137.55  | 1388.117 | 1733.84  | 1486.212 |
| TELOPHASE    | 481.877 | 544.97  | 799.06  |         | 990.552  | 1377.01  | 712.772  |          |

Table 7.2. Volume measurements for each of the cells processed for 3D-CLEM in the mitotic atlas.

VOLUME  $\mu\text{M}^3$ 

| STAGE        | Light   |         |         |         | Electron |         |         |         |
|--------------|---------|---------|---------|---------|----------|---------|---------|---------|
| PROPHASE     | 707.695 | 616.207 | 438.25  |         | 138.798  | 198.575 | 216.258 |         |
| PROMETAPHASE | 578.406 | 798.138 | 371.203 | 338.25  | 226.198  | 192.823 | 162.723 | 192.516 |
| METAPHASE    | 416.357 | 421.054 |         |         | 206.768  | 267.621 |         |         |
| ANAPHASE     | 475.032 | 322.174 | 523.961 | 411.813 | 178.405  | 238.81  | 318.29  | 147.212 |
| TELOPHASE    | 193.146 | 194.292 | 539.743 |         | 301.844  | 202.41  | 273.807 |         |

## 8. References

- Adolph, K. W., Cheng, S. M., & Laemmli, U. K. (1977). Role of nonhistone proteins in metaphase chromosome structure. *Cell*, 12(3), 805–816. [https://doi.org/10.1016/0092-8674\(77\)90279-3](https://doi.org/10.1016/0092-8674(77)90279-3)
- Afzelius, B. A. (1992). Section staining for electron microscopy using tannic acid as a mordant: A simple method for visualization of glycogen and collagen. *Microscopy Research and Technique*, 21(1), 65–72. <https://doi.org/10.1002/jemt.1070210110>
- Akera, T., Chmátal, L., Trimm, E., Yang, K., Aonbangkhen, C., Chenoweth, D. M., Janke, C., Schultz, R. M., & Lampson, M. A. (2017). Spindle asymmetry drives non-Mendelian chromosome segregation. *Science*, 358(6363), 668–672. <https://doi.org/10.1126/science.aan0092>
- Antonin, W., & Neumann, H. (2016). Chromosome condensation and decondensation during mitosis. *Current Opinion in Cell Biology*, 40, 15–22. <https://doi.org/10.1016/j.ceb.2016.01.013>
- Avery, O. T., Macleod, C. M., & McCarty, M. (1944). STUDIES ON THE CHEMICAL NATURE OF THE SUBSTANCE INDUCING TRANSFORMATION OF PNEUMOCOCCAL TYPES: INDUCTION OF TRANSFORMATION BY A DESOXYRIBONUCLEIC ACID FRACTION ISOLATED FROM PNEUMOCOCCUS TYPE III. *The Journal of Experimental Medicine*, 79(2), 137–158. <https://doi.org/10.1084/jem.79.2.137>

- Batty, P., & Gerlich, D. W. (2019). Mitotic Chromosome Mechanics: How Cells Segregate Their Genome. *Trends in Cell Biology*, 29(9), 717–726. <https://doi.org/10.1016/j.tcb.2019.05.007>
- Beagan, J. A., & Phillips-Cremins, J. E. (2020). On the existence and functionality of topologically associating domains. *Nature Genetics*, 52(1), 8–16. <https://doi.org/10.1038/s41588-019-0561-1>
- Bellou, E., Zielinska, A. P., Mönnich, E. U., Schweizer, N., Politi, A. Z., Wellecke, A., Sibold, C., Tandler-Schneider, A., & Schuh, M. (2024). Chromosome architecture and low cohesion bias acrocentric chromosomes towards aneuploidy during mammalian meiosis. *Nature Communications*, 15(1), 10713. <https://doi.org/10.1038/s41467-024-54659-3>
- Bolles Lee, A. (1920). The Structure of certain Chromosomes and the Mechanism of their Division. *Journal of Cell Science*, s2-65(257), 1–32. <https://doi.org/10.1242/jcs.s2-65.257.1>
- Bongso, A., Chye, N. S., Ratnam, S., Sathananthan, H., & Wong, P. C. (1988). Chromosome anomalies in human oocytes failing to fertilize after insemination in vitro. *Human Reproduction*, 3(5), 645–649. <https://doi.org/10.1093/oxfordjournals.humrep.a136760>
- Booth, D. G., Beckett, A. J., Molina, O., Samejima, I., Masumoto, H., Kouprina, N., Larionov, V., Prior, I. A., & Earnshaw, W. C. (2016). 3D-CLEM Reveals that a Major Portion of Mitotic Chromosomes Is Not Chromatin. *Molecular Cell*, 64(4), 790–802. <https://doi.org/10.1016/j.molcel.2016.10.009>

- Booth, D. G., & Earnshaw, W. C. (2017). Ki-67 and the Chromosome Periphery Compartment in Mitosis. *Trends in Cell Biology*, 27(12), 906–916. <https://doi.org/10.1016/j.tcb.2017.08.001>
- Booth, D. G., Takagi, M., Sanchez-Pulido, L., Petfalski, E., Vargiu, G., Samejima, K., Imamoto, N., Ponting, C. P., Tollervey, D., Earnshaw, W. C., & Vagnarelli, P. (2014). Ki-67 is a PP1-interacting protein that organises the mitotic chromosome periphery. *eLife*, 3, e01641. <https://doi.org/10.7554/eLife.01641>
- Brooker, A. S., & Berkowitz, K. M. (2014). The roles of cohesins in mitosis, meiosis, and human health and disease. *Methods in Molecular Biology (Clifton, N.J.)*, 1170, 229–266. [https://doi.org/10.1007/978-1-4939-0888-2\\_11](https://doi.org/10.1007/978-1-4939-0888-2_11)
- Brosens, J. J., Bennett, P. R., Abrahams, V. M., Ramhorst, R., Coomarasamy, A., Quenby, S., Lucas, E. S., & McCoy, R. C. (2022). Maternal selection of human embryos in early gestation: Insights from recurrent miscarriage. *Seminars in Cell & Developmental Biology*, 131, 14–24. <https://doi.org/10.1016/j.semcdb.2022.01.007>
- Bucana, C., Hoyer, L. C., Hobbs, B., Breesman, S., McDaniel, M., & Hanna, M. G. (1976). Morphological evidence for the translocation of lysosomal organelles from cytotoxic macrophages into the cytoplasm of tumor target cells. *Cancer Research*, 36(12), 4444–4458.
- Campbell, J. M., Mahbub, S. B., Bertoldo, M. J., Habibalahi, A., Goss, D. M., Ledger, W. L., Gilchrist, R. B., Wu, L. E., & Goldys, E. M. (2022). Multispectral autofluorescence characteristics of reproductive aging in

old and young mouse oocytes. *Biogerontology*, 23(2), 237–249.

<https://doi.org/10.1007/s10522-022-09957-y>

Cattoretti, G., Becker, M. H. G., Key, G., Duchrow, M., Schlüuter, C., Galle, J., &

Gerdes, J. (1992). Monoclonal antibodies against recombinant parts of the

Ki-67 antigen (MIB 1 and MIB 3) detect proliferating cells in microwave-

processed formalin-fixed paraffin sections. *The Journal of Pathology*,

168(4), 357–363. <https://doi.org/10.1002/path.1711680404>

Cavazza, T., Takeda, Y., Politi, A. Z., Aushev, M., Aldag, P., Baker, C., Choudhary,

M., Bucevičius, J., Lukinavičius, G., Elder, K., Blayney, M., Lucas-Hahn, A.,

Niemann, H., Herbert, M., & Schuh, M. (2021). Parental genome

unification is highly error-prone in mammalian embryos. *Cell*, 184(11),

2860-2877.e22. <https://doi.org/10.1016/j.cell.2021.04.013>

Chaigne, A., Verlhac, M.-H., & Terret, M.-E. (2012). Spindle positioning in

mammalian oocytes. *Experimental Cell Research*, 318(12), 1442–1447.

<https://doi.org/10.1016/j.yexcr.2012.02.019>

Champion, L., Pawar, S., Luithle, N., Ungricht, R., & Kutay, U. (2019). Dissociation

of membrane-chromatin contacts is required for proper chromosome

segregation in mitosis. *Molecular Biology of the Cell*, 30(4), 427–440.

<https://doi.org/10.1091/mbc.E18-10-0609>

Chen, X., Zheng, B., & Liu, H. (2011). Optical and digital microscopic imaging

techniques and applications in pathology. *Analytical Cellular Pathology*

(*Amsterdam*), 34(1–2), 5–18. <https://doi.org/10.3233/ACP-2011-0006>

Christopikou, D., Tsorva, E., Economou, K., Shelley, P., Davies, S., Mastrominas,

M., & Handyside, A. H. (2013). Polar body analysis by array comparative

genomic hybridization accurately predicts aneuploidies of maternal meiotic origin in cleavage stage embryos of women of advanced maternal age. *Human Reproduction (Oxford, England)*, 28(5), 1426–1434. <https://doi.org/10.1093/humrep/det053>

Cisneros-Soberanis, F., Simpson, E. L., Beckett, A. J., Pucekova, N., Corless, S., Kochanova, N. Y., Prior, I. A., Booth, D. G., & Earnshaw, W. C. (2024). Near millimolar concentration of nucleosomes in mitotic chromosomes from late prometaphase into anaphase. *Journal of Cell Biology*, 223(11), e202403165. <https://doi.org/10.1083/jcb.202403165>

Coleman, L. C., & Hillary, B. B. (1941). The Minor Coil in Meiotic Chromosomes and Associated Phenomena as Revealed by the Feulgen Technique. *American Journal of Botany*, 28(6), 464–469. <https://doi.org/10.2307/2437046>

Combs, C. A. (2010). Fluorescence Microscopy: A Concise Guide to Current Imaging Methods. *Current Protocols in Neuroscience*, 50(1). <https://doi.org/10.1002/0471142301.ns0201s50>

Corpet, A., Kleijwegt, C., Roubille, S., Juillard, F., Jacquet, K., Texier, P., & Lomonte, P. (2020). PML nuclear bodies and chromatin dynamics: Catch me if you can! *Nucleic Acids Research*, 48(21), 11890–11912. <https://doi.org/10.1093/nar/gkaa828>

Currie, C. E., Ford, E., Benham Whyte, L., Taylor, D. M., Mihalas, B. P., Erent, M., Marston, A. L., Hartshorne, G. M., & McAinsh, A. D. (2022). The first mitotic division of human embryos is highly error prone. *Nature Communications*, 13(1), 6755. <https://doi.org/10.1038/s41467-022-34294-6>

- Cuylen, S., Blaukopf, C., Politi, A. Z., Müller-Reichert, T., Neumann, B., Poser, I., Ellenberg, J., Hyman, A. A., & Gerlich, D. W. (2016). Ki-67 acts as a biological surfactant to disperse mitotic chromosomes. *Nature*, *535*(7611), 308–312. <https://doi.org/10.1038/nature18610>
- de Castro, I. J., Budzak, J., Di Giacinto, M. L., Ligammari, L., Gokhan, E., Spanos, C., Moralli, D., Richardson, C., de las Heras, J. I., Salatino, S., Schirmer, E. C., Ullman, K. S., Bickmore, W. A., Green, C., Rappsilber, J., Lamble, S., Goldberg, M. W., Vinciotti, V., & Vagnarelli, P. (2017). Repo-Man/PP1 regulates heterochromatin formation in interphase. *Nature Communications*, *8*(1), 14048. <https://doi.org/10.1038/ncomms14048>
- Dixon, J. R., Selvaraj, S., Yue, F., Kim, A., Li, Y., Shen, Y., Hu, M., Liu, J. S., & Ren, B. (2012). Topological domains in mammalian genomes identified by analysis of chromatin interactions. *Nature*, *485*(7398), 376–380. <https://doi.org/10.1038/nature11082>
- Drpic, D., Almeida, A. C., Aguiar, P., Renda, F., Damas, J., Lewin, H. A., Larkin, D. M., Khodjakov, A., & Maiato, H. (2018). Chromosome Segregation Is Biased by Kinetochores Size. *Current Biology: CB*, *28*(9), 1344-1356.e5. <https://doi.org/10.1016/j.cub.2018.03.023>
- Duchrow, M., Schlüter, C., Wohlenberg, C., Flad, H. D., & Gerdes, J. (1996). Molecular characterization of the gene locus of the human cell proliferation-associated nuclear protein defined by monoclonal antibody Ki-67. *Cell Proliferation*, *29*(1), 1–12.
- Dwiranti, A., Arifudin, F. S., Wako, T., & Fukui, K. (2021). Imaging the inner structure of chromosomes: Contribution of focused ion beam/scanning

electron microscopy to chromosome research. *Chromosome Research*, 29(1), 51–62. <https://doi.org/10.1007/s10577-021-09650-9>

Earnshaw, W. C., Halligan, B., Cooke, C. A., Heck, M. M., & Liu, L. F. (1985). Topoisomerase II is a structural component of mitotic chromosome scaffolds. *The Journal of Cell Biology*, 100(5), 1706–1715. <https://doi.org/10.1083/jcb.100.5.1706>

Earnshaw, W. C., & Laemmli, U. K. (1983). Architecture of metaphase chromosomes and chromosome scaffolds. *Journal of Cell Biology*, 96(1), 84–93. <https://doi.org/10.1083/jcb.96.1.84>

Elliott, A. D. (2020). Confocal Microscopy: Principles and Modern Practices. *Current Protocols in Cytometry*, 92(1), e68. <https://doi.org/10.1002/cpcy.68>

Eskat, A., Deng, W., Hofmeister, A., Rudolphi, S., Emmerth, S., Hellwig, D., Ulbricht, T., Döring, V., Bancroft, J. M., McAinsh, A. D., Cardoso, M. C., Meraldi, P., Hoischen, C., Leonhardt, H., & Diekmann, S. (2012). Step-Wise Assembly, Maturation and Dynamic Behavior of the Human CENP-P/O/R/Q/U Kinetochore Sub-Complex. *PLoS ONE*, 7(9), e44717. <https://doi.org/10.1371/journal.pone.0044717>

Fachinetti, D., Folco, H. D., Nechemia-Arbely, Y., Valente, L. P., Nguyen, K., Wong, A. J., Zhu, Q., Holland, A. J., Desai, A., Jansen, L. E. T., & Cleveland, D. W. (2013). A two-step mechanism for epigenetic specification of centromere identity and function. *Nature Cell Biology*, 15(9), 1056–1066. <https://doi.org/10.1038/ncb2805>

- Fan, Y., Yang, Q., Lin, Y., Fu, X., & Shu, J. (2025). The effect of endometriosis on oocyte quality: Mechanisms, diagnosis and treatment. *Archives of Gynecology and Obstetrics*. <https://doi.org/10.1007/s00404-025-07965-0>
- Ferrandiz, N., Downie, L., Starling, G. P., & Royle, S. J. (2022). Endomembranes promote chromosome missegregation by ensheathing misaligned chromosomes. *Journal of Cell Biology*, 221(6), e202203021. <https://doi.org/10.1083/jcb.202203021>
- Flemming, W. (1882). *Zellsubstanz, Kern und Zelltheilung*. Vogel.
- Fragouli, E., Alfarawati, S., Spath, K., & Wells, D. (2014). Morphological and cytogenetic assessment of cleavage and blastocyst stage embryos. *Molecular Human Reproduction*, 20(2), 117–126. <https://doi.org/10.1093/molehr/gat073>
- Franasiak, J. M., Forman, E. J., Hong, K. H., Werner, M. D., Upham, K. M., Treff, N. R., & Scott, R. T. (2014). The nature of aneuploidy with increasing age of the female partner: A review of 15,169 consecutive trophoctoderm biopsies evaluated with comprehensive chromosomal screening. *Fertility and Sterility*, 101(3), 656-663.e1. <https://doi.org/10.1016/j.fertnstert.2013.11.004>
- Fukui, K., & Uchiyama, S. (2007). Chromosome protein framework from proteome analysis of isolated human metaphase chromosomes. *The Chemical Record*, 7(4), 230–237. <https://doi.org/10.1002/tcr.20120>
- Fyodorov, D. V., Zhou, B.-R., Skoultchi, A. I., & Bai, Y. (2018). Emerging roles of linker histones in regulating chromatin structure and function. *Nature*

*Reviews. Molecular Cell Biology*, 19(3), 192–206.

<https://doi.org/10.1038/nrm.2017.94>

Garza-Lopez, E., Vue, Z., Katti, P., Neikirk, K., Biete, M., Lam, J., Beasley, H. K.,

Marshall, A. G., Rodman, T. A., Christensen, T. A., Salisbury, J. L., Vang, L.,

Mungai, M., AshShareef, S., Murray, S. A., Shao, J., Streeter, J., Glancy, B.,

Pereira, R. O., ... Hinton, A. (2021). Protocols for Generating Surfaces and

Measuring 3D Organelle Morphology Using Amira. *Cells*, 11(1), 65.

<https://doi.org/10.3390/cells11010065>

Gerdes, J., Lemke, H., Baisch, H., Wacker, H. H., Schwab, U., & Stein, H. (1984).

Cell cycle analysis of a cell proliferation-associated human nuclear antigen defined by the monoclonal antibody Ki-67. *Journal of Immunology (Baltimore, Md.: 1950)*, 133(4), 1710–1715.

Gerdes, J., Schwab, U., Lemke, H., & Stein, H. (1983). Production of a mouse

monoclonal antibody reactive with a human nuclear antigen associated with cell proliferation. *International Journal of Cancer*, 31(1), 13–20.

<https://doi.org/10.1002/ijc.2910310104>

Gershony, O., Pe'er, T., Noach-Hirsh, M., Elia, N., & Tzur, A. (2014). Cytokinetic

abscission is an acute G1 event. *Cell Cycle*, 13(21), 3436–3441.

<https://doi.org/10.4161/15384101.2014.956486>

Greaney, J., Wei, Z., & Homer, H. (2018). Regulation of chromosome segregation

in oocytes and the cellular basis for female meiotic errors. *Human Reproduction Update*, 24(2), 135–161.

<https://doi.org/10.1093/humupd/dmx035>

- Green, R. A., Paluch, E., & Oegema, K. (2012). Cytokinesis in Animal Cells. *Annual Review of Cell and Developmental Biology*, 28(Volume 28, 2012), 29–58.  
<https://doi.org/10.1146/annurev-cellbio-101011-155718>
- Griffith, J. D., & Bonner, J. F. (1973). Chromatin-like Aggregates of Uranyl Acetate. *Nature New Biology*, 244(133), 80–81.  
<https://doi.org/10.1038/newbio244080a0>
- Gruhn, J. R., Zielinska, A. P., Shukla, V., Blanshard, R., Capalbo, A., Cimadomo, D., Nikiforov, D., Chan, A. C.-H., Newnham, L. J., Vogel, I., Scarica, C., Krapchev, M., Taylor, D., Kristensen, S. G., Cheng, J., Ernst, E., Bjørn, A.-M. B., Colmorn, L. B., Blayney, M., ... Hoffmann, E. R. (2019). Chromosome errors in human eggs shape natural fertility over reproductive life span. *Science*, 365(6460), 1466–1469.  
<https://doi.org/10.1126/science.aav7321>
- Hassold, T., & Hunt, P. (2001). To err (meiotically) is human: The genesis of human aneuploidy. *Nature Reviews. Genetics*, 2(4), 280–291.  
<https://doi.org/10.1038/35066065>
- Heasman, J. (2002). Morpholino Oligos: Making Sense of Antisense? *Developmental Biology*, 243(2), 209–214.  
<https://doi.org/10.1006/dbio.2001.0565>
- Hernandez-Verdun, D., & Gautier, T. (1994). The chromosome periphery during mitosis. *BioEssays: News and Reviews in Molecular, Cellular and Developmental Biology*, 16(3), 179–185.  
<https://doi.org/10.1002/bies.950160308>

- Hershey, A. D., & Chase, M. (1952). INDEPENDENT FUNCTIONS OF VIRAL PROTEIN AND NUCLEIC ACID IN GROWTH OF BACTERIOPHAGE. *The Journal of General Physiology*, 36(1), 39–56.
- Hirano, T. (2012). Condensins: Universal organizers of chromosomes with diverse functions. *Genes & Development*, 26(15), 1659–1678. <https://doi.org/10.1101/gad.194746.112>
- Hnisz, D., Day, D. S., & Young, R. A. (2016). Insulated Neighborhoods: Structural and Functional Units of Mammalian Gene Control. *Cell*, 167(5), 1188–1200. <https://doi.org/10.1016/j.cell.2016.10.024>
- Hofmann, K., & Bucher, P. (1995). The FHA domain: A putative nuclear signalling domain found in protein kinases and transcription factors. *Trends in Biochemical Sciences*, 20(9), 347–349. [https://doi.org/10.1016/S0968-0004\(00\)89072-6](https://doi.org/10.1016/S0968-0004(00)89072-6)
- Holder, J., Poser, E., & Barr, F. A. (2019). Getting out of mitosis: Spatial and temporal control of mitotic exit and cytokinesis by PP1 and PP2A. *FEBS Letters*, 593(20), 2908–2924. <https://doi.org/10.1002/1873-3468.13595>
- Holland, A. J., & Cleveland, D. W. (2009). Boveri revisited: Chromosomal instability, aneuploidy and tumorigenesis. *Nature Reviews Molecular Cell Biology*, 10(7), Article 7. <https://doi.org/10.1038/nrm2718>
- Hsu, C. R., Sangha, G., Fan, W., Zheng, J., & Sugioka, K. (2023). Contractile ring mechanosensation and its anillin-dependent tuning during early embryogenesis. *Nature Communications*, 14(1), 8138. <https://doi.org/10.1038/s41467-023-43996-4>

- Hsu, T. C., Arrighi, F. E., Klevecz, R. R., & Brinkley, B. R. (1965). The nucleoli in mitotic divisions of mammalian cells in vitro. *The Journal of Cell Biology*, 26(2), 539–553. <https://doi.org/10.1083/jcb.26.2.539>
- Hudson, D. F., Marshall, K. M., & Earnshaw, W. C. (2009). Condensin: Architect of mitotic chromosomes. *Chromosome Research: An International Journal on the Molecular, Supramolecular and Evolutionary Aspects of Chromosome Biology*, 17(2), 131–144. <https://doi.org/10.1007/s10577-008-9009-7>
- Hug, C. B., & Vaquerizas, J. M. (2018). The Birth of the 3D Genome during Early Embryonic Development. *Trends in Genetics: TIG*, 34(12), 903–914. <https://doi.org/10.1016/j.tig.2018.09.002>
- Icha, J., Weber, M., Waters, J. C., & Norden, C. (2017). Phototoxicity in live fluorescence microscopy, and how to avoid it. *BioEssays*, 39(8), 1700003. <https://doi.org/10.1002/bies.201700003>
- Im, K., Mareninov, S., Diaz, M. F. P., & Yong, W. H. (2019). An introduction to Performing Immunofluorescence Staining. *Methods in Molecular Biology (Clifton, N.J.)*, 1897, 299–311. [https://doi.org/10.1007/978-1-4939-8935-5\\_26](https://doi.org/10.1007/978-1-4939-8935-5_26)
- Information (US), N. C. for B. (1998). Chromosome Map. In *Genes and Disease [Internet]*. National Center for Biotechnology Information (US). <https://www.ncbi.nlm.nih.gov/books/NBK22266/>
- Kadauke, S., & Blobel, G. A. (2009). Chromatin loops in gene regulation. *Biochimica Et Biophysica Acta*, 1789(1), 17–25. <https://doi.org/10.1016/j.bbagr.2008.07.002>

- Kamentsky, L., Jones, T. R., Fraser, A., Bray, M.-A., Logan, D. J., Madden, K. L., Ljosa, V., Rueden, C., Eliceiri, K. W., & Carpenter, A. E. (2011). Improved structure, function and compatibility for CellProfiler: Modular high-throughput image analysis software. *Bioinformatics*, *27*(8), 1179–1180. <https://doi.org/10.1093/bioinformatics/btr095>
- Kasapoglu, I., Kuspinar, G., Saribal, S., Turk, P., Avci, B., & Uncu, G. (2018). Detrimental effects of endometriosis on oocyte morphology in intracytoplasmic sperm injection cycles: A retrospective cohort study. *Gynecological Endocrinology*, *34*(3), 206–211. <https://doi.org/10.1080/09513590.2017.1391203>
- Kopáni, M., Vraníková, B., Kosnáč, D., Zeman, M., Šišovský, V., Polakovičová, S., & Biró, C. (2019). Pineal gland calcification under hypoxic conditions. *Physiological Research*, S405–S413. <https://doi.org/10.33549/physiolres.934378>
- Kouzarides, T. (2007). Chromatin modifications and their function. *Cell*, *128*(4), 693–705. <https://doi.org/10.1016/j.cell.2007.02.005>
- Krude, T., & Elgin, S. C. (1996). Pushing nucleosomes around. Chromatin. *Current Biology: CB*, *6*(5), 511–515. [https://doi.org/10.1016/s0960-9822\(02\)00529-8](https://doi.org/10.1016/s0960-9822(02)00529-8)
- Kubicek, D., Hornak, M., Horak, J., Navratil, R., Tauwinklova, G., Rubes, J., & Vesela, K. (2019). Incidence and origin of meiotic whole and segmental chromosomal aneuploidies detected by karyomapping. *Reproductive Biomedicine Online*, *38*(3), 330–339. <https://doi.org/10.1016/j.rbmo.2018.11.023>

- Kumari, R., & Jat, P. (2021). Mechanisms of Cellular Senescence: Cell Cycle Arrest and Senescence Associated Secretory Phenotype. *Frontiers in Cell and Developmental Biology*, 9. <https://doi.org/10.3389/fcell.2021.645593>
- Lansdorp, P. M. (2008). Telomeres, stem cells, and hematology. *Blood*, 111(4), 1759–1766. <https://doi.org/10.1182/blood-2007-09-084913>
- Larijani, B., & Poccia, D. L. (2009). Nuclear Envelope Formation: Mind the Gaps. *Annual Review of Biophysics*, 38(Volume 38, 2009), 107–124. <https://doi.org/10.1146/annurev.biophys.050708.133625>
- Lewis, C. D., & Laemmli, U. K. (1982). Higher order metaphase chromosome structure: Evidence for metalloprotein interactions. *Cell*, 29(1), 171–181. [https://doi.org/10.1016/0092-8674\(82\)90101-5](https://doi.org/10.1016/0092-8674(82)90101-5)
- Liang, P., Xu, Y., Zhang, X., Ding, C., Huang, R., Zhang, Z., Lv, J., Xie, X., Chen, Y., Li, Y., Sun, Y., Bai, Y., Songyang, Z., Ma, W., Zhou, C., & Huang, J. (2015). CRISPR/Cas9-mediated gene editing in human tripronuclear zygotes. *Protein & Cell*, 6(5), 363–372. <https://doi.org/10.1007/s13238-015-0153-5>
- Liu, J., Wang, L., Wang, Z., & Liu, J.-P. (2019). Roles of Telomere Biology in Cell Senescence, Replicative and Chronological Ageing. *Cells*, 8(1), 54. <https://doi.org/10.3390/cells8010054>
- Longo, F. J., & Chen, D.-Y. (1985). Development of cortical polarity in mouse eggs: Involvement of the meiotic apparatus. *Developmental Biology*, 107(2), 382–394. [https://doi.org/10.1016/0012-1606\(85\)90320-3](https://doi.org/10.1016/0012-1606(85)90320-3)
- Lu, X., Gao, Z., Qin, D., & Li, L. (2017). A Maternal Functional Module in the Mammalian Oocyte-To-Embryo Transition. *Trends in Molecular Medicine*, 23(11), 1014–1023. <https://doi.org/10.1016/j.molmed.2017.09.004>

- Luckner, M., & Wanner, G. (2018). Precise and economic FIB/SEM for CLEM: With 2 nm voxels through mitosis. *Histochemistry & Cell Biology*, *150*(2), 149–170. <https://doi.org/10.1007/s00418-018-1681-x>
- Maeshima, K., Eltsov, M., & Laemmli, U. K. (2005). Chromosome structure: Improved immunolabeling for electron microscopy. *Chromosoma*, *114*(5), 365–375. <https://doi.org/10.1007/s00412-005-0023-7>
- Maeshima, K., & Laemmli, U. K. (2003). A Two-Step Scaffolding Model for Mitotic Chromosome Assembly. *Developmental Cell*, *4*(4), 467–480. [https://doi.org/10.1016/S1534-5807\(03\)00092-3](https://doi.org/10.1016/S1534-5807(03)00092-3)
- Magidson, V., Paul, R., Yang, N., Ault, J. G., O’Connell, C. B., Tikhonenko, I., McEwen, B. F., Mogilner, A., & Khodjakov, A. (2015). Adaptive changes in the kinetochore architecture facilitate proper spindle assembly. *Nature Cell Biology*, *17*(9), 1134–1144. <https://doi.org/10.1038/ncb3223>
- Maiato, H., DeLuca, J., Salmon, E. D., & Earnshaw, W. C. (2004). The dynamic kinetochore-microtubule interface. *Journal of Cell Science*, *117*(23), 5461–5477. <https://doi.org/10.1242/jcs.01536>
- Matsuda, A., Shao, L., Boulanger, J., Kervrann, C., Carlton, P. M., Kner, P., Agard, D., & Sedat, J. W. (2010). Condensed Mitotic Chromosome Structure at Nanometer Resolution Using PALM and EGFP- Histones. *PLOS ONE*, *5*(9), e12768. <https://doi.org/10.1371/journal.pone.0012768>
- Matthews, H. K., Bertoli, C., & de Bruin, R. A. M. (2022). Cell cycle control in cancer. *Nature Reviews Molecular Cell Biology*, *23*(1), 74–88. <https://doi.org/10.1038/s41580-021-00404-3>

- Mazumdar, M., Lee, J.-H., Sengupta, K., Ried, T., Rane, S., & Misteli, T. (2006). Tumor Formation via Loss of a Molecular Motor Protein. *Current Biology*, 16(15), 1559–1564. <https://doi.org/10.1016/j.cub.2006.06.029>
- McAinsh, A. D., & Kops, G. J. P. L. (2023). Principles and dynamics of spindle assembly checkpoint signalling. *Nature Reviews Molecular Cell Biology*, 24(8), 543–559. <https://doi.org/10.1038/s41580-023-00593-z>
- McClintock, B. (1934). The relation of a particular chromosomal element to the development of the nucleoli in *Zea mays*. *Zeitschrift Für Zellforschung Und Mikroskopische Anatomie*, 21(2), 294–326. <https://doi.org/10.1007/BF00374060>
- Mckeon, F., Tuffanelli, D., Kobayashi, S., & Kirschner, M. (1984). The redistribution of a conserved nuclear envelope protein during the cell cycle suggests a pathway for chromosome condensation. *Cell*, 36(1), 83–92. [https://doi.org/10.1016/0092-8674\(84\)90076-X](https://doi.org/10.1016/0092-8674(84)90076-X)
- McKinley, K. L., & Cheeseman, I. M. (2016). The molecular basis for centromere identity and function. *Nature Reviews. Molecular Cell Biology*, 17(1), 16–29. <https://doi.org/10.1038/nrm.2015.5>
- McNamara, G., Difilippantonio, M., Ried, T., & Bieber, F. R. (2017). Microscopy and Image Analysis. *Current Protocols in Human Genetics*, 94(1), 4.4.1-4.4.89. <https://doi.org/10.1002/cphg.42>
- Meshorer, E., & Plath, K. (2020). Chromatin and Nuclear Architecture in Stem Cells. *Stem Cell Reports*, 15(6), 1155–1157. <https://doi.org/10.1016/j.stemcr.2020.11.012>

- Metz, C. W. (1934). The Rôle of the “Chromosome Sheath” in Mitosis, and Its Possible Relation to Phenomena of Mutation. *Proceedings of the National Academy of Sciences*, 20(3), 159–163. <https://doi.org/10.1073/pnas.20.3.159>
- Meunier, S., & Vernos, I. (2012). Microtubule assembly during mitosis – from distinct origins to distinct functions? *Journal of Cell Science*, 125(12), 2805–2814. <https://doi.org/10.1242/jcs.092429>
- Mosgöller, W., Leitch, A. R., Brown, J. K., & Heslop-Harrison, J. S. (1991). Chromosome arrangements in human fibroblasts at mitosis. *Human Genetics*, 88(1), 27–33. <https://doi.org/10.1007/BF00204924>
- Moulton, J. D. (2006). Using Morpholinos to Control Gene Expression. *Current Protocols in Nucleic Acid Chemistry*, 27(1), 4301–43024. <https://doi.org/10.1002/0471142700.nc0430s27>
- Muñoz-Espín, D., & Serrano, M. (2014). Cellular senescence: From physiology to pathology. *Nature Reviews. Molecular Cell Biology*, 15(7), 482–496. <https://doi.org/10.1038/nrm3823>
- Musacchio, A., & Desai, A. (2017). A Molecular View of Kinetochore Assembly and Function. *Biology*, 6(1), 5. <https://doi.org/10.3390/biology6010005>
- Myers, S. M., & Collins, I. (2016). Recent Findings and Future Directions for Interpolar Mitotic Kinesin Inhibitors in Cancer Therapy. *Future Medicinal Chemistry*, 8(4), 463–489. <https://doi.org/10.4155/fmc.16.5>
- Nabais, C., Peneda, C., & Bettencourt-Dias, M. (2020). Evolution of centriole assembly. *Current Biology*, 30(10), R494–R502. <https://doi.org/10.1016/j.cub.2020.02.036>

- Nagaoka, S. I., Hassold, T. J., & Hunt, P. A. (2012). Human aneuploidy: Mechanisms and new insights into an age-old problem. *Nature Reviews. Genetics*, *13*(7), 493–504. <https://doi.org/10.1038/nrg3245>
- Nagasaka, K., Hossain, M. J., Roberti, M. J., Ellenberg, J., & Hirota, T. (2016). Sister chromatid resolution is an intrinsic part of chromosome organization in prophase. *Nature Cell Biology*, *18*(6), 692–699. <https://doi.org/10.1038/ncb3353>
- Nägeli, C. W. von, & Nägeli, K. W. (1884). *Mechanisch-physiologische Theorie der Abstammungslehre*. A. München.
- Nakagawa, S., & FitzHarris, G. (2017). Intrinsically Defective Microtubule Dynamics Contribute to Age-Related Chromosome Segregation Errors in Mouse Oocyte Meiosis-I. *Current Biology*, *27*(7), 1040–1047. <https://doi.org/10.1016/j.cub.2017.02.025>
- Naumova, N., Imakaev, M., Fudenberg, G., Zhan, Y., Lajoie, B. R., Mirny, L. A., & Dekker, J. (2013). Organization of the mitotic chromosome. *Science (New York, N.Y.)*, *342*(6161), 948–953. <https://doi.org/10.1126/science.1236083>
- Navarro, A. P., & Cheeseman, I. M. (2021). Kinetochore assembly throughout the cell cycle. *Seminars in Cell & Developmental Biology*, *117*, 62–74. <https://doi.org/10.1016/j.semcd.2021.03.008>
- Nora, E. P., Lajoie, B. R., Schulz, E. G., Giorgetti, L., Okamoto, I., Servant, N., Piolot, T., van Berkum, N. L., Meisig, J., Sedat, J., Gribnau, J., Barillot, E., Blüthgen, N., Dekker, J., & Heard, E. (2012). Spatial partitioning of the regulatory landscape of the X-inactivation centre. *Nature*, *485*(7398), 381–385. <https://doi.org/10.1038/nature11049>

- Nurk, S., Koren, S., Rhie, A., Rautiainen, M., Bzikadze, A. V., Mikheenko, A., Vollger, M. R., Altemose, N., Uralsky, L., Gershman, A., Aganezov, S., Hoyt, S. J., Diekhans, M., Logsdon, G. A., Alonge, M., Antonarakis, S. E., Borchers, M., Bouffard, G. G., Brooks, S. Y., ... Phillippy, A. M. (2022). The complete sequence of a human genome. *Science*, *376*(6588), 44–53. <https://doi.org/10.1126/science.abj6987>
- Nurse, P. (2000). A Long Twentieth Century of the Cell Cycle and Beyond. *Cell*, *100*(1), 71–78. [https://doi.org/10.1016/S0092-8674\(00\)81684-0](https://doi.org/10.1016/S0092-8674(00)81684-0)
- Ohkura, H. (2015). Meiosis: An Overview of Key Differences from Mitosis. *Cold Spring Harbor Perspectives in Biology*, *7*(5), a015859. <https://doi.org/10.1101/cshperspect.a015859>
- Ohta, S., Bukowski-Wills, J.-C., Sanchez-Pulido, L., Alves, F. de L., Wood, L., Chen, Z. A., Platani, M., Fischer, L., Hudson, D. F., Ponting, C. P., Fukagawa, T., Earnshaw, W. C., & Rappsilber, J. (2010). The Protein Composition of Mitotic Chromosomes Determined Using Multiclassifier Combinatorial Proteomics. *Cell*, *142*(5), 810–821. <https://doi.org/10.1016/j.cell.2010.07.047>
- Ong, C.-T., & Corces, V. G. (2014). CTCF: An architectural protein bridging genome topology and function. *Nature Reviews. Genetics*, *15*(4), 234–246. <https://doi.org/10.1038/nrg3663>
- Pan, H., Ma, P., Zhu, W., & Schultz, R. M. (2008). Age-associated increase in aneuploidy and changes in gene expression in mouse eggs. *Developmental Biology*, *316*(2), 397–407. <https://doi.org/10.1016/j.ydbio.2008.01.048>

- Paulson, J. R., Hudson, D. F., Cisneros-Soberanis, F., & Earnshaw, W. C. (2021). Mitotic chromosomes. *Seminars in Cell & Developmental Biology*, 117, 7–29. <https://doi.org/10.1016/j.semcdb.2021.03.014>
- Paulson, J. R., & Laemmli, U. K. (1977). The structure of histone-depleted metaphase chromosomes. *Cell*, 12(3), 817–828. [https://doi.org/10.1016/0092-8674\(77\)90280-X](https://doi.org/10.1016/0092-8674(77)90280-X)
- Paweletz, N. (2001). Walther Flemming: Pioneer of mitosis research. *Nature Reviews Molecular Cell Biology*, 2(1), Article 1. <https://doi.org/10.1038/35048077>
- Peddie, C. J., Genoud, C., Kreshuk, A., Meechan, K., Micheva, K. D., Narayan, K., Pape, C., Parton, R. G., Schieber, N. L., Schwab, Y., Titze, B., Verkade, P., Aubrey, A., & Collinson, L. M. (2022). Volume electron microscopy. *Nature Reviews. Methods Primers*, 2, 51. <https://doi.org/10.1038/s43586-022-00131-9>
- Pennycook, B. R., & Barr, A. R. (2020). Restriction point regulation at the crossroads between quiescence and cell proliferation. *FEBS Letters*, 594(13), 2046–2060. <https://doi.org/10.1002/1873-3468.13867>
- Phengchat, R., Hayashida, M., Ohmido, N., Homeniuk, D., & Fukui, K. (2019). 3D observation of chromosome scaffold structure using a 360° electron tomography sample holder. *Micron (Oxford, England: 1993)*, 126, 102736. <https://doi.org/10.1016/j.micron.2019.102736>
- Pincus, G., & Enzmann, E. V. (1935). THE COMPARATIVE BEHAVIOR OF MAMMALIAN EGGS IN VIVO AND IN VITRO. *Journal of Experimental Medicine*, 62(5), 665–675. <https://doi.org/10.1084/jem.62.5.665>

- Pluta, A. F., Mackay, A. M., Ainsztein, A. M., Goldberg, I. G., & Earnshaw, W. C. (1995). The centromere: Hub of chromosomal activities. *Science (New York, N.Y.)*, *270*(5242), 1591–1594. <https://doi.org/10.1126/science.270.5242.1591>
- Poonperm, R., Takata, H., Hamano, T., Matsuda, A., Uchiyama, S., Hiraoka, Y., & Fukui, K. (2015). Chromosome Scaffold is a Double-Stranded Assembly of Scaffold Proteins. *Scientific Reports*, *5*, 11916. <https://doi.org/10.1038/srep11916>
- Rhodes, A. (2013). 4—Fixation of tissues. In S. K. Suvarna, C. Layton, & J. D. Bancroft (Eds.), *Bancroft's Theory and Practice of Histological Techniques (Seventh Edition)* (pp. 69–93). Churchill Livingstone. <https://doi.org/10.1016/B978-0-7020-4226-3.00004-4>
- Ris, H., & Witt, P. L. (1981). Structure of the mammalian kinetochore. *Chromosoma*, *82*(2), 153–170. <https://doi.org/10.1007/BF00286101>
- Robin, C., Uk, A., Decanter, C., Behal, H., Collinet, P., Rubod, C., Barbotin, A.-L., & Robin, G. (2021). Impact of endometriosis on oocyte morphology in IVF-ICSI: Retrospective study of a cohort of more than 6000 mature oocytes. *Reproductive Biology and Endocrinology*, *19*(1), 160. <https://doi.org/10.1186/s12958-021-00798-x>
- Rubin, S. M., Sage, J., & Skotheim, J. M. (2020). Integrating Old and New Paradigms of G1/S Control. *Molecular Cell*, *80*(2), 183–192. <https://doi.org/10.1016/j.molcel.2020.08.020>
- Russell, M. R. G., Lerner, T. R., Burden, J. J., Nkwe, D. O., Pelchen-Matthews, A., Domart, M.-C., Durgan, J., Weston, A., Jones, M. L., Peddie, C. J.,

- Carzaniga, R., Florey, O., Marsh, M., Gutierrez, M. G., & Collinson, L. M. (2017). 3D correlative light and electron microscopy of cultured cells using serial blockface scanning electron microscopy. *Journal of Cell Science*, *130*(1), 278–291. <https://doi.org/10.1242/jcs.188433>
- Sagata, N. (1996). Meiotic metaphase arrest in animal oocytes: Its mechanisms and biological significance. *Trends in Cell Biology*, *6*(1), 22–28. [https://doi.org/10.1016/0962-8924\(96\)81034-8](https://doi.org/10.1016/0962-8924(96)81034-8)
- Samejima, K., Gibcus, J. H., Abraham, S., Cisneros-Soberanis, F., Samejima, I., Beckett, A. J., Pučeková, N., Abad, M. A., Medina-Pritchard, B., Paulson, J. R., Xie, L., Jeyapakash, A. A., Prior, I. A., Mirny, L. A., Dekker, J., Goloborodko, A., & Earnshaw, W. C. (2024). Rules of engagement for condensins and cohesins guide mitotic chromosome formation. *bioRxiv*, 2024.04.18.590027. <https://doi.org/10.1101/2024.04.18.590027>
- Samejima, K., Samejima, I., Vagnarelli, P., Ogawa, H., Vargiu, G., Kelly, D. A., de Lima Alves, F., Kerr, A., Green, L. C., Hudson, D. F., Ohta, S., Cooke, C. A., Farr, C. J., Rappsilber, J., & Earnshaw, W. C. (2012). Mitotic chromosomes are compacted laterally by KIF4 and condensin and axially by topoisomerase II $\alpha$ . *The Journal of Cell Biology*, *199*(5), 755–770. <https://doi.org/10.1083/jcb.201202155>
- Sathananthan, A. H. (1997). Ultrastructure of the human egg. *Human Cell*, *10*(1), 21–38.
- Schalch, T., Duda, S., Sargent, D. F., & Richmond, T. J. (2005). X-ray structure of a tetranucleosome and its implications for the chromatin fibre. *Nature*, *436*(7047), 138–141. <https://doi.org/10.1038/nature03686>

- Schalch, T., & Steiner, F. A. (2017). Structure of centromere chromatin: From nucleosome to chromosomal architecture. *Chromosoma*, *126*(4), 443–455. <https://doi.org/10.1007/s00412-016-0620-7>
- Scheuerlein, H., Henschke, F., & Köckerling, F. (2017). Wilhelm von Waldeyer-Hartz—A Great Forefather: His Contributions to Anatomy with Particular Attention to “His” Fascia. *Frontiers in Surgery*, *4*. <https://www.frontiersin.org/articles/10.3389/fsurg.2017.00074>
- Schlaitz, A., J, T., Cc, W., Jr, Y., & R, H. (2013). REEP3/4 ensure endoplasmic reticulum clearance from metaphase chromatin and proper nuclear envelope architecture. *Developmental Cell*, *26*(3). <https://doi.org/10.1016/j.devcel.2013.06.016>
- Schlüter, C., Duchrow, M., Wohlenberg, C., Becker, M. H., Key, G., Flad, H. D., & Gerdes, J. (1993). The cell proliferation-associated antigen of antibody Ki-67: A very large, ubiquitous nuclear protein with numerous repeated elements, representing a new kind of cell cycle-maintaining proteins. *The Journal of Cell Biology*, *123*(3), 513–522. <https://doi.org/10.1083/jcb.123.3.513>
- Schmidt, M. H. H., Broll, R., Bruch, H.-P., Finniss, S., Bögler, O., & Duchrow, M. (2004). Proliferation marker pKi-67 occurs in different isoforms with various cellular effects. *Journal of Cellular Biochemistry*, *91*(6), 1280–1292. <https://doi.org/10.1002/jcb.20016>
- Scholzen, T., & Gerdes, J. (2000). The Ki-67 protein: From the known and the unknown. *Journal of Cellular Physiology*, *182*(3), 311–322.

[https://doi.org/10.1002/\(SICI\)1097-4652\(200003\)182:3<311::AID-JCP1>3.0.CO;2-9](https://doi.org/10.1002/(SICI)1097-4652(200003)182:3<311::AID-JCP1>3.0.CO;2-9)

Schweizer, N., Pawar, N., Weiss, M., & Maiato, H. (2015). An organelle-exclusion envelope assists mitosis and underlies distinct molecular crowding in the spindle region. *The Journal of Cell Biology*, 210(5), 695–704. <https://doi.org/10.1083/jcb.201506107>

Sclafani, R. A., & Holzen, T. M. (2007). Cell Cycle Regulation of DNA Replication. *Annual Review of Genetics*, 41, 237–280. <https://doi.org/10.1146/annurev.genet.41.110306.130308>

Severson, A. F., von Dassow, G., & Bowerman, B. (2016). Oocyte Meiotic Spindle Assembly and Function. *Current Topics in Developmental Biology*, 116, 65–98. <https://doi.org/10.1016/bs.ctdb.2015.11.031>

SEZEN, S. C., & CINCIK, M. (2003). Oocyte Membrane Maturation and Oocyte-Sperm Relationship: Transmission Electron Microscopy Study. *Archives of Andrology*, 49(4), 297–305. <https://doi.org/10.1080/01485010390204986>

Shay, J. W., & Wright, W. E. (2019). Telomeres and telomerase: Three decades of progress. *Nature Reviews. Genetics*, 20(5), 299–309. <https://doi.org/10.1038/s41576-019-0099-1>

Simionescu, N., & Simionescu, M. (1976). Galloylglucoses of low molecular weight as mordant in electron microscopy. I. Procedure, and evidence for mordanting effect. *The Journal of Cell Biology*, 70(3), 608–621. <https://doi.org/10.1083/jcb.70.3.608>

Simpson, E. L., Wetherall, B., Byrska, A., Cheeseman, L. P., Mendonca, T., Xing, X., Beckett, A. J., Maiato, H., Sarginson, A., Prior, I. A., Hartshorne, G. M.,

- McAinsh, A. D., Madgwick, S., & Booth, D. G. (2024). *The Chromosome Periphery is an Essential Compartment of Oocyte Chromosomes* (p. 2024.12.20.629576). bioRxiv. <https://doi.org/10.1101/2024.12.20.629576>
- Sobecki, M., Mrouj, K., Camasses, A., Parisis, N., Nicolas, E., Llères, D., Gerbe, F., Prieto, S., Krasinska, L., David, A., Eguren, M., Birling, M.-C., Urbach, S., Hem, S., Déjardin, J., Malumbres, M., Jay, P., Dulic, V., Lafontaine, D. L., ... Fisher, D. (2016). The cell proliferation antigen Ki-67 organises heterochromatin. *eLife*, 5, e13722. <https://doi.org/10.7554/eLife.13722>
- Stamatiou, K., Chmielewska, A., Ohta, S., Earnshaw, W. C., & Vagnarelli, P. (2023). CCDC86 is a novel Ki-67-interacting protein important for cell division. *Journal of Cell Science*, 136(2), jcs260391. <https://doi.org/10.1242/jcs.260391>
- Stenström, L., Mahdessian, D., Gnann, C., Cesnik, A. J., Ouyang, W., Leonetti, M. D., Uhlén, M., Cuylen-Haering, S., Thul, P. J., & Lundberg, E. (2020). Mapping the nucleolar proteome reveals a spatiotemporal organization related to intrinsic protein disorder. *Molecular Systems Biology*, 16(8), e9469. <https://doi.org/10.15252/msb.20209469>
- Stylianidou, S., Brennan, C., Nissen, S. B., Kuwada, N. J., & Wiggins, P. A. (2016). SuperSegger: Robust image segmentation, analysis and lineage tracking of bacterial cells. *Molecular Microbiology*, 102(4), 690–700. <https://doi.org/10.1111/mmi.13486>
- Sullivan, B. A. (2013). Centromeres. In W. J. Lennarz & M. D. Lane (Eds.), *Encyclopedia of Biological Chemistry (Second Edition)* (pp. 446–450). Academic Press. <https://doi.org/10.1016/B978-0-12-378630-2.00471-0>

- Sutton, W. S. (1903). THE CHROMOSOMES IN HEREDITY. *The Biological Bulletin*, 4(5), 231–250. <https://doi.org/10.2307/1535741>
- Takagi, M., Nishiyama, Y., Taguchi, A., & Imamoto, N. (2014). Ki67 Antigen Contributes to the Timely Accumulation of Protein Phosphatase 1 $\gamma$  on Anaphase Chromosomes \*. *Journal of Biological Chemistry*, 289(33), 22877–22887. <https://doi.org/10.1074/jbc.M114.556647>
- Takata, H., Uchiyama, S., Nakamura, N., Nakashima, S., Kobayashi, S., Sone, T., Kimura, S., Lahmers, S., Granzier, H., Labeit, S., Matsunaga, S., & Fukui, K. (2007). A comparative proteome analysis of human metaphase chromosomes isolated from two different cell lines reveals a set of conserved chromosome-associated proteins. *Genes to Cells*, 12(3), 269–284. <https://doi.org/10.1111/j.1365-2443.2007.01051.x>
- Takenouchi, O., Sakakibara, Y., & Kitajima, T. S. (2024). Live chromosome identifying and tracking reveals size-based spatial pathway of meiotic errors in oocytes. *Science*, 385(6706), eadn5529. <https://doi.org/10.1126/science.adn5529>
- Tandle, A., & Camphausen, K. (2016). Mitotic Protein Kinase 1: Role in Spindle Assembly Checkpoint Revisited. *Journal of Cancer Clinical Trials*, 1(2), 111.
- Tate, V. E., & Philipson, L. (1979). Parental adenovirus DNA accumulates in nucleosome-like structures in infected cells. *Nucleic Acids Research*, 6(8), 2769–2785. <https://doi.org/10.1093/nar/6.8.2769>
- Tatíčková, M., Trebichalská, Z., Kyjovská, D., Otevřel, P., Kloudová, S., & Holubcová, Z. (2023). The ultrastructural nature of human oocytes'

- cytoplasmic abnormalities and the role of cytoskeleton dysfunction. *F&S Science*, 4(4), 267–278. <https://doi.org/10.1016/j.xfss.2023.09.002>
- Toft, C. L. F., Ingerslev, H. J., Kesmodel, U. S., Diemer, T., Degn, B., Ernst, A., Okkels, H., Kjartansdóttir, K. R., & Pedersen, I. S. (2020). A systematic review on concurrent aneuploidy screening and preimplantation genetic testing for hereditary disorders: What is the prevalence of aneuploidy and is there a clinical effect from aneuploidy screening? *Acta Obstetricia Et Gynecologica Scandinavica*, 99(6), 696–706. <https://doi.org/10.1111/aogs.13823>
- Traut, W., Endl, E., Scholzen, T., Gerdes, J., & Winking, H. (2002). The temporal and spatial distribution of the proliferation associated Ki-67 protein during female and male meiosis. *Chromosoma*, 111(3), 156–164. <https://doi.org/10.1007/s00412-002-0202-8>
- Trebichalská, Z., Javůrek, J., Tatičková, M., Kyjovská, D., Kloudová, S., Otevřel, P., Hampl, A., & Holubcová, Z. (2021). High-Resolution 3D Reconstruction of Human Oocytes Using Focused Ion Beam Scanning Electron Microscopy. *Frontiers in Cell and Developmental Biology*, 9. <https://doi.org/10.3389/fcell.2021.755740>
- Trebichalská, Z., Kyjovská, D., Kloudová, S., Otevřel, P., Hampl, A., & Holubcová, Z. (2021). Cytoplasmic maturation in human oocytes: An ultrastructural study †. *Biology of Reproduction*, 104(1), 106–116. <https://doi.org/10.1093/biolre/ioaa174>
- Tremethick, D. J. (2007). Higher-order structures of chromatin: The elusive 30 nm fiber. *Cell*, 128(4), 651–654. <https://doi.org/10.1016/j.cell.2007.02.008>

- Tripathi, A., Kumar, K. V. P., & Chaube, S. K. (2010). Meiotic cell cycle arrest in mammalian oocytes. *Journal of Cellular Physiology*, 223(3), 592–600. <https://doi.org/10.1002/jcp.22108>
- Turner, K. J., Vasu, V., & Griffin, D. K. (2019). Telomere Biology and Human Phenotype. *Cells*, 8(1), 73. <https://doi.org/10.3390/cells8010073>
- Ul-Hamid, A. (2018). Components of the SEM. In A. Ul-Hamid (Ed.), *A Beginners' Guide to Scanning Electron Microscopy* (pp. 15–76). Springer International Publishing. [https://doi.org/10.1007/978-3-319-98482-7\\_2](https://doi.org/10.1007/978-3-319-98482-7_2)
- Uxa, S., Castillo-Binder, P., Kohler, R., Stangner, K., Müller, G. A., & Engeland, K. (2021). Ki-67 gene expression. *Cell Death & Differentiation*, 28(12), 3357–3370. <https://doi.org/10.1038/s41418-021-00823-x>
- Van Blerkom, J. (1990). Occurrence and developmental consequences of aberrant cellular organization in meiotically mature human oocytes after exogenous ovarian hyperstimulation. *Journal of Electron Microscopy Technique*, 16(4), 324–346. <https://doi.org/10.1002/jemt.1060160405>
- van Rijnsoever, C., Oorschot, V., & Klumperman, J. (2008). Correlative light-electron microscopy (CLEM) combining live-cell imaging and immunolabeling of ultrathin cryosections. *Nature Methods*, 5(11), 973–980. <https://doi.org/10.1038/nmeth.1263>
- Vanneste, D., Ferreira, V., & Vernos, I. (2011). Chromokinesins: Localization-dependent functions and regulation during cell division. *Biochemical Society Transactions*, 39(5), 1154–1160. <https://doi.org/10.1042/BST0391154>

- Verlinsky, Y., Ginsberg, N., Lifchez, A., Valle, J., Moise, J., & Strom, C. M. (1990). Analysis of the first polar body: Preconception genetic diagnosis. *Human Reproduction (Oxford, England)*, 5(7), 826–829. <https://doi.org/10.1093/oxfordjournals.humrep.a137192>
- Walther, N., Hossain, M. J., Politi, A. Z., Koch, B., Kueblbeck, M., Ødegård-Fougner, Ø., Lampe, M., & Ellenberg, J. (2018). A quantitative map of human Condensins provides new insights into mitotic chromosome architecture. *The Journal of Cell Biology*, 217(7), 2309–2328. <https://doi.org/10.1083/jcb.201801048>
- Watson, J. D., & Crick, F. H. C. (1953). Molecular Structure of Nucleic Acids: A Structure for Deoxyribose Nucleic Acid. *Nature*, 171(4356), 737–738. <https://doi.org/10.1038/171737a0>
- Webster, A., & Schuh, M. (2017). Mechanisms of Aneuploidy in Human Eggs. *Trends in Cell Biology*, 27(1), 55–68. <https://doi.org/10.1016/j.tcb.2016.09.002>
- Wouters, C. H., & Koerten, H. K. (1982). Combined light microscope and scanning electron microscope, a new instrument for cell biology. *Cell Biology International Reports*, 6(10), 955–959. [https://doi.org/10.1016/0309-1651\(82\)90007-8](https://doi.org/10.1016/0309-1651(82)90007-8)
- Wynne, D. J., & Funabiki, H. (2016). Heterogeneous architecture of vertebrate kinetochores revealed by three-dimensional superresolution fluorescence microscopy. *Molecular Biology of the Cell*, 27(22), 3395–3404. <https://doi.org/10.1091/mbc.E16-02-0130>

- Xu, N., & Chang, D. C. (2007). Different Thresholds of MPF Inactivation are Responsible for Controlling Different Mitotic Events in Mammalian Cell Division. *Cell Cycle*, 6(13), 1639–1645. <https://doi.org/10.4161/cc.6.13.4385>
- Yang, Y., Tan, W., Chen, C., Jin, L., & Huang, B. (2022). Correlation of the position and status of the polar body from the fertilized oocyte to the euploid status of blastocysts. *Frontiers in Genetics*, 13. <https://doi.org/10.3389/fgene.2022.1006870>
- Yerushalmi, R., Woods, R., Ravdin, P. M., Hayes, M. M., & Gelmon, K. A. (2010). Ki67 in breast cancer: Prognostic and predictive potential. *The Lancet Oncology*, 11(2), 174–183. [https://doi.org/10.1016/S1470-2045\(09\)70262-1](https://doi.org/10.1016/S1470-2045(09)70262-1)
- ZEISS MultiSEM: The World's Fastest Scanning Electron Microscope*. (n.d.). Retrieved 24 March 2025, from <https://www.zeiss.com/microscopy/en/products/sem-fib-sem/sem/multisem.html>
- Zickler, D., & Kleckner, N. (1998). THE LEPTOTENE-ZYGOTENE TRANSITION OF MEIOSIS. *Annual Review of Genetics*, 32(Volume 32, 1998), 619–697. <https://doi.org/10.1146/annurev.genet.32.1.619>
- Zielinska, A. P., Bellou, E., Sharma, N., Frombach, A.-S., Seres, K. B., Gruhn, J. R., Blayney, M., Eckel, H., Moltrecht, R., Elder, K., Hoffmann, E. R., & Schuh, M. (2019). Meiotic Kinetochores Fragment into Multiple Lobes upon Cohesin Loss in Aging Eggs. *Current Biology: CB*, 29(22), 3749–3765.e7. <https://doi.org/10.1016/j.cub.2019.09.006>

Zielinska, A. P., & Schuh, M. (2018). Chapter 17—A microscopy-based approach for studying meiosis in live and fixed human oocytes. In H. Maiato & M. Schuh (Eds.), *Methods in Cell Biology* (Vol. 145, pp. 315–333). Academic Press. <https://doi.org/10.1016/bs.mcb.2018.03.039>